November 2020

Fluid-Driven Fracture Initiation from Oil and Gas Wells Considering Lifetime Stresses

Andreas Michael

FLUID-DRIVEN FRACTURE INITIATION FROM OIL AND GAS WELLS CONSIDERING LIFETIME STRESSES

A Dissertation

Submitted to the Graduate Faculty of the
Louisiana State University and
Agricultural and Mechanical College
in partial fulfillment of the
requirements for the degree of
Doctor of Philosophy

in

The Department of Petroleum Engineering

by
Andreas Michael
B.S.P.E., The University of Texas at Austin, 2013
M.S.E., The University of Texas at Austin, 2016
December 2020

To my late grandfather,

Andreas Ch. «Ωρολογάς» Gypsiotis (1940-2020)

and great aunt,

Andriani Petrou (1928-2018)

who did not live to see the end of this journey.

Acknowledgements

To Dr. Ipsita Gupta, for her meticulous efforts, I owe a great deal. This dissertation was possible because of her astute formulation of a stimulating concept, as well as support and encouragement throughout my time at the Louisiana State University. It is a rarity for a doctoral student to find success without proper guidance.

Dr. Karsten E. Thompson and Dr. Yuanhang Chen have done much to guide my research, ensuring that the final product is representative of what is expected from a department which comprises the main thrust of petroleum engineering worldwide. Pragmatism and relevance should count as the "vices" of our department.

Incoming students, especially foreign undergraduates, tend to be "alien" to their future profession and have no clear-cut objectives. Drawn by reputation, students try hard to enter one of the most prestigious universities in their discipline. Nevertheless, departmental rankings may be quite indifferent not only to the student's prospects, but also to the realities of the profession. The fact that a department is considered "number one" does not make it a good place for a student to attend; it may very well be one of the worst.

Dr. Matthew T. Balhoff was influential in encouraging me to enroll at LSU (as a good alum) and this ought to be recognized. Having a logical and "down-to-earth" thinking process, it should come at nobody's surprise that I wished for him to serve as an external member in my Advisory Committee.

Dr. Juan M. Lorenzo's participation in my Advisory Committee brought expertise on hydraulic fracture growth from his remarkable experimental work. Special thanks go to Dr. Brian F. Snyder for completing my Advisory Committee as the Dean's Representative.

There were many people that indirectly influenced my research path. I have to thank Dr. Mark W. McClure of ResFrac Corporation for informal discussions that had a positive

impact on Chapter 6. Alike, I must thank journal reviewers, paper contest judges, as well as mention a few individuals from my time at The University of Texas at Austin. Dr. Hunjoo P. Lee and Dr. S. Omid Razavi are recognized for their part in the development of the original version of the numerical model used in Chapter 4 and my previous advisors, Dr. Jon E. Olson and Dr. D. Nicolas Espinoza are kindly acknowledged.

Thank you to my officemates at PFT 2240 and colleagues in the Geofluids Modeling Group, who made my time in Louisiana enjoyable. They are Youssuf A. Elnoamany, MaKuachukwu Mbaegbu, Sulav Dhakal, Temitope A. Ajayi, Florencia A. Vasquez Cordoba, German A. Abzaletdinov, Zahidullah Farid, Gerardo E. Sepulveda, and the late Hope I. Asala, whose memory I shall forever cherish.

Without a doubt, my biggest achievement while at LSU was winning SPE's PetroBowl Championship in Calgary. Thanks to everyone who contributed to this great success for our department, especially to my fellow World Champions, Trevor J. Quatroy and Giuseppe D. Feo, for making sure we win, even when my buzzer malfunctioned. Similarly, big thanks to "Jerry" for his instrumental role – we won this in Baton Rouge.

The most enjoyable experience while at LSU was writing for *The Way Ahead*, SPE's magazine for young professionals. For this I have to thank amongst others, Dr. Michael B. Cronin, Asif Zafar, and Anjana S. Narayanan.

Finally, my parents Michalis and Despo, sister Nona Michael, as well as Natalie G. Wilson and her family, for their personal presence, which saw me through a most difficult and demanding part of my life. I would dare not forget to thank my cats (Cypriot and American) for their warm companionship over the years.

To all I owe my gratitude. Louisiana is the best. Geaux Tigers!

ΔΕΝ ΞΕΧΝΩ ΚΑΙ ΑΓΩΝΙΖΟΜΑΙ

Table of Contents

List of Tables

List of Figures

xiii

xvi

Nomenclature

A = Biot's poroelastic constant

$A_\emptyset$ = relative stress magnitude

b_i = acceleartion component of body force (i = 1, 2, 3), $L^2 T^{-1}$ $[ft^2/s]$

B_o = formation volume factor of the oil phase [RB/STB]

C = tensor of coefficients for Hooke's law, $ML^{-1} T^{-2}$ [psi]

C_c = vertical intercept (offset) correction factor

C_m = slope correction factor

D = depth along the well, L [ft]

d_{csg} = casing shoe depth, L [ft]

d_{res} = average reservoir depth, L [ft]

E = Young's modulus, $ML^{-1} T^{-2}$ [psi]

f = forces per unit volume acting on the rock, MLT^{-2} $[lb_f]$

F_{CD} = fracture conductivity, L^3 [mD · ft]

G = shear modulus, $ML^{-1} T^{-2}$ [psi]

g = gravitational constant, LT^{-2} $[ft/s^2]$

H = simulation block height, L [ft]

h = net payzone height, L [ft]

H_f = fracture height, L [ft]

J = reservoir productivity index, $L^4 T M^{-1}$ [STB/(day ∗ psi)]

K = bulk modulus, $ML^{-1} T^{-2}$ [psi]

k = reservoir formation permeability, L^2 [mD]

K_b = drained bulk modulus of the rock, $ML^{-1} T^{-2}$ [psi]

K_g = bulk modulus of the solid rock grains (undrained), $ML^{-1}T^{-2}$ [psi]

k_{crit} = critical reservoir permeability, L^2 [mD]

L = simulation block length, L [ft]

l_{lat} = horizontal well's lateral length, L [ft]

l_{perf} = perforation length, L [ft]

LOP = leak − off pressure, $ML^{-1}T^{-2}$ [psi]

M = P − wave modulus, $ML^{-1}T^{-2}$ [psi]

N = number of steps used in the multi − step/"incremental" shut − in procedure

n = parameter used to claculate $A_\emptyset$ varying from 0 to 3 per stress regime

p_b = breakdown pressure, $ML^{-1}T^{-2}$ [psi]

p_{bL} = breakdown pressure (longitudinal fracture initiation), $ML^{-1}T^{-2}$ [psi]

p_{bT} = breakdown pressure (transverse fracture initiation), $ML^{-1}T^{-2}$ [psi]

$p_{b,upper}$ = upper − bound of the breakdown pressure window, $ML^{-1}T^{-2}$ [psi]

p_{cem} = cement slurry hydrostatic pressure, $ML^{-1}T^{-2}$ [psi]

p_{cap} = capping stack pressure, $ML^{-1}T^{-2}$ [psi]

p_{fc} = fracture closure pressure (from leakoff tests), $ML^{-1}T^{-2}$ [psi]

$p_{frac,L}$ = longitudinal fracture initiation pressure, $ML^{-1}T^{-2}$ [psi]

$p_{frac,T}$ = transverse fracture initiation pressure, $ML^{-1}T^{-2}$ [psi]

p_{iL} = longitudinal DITF initiation pressure, $ML^{-1}T^{-2}$ [psi]

p_{iT} = transverse DITF initiation pressure, $ML^{-1}T^{-2}$ [psi]

p_{ini} = initial reservoir pressure, $ML^{-1}T^{-2}$ [psi]

p_p = rock formation pore pressure, $ML^{-1}T^{-2}$ [psi]

p_{perf} = perforation pressure, $ML^{-1}T^{-2}$ [psi]

p_{prop} = fracture propagation pressure, $ML^{-1}T^{-2}$ [psi]

p_w = wellbore pressure, $ML^{-1}T^{-2}$ [psi]

p_{wf} = bottomhole flowing pressure, $ML^{-1}T^{-2}$ [psi]

p_{wh} = wellhead pressure, $ML^{-1}T^{-2}$ [psi]

p_{ws} = wellbore shut $-$ in pressure, L [in]

q = discharge flowrate, L^3T^{-1} [STB/day]

q_{crit} = critical discharge flowrate, L^3T^{-1} [STB/day]

q_{res} = equivalent (reservoir) flowrate, L^3T^{-1} [STB/day]

r = radius from the center of the wellbore, L [ft]

r_b = wellbore breakout radius (or "depth"), L [ft]

r_e = drainage radius, L [ft]

R_i = casing wall inner radius, L [ft]

R_o = casing wall outer radius, L [ft]

r_{perf} = perforation radius, L [ft]

r_w = wellbore radius, L [ft]

S = 3D stress tensor, $ML^{-1}T^{-2}$ [psi]

S_1 = greatest compressive principal stress, $ML^{-1}T^{-2}$ [psi]

S_2 = intermediate principal stress, $ML^{-1}T^{-2}$ [psi]

S_3 = least compressive principal stress, $ML^{-1}T^{-2}$ [psi]

S_{1p} = principal stress acting along the 1p $-$ direction, $ML^{-1}T^{-2}$ [psi]

S_{2p} = principal stress acting along the 2p $-$ direction, $ML^{-1}T^{-2}$ [psi]

S_{3p} = principal stress acting along the 3p $-$ direction, $ML^{-1}T^{-2}$ [psi]

S_{Hmax} = maximum horizontal principal stress, $ML^{-1}T^{-2}$ [psi]

$$S_{hmin} = \text{minimum horizontal principal stress}, ML^{-1}T^{-2} \text{ [psi]}$$

$$S_{ij} = \text{normal and shear stress components (i, j = x, y, z)}, ML^{-1}T^{-2} \text{ [psi]}$$

$$S_p = \text{principal stress tensor}, ML^{-1}T^{-2} \text{ [psi]}$$

$$S_v = \text{vertical principal stress (overburden)}, ML^{-1}T^{-2} \text{ [psi]}$$

$$S_{yy} = \text{wellbore axial stress (total, along the y} - \text{axis)}, ML^{-1}T^{-2} \text{ [psi]}$$

$$S_{zz} = \text{wellbore axial stress (total, along the z} - \text{axis)}, ML^{-1}T^{-2} \text{ [psi]}$$

$$S_{\theta\theta} = \text{wellbore tangential stress (total)}, ML^{-1}T^{-2} \text{ [psi]}$$

$$T = \text{formation tensile strength}, ML^{-1}T^{-2} \text{ [psi]}$$

$$T_{crit} = \text{critical tensile strength}, ML^{-1}T^{-2} \text{ [psi]}$$

$$t_p = \text{discharge period before well shut} - \text{in}, T \text{ [days]}$$

$$u = \text{displacement}, L \text{ [ft]}$$

$$V = \text{volume of solid mass}, L^3 \text{ [ft}^3\text{]}$$

$$W = \text{simulation block width}, L \text{ [ft]}$$

$$w_f = \text{fracture width}, L \text{ [ft]}$$

$$x_f = \text{fracture half} - \text{length}, L \text{ [ft]}$$

$$z = \text{reference depth}, L \text{ [ft]}$$

$$z_w = \text{water depth}, L \text{ [ft]}$$

$$\nabla = \text{gradient operator}$$

Greek Letters

$$\alpha_B = \text{Biot's poroelastic coefficient}$$

$$\gamma_o = \text{oil specific gravity}$$

$$\delta_{ij} = \text{Kronecker delta (equal to 1 when i = j and 0 when i} \neq \text{j)}$$

ε_{ij} = normal and shear strain components (i, j = x, y, z), $ML^{-1}T^{-2}$ [psi]

ε_{rr} = radial strain

$\varepsilon_{r\theta}$ = shear strain

ε_{zz} = axial strain (along the z − axis)

$\varepsilon_{\theta\theta}$ = tangential (or circumferential or "hoop") strain

θ = angle around the wellbore taken from S_v in the $S_v - S_{Hmax}$ plane [°]

θ_b = angular span of wellbore breakouts [°]

θ_p = angle around the perforation from the wellbore axial stress direction [°]

λ = Lamé's first parameter (can be negative), $ML^{-1}T^{-2}$ [psi]

μ = fault's friction coefficient (tangent of the friction angle)

μ_o = oil viscosity, $ML^{-1}T^{-1}$ [cp]

ν = Poisson's ratio

ρ = density, ML^{-3} [ppg]

$\bar{\rho}$ = mean density of the overburden rock, ML^{-3} [ppg]

ρ_{cem} = density of cement slurry, ML^{-3} [ppg]

ρ_{frac} = density of fracturing fluid, ML^{-3} [ppg]

σ_e = von Mises stresss equivalent, $ML^{-1}T^{-2}$ [psi]

σ_{ij} = effective normal and shear stress components (i, j = x, y, z), $ML^{-1}T^{-2}$ [psi]

σ_{rr} = wellbore radial stress (effective), $ML^{-1}T^{-2}$ [psi]

$\sigma_{rr,csg}$ = casing wall radial stress, $ML^{-1}T^{-2}$ [psi]

$\sigma_{r\theta}$ = wellbore shear stress (effective), $ML^{-1}T^{-2}$ [psi]

σ_{yield} = casing yield stress, $ML^{-1}T^{-2}$ [psi]

σ_{yy} = horizontal well axial stress (effective, along the y − axis), $ML^{-1}T^{-2}$ [psi]

$$\sigma_{zz} = \text{vertical well axial stress (effective, along the z} - \text{axis)}, ML^{-1}T^{-2} \text{ [psi]}$$

$$\sigma_{zz,csg} = \text{casing wall axial stress (effective, along the z} - \text{axis)}, ML^{-1}T^{-2} \text{ [psi]}$$

$$\sigma_{\theta\theta} = \text{wellbore tangential/"hoop" stress (effective)}, ML^{-1}T^{-2} \text{ [psi]}$$

$$\sigma_{\theta\theta,csg} = \text{casing wall tangential stress}, ML^{-1}T^{-2} \text{ [psi]}$$

$$\sigma_{\theta\theta_p} = \text{tangential stress on the perforation base (effective)}, ML^{-1}T^{-2} \text{ [psi]}$$

$$\sigma_{\theta L} = \text{longitudinal fracturing stress}, ML^{-1}T^{-2} \text{ [psi]}$$

$$\sigma_{\theta T} = \text{transverse fracturing stress}, ML^{-1}T^{-2} \text{ [psi]}$$

$$\Phi = \text{stress function}, ML^{-1}T^{-2} \text{ [psi]}$$

$$\Delta p_w = \text{change in wellbore pressure}, ML^{-1}T^{-2} \text{ [psi]}$$

$$\Delta t = \text{elapsed time since the beginning of the well shut} - \text{in}, T \text{ [days]}$$

Acronyms

$$2D = \text{two} - \text{dimensional}$$

$$3D = \text{three} - \text{dimensional}$$

$$EMW = \text{equivalent mud weight}, ML^{-3} \text{ [ppg]}$$

$$EUR = \text{economic ultimate recovery}, L^3 \text{ [STB]}$$

$$BOEMRE = \text{Bureau of Ocean Energy, Management, Regulation, and Enforcement}$$

$$DR = \text{discounted recovery}, L^3 \text{ [STB]}$$

$$IP = \text{initial production}, L^3T^{-1} \text{ [STB/day]}$$

$$KPI = \text{key performance index}$$

$$LHS = \text{left} - \text{hand side}$$

$$MMSTB = \text{million stock tank barrels}, L^3$$

$$NPV = \text{net present value [US\$]}$$

PFP = preferred fracture plane

PPA = preferred perforation alignment

PV = present value [US$]

RB = reservoir barrels, L^3

RHS = right − hand side

STB = stock tank barrels, L^3

Abstract

Fluid-driven fracture initiation from oil and gas wells is examined in detail. The dissertation covers three subtopics: drilling, completion (stimulations), and post-blowout capping-induced fracture initiation.

Drilling-induced tensile fractures (DITFs) are located in an azimuth orthogonal to wellbore breakouts and are observed from image logs obtained during drilling operations. Fully analytical criteria for the orientation of DITFs initiating from wells in porous, permeable media are derived considering fluid infiltration from a pressurized wellbore. DITF orientation (longitudinal or transverse-to-the-wellbore) is used to constrain the magnitude of the local maximum horizontal principal stress. The range of the possible stress states is indicated on dimensionless plots *vis-à-vis* a given DITF orientation and *in-situ* stress regime.

Completion-induced hydraulic fractures (CIHFs) are initiated from perforated wells during stimulation practices, aimed at improving the permeability in the near-wellbore region. For application in low permeability formations, such as shale reservoirs, transverse fractures are more desired from a productivity perspective. A horizontal well with multiple transverse fractures outperforms the same horizontal well with a gigantic longitudinal fracture. Closed-form analytical approximations from the literature for the longitudinal and transverse fracturing stresses are modified to incorporate pore pressure effects and then used to develop a criterion for the orientation of fractures initiating from perforated wells. The validity of this criterion is numerically assessed and found to overestimate transverse fracture initiation, which occurs under a narrow range of conditions; when (i) the formation tensile strength is below a critical value, and (ii) the breakdown pressure within a

"window." At a known breakdown pressure, the fracture initiation pressure can be determined semi-analytically.

Following blowouts after mismanaged loss of well control situations, tensile fractures can initiate during capping stack shut-in. Upward propagation of these fractures can provide a broaching pathway for reservoir fluids towards the seafloor leading to an ecological disaster. Being able to predict fracture initiation, *a-priori* to post-blowout capping, thus preventing broaching from taking place is of considerable importance. Capping stack shut-in procedures can be optimized using the post-blowout discharge flowrates. A deepwater Gulf of Mexico case study is performed, extended to a comprehensive stability analysis of the casing-cement sheath-rock formation system.

Chapter 1. Introduction

Fluid-driven fracturing during the lifetime of a well – whether intentional or circumstantial – is a major research topic for petroleum engineers. Fractures induced during drilling visible from image logs can provide insight on the local *in-situ* stress tensor and hence the subsurface stress regime. Hydraulic fractures induced during stimulation treatments provide a pathway for hydrocarbons to reach the wellbore in low permeability formations. At the same time, however, loss of well control can lead to situations where fracturing from the drilled, openhole section of the wellbore can provide a pathway for reservoir fluids to broach to overlying formations, surface or the seafloor.

1.1 RESEARCH SCOPE AND OBJECTIVES

In this dissertation, fluid-driven fracture initiation is examined analytically and numerically for drilling, completions (during stimulation treatments), and loss of well control situations. The goal is to improve our understanding on fracture initiation in porous, permeable media considering the influence of key independent variables, such as the in-situ stress state, (geo)mechanics, and fluid properties. The primary objectives of this research are the following:

- Derivation of closed-form analytical orientation (longitudinal or transverse) criteria for tensile fracture initiation during drilling and completions from non-perforated and perforated wells, respectively, and analysis of tensile fracture initiation from loss of well control events.

- Numerical assessment of the orientation criterion for fracture initiation from perforated horizontal wells developed using closed-form analytical approximations.

- Validation of the analytical and numerical approaches using laboratory-scale experiments from the literature.

- Development of a robust modeling approach for *a-priori* prediction of the orientation of fracture initiation and the fracture initiation pressure from perforated wells if the *in-situ* stress state, rock mechanical properties and perforation geometry are known.

- Application on case studies on hydrocarbon-bearing shale plays, namely the Barnett, Bakken, Fayetteville, Haynesville, Niobrara, and Marcellus in the United States, and Vaca Muerta in Argentina.

- Development of coupled reservoir-geomechanical workflow for fracture initiation prediction, during post-blowout capping applied to typical deepwater Gulf of Mexico (GoM) parameters.
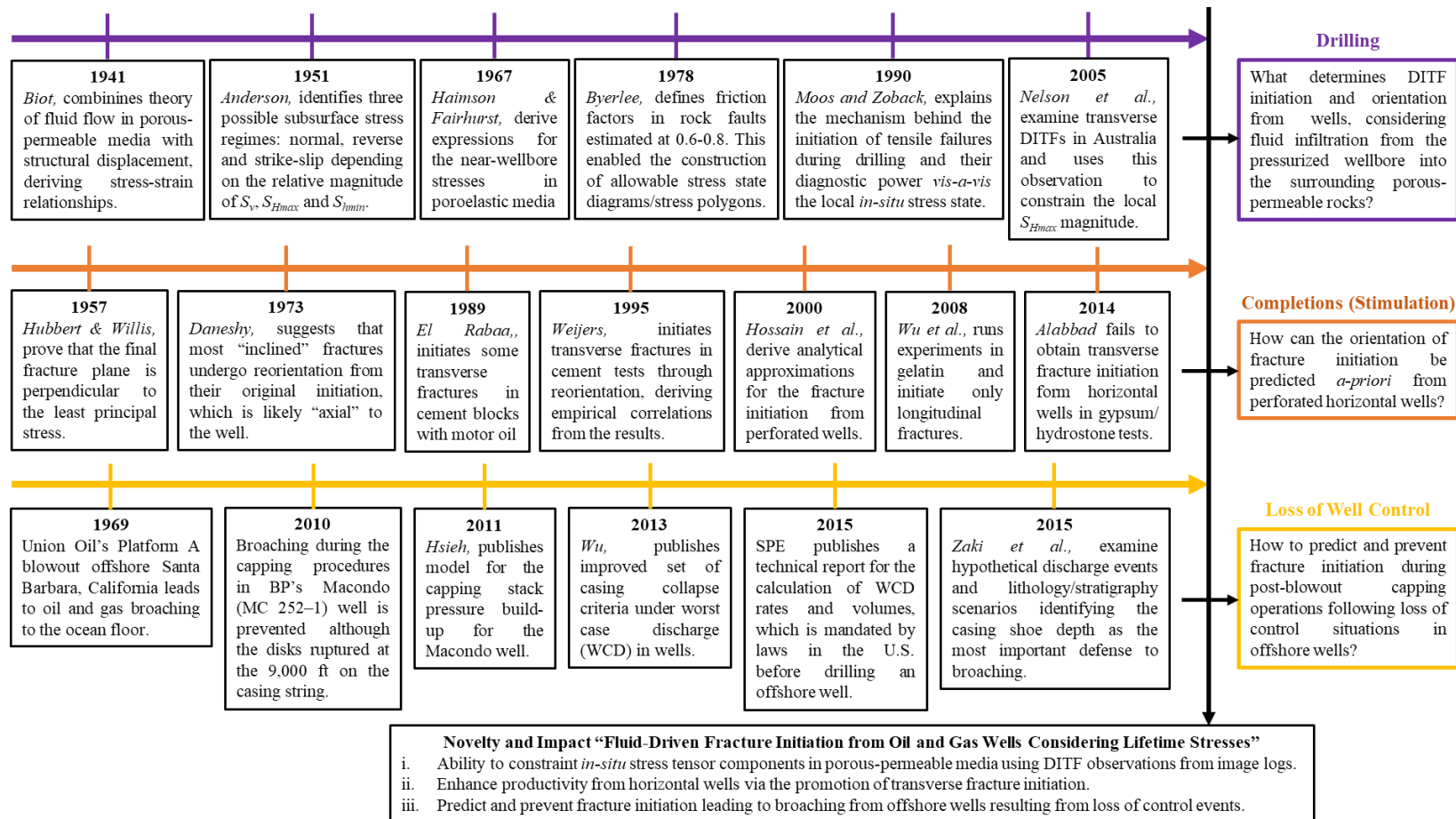
Figure 1.1.   Chronological series of the literature milestones for the topics of fluid-driven fracture initiation studied: drilling, completions (stimulation), and loss of well control.

1.2 DISSERTATION OUTLINE

1.2.1 Structure

This dissertation consists of nine chapters. The content of each of the following chapter is summarized below:

Chapter 2 reviews existing literature dealing with fundamental rock mechanics concepts influencing fluid-driven fracture initiation. The governing and constitutive equations of the linear elasticity theory are presented along with the modifications made to extend to poroelasticity. The subsurface *in-situ* stress regimes are reviewed based on Anderson (1951)'s faulting theory and the stress states possible are indicated considering the frictional limits (compressive failure via shear fault slippage). The stress state in the near-wellbore region are shown for poroelastic media and fracture initiation resulting from exceeding the tensile failure criterion is discussed. Chapter 2 provides the fundamentals on which this research is based. The chapters following Chapter 2 focus on research questions and the individual scenarios of fracture initiation that occur during the lifetime of a well (drilling, completions, and loss of well control).

In Chapter 3, derivation of a fully-exact analytical orientation criterion is presented for drilling-induced tensile fracture (DITF) initiation from non-perforated wells in porous-permeable rocks, considering fluid infiltration from the wellbore. The orientation of DITFs from a well can be used to constrain the local *in-situ* tensor. Thereafter an orientation criterion is developed for completion-induced hydraulic fracture (CIHF) initiation from perforated wells using closed-form analytical approximations for the longitudinal and transverse fracturing stresses from the literature, modified to incorporate pore pressure effects. Transverse CIHF initiation is found to occur when the breakdown pressure is within a certain range ("window"). The analytically-approximated criterion is applied on

seven shale plays (Barnett, Bakken, Fayetteville, Haynesville, Niobrara, Marcellus, and Vaca Muerta). Results indicate that transverse CIHF initiation is the likely outcome in six out of the seven cases (excluding the Vaca Muerta Shale).

In Chapter 4, a true-3D numerical model written in $FLAC^{3D}$ – a finite volume simulator for geomechanics-based problems – is used to assess the validity of the analytically-approximated orientation criterion for fracture initiation from perforated horizontal wells. The numerical results indicate that the analytical approximations overestimate transverse fracture initiation, which is a rarity compared to longitudinal fracture initiation. In addition to the breakdown pressure window a second constraint to transverse fracture initiation is observed – the critical tensile strength. Formation tensile strengths above this magnitude cannot yield transverse fracture initiation at any breakdown pressure value. The frequent occurrence of longitudinal fracture initiation leads to tendencies for fracture reorientation in the near-wellbore region. This in turn causes near-wellbore fluid tortuosity, which triggers completion and production-related problems.

Chapter 5 presents a procedure for the development of a correction factor set for the closed-form analytical approximations presented on Chapters 4 (slightly more simplified to those presented in Chapter 3) to make them match the exact numerical solutions. Then the resultant semi-analytical modeling approach (numerically-developed correction factors to closed-form analytical solutions) is used to predict fracture initiation pressure and the orientation of fracture initiation expected for an application example on a Barnett Shale case study.

In Chapter 6, the semi-analytical modeling approach presented on Chapter 5 is used to develop correction factor sets for the seven shale plays used in Chapters 3 and 4. Hence, a comparative study is performed on the same seven shale plays (Barnett, Bakken, Fayetteville, Haynesville, Niobrara, Marcellus and Vaca Muerta) to assess the use of

oriented perforating either for the promotion of transverse fracture initiation, or when this is not possible, minimize the initiation pressure for longitudinal fracture initiation.

Chapter 7 investigates fluid-driven fracture initiation following loss of well control situations, like that resulting in a blowout. These are tensile fractures initiated during post-blowout capping procedures. Quantitative information from the preceding post-blowout discharge period is used to indicate fracture initiation, or lack thereof. A workflow is developed to optimize multi-step/"incremental" capping stack shut-in strategy in regards to the number of steps and the duration per step, such that fracture initiation is prevented. The workflow was applied on a hypothetical case study on deepwater GoM.

Chapter 8 presents analytical modeling of the stress distribution of a casing–cementing sheath–rock formation system. The stress state within the casing walls is modeled according to existing relationships for linearly elastic thick-walled cylinders, while the stress state within the surrounding rock formation is given by existing relationships for the vicinity around a pressurized cylindrical cavity in a porous-permeable medium, as in Chapter 3. The stress state within the cement sheath is dictated by experimental results from the literature. The impact of the extreme stress variations taking place during loss of well control situations (post-blowout discharge and capping stages) is examined via a hypothetical case study using numbers typical to deepwater GoM (same as in Chapter 7).

Chapter 9 summarizes the general findings of the research questions and hypotheses investigated in this dissertation and presents conclusions in light of the overall concepts developed and explored in this dissertation.
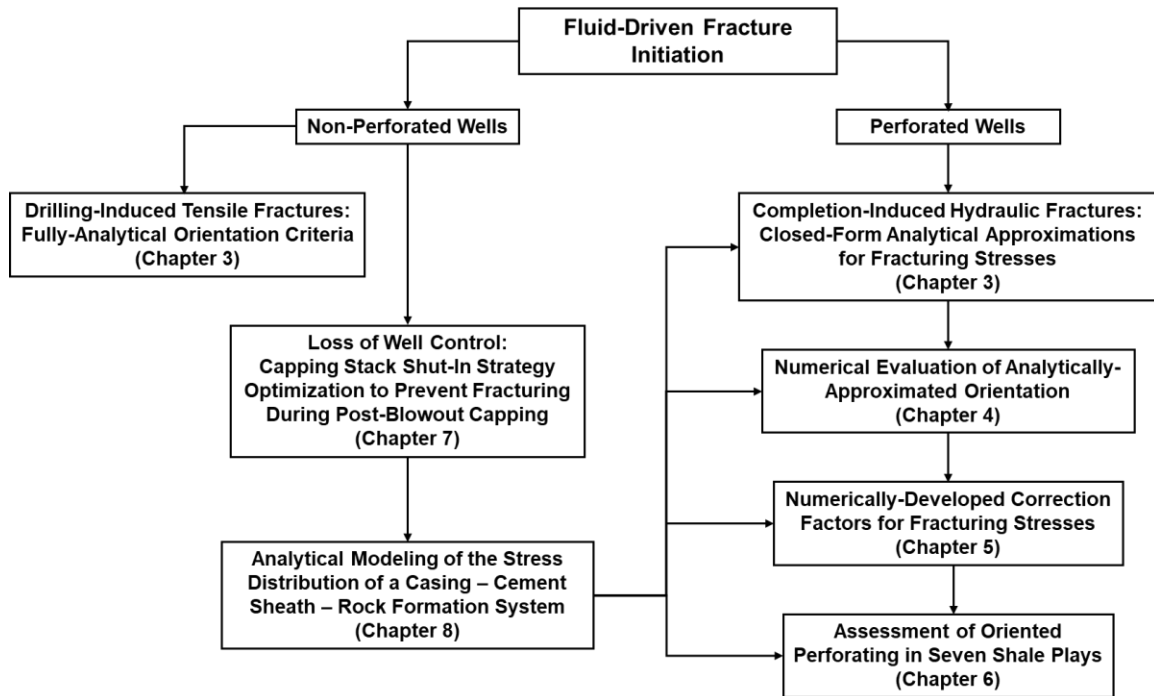
Figure 1.2. Flowchart of illustrating the dissertation's structure, the topics it comprises and their interrelations.

1.2.2   Notation, Units, and Sign Convention

General terminology and units from the petroleum industry is used. A full list of the symbols used and their definitions is presented in the Nomenclature section. Appendix A presents the conversion factors between the SI/metric and oilfield/English units. Contrary to most texts on engineering mechanics where tension is assumed to have positive direction, rock mechanics considers compressive stresses are positive. In this research all equations are presented with the compressive stress component being positive, consistent with existing literature in petroleum geomechanics.

7

Chapter 2. Rock Mechanics and Fracture Initiation Fundamentals

An accelerated interest in unconventional shale exploitation using hydraulic fracturing brought about detailed studies of the rock mechanics. Many of the ensuing developments applied classic fracture mechanics. This chapter reviews the basic principles of rock mechanics and the major themes of the existing literature on the geomechanics of compressive and tensile fracture initiation, important for the exploration of the research questions and hypotheses investigated in this dissertation.

2.1 ELASTIC BEHAVIOR OF ROCKS: GOVERNING EQUATIONS

2.1.1 Continuum Mechanics for Solid Materials

Continuum mechanics refers to the sublet of mechanics, which deals with the mechanical behavior of a continuous mass as opposed to separate particles, developed by the French mathematician, Augustin-Luis Cauchy during the 19th century.

2.1.1.1 Stress Tensor in 3D Space

Considering a solid mass element in an orthogonal coordinate system comprised of three, mutually-orthogonal directions 1, 2, and 3, all stresses can be grouped together in a matrix, $\boldsymbol{S}$, such

$$\boldsymbol{S} \equiv \begin{bmatrix} S_{11} & S_{12} & S_{13} \\ S_{21} & S_{22} & S_{23} \\ S_{31} & S_{32} & S_{33} \end{bmatrix} \tag{2.1}$$

where the diagonal corresponds to normal stresses and off-diagonal terms represent shear stresses. Figure 2.1a shows the graphical representation of the 3D stress tensor. Assuming

angular momentum equilibrium, where the solid element is not spinning around any of the three axes, makes off-diagonal stresses symmetric, thus S becomes symmetric with respect to the diagonal.

Every tensor containing non-zero off-diagonal terms (as in Eq. 2.1) can be simplified to a tensor with its eigenvalues on the diagonal and zero off-diagonal terms at orientation in the 3D space, which coincides with the eigenvectors (Figure 2.1b). For a symmetric S composed of real values, three eigenvalues can be calculated, what is known as the principal stresses, S_{1p}, S_{2p}, and S_{3p}. Each principal stress represents an eigenvalue, associated with a principal direction ($1p$, $2p$, and $3p$); an eigenvector (Eq. 2.2). The stress tensor in a coordinate system aligned with the principal stress direction, S_p, is populated by the three eigenvalues (principal stresses) in its diagonal and zeros in all off-diagonal terms.

$$S_p \equiv \begin{bmatrix} S_{1p} & 0 & 0 \\ 0 & S_{2p} & 0 \\ 0 & 0 & S_{3p} \end{bmatrix} \tag{2.2}$$
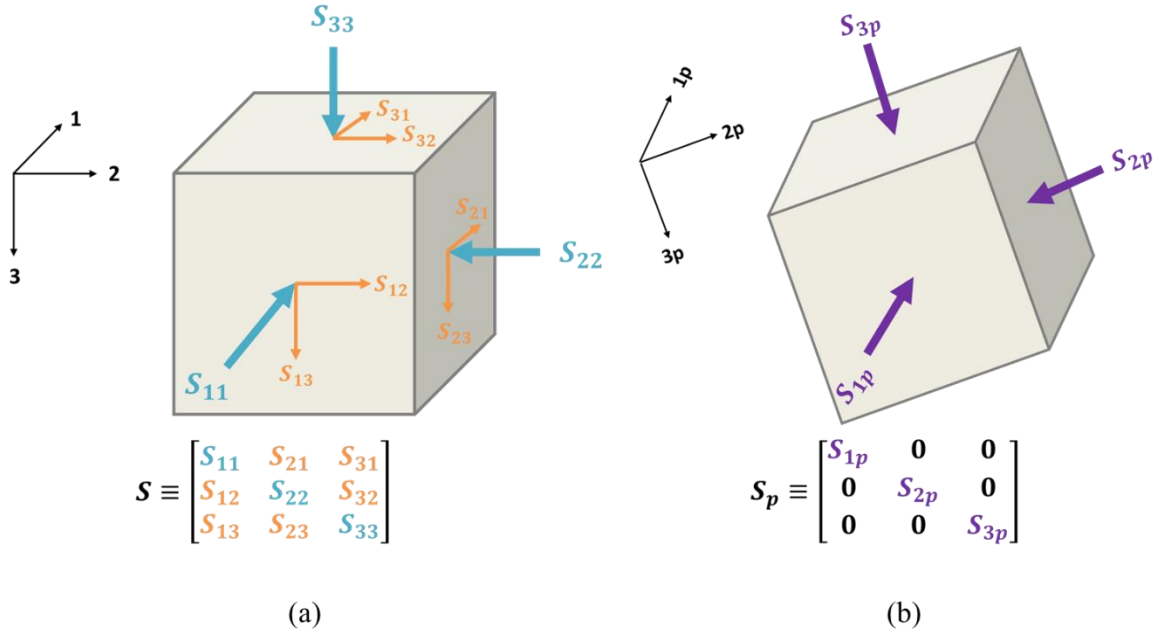
Figure 2.1. Graphical and mathematical representation of (a) the stress tensor, S, arbitrarily-oriented in 3D space (directions 1, 2, and 3), and (b) the principal stresses (tensor S_P) and the associated principal stress directions ($1p$, 2_p, and 3_p).

2.1.1.2 Cauchy's Stress Equilibrium Equations

Stress equilibrium mandates the summation of all forces in every direction to be resulting to a net zero. For example, summation of the forces in direction 1, considers the body force term, $\rho V b_1$, which is proportional to the density and volume of the solid mass, ρ and V, respectively as well as the acceleration component, b_1, requiring

$$\sum F_1 = 0$$

$$\sum F_1 \equiv S_{11}dx_2dx_3 - \left[S_{11} + \frac{\partial S_{11}}{\partial x_1}dx_1\right]dx_2dx_3$$
$$+S_{21}dx_1dx_3 - \left[S_{21} + \frac{\partial S_{21}}{\partial x_2}dx_2\right]dx_1dx_3$$
$$+S_{31}dx_1dx_2 - \left[S_{31} + \frac{\partial S_{31}}{\partial x_3}dx_3\right]dx_1dx_2 - \rho(dx_1dx_2dx_3) = 0$$

(2.3)

10

Dividing by the volume of the solid mass, $dx_1 dx_2 dx_3$, simplifies Eq. 2.3 to

$$\frac{\partial S_{11}}{\partial x_1} + \frac{\partial S_{21}}{\partial x_2} + \frac{\partial S_{31}}{\partial x_3} - \rho b_1 = 0 \tag{2.4}$$

Generalizing stress equilibrium in all three directions (1, 2, and 3) yields Cauchy's equations of stress equilibrium

$$\begin{aligned}
\frac{\partial S_{11}}{\partial x_1} + \frac{\partial S_{21}}{\partial x_2} + \frac{\partial S_{31}}{\partial x_3} - \rho b_1 = 0 \\
\frac{\partial S_{12}}{\partial x_1} + \frac{\partial S_{22}}{\partial x_2} + \frac{\partial S_{32}}{\partial x_3} - \rho b_2 = 0 \\
\frac{\partial S_{13}}{\partial x_1} + \frac{\partial S_{23}}{\partial x_2} + \frac{\partial S_{33}}{\partial x_3} - \rho b_3 = 0
\end{aligned} \tag{2.5}$$

2.1.1.3 Time-Dependent Solution: Cauchy's Equation of Motion

For a stationary continuous mass body, arbitrarily-shaped and arbitrarily-oriented in 3D space, there are six unknowns and three equations (Eq. 2.5). If the mass body is moving at velocity $\partial u / \partial t$, the terms on the right-hand side (RHS) containing the acceleration term is non-zero, yielding nine unknowns from three equations:

$$\begin{aligned}
\frac{\partial S_{11}}{\partial x_1} + \frac{\partial S_{21}}{\partial x_2} + \frac{\partial S_{31}}{\partial x_3} - \rho b_1 = \frac{\partial^2}{\partial t^2}(\rho u_1) \\
\frac{\partial S_{12}}{\partial x_1} + \frac{\partial S_{22}}{\partial x_2} + \frac{\partial S_{32}}{\partial x_3} - \rho b_2 = \frac{\partial^2}{\partial t^2}(\rho u_2) \\
\frac{\partial S_{13}}{\partial x_1} + \frac{\partial S_{23}}{\partial x_2} + \frac{\partial S_{33}}{\partial x_3} - \rho b_3 = \frac{\partial^2}{\partial t^2}(\rho u_3)
\end{aligned} \tag{2.6}$$

where the induced displacement is $u = (u_1, u_2, u_3)$.

The general solution of a time-dependent problem (Eq. 2.6) with arbitrary boundary conditions requires knowledge of equations, which relate displacement to strains (kinematic) and displacement to stresses (constitutive).

2.1.2 Constitutive and Kinematic Equations for Linear (Isotropic) Elasticity

For displacements and displacement gradients small enough in rock mass, the theory of linear elasticity is valid. The conservation of mass and equations of motion are satisfied in the non-deformed reference configuration. Using conservation of momentum the Cauchy's equations (in vector notation) of motion are obtained as

$$\nabla \boldsymbol{S} + f = \rho \frac{\partial^2 u}{\partial t^2} \tag{2.7}$$

where ρ is the density of the rock mass, $\partial^2 u / \partial t^2$ is the acceleration of the solid rock mass, f is the net sum of the forces per unit volume acting on the rock, and $\boldsymbol{S}$ is the stress tensor, which in Cartesian coordinates (x, y, and z) is

$$\boldsymbol{S} \equiv \begin{bmatrix} S_{xx} & S_{xy} & S_{xz} \\ S_{yx} & S_{yy} & S_{yz} \\ S_{zx} & S_{zy} & S_{zz} \end{bmatrix} \tag{2.8}$$

S_{ii} are terms where $i, j = x, y, z$ indicate normal stresses and S_{ij} are terms where $i \neq j$, indicate shear stresses. For a static case, $\partial^2 u / \partial t^2$ is zero and thus Eq. 2.7 is reduced back to

$$\nabla \boldsymbol{S} + f = 0 \tag{2.9}$$

which is equivalent to Eq. 2.5. $S_{ij} = S_{ji}$ decreases the number of unknowns in σ from nine to six and constitutive equations describing the stress-strain relationships of elastic solid materials are used to solve for the stresses. These constitutive equations are based on Hooke's law (force applied $\propto$ displacement),

$$S = C\varepsilon \tag{2.10}$$

where C is a tensor of coefficients, which is determined by the rock's mechanical properties and ε is the strain tensor, such that

$$\varepsilon \equiv \begin{bmatrix} \varepsilon_{xx} & \varepsilon_{xy} & \varepsilon_{xz} \\ \varepsilon_{yx} & \varepsilon_{yy} & \varepsilon_{yz} \\ \varepsilon_{zx} & \varepsilon_{zy} & \varepsilon_{zz} \end{bmatrix} \tag{2.11}$$

where $i = j$ for ε_{ij} terms indicate normal strains and $i \neq j$ indicates shear strains. Treating all strain components in ε in relation to the displacement, $u = (u_x, u_y, u_z)$ expands Eq. 2.11 into

$$\varepsilon \equiv \begin{bmatrix} \dfrac{\partial u_x}{\partial x} & \dfrac{1}{2}\left(\dfrac{\partial u_x}{\partial y} + \dfrac{\partial u_y}{\partial x}\right) & \dfrac{1}{2}\left(\dfrac{\partial u_x}{\partial z} + \dfrac{\partial u_z}{\partial x}\right) \\ \dfrac{1}{2}\left(\dfrac{\partial u_y}{\partial x} + \dfrac{\partial u_x}{\partial y}\right) & \dfrac{\partial u_y}{\partial y} & \dfrac{1}{2}\left(\dfrac{\partial u_y}{\partial z} + \dfrac{\partial u_z}{\partial y}\right) \\ \dfrac{1}{2}\left(\dfrac{\partial u_z}{\partial x} + \dfrac{\partial u_x}{\partial z}\right) & \dfrac{1}{2}\left(\dfrac{\partial u_z}{\partial y} + \dfrac{\partial u_y}{\partial z}\right) & \dfrac{\partial u_z}{\partial z} \end{bmatrix} \tag{2.12}$$

For a linearly elastic, isotropic solid material, only two moduli are necessary for expressing all non-zero coefficients in C. These moduli are Lamé's first parameter, λ, P-wave modulus M, bulk modulus, K, shear modulus, G, Young's (or elastic) modulus, E,

13

and Poisson's ratio, ν. Table 2.1 shows the conversion equations for the six elastic moduli. Given any two, the four remaining moduli can be calculated using the displayed equations.

Table 2.1. Conversion equations for the six elastic moduli: bulk modulus, K, Young's modulus, E, Lamé's first parameter, λ, shear modulus, G, Poisson's ratio, ν, and P-wave modulus, M.

	K	E	λ	G	ν	M
$K \& E$	–	–	$\dfrac{3K(3K-E)}{9K-E}$	$\dfrac{3KE}{9K-E}$	$\dfrac{3K-E}{6K}$	$\dfrac{3K(3K+E)}{9K-E}$
$K \& \lambda$	–	$\dfrac{9K(K-\lambda)}{3K-\lambda}$	–	$\dfrac{3(K-\lambda)}{2}$	$\dfrac{\lambda}{3K-\lambda}$	$3K-2\lambda$
$K \& G$	–	$\dfrac{9KG}{3K+G}$	$K-\dfrac{2G}{3}$	–	$\dfrac{3K-2G}{2(3K+G)}$	$K+\dfrac{4G}{3}$
$K \& \nu$	–	$3K-6\nu$	$\dfrac{3K\nu}{K+\nu}$	$\dfrac{3K-6\nu}{2+2\nu}$	–	$\dfrac{3K-3\nu}{1+\nu}$
$K \& M$	–	$\dfrac{9K(M-K)}{3K+M}$	$\dfrac{3K-M}{2}$	$\dfrac{3(M-K)}{4}$	$\dfrac{3K-M}{3K+M}$	–
$E \& \lambda^{\prime}$	$\dfrac{E+3\lambda+R}{6}$	–	–	$\dfrac{E-3\lambda+R}{4}$	$\dfrac{2\lambda}{E+\lambda+R}$	$\dfrac{E+\lambda+R}{2}$
$E \& G$	$\dfrac{EG}{3(3G-E)}$	–	$\dfrac{G(E-2G)}{3G-E}$	–	$\dfrac{E}{2G}-1$	$\dfrac{G(4G-E)}{3G-E}$
$E \& \nu$	$\dfrac{E}{3-6\nu}$	–	$\dfrac{E\nu}{(1+\nu)(1-2\nu)}$	$\dfrac{E}{2+2\nu}$	–	$\dfrac{E(1-\nu)}{(1+\nu)(1-2\nu)}$
$E \& M^{\prime\prime}$	$\dfrac{3M-E+V}{6}$	–	$\dfrac{M-E+V}{4}$	$\dfrac{3M+E-V}{8}$	$\dfrac{E-M+V}{4M}$	–
$\lambda \& G$	$\lambda+\dfrac{2G}{3}$	$\dfrac{G(3\lambda-2G)}{\lambda+G}$	–	–	$\dfrac{\lambda}{2(\lambda+G)}$	$\lambda+2G$
$\lambda \& \nu^{\prime\prime\prime}$	$\dfrac{\lambda(1+\nu)}{3\nu}$	$\dfrac{\lambda(1+\nu)(1-2\nu)}{\nu}$	–	$\dfrac{\lambda(1-2\nu)}{2\nu}$	–	$\dfrac{\lambda(1-\nu)}{\nu}$
$\lambda \& M$	$\dfrac{M+2\lambda}{3}$	$\dfrac{(M-\lambda)(M+2\lambda)}{M+\lambda}$	–	$\dfrac{M-\lambda}{2}$	$\dfrac{\lambda}{M+\lambda}$	–
$G \& \nu$	$\dfrac{2G(1+\nu)}{3-6\nu}$	$2G(1+\nu)$	$\dfrac{2G\nu}{1-2\nu}$	–	–	$\dfrac{2G(1-\nu)}{1-2\nu}$
$G \& M$	$M-\dfrac{4G}{3}$	$\dfrac{G(3M-4G)}{M-G}$	$M-2G$	–	$\dfrac{M-2G}{2(M-G)}$	–
$\nu \& M$	$\dfrac{M(1+\nu)}{3(1-\nu)}$	$\dfrac{M(1+\nu)(1-2\nu)}{1-\nu}$	$\dfrac{M\nu}{1-\nu}$	$\dfrac{M(1-2\nu)}{2(1-\nu)}$	–	–

$^{\prime}\ R = \sqrt{E^2 + 9\lambda^2 + 2E\lambda}$
$^{\prime\prime}\ V = \pm\sqrt{E^2 + 9M^2 - 10EM}$
$^{\prime\prime\prime}$ Not applicable at $\lambda, \nu = 0$

Often E and v are used (see the row in the purple box on Table 2.1) which are defined as

$$E = \frac{S_{ii}}{\varepsilon_{ii}} \tag{2.13}$$

$$v = -\frac{\varepsilon_{ii}}{\varepsilon_{jj}} \tag{2.14}$$

This simplifies Hooke's law in a 3D space to

$$S_{ii} = \frac{E}{1+v}\left(\varepsilon_{u} + \frac{v}{1-2v}\left[\varepsilon_{xx} + \varepsilon_{yy} + \varepsilon_{zz}\right]\right) \tag{2.15}$$

$$S_{ij} = \frac{E}{2(1+v)}\varepsilon_{ij} \tag{2.16}$$

Substituting Eq. 2.12 into Eqs. 2.15 and 2.16 and Eqs. 2.15 and 2.16 into Eq. 2.9 converts the Cauchy's equation of motion to

$$\nabla C \nabla \mathbf{u} + f = 0 \tag{2.17}$$

with $\mathbf{C}$ defined as

$$C = \begin{bmatrix} \begin{pmatrix} 2G+\lambda & 0 & 0 \\ 0 & G & 0 \\ 0 & 0 & G \end{pmatrix} & \begin{pmatrix} 0 & \lambda & 0 \\ G & 0 & 0 \\ 0 & 0 & 0 \end{pmatrix} & \begin{pmatrix} 0 & 0 & \lambda \\ 0 & 0 & 0 \\ G & 0 & 0 \end{pmatrix} \\ \begin{pmatrix} 0 & G & 0 \\ \lambda & 0 & 0 \\ 0 & 0 & 0 \end{pmatrix} & \begin{pmatrix} G & 0 & 0 \\ 0 & 2G+\lambda & 0 \\ 0 & 0 & G \end{pmatrix} & \begin{pmatrix} 0 & 0 & 0 \\ 0 & 0 & \lambda \\ 0 & G & 0 \end{pmatrix} \\ \begin{pmatrix} 0 & 0 & G \\ 0 & 0 & 0 \\ \lambda & 0 & 0 \end{pmatrix} & \begin{pmatrix} 0 & 0 & 0 \\ 0 & 0 & G \\ 0 & \lambda & 0 \end{pmatrix} & \begin{pmatrix} G & 0 & 0 \\ 0 & G & 0 \\ 0 & 0 & 2G+\lambda \end{pmatrix} \end{bmatrix} \tag{2.18}$$

Applying the two-dimensional (2D) plane strain approximation and setting the displacement in the z-direction at zero, makes $\varepsilon_{zz} = \varepsilon_{xz} \equiv \varepsilon_{zx} = \varepsilon_{yz} \equiv \varepsilon_{zy} = 0$. The displacements in the x and y-direction no longer depend on z. This further simplifies C to

$$C = \begin{bmatrix} \begin{pmatrix} 2G+\lambda & 0 \\ 0 & G \end{pmatrix} & \begin{pmatrix} 0 & \lambda \\ G & 0 \end{pmatrix} \\ \begin{pmatrix} 0 & \lambda \\ G & 0 \end{pmatrix} & \begin{pmatrix} G & 0 \\ 0 & 2G+\lambda \end{pmatrix} \end{bmatrix} \tag{2.19}$$

2.1.3 Extension to Poroelasticity

Rocks tend to be porous with fluids present in those pores as well cracks present. The pressure of the fluid in the pores counteracts the pressures exerted by the principal stresses, thus modifications should be made to the linear elasticity theory, to reliably model small deformations in saturated porous solid rocks.

Biot's poroelasticity (Biot, 1941) is a theory of acoustic propagation in porous, elastic media. The presence of pore pressure, p_p, counteracts the compression imposed by the *in-situ* tectonic and overburden stresses. Thus, rock strength, elastic moduli, and frictional strength becomes dependent on the effective stress,

$$\sigma_{ij} = S_{ij} - \alpha_B \delta_{ij} p_p \tag{2.20}$$

where σ_{ij} are the effective stress components, δ_{ij} is the Kronecker delta, and α_B is the Biot's poroelastic coefficient, defined by

$$\alpha_B = 1 - \frac{K_b}{K_g} \tag{2.21}$$

where K_b is the drained bulk modulus of the rock and K_g is the undrained bulk modulus of the solid rock grains, with $\alpha_B = 1$ corresponding to an extremely compliant rock and $\alpha_B = 0$ corresponding to a rock with almost no pores.

Similar to linear elasticity, the constitutive equations for ideal poroelastic material are also linear. Neglecting thermal effects, the stress-strain behavior depends on the deformation regime; drained at constant p_p and undrained at variable p_p. For drained regime in the governing equations for linear elasticity, stresses, strains and elastic moduli are replaced by their corresponding effective counterparts yielding

$$\varepsilon_{ij} = \frac{1}{2G}\left(S_{ij} - \delta_{ij}\left[\frac{S_{xx} + S_{yy} + S_{zz}}{3}\right]\right) + \frac{\delta_{ij}}{3K}\left(\left[\frac{S_{xx} + S_{yy} + S_{zz}}{3}\right] - \alpha_B p_p\right) \tag{2.22}$$

For exclusively shear deformations, $\varepsilon_{ij} = S_{ij}/(2G)$ and hence shear stresses and strains are independent of p_p.

2.2   SUBSURFACE STRESS STATE

2.2.1   *In-Situ* Principal Stresses

The stress state in the subsurface can be fully characterized by three *in-situ* principal stresses, which act in mutually-orthogonal directions (S_1, S_2, and S_3, where $S_1 > S_2 > S_3$). The principal stresses are normal stresses oriented in planes that make all shear stresses to

diminish to zero. These are the eigenvalues of the *in-situ* stress tensor (Eq. 2.8), while the directions at which these stresses act are indicated by the eigenvectors.

$$\begin{pmatrix} S_1 \\ S_2 \\ S_3 \end{pmatrix} \equiv \begin{pmatrix} \sigma_1 + p_p \\ \sigma_2 + p_p \\ \sigma_3 + p_p \end{pmatrix} = \begin{bmatrix} 2G + \lambda & \lambda & \lambda \\ \lambda & 2G + \lambda & \lambda \\ \lambda & \lambda & 2G + \lambda \end{bmatrix} \begin{pmatrix} \varepsilon_1 \\ \varepsilon_2 \\ \varepsilon_3 \end{pmatrix} \qquad (2.23)$$

2.2.2 Anderson's Faulting Theory

Anisotropic stress causes tectonic deformations. In most cases, one of those stresses is aligned vertically and is denoted by S_v, with the remaining two acting horizontally (Anderson, 1951). The most compressive horizontal stress is denoted by S_{Hmax} and the least compressive is denoted by S_{hmin} (Figure 2.2). The relative magnitude of the *in-situ* principal stresses dictates the subsurface stress regime, which can be:

i.   Normal faulting stress regime ($S_v > S_{Hmax} > S_{hmin}$),

ii. Reverse (or thrust) faulting stress regime ($S_{Hmax} > S_{hmin} > S_v$), or

iii. Strike-slip faulting stress regime ($S_{Hmax} > S_v > S_{hmin}$).

Each of the three regimes induces the corresponding fault tectonic movement. The *in-situ* stress state imposes the strongest influence on fracture initiation and propagation.
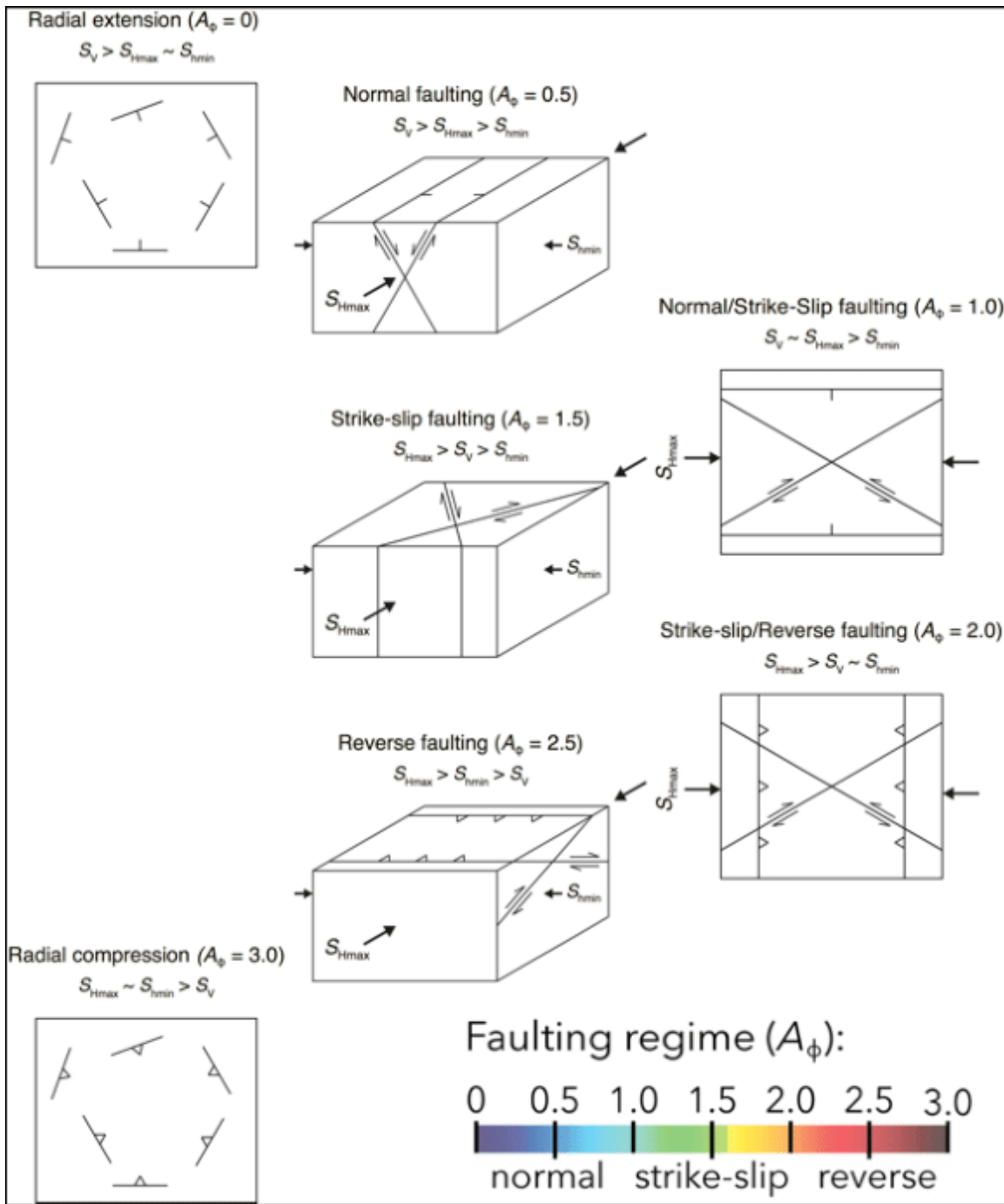
Figure 2.2. *In-situ* stress regimes from Anderson's faulting theory (Anderson, 1951): normal, strike-slip, and thrust (or reverse) faulting, extended to intermediate and limiting stress states. Per Simpson (1997), each stress regime is assigned a value ranging from zero to three (from Lund Snee, 2020).

Figure 2.3 shows the variation of in-situ stress states in North America from Lund Snee and Zoback (2018). The black lines represent the local S_{Hmax} direction for depths throughout the upper brittle crust and the color indicates of the local in-situ stress regime. The relative stress magnitudes are quantified using the parameter $A_\emptyset$ after Simpson (1997), ranging from zero for a total normal faulting stress state, known as radial extension, to three for a total reverse faulting stress state, known as radial compression (Figure 2.2). For strike-slip faulting stress states, $1 < A_\emptyset < 2$. The parameter $A_\emptyset$ relates to the absolute stress magnitudes by

$$A_\emptyset = \left(n + \frac{1}{2}\right) + (-1)^n \left(\left[\frac{S_2 - S_3}{S_1 - S_3}\right] - \frac{1}{2}\right) \tag{2.24}$$

where, S_1, S_2, and S_3 are respectively the most compressive, intermediate and least compressive *in-situ* principal stresses. Following Simpson (1997), for normal faulting stress states, $S_1 = S_v$, $S_2 = S_{Hmax}$, and $S_3 = S_{hmin}$, with parameter $n = 0$. Similarly, for strike-slip faulting stress states, $S_1 = S_{Hmax}$, $S_2 = S_v$, $S_3 = S_{hmin}$, and $n = 1$. Lastly, for reverse faulting stress states, $S_1 = S_{Hmax}$, $S_2 = S_{hmin}$, $S_3 = S_v$, and $n = 2$ (Eq. 2.24).
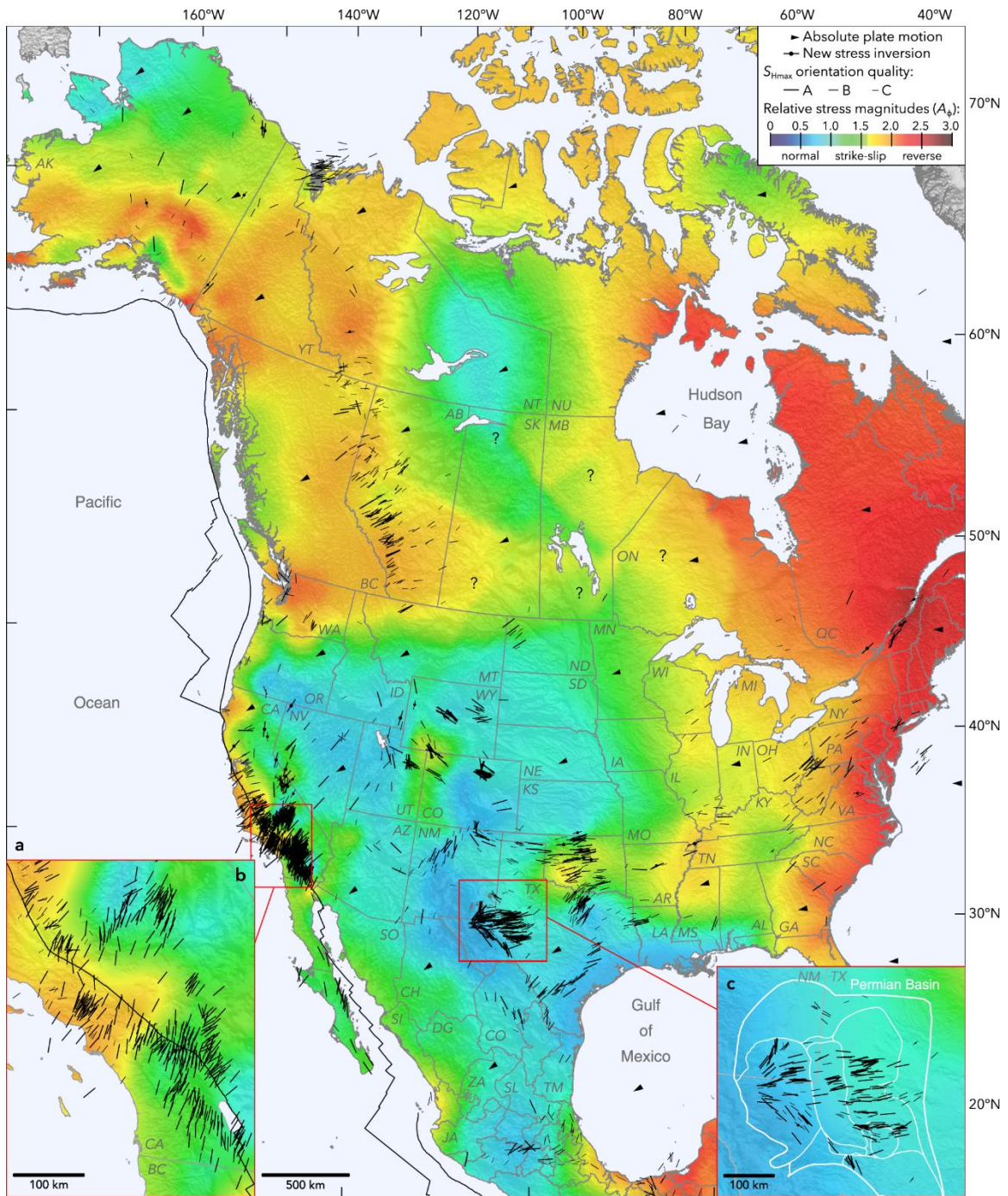
Figure 2.3.   *In-situ* stress states in North America (reproduced with permission from Lund Snee and Zoback, 2020).

2.2.3 Estimating S_v, S_{Hmax}, and S_{hmin}

The magnitude of S_v can be calculated from the total weight of the overlying rock from density logs by

$$S_v|_z = \int_0^z \rho(z)g\,dz \approx \bar{\rho}gz \qquad (2.25)$$

where $\rho(z)$ is the density at a given depth, z is the vertical depth, and g is the gravitational constant, and $\bar{\rho}$ is the mean density of the overburden rock. For offshore locations, S_v estimates must be corrected for the water depth

$$S_v|_z = \rho_w g z_w + \int_{z_w}^z \rho(z)g\,dz \approx \rho_w g z_w + \bar{\rho}g(z - z_w) \qquad (2.26)$$

where ρ_w is the water density and z_w is the local water depth.

S_{hmin} is estimated from leakoff (or minifrac/microfrac) testing (Figure 2.4) performed on wells during drilling

$$S_{hmin} = p_{fc} \qquad (2.27)$$

where p_{fc} is the fracture closure pressure.
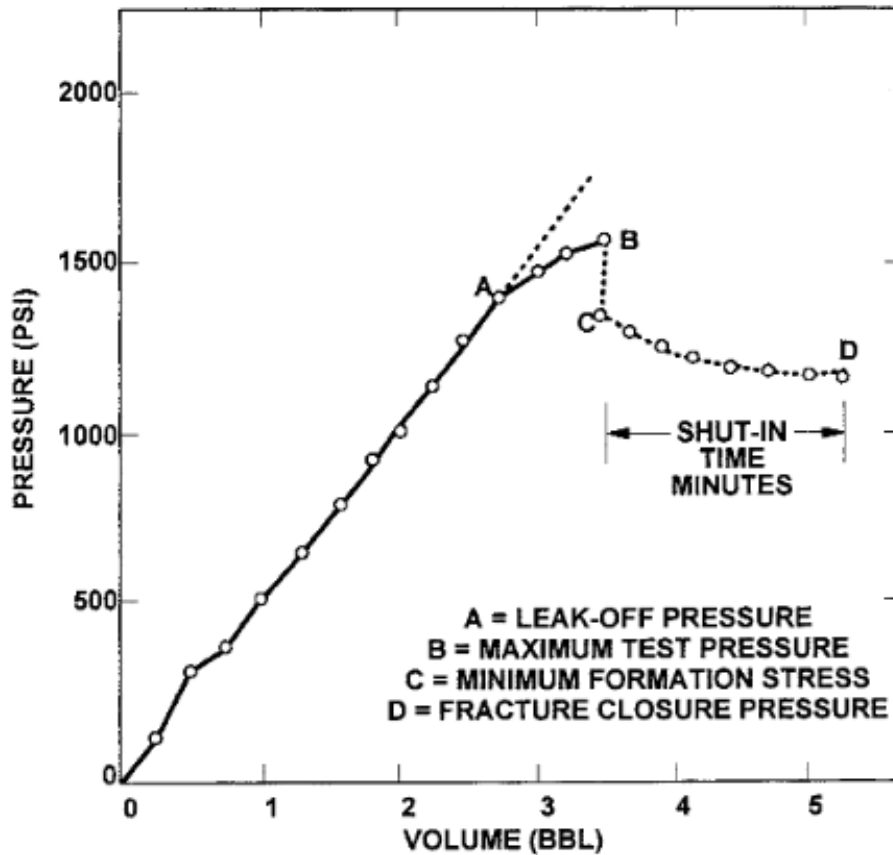
Figure 2.4.   Typical leakoff test pressure profile with injected volume (Postler, 1997).

S_{Hmax} is the hardest principal stress to quantify, as this requires additional information and assumptions (Zoback, 2014). Barton et al. (1988) proposed a procedure for determining S_{Hmax} magnitude using observations of the width of wellbore breakouts. These are compressive failures on the wellbore wall – in a direction parallel to the least compressive stress orthogonal to the borehole – appearing on image and caliper logs as dark bands axial to borehole (Figure 2.5). The bigger S_{Hmax} is compared to S_{hmin} (for vertical wells) the wider the breakouts will be (Figure 2.6). Besides knowledge of the S_{hmin}

magnitude, this technique requires that p_p, S_v, and the rock strength to prevent failure at the given stress state are known (Zoback, 2003).
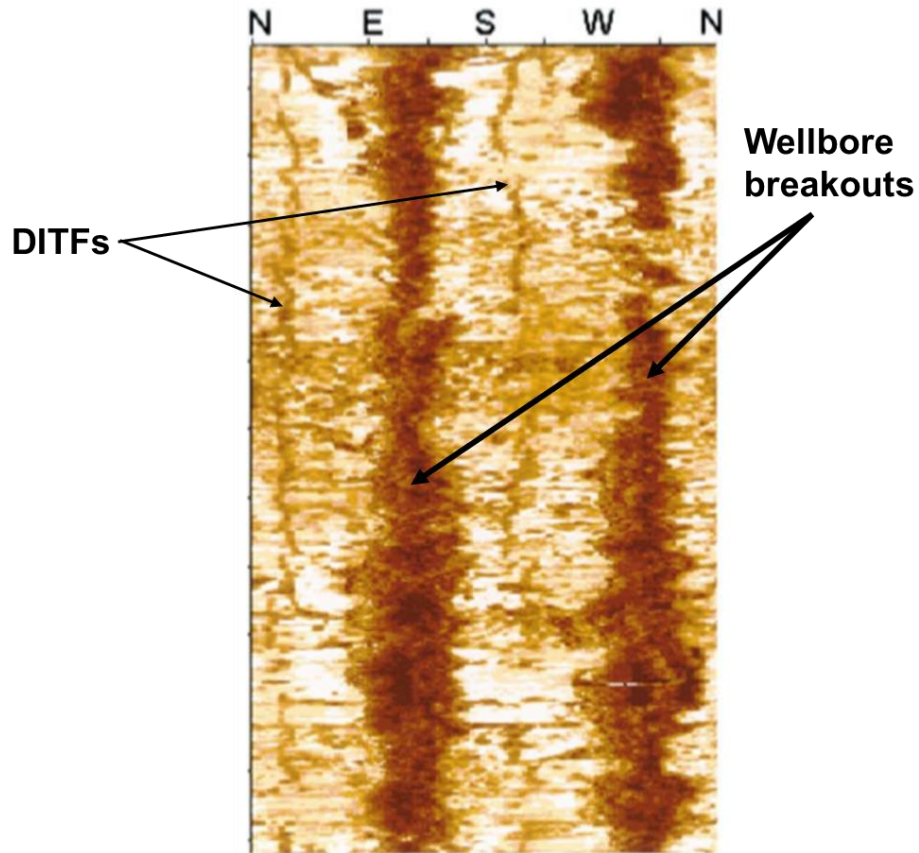
Figure 2.5. Image log from a well showing wellbore breakouts and drilling-induced tensile fractures (DITFs), orthogonally from each other. Both are manifested as dark bands with the breakout bands being much thicker compared to the DITF bands (Zoback et al., 2003).
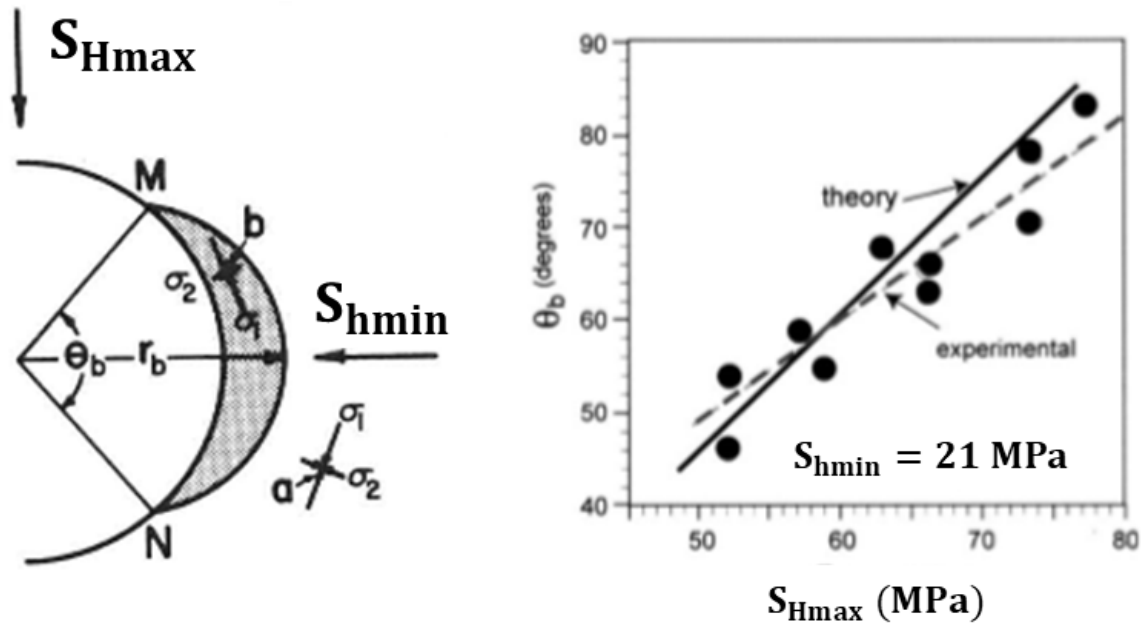
Figure 2.6.   *Left* – Wellbore breakout characterized by its radius, r_b, and angular span, θ_b (modified from Haimson and Herrick, 1986). *Right* – Relationship between θ_b and S_{Hmax} for a fixed S_{hmin}, from theoretical analysis and laboratory experiments (modified from Zoback et al., 2003).

Fault slippage induces local stress perturbations leading to rotation of the breakout azimuth along the wellbore as a function of depth (Figure 2.7). Breakouts cannot form next to a slipped fault due to the fault's stress drop. Barton and Zoback (1994) used dislocation modeling to constrain the S_{Hmax} magnitude if S_v and S_{hmin} are known, as well as the S_{Hmax} orientation and the slipped fault's strike and dip.

25
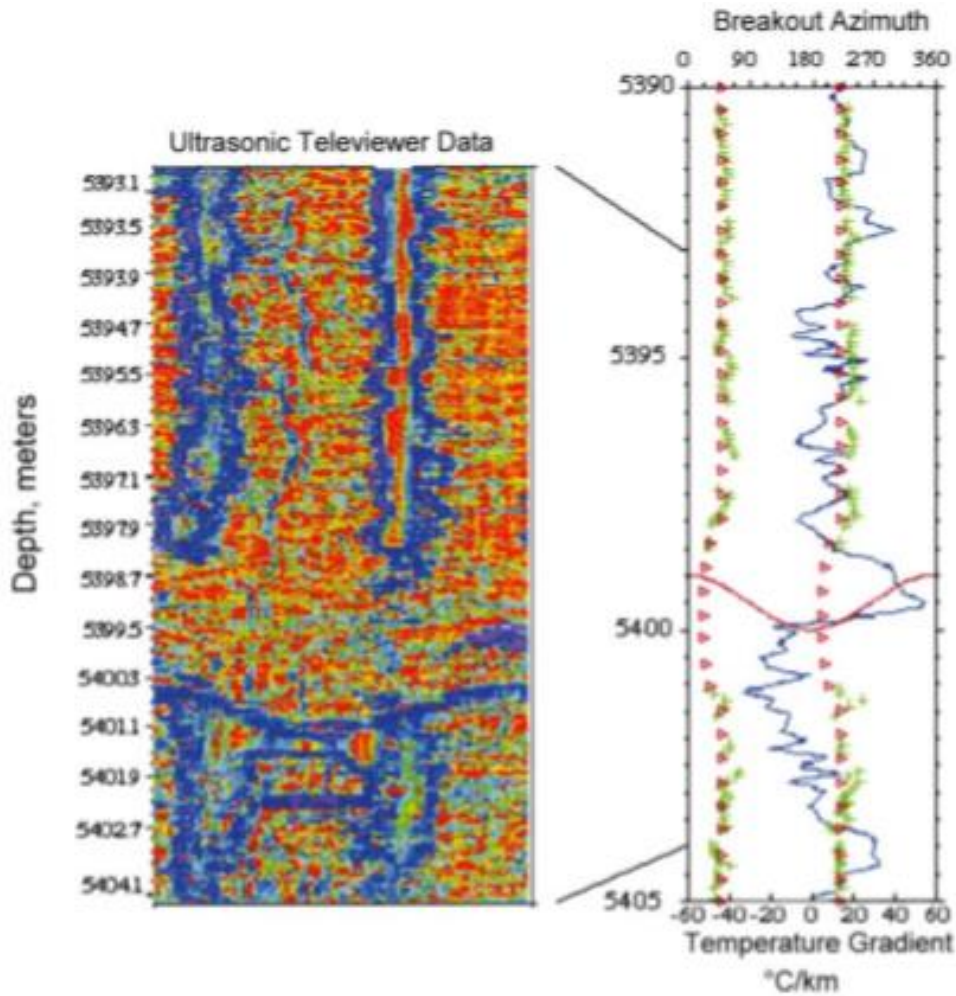
Figure 2.7. Example of wellbore breakout rotation near 5,399 m depth, which is used to model the stress perturbation induced by fault slippage in the borehole vicinity. This can be used to estimate the S_{Hmax} magnitude (from Zoback, 2003).

In addition to breakouts, information from drilling-induced tensile fractures (DITFs) can be utilized to constrain the local S_{Hmax} magnitude. DITFs appear on image and caliper logs, perpendicular to breakouts and narrower in width (Figure 2.5). The formation and orientation of DITFs – longitudinal or transverse relative to the wellbore – can provide range in which the S_{Hmax} magnitude lies. Nelson et al. (2005) used a graphical

26

technique to constrain S_{Hmax} in West Tuna area, in Gippsland Basin, Australia within a narrow range following observation of transverse DITFs from image logs in local wells.

2.3   NEAR-WELLBORE STRESS STATE

The equations describing the stress concentration in an elastic plate with a circular hole under uniform tension at infinity (Grandi et al., 2002) were derived by Kirsch (1898). Hubbert and Willis (1957) modified the relationships to incorporate the p_p-induced effects in a homogeneous, isotropic plate. Haimson and Fairhurst (1967) further modified the expressions for poroelastic media, accounting for fluid infiltration from the wellbore into the surrounding porous-permeable formation. Disregarding any thermal stresses, for a distance r from the center of a well of radius r_w in a vertical well

$$
\begin{aligned}
\sigma_{rr} = {} & \frac{1}{2}(S_{Hmax} + S_{hmin})\left(1 - \frac{r_w^2}{r^2}\right) + \frac{1}{2}(S_{Hmax} - S_{hmin})\left(1 - 4\frac{r_w^2}{r^2} + 3\frac{r_w^4}{r^4}\right)\cos 2\theta \\
& - \frac{r_w^2}{r^2}\left(\frac{1 - 2v}{1 - v}\alpha_B[p_w - p_p] - 2p_w\right)
\end{aligned}
\tag{2.28}
$$

$$
\begin{aligned}
\sigma_{\theta\theta} = {} & \frac{1}{2}(S_{Hmax} + S_{hmin})\left(1 + \frac{r_w^2}{r^2}\right) - \frac{1}{2}(S_{Hmax} + S_{hmin})\left(1 + 3\frac{r_w^4}{r^4}\right)\cos 2\theta \\
& + \frac{r_w^2}{r^2}\left(\frac{1 - 2v}{1 - v}\alpha_B[p_w - p_p] - 2p_w\right)
\end{aligned}
\tag{2.29}
$$

$$
\sigma_{zz} = S_v - 2v(S_{Hmax} - S_{hmin})\frac{r_w^2}{r^2}\cos 2\theta + \frac{r_w^2}{r^2}\left(\frac{1 - 2v}{1 - v}\alpha_B[p_w - p_p] - p_w\right)
\tag{2.30}
$$

$$
\sigma_{r\theta} = \frac{1}{2}(S_{Hmax} - S_{hmin})\left(1 + 2\frac{r_w^2}{r^2} - 3\frac{r_w^4}{r^4}\right)\sin 2\theta
\tag{2.31}
$$

where σ_{rr} is the radial stress, $\sigma_{\theta\theta}$ is the tangential (also called circumferential/"hoop") strength, σ_{zz} is the axial stress parallel to the vertical well (along the z-axis), $\sigma_{r\theta}$ is the shear stress (equal to zero at $r = r_w$), θ is the angle taken from S_{Hmax}, and p_w is the wellbore pressure. Figure 2.8 shows the configuration of the stresses on the wellbore radius for a vertical, semi-cased wellbore.
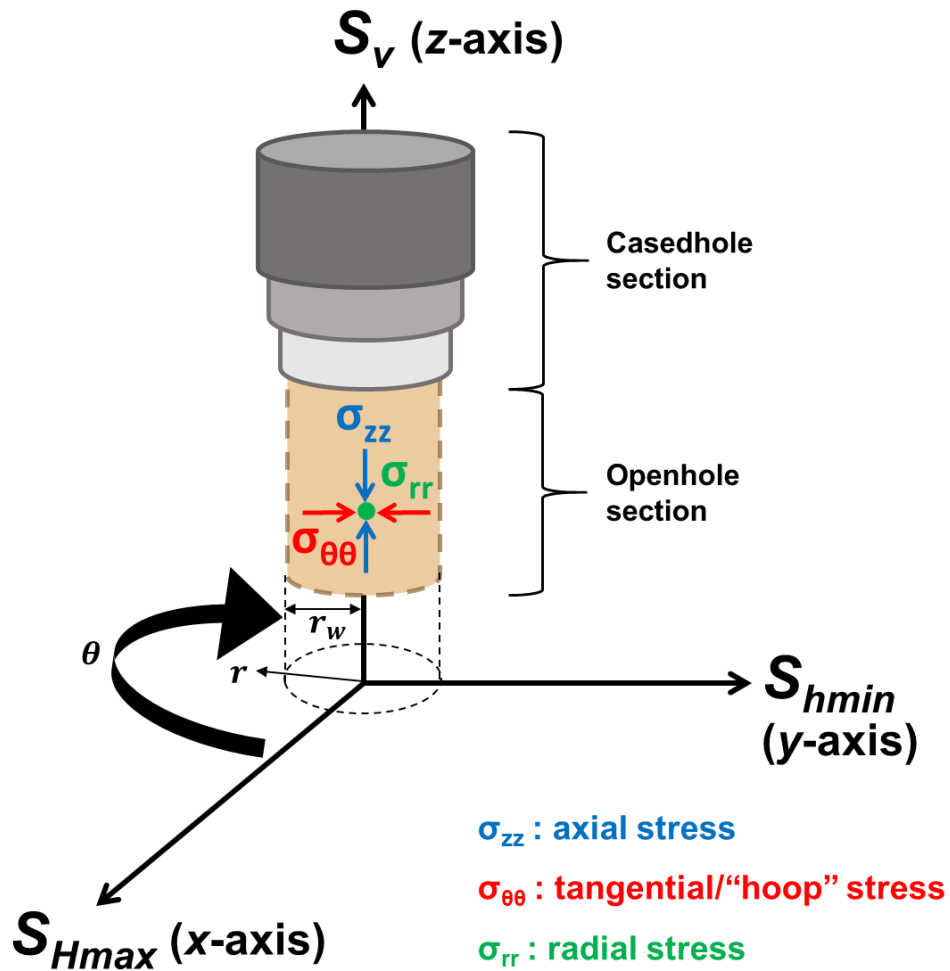
Figure 2.8. Normal cylindrical (σ_{zz}, $\sigma_{\theta\theta}$, and σ_{rr}) stresses on the wellbore radius, $r = r_w$ in the openhole section. As r increases the far-field *in-situ* stresses (S_v, S_{Hmax}, and S_{hmin}) become more dominant.

Eqs. 2.28 through 2.31 can be used to obtain the corresponding near-wellbore stresses for a horizontal well, drilled parallel to S_{hmin} (Chapters 3 and 4) by substituting all the S_{Hmax} terms with S_v, the S_{hmin} terms with S_{Hmax}, the S_v terms with S_{hmin}, keeping everything else the same. This trajectory is popular for horizontal wells in the exploitation of low permeability (tight) reservoirs (e.g., shales).

The *in-situ* stress state of the Barnett Shale in Texas ($S_v = 7{,}215$ psi, $S_{Hmax} = 4{,}550$ psi, and $S_{hmin} = 3{,}900$ psi) is used to demonstrate the impact of fluid infiltration from the wellbore using a poroelastic model (Eqs. 2.28 through 2.31) compared to the conventional linearly elastic model (Eqs. 3.1 through 3.4 in Chapter 3) for the stress-strain behavior in the near-wellbore region. Following Moos (2012), p_p is set at 3,055 psi, with ν at 0.32 and $p_w = S_{hmin}$. A horizontal well is considered parallel to S_{hmin}, which is assumed to be acting along the *y*-axis (hence the axial stress for this well trajectory is denoted by σ_{yy}). Figure 2.9 shows the variation of $\sigma_{\theta\theta}$, σ_{yy}, σ_{rr}, and $\sigma_{r\theta}$ with angle θ around the wellbore radius, considering linearly elastic (dotted lines) and poroelastic (solid lines, at $\alpha_B = 1$) models. For practical purposes, all stress magnitudes are normalized by dividing by S_v.
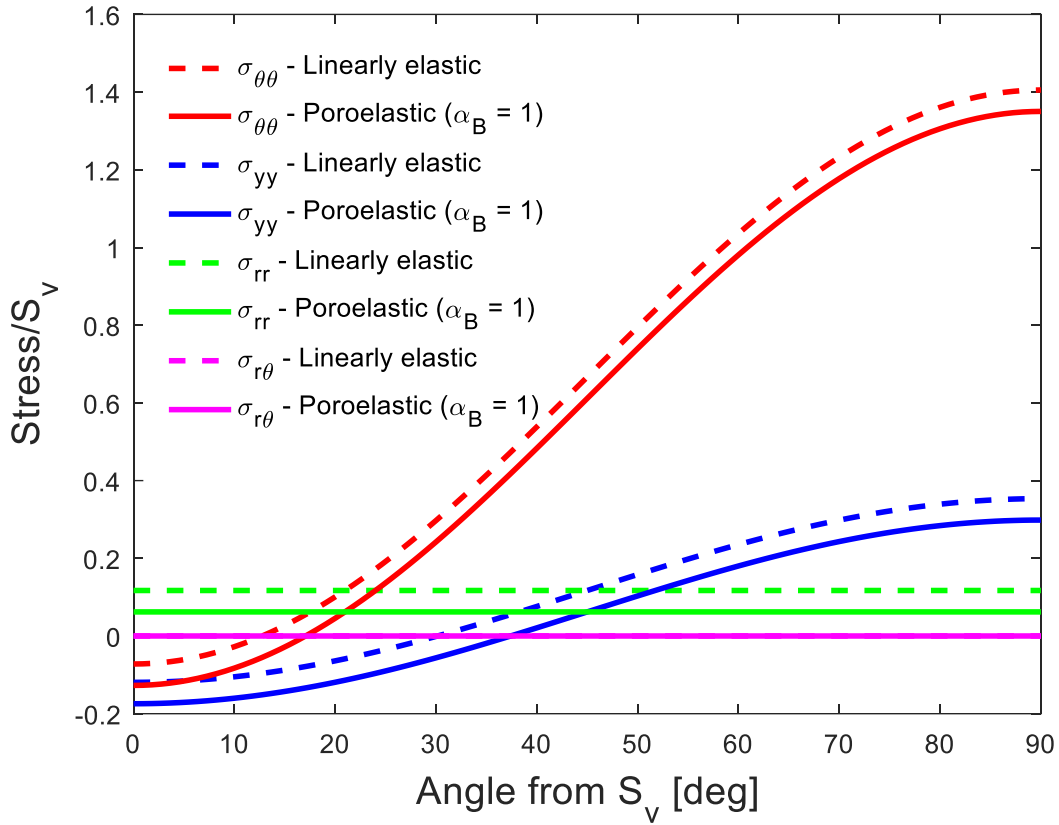
Figure 2.9.   Variation of $\sigma_{\theta\theta}$, σ_{yy}, σ_{rr}, and $\sigma_{r\theta}$ around the wellbore radius for the Barnett Shale in Texas using linearly elastic (dotted lines) and poroelastic (solid lines) models at $p_w = S_{hmin}$.

The deviation in the values of all normal stresses ($\sigma_{\theta\theta}$, σ_{yy}, and σ_{rr}) for $\alpha_B = 1$ from their respective magnitudes using the linear elasticity theory is small and remains constant for $0° \leq \theta \leq 90°$. Evidently, using $\alpha_B = 1$ does not yield the same normal stresses in the near-wellbore region as the linear elasticity theory despite yielding the same effective principal stress magnitudes (Eq. 2.20).

Furthermore, the variation of the stresses on the wellbore radius is examined over a range of p_w values. Figure 2.10 shows the magnitudes of $\sigma_{\theta\theta}$, σ_{yy}, σ_{rr}, and $\sigma_{r\theta}$ with p_w

ranging from 0 to S_v for (a) the top of the hole at $\theta = 0°$ and (b) the side of the hole at $\theta = 90°$.

(a) Top of the Hole, $\theta = 0°$

(b) Side of the Hole, $\theta = 90°$

$\sigma_{\theta\theta}$ - Linearly elastic
$\sigma_{\theta\theta}$ - Poroelastic ($\alpha_B = 1$)
σ_{yy} - Linearly elastic
σ_{yy} - Poroelastic ($\alpha_B = 1$)
σ_{rr} - Linearly elastic
σ_{rr} - Poroelastic ($\alpha_B = 1$)
$\sigma_{r\theta}$ - Linearly elastic
$\sigma_{r\theta}$ - Poroelastic ($\alpha_B = 1$)
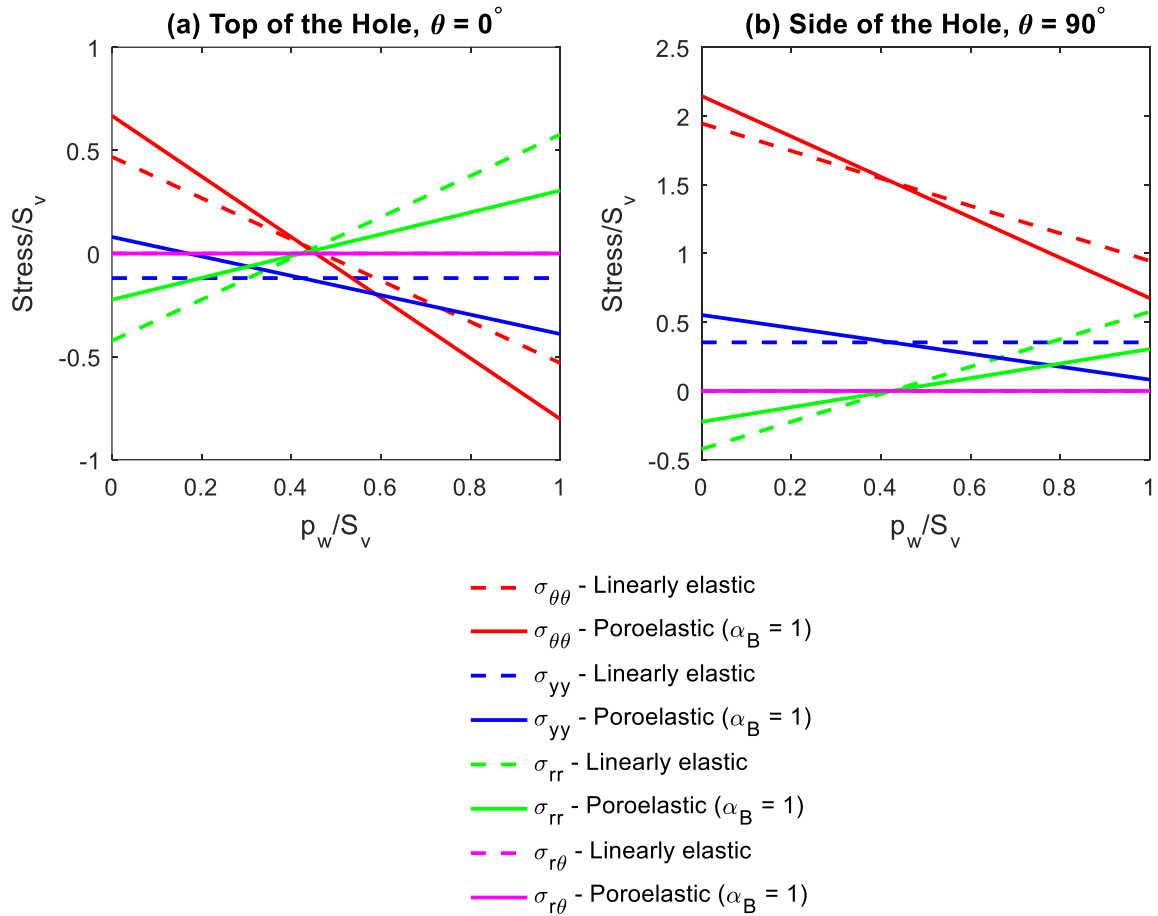
Figure 2.10. Variation of $\sigma_{\theta\theta}$, σ_{yy}, σ_{rr}, and $\sigma_{r\theta}$ for the Barnett Shale in Texas using linearly elastic (dotted lines) and poroelastic (solid lines) models for $0 \leq p_w \leq S_v$. Two locations at $r = r_w$ are shown: (a) top of the hole at $\theta = 0°$ and (b) side of the hole at $\theta = 90°$.

The discrepancy between the linearly elastic and poroelastic models increases as $(p_w - p_p)$ increases and the two models indicate identical solutions at $p_w = p_p$. The value of $\sigma_{r\theta}$ is unaffected by p_w and p_p as well as the constitutive model, remaining at zero.

2.4   STRESSES IN THE CASING WALL

During the 19th century, Gabriel Lamé and B. P. E. Clapeyron derived analytical expressions for the stresses inside "thick-walled cylinders," which apply to strings of steel casing. Similar to Kirsch (1898), three normal stresses in cylindrical coordinates (Eq. 2.32-2.34) are used to characterize the stress state inside the casing walls.

$$\sigma_{rr,csg} = \frac{p_w R_i^2 - p_p R_o^2}{R_o^2 - R_i^2} - \frac{R_o^2 R_i^2 (p_w - p_p)}{r^2 (R_o - R_i)} \tag{2.32}$$

$$\sigma_{\theta\theta,csg} = \frac{p_w R_i^2 - p_p R_o^2}{R_o^2 - R_i^2} + \frac{R_o^2 R_i^2 (p_w - p_p)}{r^2 (R_o - R_i)} \tag{2.33}$$

$$\sigma_{zz,csg} = \frac{p_w R_i^2 - p_p R_o^2}{R_o^2 - R_i^2} \tag{2.34}$$

where, R_i and R_o are the inner and outer radii of the casing wall, respectively with $R_i \leq r \leq R_o$. The axial, tangential and radial stresses in the casing wall are indicated by $\sigma_{zz,csg}$, $\sigma_{\theta\theta,csg}$, and $\sigma_{rr,csg}$, respectively (Figure 2.11).
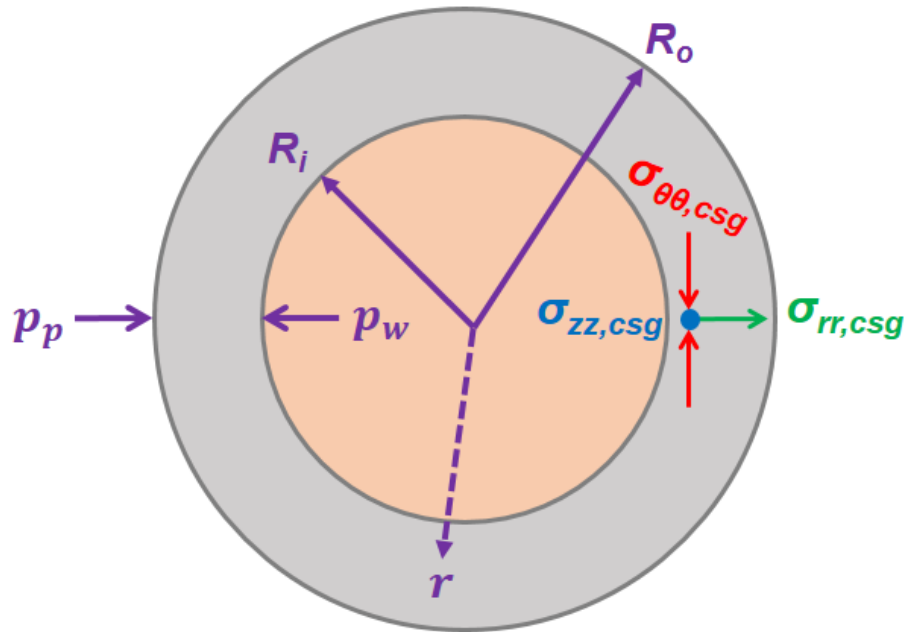
Figure 2.11. Normal stresses configuration inside a "thick-walled" cylindrical casing.

2.5 FRACTURE MECHANICS

2.5.1 Modes of Fracture

There are three fracture modes (Figure 2.12). Mode I refers to fractures where the normal stress direction is perpendicular to the crack surface making the fracture propagate in the direction crack plane. Mode II fractures propagate between crack faces and correspond to in-plane shear forces. Mode III fractures are shear displacements parallel to the crack plane induced by out-of-plane shear. In several cases, a crack exhibits features of more than one mode, resulting in mixed mode fractures.
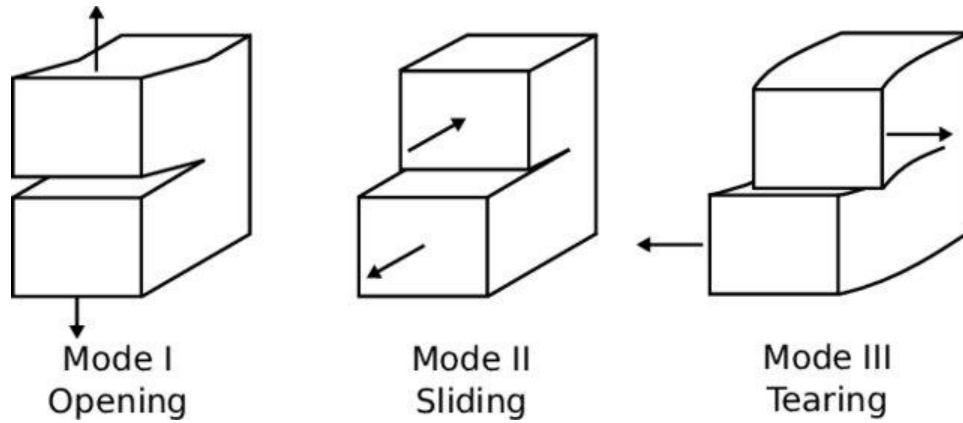
Figure 2.12. The three fracture modes: opening/tensile Mode I, sliding/in-plane shear Mode II, and tearing/out-of-plane shear Mode III (from Brunet et al., 2020).

2.5.2   Stress State Stability *vis-à-vis* Shear Fault Slippage

The range of *in-situ* stress states, which can occur in the Earth's subsurface can be visualized using a simple 2D plot called the allowable stress state diagram, also called a stress polygon (Nelson et al., 2005; Zoback, 2014, Michael, 2019a). This plot has S_{Hmax} normalized by S_v on the vertical axis and S_{hmin} normalized by S_v on the horizontal axis (Figure 2.13). The dotted-diagonal is the line of horizontal isotropy, where $S_{Hmax} = S_{hmin}$ and the solid black lines represent the frictional limits according to Eq. 2.35 for rock friction factors, $\mu = 0.6$ (thicker line) and $\mu = 0.8$ (thinner line), consistent with Byerlee (1978)'s findings. Any stress state outside those bounds is virtually unstable; if a fault exists under those stress state conditions, it will automatically fail in shear as there will be fault slippage.

$$\frac{S_1 - p_p}{S_3 - p_p} \leq \left(\mu + \sqrt{(1 + \mu^2)}\right)^2 \qquad (2.35)$$
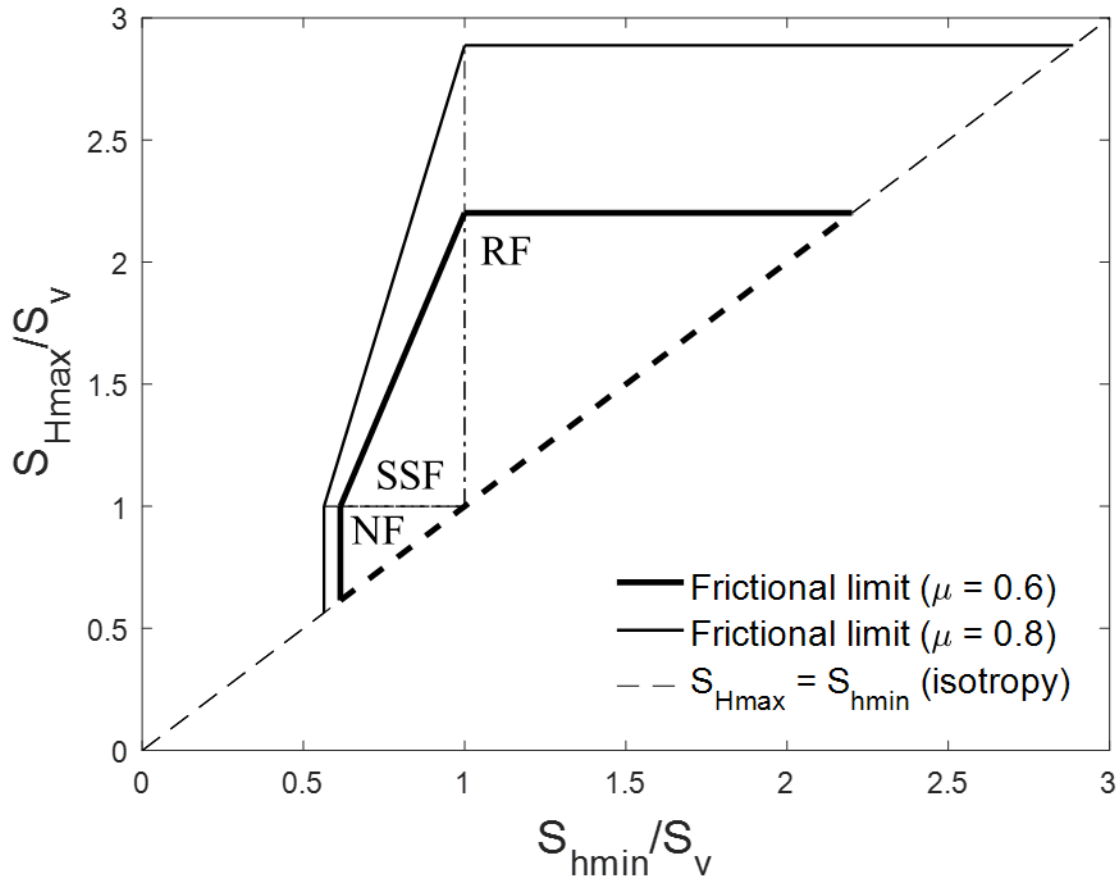
Figure 2.13. Allowable region for *in-situ* stress states in the Earth's subsurface (modified from Michael and Gupta, 2019e). The dotted diagonal line represents horizontal isotropy ($S_{Hmax} = S_{hmin}$), the thicker solid lines represent the frictional limits at $\mu = 0.6$ and the thinner lines represent the frictional limits at $\mu = 0.8$. The region bounded by the frictional limits and the horizontal isotropy diagonal, represents the range of possible subsurface stress states (NF: normal faulting, RF: reverse faulting and SSF: strike-slip faulting – Anderson, 1951).

Eq. 2.35 is called the Mohr-Coulomb (also known as the Coulomb-Navier) failure criterion and assumes that frictional sliding takes place when the ratio of shear stress to normal stress becomes equal to the rock's friction coefficient. Hence, compressive failure

is only a function of the difference between S_1 and S_3. Besides μ, the size of the polygon also depends on p_p. Following Eq. 2.35, an increase in p_p for instance in the vicinity around an active injection well shrinks the polygon decreasing the range of stable stress state making shear fault slippage more likely, assuming all other variables remain constant.

The $A_\emptyset$ distribution (Eq. 2.24) of the stress states stable in the Earth's subsurface is shown on Figure 2.14. The coloring scheme used is the same as for Figures 2.2 and 2.3.
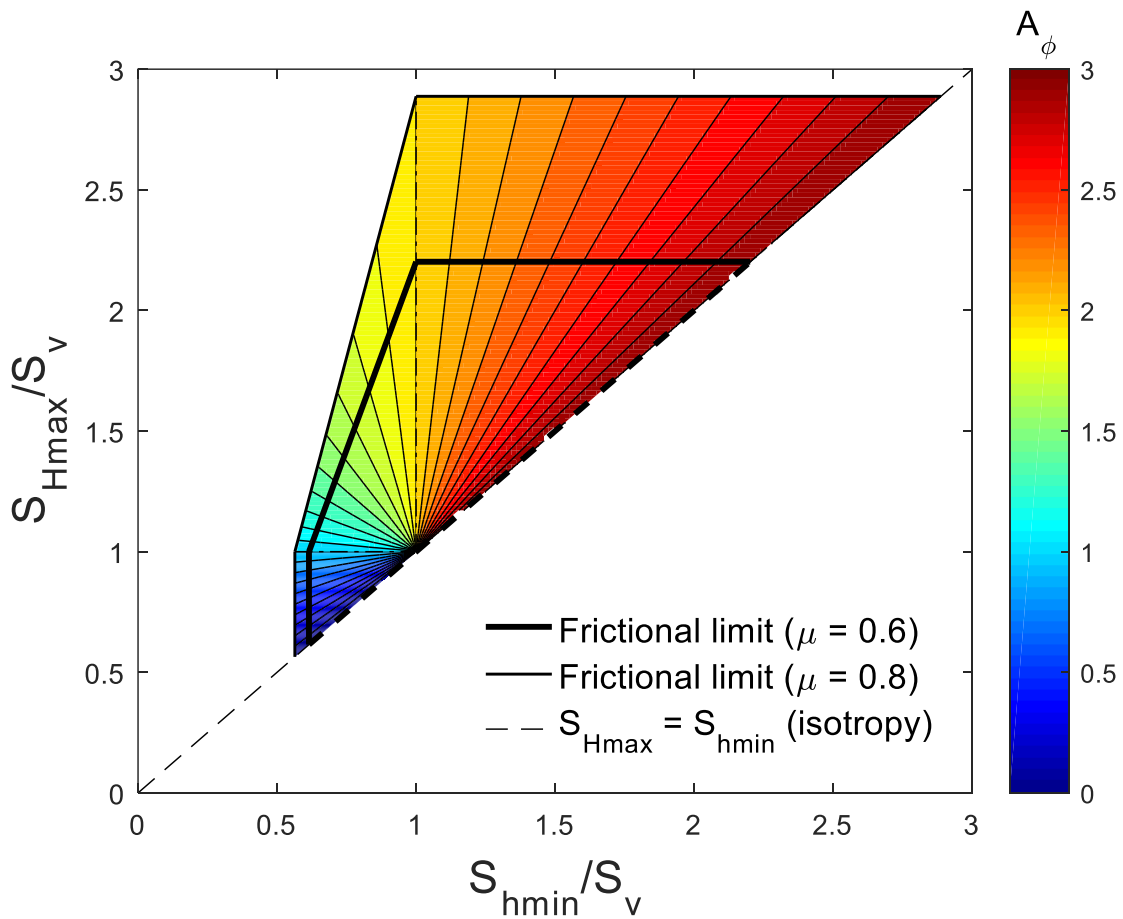
Figure 2.14. Allowable stress diagram (stress polygon) colored according to $A_\emptyset$, quantifying the relative stress magnitude.

2.5.3 Tensile Fractures from the Borehole

Tensile "Mode I" fractures initiate from locations with tensile overstress, when the tensile failure criterion (Eq. 2.36) is exceeded. This occurs when a stress acting at a location becomes more tensile than the tensile strength of the material. In a porous rock with tensile strength, T, when subjected to triaxial stress loading (S_1, S_2, and S_3), the criterion becomes

$$S_3 - p_p < -T \tag{2.36}$$

which leads to a fracture "opening" parallel to S_3 propagating in the plane of S_1 and S_3, which is known as the preferred fracture plane (PFP) from Hubbert and Willis (1957).

The wellbore wall can be the location for tensile fracture initiation when a normal stress acting on the wellbore radius becomes more tensile than T. Considering that almost all variables in Eqs. 2.28 through 2.30 are virtually constant, any variations in the magnitude of these normal stresses (σ_{rr}, $\sigma_{\theta\theta}$, and σ_{zz}) are driven either by variations in p_w or in some rarer occasions, p_p. Both p_w and p_p act as tensile stresses themselves on the wellbore and pore walls, respectively. Therefore, an increase in either p_w and p_p makes tensile fracturing more likely. Figure 2.15 and 2.16 illustrates tensile fracture initiation following a p_w increase above the least compressive principal stress in two and three dimensions, respectively.

$$p_w < S_2 < S_1 \qquad S_2 < p_w < S_1$$
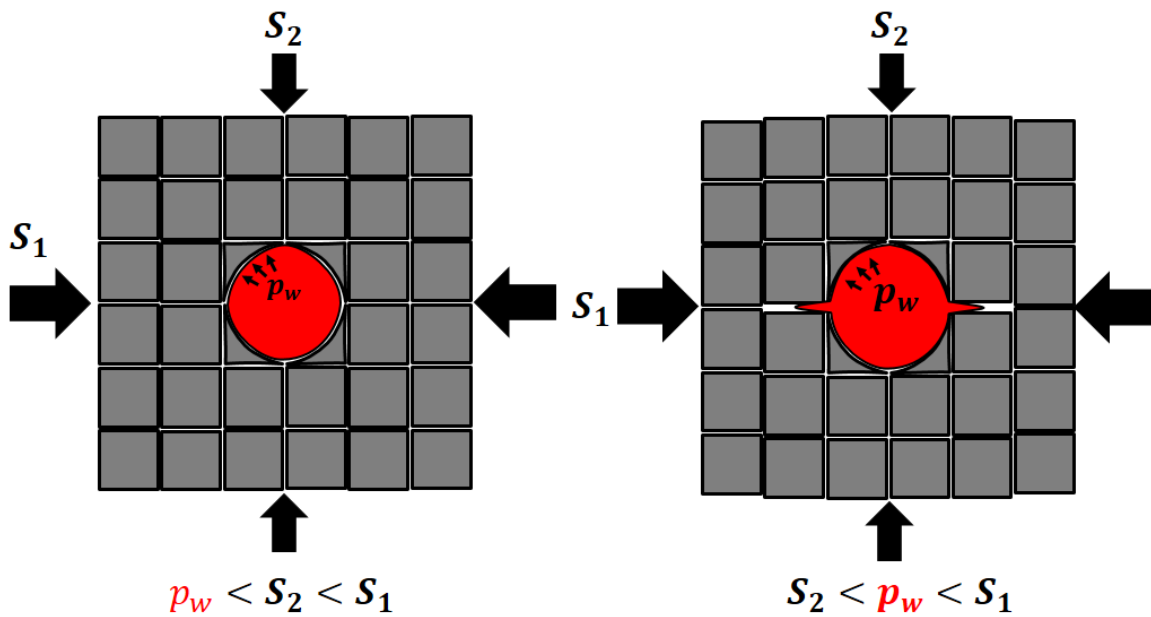
Figure 2.15. Tensile fracture initiation in 2D when p_w surpasses the least compressive principal stress, S_2. The fracture opens against S_2 and propagates in the direction of the greatest compressive principal, S_1 (from Michael, 2016b).

$$p_w < S_3 < S_2 < S_1 \qquad S_3 < p_w < S_2 < S_1$$
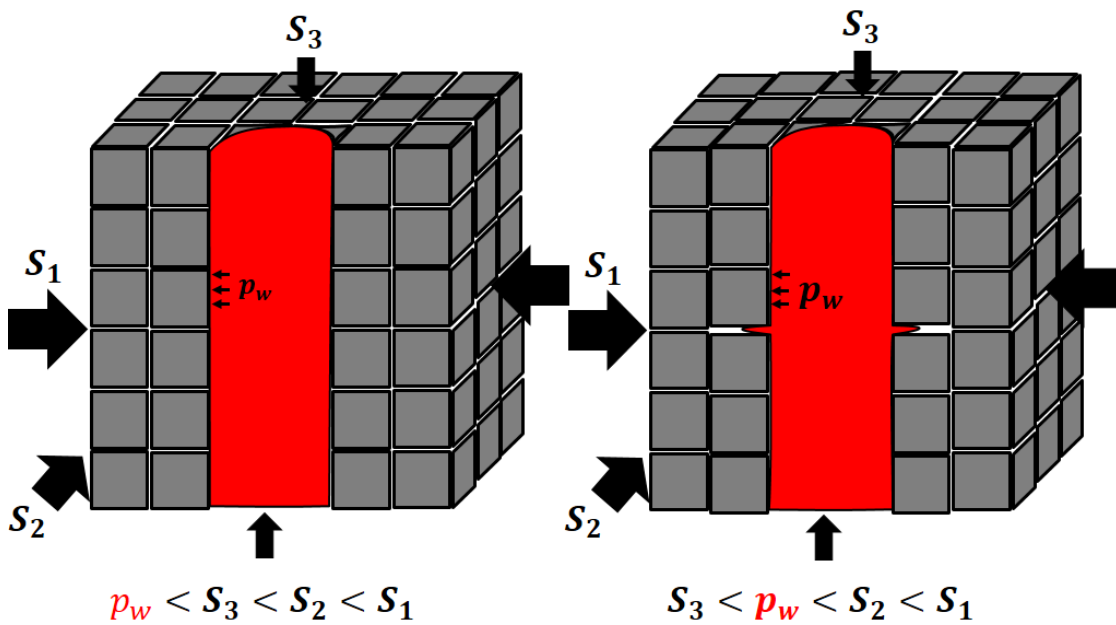
Figure 2.16. Tensile fracture initiation in 3D when p_w surpasses the least compressive principal stress, S_3. The fracture opens against S_3 and propagates in the plane of the greatest and intermediate compressive principal stresses, S_1 and S_2, respectively (from Michael, 2016b).

2.5.4 Fracture Orientation and Performance

The geometric orientation of fractures initiated from pressurized wellbores is determined by the local stress state. As mentioned in Section 2.5.3, tensile fractures propagate along PFP and thus, opening against the least compressive principal stress. The fracture half-length, x_f, and height, H_f, are within PFP, while fracture width, w_f, is orthogonal to PFP, parallel to the least compressive principal stress. For horizontal wells in normal or strike-slip stress states, PFP is vertical, on the plane of S_v with S_{Hmax} (see Chapters 3 through 6). In reverse faulting stress states, PFP is horizontal, on the plane of S_{Hmax} with S_{hmin} (see Chapter 5).

In horizontal wells drilled parallel to S_{Hmax}, induced fractures that propagate axially-to-the-wellbore, hence known as "longitudinal fractures" (Figure 2.17). For wells drilled parallel to S_{hmin} (common oilfield practice), the induced fractures propagate orthogonally-to-the-wellbore and are hence called "transverse fractures" (Figure 2.18). Table 2.2 summarizes the fracture propagation orientation resulting from three extreme well trajectories; vertical, horizontal along S_{Hmax}, and horizontal along S_{hmin} in normal, strike-slip, and reverse faulting stress states.
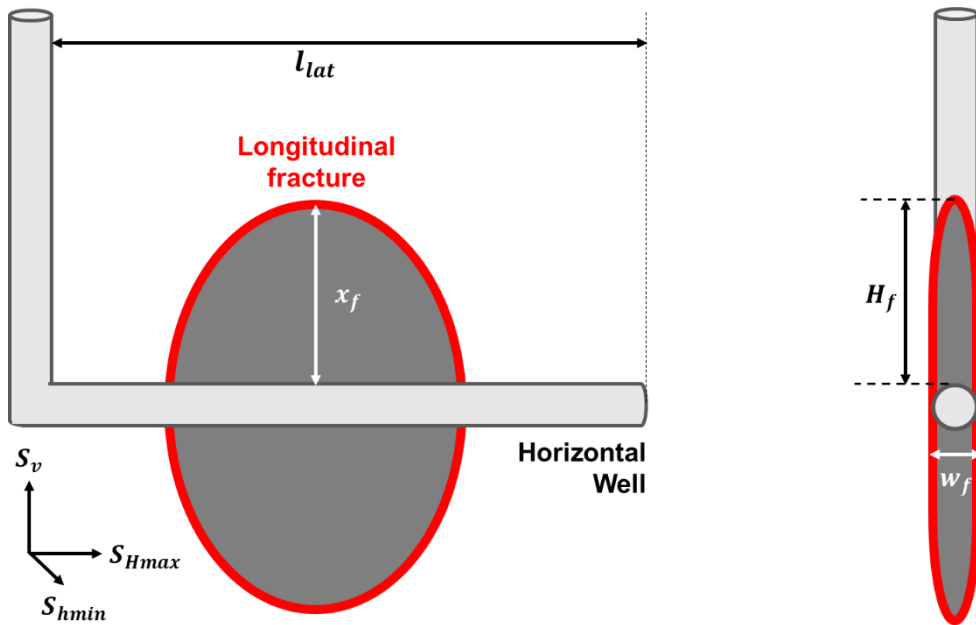
Figure 2.17.　Longitudinal fracturing induced from a horizontal well parallel to S_{Hmax}.
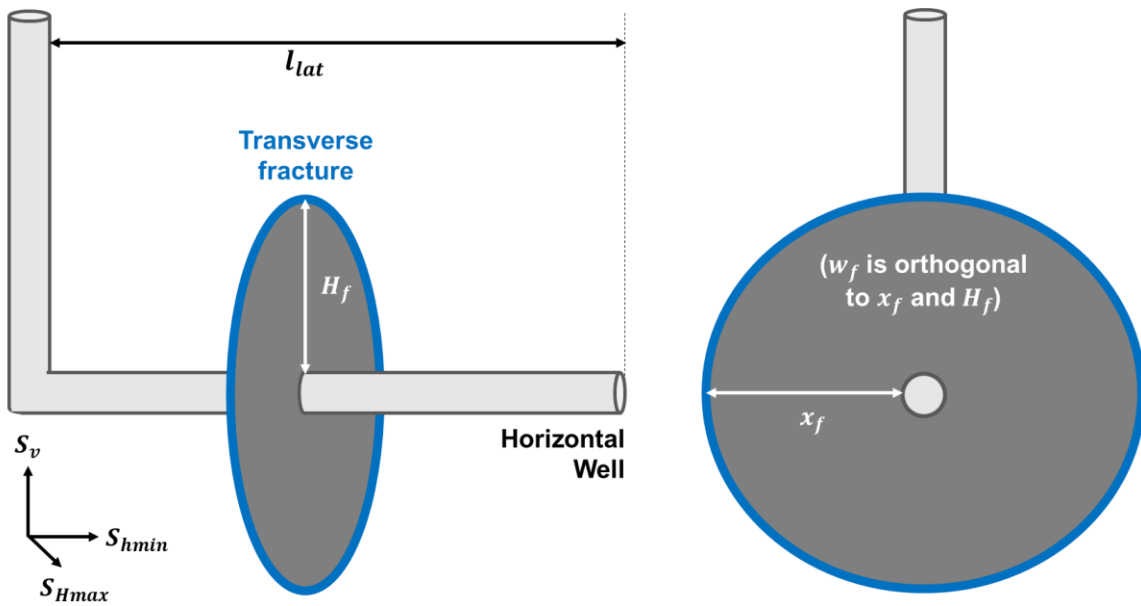
Figure 2.18.　Transverse fracturing induced from a horizontal well parallel to S_{hmin}.

Table 2.2. Fracture propagation planes for three extreme well trajectories in normal, strike-slip, and reverse faulting stress states.

	Normal	Strike-slip	Reverse
Preferred fracture plane (PFP)	$S_v - S_{Hmax}$	$S_{Hmax} - S_v$	$S_{Hmax} - S_{hmin}$
Vertical wells	Longitudinal	Longitudinal	Transverse[I]
Horizontal wells along S_{Hmax}	Longitudinal	Longitudinal	Longitudinal
Horizontal wells along S_{hmin}	Transverse[II]	Transverse	Longitudinal

[I] Transverse fractures from <u>vertical wells</u> extend horizontally, with respect to x_f and H_f, and vertically with respect to w_f.
[II] Transverse fractures from <u>horizontal wells</u> extend vertically, with respect to x_f and H_f, and horizontally with respect to w_f.

An extensive performance comparison between longitudinally and transversely-fractured horizontal wells in oil and gas reservoirs was performed by Yang (2014). Table 2.3 summarizes the conclusions of Yang's (2014) analysis. The key performance indicators (KPI) considered were initial production (IP), economic ultimate recovery (EUR), discounted recovery (DR), present value (PV), and net present value (NPV) over variable reservoir permeability, k. The results indicate a threshold permeability value, the critical permeability, k_{crit}, above which longitudinally-fractured wells outperform transversely-fractured wells. At k values immediately below the critical value, a transition zone occurs, where the number of fractures determines which fracture orientation (longitudinal or transverse) maximizes performance. The magnitude of k_{crit} is highly dependent on x_f, lateral length, l_{lat}, fracture conductivity, F_{CD}, as well as the completion method used (Yang, 2014).

Table 2.3. Summary of Yang's (2014) conclusions on her performance comparison between longitudinally and transversely-fractured horizontal wells.

Completion method	KPI	Oil reservoirs k_{crit} (mD)	Gas reservoirs k_{crit} (mD)
Openhole	-	0.1	0.01[III]
Openhole	50 year-PV	0.4	0.04
Casedhole	All	0.00005-5[IV]	-
Casedhole	50 year-PV	-	1.5[V]
Casedhole	EUR	-	0.5[V]
Casedhole	All	0.00005-5[V]	-

[I] F_{CD} was found to only affect transversely-fractured well performance at a fixed x_f in <u>gas</u> reservoirs of $k < 0.01$ mD. The advantage of higher F_{CD} increases at lower k.
[II] In <u>oil</u> reservoirs of $k > 0.1$ mD, openhole completion improves well performance in either longitudinally or transversely-fractured horizontal wells. For oil reservoirs of $k < 0.01$ mD, the completion method does not make much difference for either fracture orientations.
[III] In <u>gas</u> reservoirs of $k > 0.01$ mD, openhole completion improves well performance in either longitudinally or transversely-fractured horizontal wells.
[IV] In <u>oil</u> reservoirs of $0.00005 \leq k \leq 5$ mD, higher l_{lat} increases well performance. At $k > 5$ mD, for a given drainage area, l_{lat} does not impact well performance.
[V] In <u>gas</u> reservoirs of $0.00005 \leq k \leq 1$ mD, higher l_{lat} increases well performance. At $k > 1$ mD, for a given drainage area, l_{lat} does not impact well performance.

Despite fracture propagation been dictated by the wellbore trajectory, relative to the *in-situ* (far-field) stresses, fracture initiation is not necessarily along the PFP. Initiation of fractures along a plane which is not parallel to PFP, leads to premature termination or fracture reorientation in the near-wellbore region (El Rabaa, 1989; Hallam and Last, 1991; Owens et al., 1992; Weijers, 1992; Olson, 1995). Fracture reorientation induces near-wellbore tortuosity (Michael, 2019a; Huang et al., 2020; Michael et al., 2020), which in turn triggers various completion and production related problems, such as early screenouts and poor post-stimulation well performance (Barree and Miskimins, 2015; Michael, 2019a; Michael et al., 2020).

Chapters 3 through 6 provide a thorough investigation of the orientation of fracture initiation, its ramifications in low permeability reservoirs, and its optimization.

2.5.5 Casing Integrity

The von Mises (1913) criterion of maximum energy distortion, which is used to assess the integrity of "thick-walled cylinders" over a range of conditions, is applied to cylindrical steel casing at a variable p_w. In its simple form, under plane strain assumption, radial stresses are neglected and the criterion can be presented on a 2D plot (Figure 2.19). The tangential stress inside the casing wall, $\sigma_{\theta\theta,csg}$ (Eq. 2.33) is plotted on the vertical axis, with the axial stress inside the casing, $\sigma_{zz,csg}$ (Eq. 2.34) wall plotted on the horizontal axis. Both axes variables are normalized by the yield stress of the casing, σ_{yield}. According to the von Mises (1913)'s theory, the two stresses in the casing wall ($\sigma_{\theta\theta,csg}$ and $\sigma_{zz,csg}$) can be lumped into one term σ_e, or the "von Mises stress equivalent" as defined by Eq. 2.37, which results in an ellipse as shown on Figure 2.19.

$$(\sigma_e)^2 \equiv \left(\sigma_{\theta\theta,csg}\right)^2 - \sigma_{\theta\theta,csg}\sigma_{zz,csg} + \left(\sigma_{zz,csg}\right)^2 < \left(\sigma_{yield}\right)^2 \qquad (2.37)$$

Points outside the ellipsoid indicate casing failure; burst versus collapse from the vertical axis and tension versus compression on the horizontal axis. Chapters 7 and 8 addresses the stability to failure of the casing in place during the extreme stress loads acting on the casing string during loss of well control, following a blowout.

43
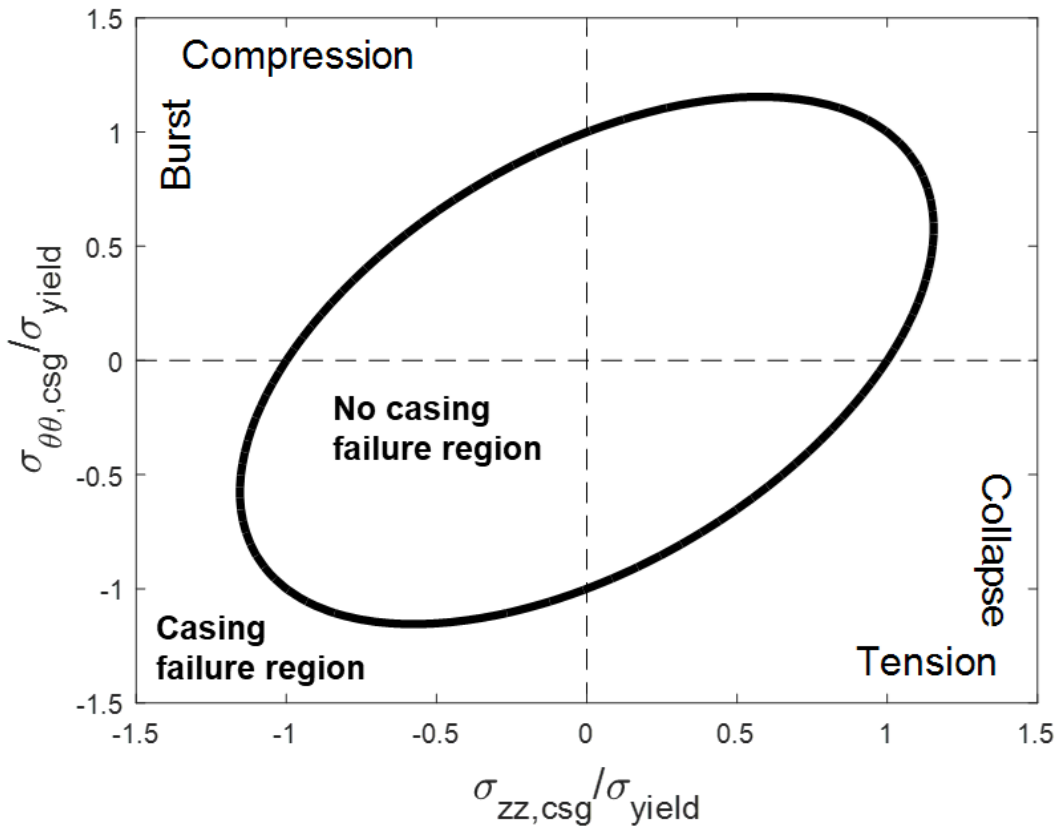
Figure 2.19. The von Mises failure criterion applied to casing failure. As long as the conditions remain within the ellipse, no casing failure will take place. Points outside the ellipse indicate casing failure.

2.5.6 Cement Sheath Integrity

There are four main failure mechanisms observable in the cement sheath, which can compromise the integrity of the casing-cement sheath-rock formation system. These were described by Bois et al. (2011; 2012) as (i) inner and outer debonding, (ii) radial cracking, (iii) shear cracking, and (iv) disking (Figure 2.20). For each failure mechanism an analytical criterion specifies the conditions under which the failure takes place.
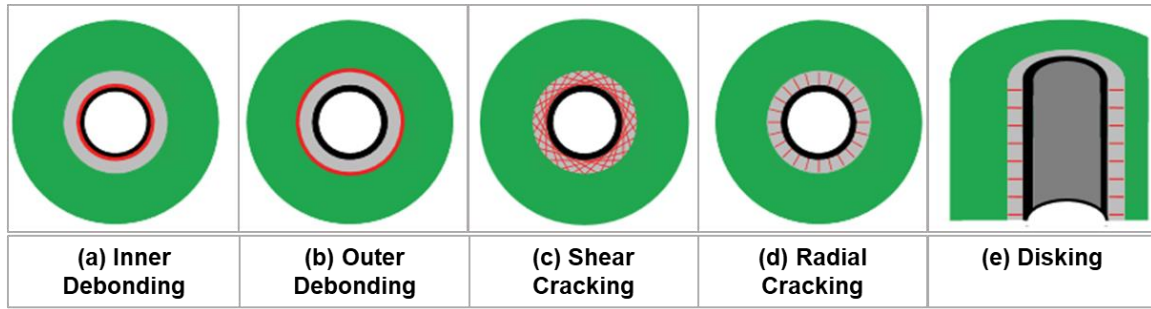
Figure 2.20. The four different mechanisms of cement sheath failure. Failures are indicated with red, while the casing is colored black, the cement sheath in grey, and the surrounding rock formation in green (modified from Bois et al., 2011).

Inner and outer debonding (Figure 2.20a and 2.20b) occurs when the radial stress in the cement sheath $\sigma_{rr,cem}$ becomes more tensile than the tensile strength of the cement, T_{cem}, either at the casing-cement or cement-rock formation interface (first or second interface, respectively). Radial cracking (Figure 2.20d) also falls in the category of tensile failures and takes place when the tangential stress within the cement sheath, $\sigma_{\theta\theta,cem}$, exceeds T_{cem}. Radial cracks are oriented longitudinally to the wellbore axis. Disking (Figure 2.20e) refers to fractures oriented transversely to the wellbore axis, which initiate when the axial stress within the cement sheath, $\sigma_{zz,cem}$, becomes more tensile than T_{cem}.

Shear cracking (Figure 2.20c) is unlike debonding, radial cracking, and disking, a case of shear failure. The criterion used to indicate shear failure induced by compression in solid mechanics is the Mohr-Coulomb criterion. The theory suggests that shear failure occurs when the shear stress within the cement sheath, $\sigma_{r\theta,cem}$, is more compressive than the maximum allowable shear stress, such

$$\sigma_{r\theta,cem} > [C_o + \mu\sigma_n]_{cem} \tag{2.38}$$

where C_o and µ are respectively the cohesion and friction factor of the cement (different than the corresponding values of the rock, although the theory still applies to any intact solid material, porous and non-porous) and σ_n is the normal stress on the plane of failure, defined as

$$\sigma_n = \frac{\sigma_1 + \sigma_3}{2} + \left(\frac{\sigma_1 - \sigma_3}{2}\right) \cos 2\beta \qquad (2.39)$$

where σ_1 and σ_3 are respectively, the greatest and least compressive effective principal stresses per Eqs. 2.20 and 2.23, β is the failure angle (Figure 2.21; angle between the normal to the failure plane and σ_1), and $\sigma_{r\theta}$ (general term for shear stress applicable to any intact solid material; per the nomenclature used, $\sigma_{r\theta,cem}$ refers to the $\sigma_{r\theta}$ of the cement sheath), is expressed by

$$\sigma_{r\theta} = \frac{\sigma_1 - \sigma_3}{2} \sin 2\beta \qquad (2.40)$$
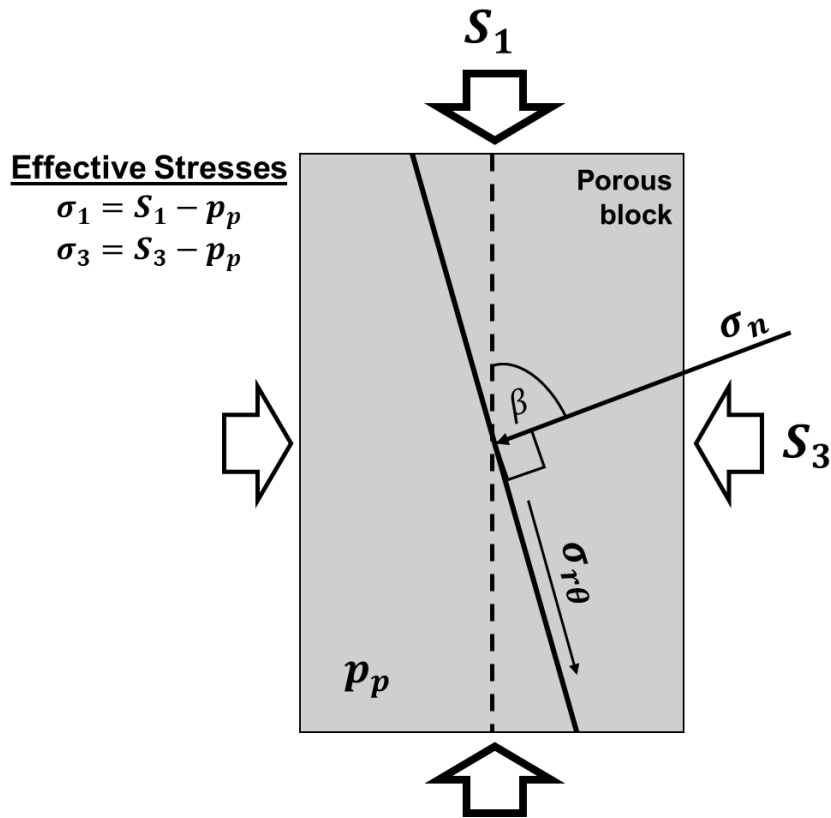
Figure 2.21. The definition of failure angle for a solid porous medium, β, for an arbitrarily-oriented plane of shear compressive failure.

A graphical representation of a shear stability analysis can be performed using a Mohr Circle diagram shown on Figure 2.22 for a solid biaxially loaded with compressive stresses S_1 and S_3 and pore pressure, p_p. Shear failure takes place at the point, where the Mohr Circle, drawn using Eq. 2.40, intersects the Mohr-Coulomb failure line (Eq. 2.38), which indicates the limits of what is commonly referred to as the "Mohr-Coulomb failure envelope." Figure 2.23 shows the relative impact of p_p on the Mohr Circle diagram with high p_p values pushing the Mohr Circle towards the shear failure zone, making the material in question more vulnerable to shear failure and vice versa.
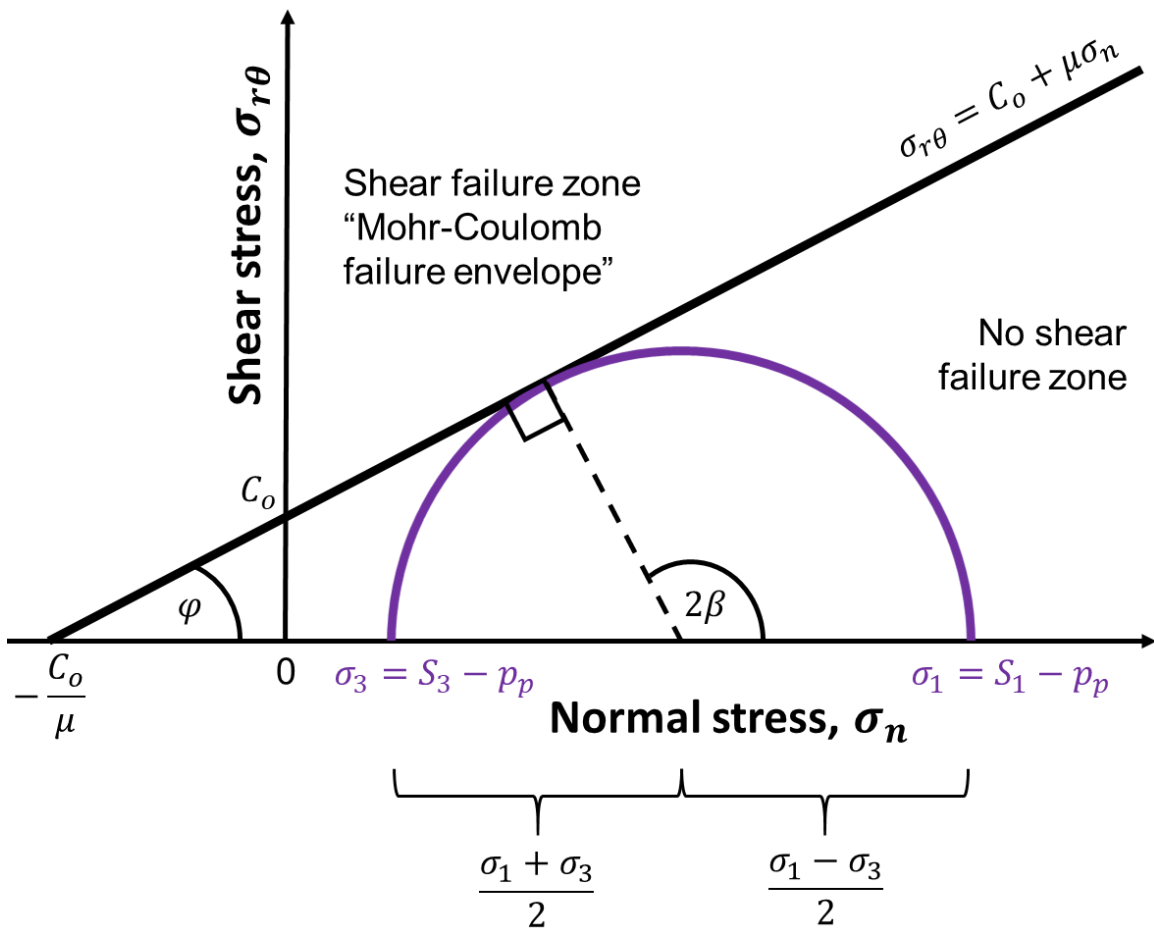
Figure 2.22. Mohr Circle diagram illustrating the point of initial shear failure via compression for an intact porous solid material using the Mohr-Coulomb failure criterion.
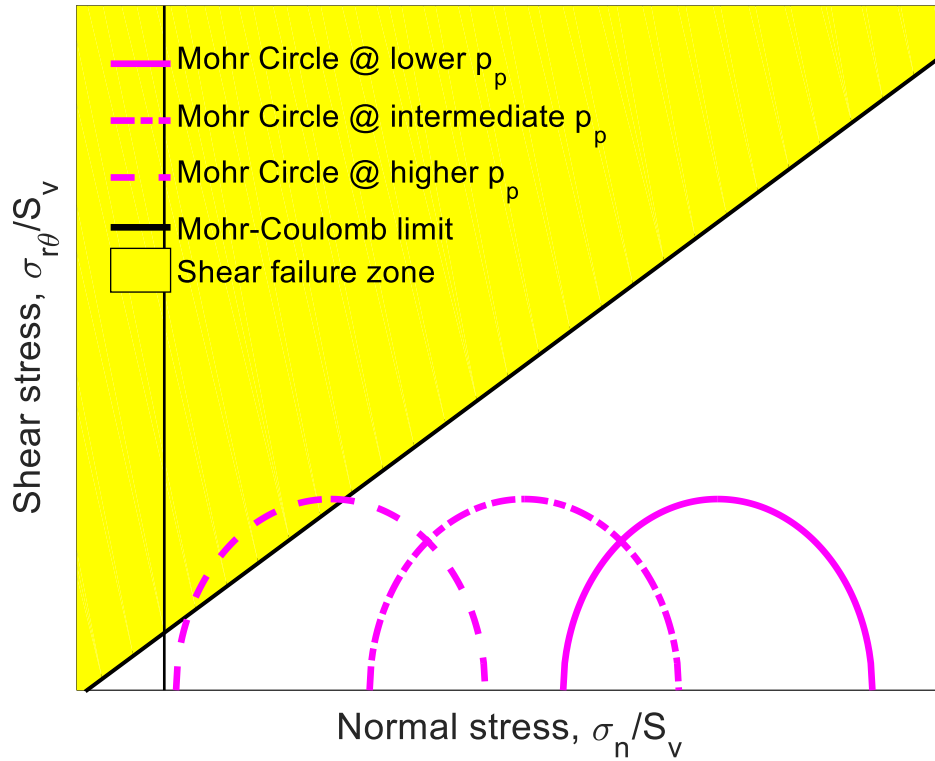
Figure 2.23. The impact of p_p on the shear failure stability of an intact porous solid material. All else equal, higher p_p values make the solid more vulnerable to shear compressive failure and vice versa.

For each scenario, the exact point of failure can be illustrated using a Mohr Circle diagram (Figure 2.22) and the magnitudes of the normal and shear stresses can be determined using Eqs. 2.39 and 2.40, respectively. Using a Mohr Circle diagram, the orientation of the shear failure plane, given by β is quantified by

$$\beta = \frac{\varphi}{2} + \frac{\pi}{4} \tag{2.41}$$

where the internal friction angle of the solid material, φ, is related to μ by

49

$$\mu = \tan \varphi \tag{2.42}$$

Hence, the Mohr-Coulomb theory suggests that at a fixed angle φ, angle β is independent of the stress state. Also, with φ restricted at a range of $0° \leq \varphi \leq 90°$ implies that β ranges at $45° \leq \beta \leq 90°$. Eq. 2.42 allows the Mohr-Coulomb failure criterion (Eq. 2.38) to also be expressed as

$$\sigma_{r\theta} > C_o + (\tan \varphi)\sigma_n \tag{2.43}$$

for shear compressive failure to initiate within the cement sheath, generalized to any intact porous solid material. At the point of failure, the Mohr-Coulomb failure criterion is practically expressed (Jaeger et al., 2007) as

$$\sigma_1 = \frac{2C_o \cos \varphi}{1 - \sin \varphi} + \left(\frac{1 + \sin \varphi}{1 - \sin \varphi}\right)\sigma_3 \tag{2.44}$$

which is an equation used to optimize mud weight during drilling for wellbore stability purposes (Lee et al., 2011).

Chapter 8 discusses the cement sheath's stability to failure, during reservoir depletion following a prolonged post-blowout discharge period, or a high discharge flowrate scenario during loss of well control.

Chapter 3. Analytical Orientation Criteria for Fracture Initiation During Drilling and Completions

In this chapter, analytically-developed criteria are presented for the orientation of fracture initiation in porous-permeable rocks considering fluid infiltration from non-perforated and perforated wellbores. For non-perforated wellbores, this is a fully-exact analytical solution representing the initiation of drilling-induced tensile fractures (DITFs). For perforated wells, a set of analytical approximations are derived for fracture initiation representing completion-induced hydraulic fractures (CIHFs). DITF orientation is used to constrain the *in-situ* stress tensor, especially in the case of transverse DITFs, which are rarer than longitudinal DITFs. Results indicate that transverse CIHF initiation only occurs over a wellbore pressure-at-breakdown window, while longitudinal CIHF initiation occurs at comparatively higher wellbore pressures. Transverse CIHF initiation however, occurs more frequently than transverse DITFs, because the presence of perforations aids transverse fracture initiation. Low Biot's poroelastic coefficient and high Poisson's ratio values also aid transverse fracture initiation. The region of the *in-situ* stress states where transverse initiation is promoted can be shown in dimensionless plots. Case studies are run on seven prolific shale plays (Barnett, Bakken, Fayetteville, Haynesville, Niobrara, Marcellus, and Vaca Muerta) using breakdown pressures from the literature. Transverse CIHF initiation is found to be a highly likely outcome, as opposed to results from past studies that neglected pore pressure effects. Based on the findings of this study, recommendations are made to practitioners to enhance their chances on achieving transverse CIHF initiation in the field. These involve slow injection rates, oriented

perforation strategy and strong bonding between the casing, cement and the surrounding rock to prevent fracturing fluid leakages.

3.1 INTRODUCTION

The impact of hydraulic fracturing has been remarkable and responsible for advances in the development of tight unconventional petroleum resources such as shale oil and gas (Michael, 2014; 2016a). Fluid-driven fracture initiation depends primarily on (i) the subsurface stress state, (ii) the formation's mechanical properties and (iii) perforation presence and geometry. An understanding of these three primary factors with associated data can be used to determine *a-priori* the orientation of a fracture induced from a pressurized wellbore. Some additional secondary factors are fluid-related such as (iv) injection rate and (v) fracturing fluid viscosity (Hubbert and Willis, 1957; Hossain et al., 2000; Fallahzadeh et al., 2017). Waters and Weng (2016) suggested that perforation gun features such as, (vi) diameter and (vii) eccentricity can influence the location and orientation of fracture initiation. For multi-frac operations, parameters of the perforation cluster design, as (ix) perforation density and (x) phasing will impact fracture initiation (Behrmann and Elbel, 1991; Van de Ketterij and de Pater, 1997; Behrmann and Nolte, 1998).

In this study, we develop analytical criteria for the orientation of fracture initiation from horizontal wellbores in porous-permeable media, considering fluid infiltration. Fracture initiation often follows a plane different from the final fracture propagation plane. Stress reorientation in the near-wellbore region may promote fracture initiation of different orientation than that dictated by the far-field, *in-situ* stresses (Hubbert and Willis, 1957).

For the special case of horizontal wellbores, fluid-driven fracture initiation can assume arbitrary orientations with respect to the wellbore, with the two main extreme configurations being longitudinal and transverse (Figure 3.1). Longitudinal, or "axial" fractures, propagate in a plane parallel to the axis of the wellbore and are best promoted by horizontal wells drilled along the direction of the larger horizontal principal stress, S_{Hmax}. Transverse, or "lateral" fractures, propagate in planes orthogonal to the wellbore axis and are best promoted when a horizontal wellbore is drilled parallel to the minimum horizontal principal stress, S_{hmin}.
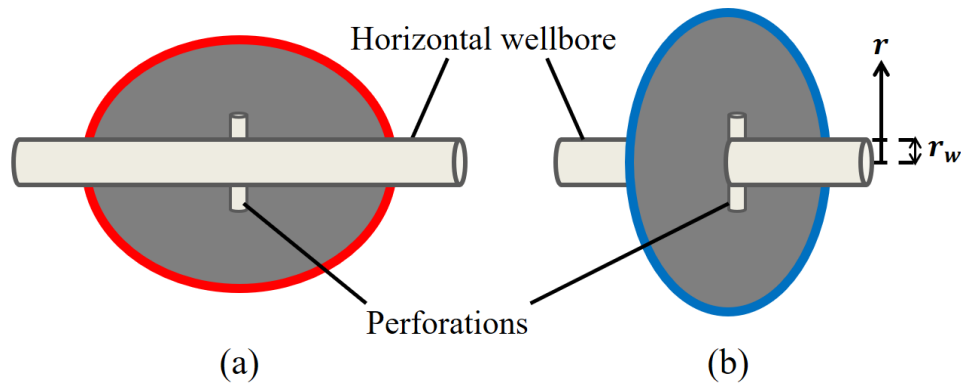
Figure 3.1. Fracture orientation configurations, (a) longitudinal and (b) transverse-to-the-wellbore. The variable r represents a distance from the center of the wellbore and it cannot be smaller than the wellbore radius, r_w.

During drilling fractures may initiate from openhole wellbores before those are cased, cemented and perforated. These fractures are called drilling-induced tensile fractures (DITFs). DITFs are used as diagnostic tools, providing constraints on the magnitude of *in-situ* stress tensor components, local to the well (Peška and Zoback, 1995a and 1995b; Wiprut et al., 1997; Brudy and Zoback, 1999; Nelson et al., 2005; Jia and

Schmitt, 2014; Michael and Gupta, 2019a). DITFs observed in image logs from vertical wells have been used in the past to constrain the magnitude of S_{Hmax} (Nelson et al., 2005) assuming a linearly elastic medium. The two extreme and most prevalent orientations of DITFs – longitudinal and transverse-to-the-well – are shown in the image logs on Figure 3.2. In this study, Nelson et al. (2005) analytical criterion for DITF orientation is extended to porous-permeable media allowing infiltration of the injected fluid into the surrounding rock, in terms of the *in-situ* stress state, wellbore pressure, rock formation pore pressure and mechanical properties. This criterion is thereafter used graphically to constrain the magnitude of S_{Hmax} for a hypothetical case.
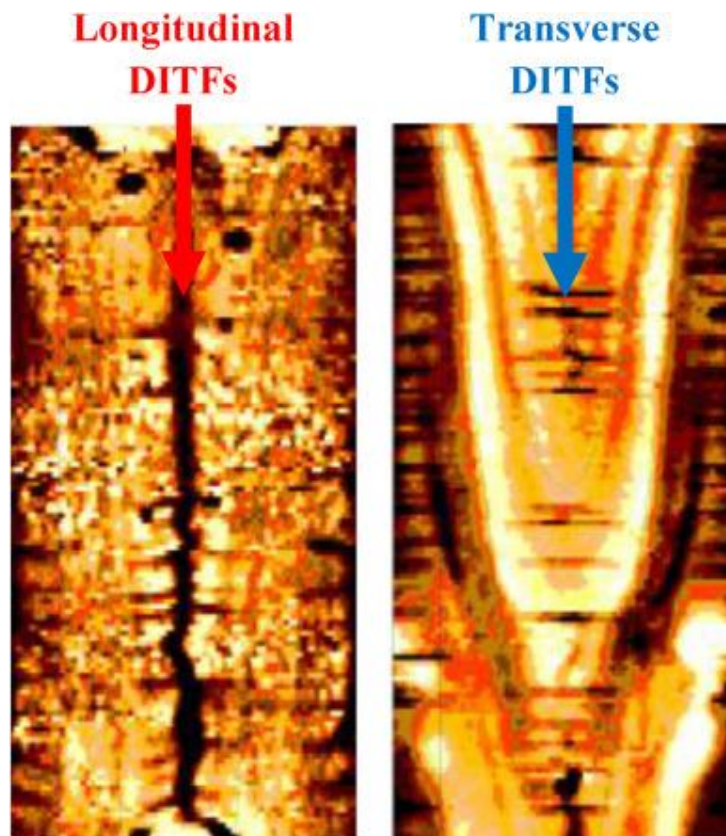
Figure 3.2. Image log examples showing longitudinal and transverse DITFs (modified from Taylor et al., 2013).

For completion-induced hydraulic fractures (CIHFs), initiated from perforated wells for stimulation purposes, the total flowrate from a horizontal well with multiple transverse fractures is much higher than from a similar well with a single large longitudinal CIHF. This makes transversely-oriented CIHFs more desirable for applications to low permeability formations, such as unconventional shales. Longitudinal CIHFs can still outperform transverse fractures in some formations of higher permeability ranges as well as frack-&-pack operations where transverse fractures underperform (Deimbacher and Economides, 1993; Economides and Martin, 2010; Economides et al., 2010), but in low permeability reservoirs, transverse fractures are preferred.

Laboratory experiments in horizontal wells (Figure 3.3) have however shown transverse fracture initiation to be a rarity compared to longitudinal; in the vast majority, transverse fractures resulted through reorientation of what was originally longitudinal fracture initiation (Daneshy, 1973; El Rabaa, 1989; Weijers, 1995; Michael, 2016b). Fracture initiation plane different than the final (perpendicular to the least stress) would mean reorientation of the fracture as it propagates from the near-wellbore region (El Rabaa, 1989; Hallam and Last, 1991; Weijers, 1992; Owens et al., 1992). This fracture reorientation induces near-wellbore tortuosities, which cause various completion and production-related problems, such as early screen-outs and problematic packer isolation in multi-stage fracture treatments. This in turn hinders post-stimulation well performance (Barree and Miskimins, 2015; Michael and Habibi, 2018) adversely affecting the net present value of the hydraulic fracture treatment (Balen et al., 1988; Michael, 2019b).
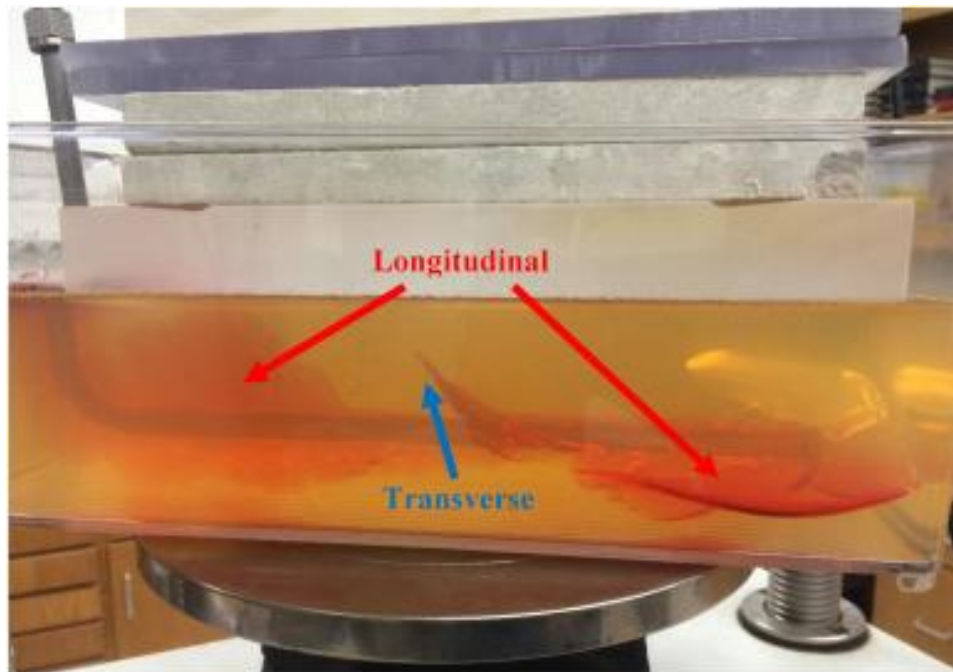
Figure 3.3.   Longitudinal and transverse fractures generated from a perforated horizontal wellbore during scaled laboratory experiments in highly concentrated gelatin (modified Michael, 2016b).

The orientation of CIHFs controls the productivity of hydrocarbon reservoirs. Production from low permeability formations is greatly improved if fractures orient transversely. An understanding of criteria that promote transverse versus longitudinal CIHF initiation for reservoir rock is thus warranted. While studies on fracture initiation have been conducted before, they have mostly neglected pore pressure effects. The criteria developed in this study, consider the tangential stresses on two points (extremes) around the perforation base; one for the initiation of longitudinal CIHF (with respect to the wellbore) and another for the initiation of transverse fractures, both considering fluid infiltration in porous-permeable media. The range of *in-situ* stress states in which transverse fracture initiation is promoted increases as Biot's poroelastic coefficient, α_B

decreases and formation Poisson's ratio *v*, increases. Fracture initiation criteria for specific cases presented can be used to predict the orientation of fracture initiation in field operations.

The resulting criteria are presented on dimensionless plots showing how various parameters affect the range of *in-situ* stress states in which transverse fracture initiation is promoted. Transverse DITFs are a rarity compared to longitudinal DITFs, although transverse CIHF initiation appears to occur more frequently compared to transverse DITFs. This is useful for completion engineers; when targeting low permeability formations, wellbores must be made to induce multiple transverse fractures, as opposed to longitudinal fractures, which are more effective in higher permeability formations. The criteria are finally applied to seven prolific shale plays; Barnett, Bakken, Fayetteville, Haynesville, Niobrara, Marcellus and Vaca Muerta assessing the conditions under which transverse CIHF initiation occurs. Results indicate higher confidence in transverse CIHF initiation when a porous-permeable medium is considered, compared to previous models developed neglecting pore pressure and fluid infiltration.

3.2   THEORETICAL BACKGROUND

As a well is drilled, the wellbore walls must sustain stresses previously supported by the rock volume that is now removed. This cylindrical cavity introduced during drilling in the subsurface medium induces stresses of variable concentration around the borehole. The magnitude of these stresses at the wellbore wall depends on the far-field, *in-situ* stress state, as well as the orientation of the drilled well (Kirsch, 1898; Hubbert and Willis, 1957; Nelson et al., 2005; Zoback, 2014) and is what determines the orientation of the DITFs that are initiated.

3.2.1   Stresses on the Wellbore Radius

The equations for the magnitude of the stresses on a uniform plate with a circular hole under uniform tension were derived by Kirsch (1898) and were then modified to include biaxial stresses and fluid pressure inside the hole by Hubbert and Willis (1957). The magnitude of the stress field can be determined from the *in-situ* principal stresses S_v, S_{Hmax} and S_{hmin} and the mechanical properties of the rock formation. Horizontal wells drilled parallel to S_{hmin} (Figure 3.4) represent the best wellbore trajectory for promoting transverse fracture initiation (Hubbert and Willis, 1957; El Rabaa, 1989; Hallam and Last, 1991).
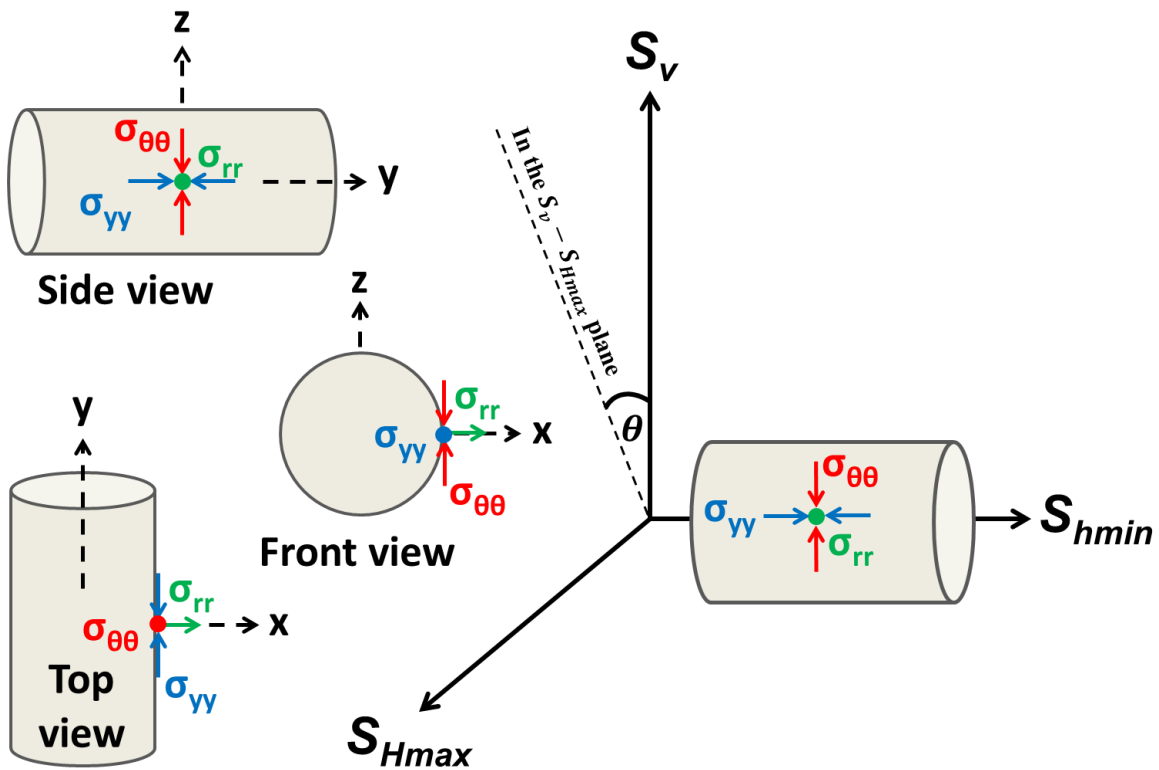
Figure 3.4.   Spatial configuration of the near-wellbore stresses for a horizontal well drilled parallel to S_{hmin}. S_{Hmax}, S_{hmin} and S_v are assumed to be along the *x*, *y* and *z*-axis, respectively. Shear stress is not shown ($\sigma_{r\theta} = 0$ at $r = r_w$).

For a well drilled in a homogeneous, isotropic, linearly elastic rock, the stresses around the wellbore are analytically defined by Zoback (2014). As shown on Figure 3.4, σ_{rr} is the radial stress, $\sigma_{\theta\theta}$ is the tangential (also known as "hoop" or circumferential: normal stress in the tangential direction) stress, σ_{yy} is the out-of-plane stress parallel to the horizontal wellbore, assumed to be parallel to the y-axis, and $\sigma_{r\theta}$ is the shear stress at the wellbore radius ($r = r_w$):

$$\sigma_{rr}|_{r=r_w} = p_w - p_p \tag{3.1}$$

$$\sigma_{\theta\theta}|_{r=r_w} = S_{Hmax} + S_v - 2(S_v - S_{Hmax})\cos 2\theta - p_p - p_w \tag{3.2}$$

$$\sigma_{yy}\big|_{r=r_w} = S_{hmin} - 2\nu(S_v - S_{Hmax})\cos 2\theta - p_p \tag{3.3}$$

$$\sigma_{r\theta}|_{r=r_w} = 0 \tag{3.4}$$

where θ is the azimuth measured from the direction of S_v (top of the hole), p_w is the wellbore pressure (fluid pressure in the borehole) and p_p is the formation pore pressure and ν is the formation's Poisson's ratio.

3.2.2 Modifications for Fluid Infiltration from the Wellbore

In the subsurface, presence of fluids in the rock pores and cracks along with any fluid movements influence the near-wellbore stresses. Hence, the description of small deformation in a fluid-saturated, porous-permeable medium requires the use of Haimson and Fairhurst (1967)'s theory on the stress effects around the wellbore due to penetration

of the injected fluid into the formation medium. The $\boldsymbol{p_p}$ term is therefore substituted by a new term which includes the Biot's poroelastic coefficient, $\boldsymbol{\alpha_B}$ which ranges from zero to one and is used to define the porous-permeable formation as,

$$\alpha_B = 1 - \frac{K_b}{K_g} \tag{3.5}$$

where K_b and K_g are the bulk moduli of the solid and the modulus of the grains, respectively. For a stiff rock the value of α_B is close to 0, because $K_b \approx K_g$ and for a soft rock, α_B approaches 1.0 with $K_b \ll K_g$. This makes the equilibrium stresses around a cylindrical wellbore take a bi-harmonic form as presented in Appendix B (Weijers, 1995; Michael and Gupta, 2019), which includes Biot's poroelastic constant,

$$A = \left(\frac{1-2v}{1-v}\right)\alpha_B \tag{3.6}$$

Eq. 3.6 is used to modify the tangential and axial stresses (Eq. 3.2 and 3.3) around a wellbore to account for fluid infiltration in the pores. Therefore, for a horizontal well parallel to S_{hmin}, the expressions of $\sigma_{\theta\theta}$ and σ_{yy} at $r = r_w$, with θ taken from the direction of S_v become,

$$\sigma_{\theta\theta}|_{r=r_w} = S_v + S_{Hmax} - 2(S_v - S_{Hmax})\cos 2\theta + A(p_w - p_p) - 2p_w \tag{3.7}$$

$$\sigma_{yy}|_{r=r_w} = S_{hmin} - 2v(S_v - S_{Hmax})\cos 2\theta + A(p_w - p_p) - p_w \tag{3.8}$$

The geometrical simplicity of the problem allows us to derive fully-exact, analytical criteria for the orientation of DITFs using the analytical expressions for the stresses at $r = r_w$ in porous-permeable media, where fluid penetration is possible. The DITF orientation can be used to constrain the magnitude of the maximum horizontal stress, S_{Hmax}; the most difficult to evaluate component of the *in-situ* stress tensor. Contrary to DITFs, the complex geometry of a perforated wellbore does not allow derivation of expressions for the exact analytical solutions of the longitudinal and transverse fracturing stresses. Thus, approximations implemented in the past in linearly elastic media are extended to porous-permeable media (allowing fluid infiltration) deriving closed-form analytical expressions for the fracturing stresses, thus helping derive a criterion for the orientation of fracture initiation from perforated wellbores.

3.3 ANALYTICAL APPROACH

Using the near-wellbore stress field, closed-form analytical criteria can be derived for determining the orientation of fracture initiation from non-perforated (i.e., during drilling) and perforated (i.e., during stimulation) wellbores.

3.3.1 DITF Initiation from Non-Perforated Wellbores

In the absence of perforations, what determines the DITF orientation from an openhole section are the magnitudes of $\sigma_{\theta\theta}$ and σ_{yy} at $r = r_w$. Transverse DITFs would initiate only if σ_{yy} is more tensile than the tensile strength of the surrounding rock, $-T$ (i.e., $\sigma_{yy} < -T$) as well as more tensile than $\sigma_{\theta\theta}$ (i.e., $\sigma_{yy} < \sigma_{\theta\theta}$). In all other conditions, the DITFs initiated will be longitudinal-to-the-wellbore (Nelson et al., 2005). This allows

61

the derivation of two closed-form analytical criteria for the initiation of transverse DITFs, for a horizontal wellbore drilled parallel to S_{hmin} in a porous-permeable medium:

$$S_{hmin} - 2v(S_v - S_{Hmax}) \cos 2\theta + (A - 1)p_w - Ap_p + T < 0 \tag{3.9}$$

$$S_{hmin} - S_v - S_{Hmax} + 2(1 - v)(S_v - S_{Hmax}) \cos 2\theta + p_w < 0 \tag{3.10}$$

3.3.2 CIHF Initiation from Perforated Wellbores

The presence of a perforation tunnel intersecting the cylindrical wellbore increases the geometrical complexity of the problem, making derivation of an analytically exact solution extremely challenging. Nevertheless, following Hossain et al. (2000), the application of three assumptions can reduce the problem to a more simplified form, for which closed-form analytical solutions can be derived:

i.   A micro-annulus existing between the cement and the rock formation, allowing the wellbore to be modeled as an openhole. This micro-annulus is promoted by some perforation parameters, such as small gun-to-casing clearance, using a capsule gun and having liquid in the wellbore during the perforation process (Behrmann and Nolte, 1998).

ii. Fractures initiate at the perforation base, which is cylindrical. Laboratory test results on sandstone and hydrostone blocks support this assumption (Behrmann and Elbel, 1991; Zhang et al., 2018).

iii. The pressure on the perforation base is equal to p_w.

Hossain et al. (2000) used analytical approximations for the longitudinal and fracturing stresses from an arbitrarily oriented perforated wellbore in linearly elastic media. These approximations were later modified by Michael et al. (2018) to incorporate the effects of p_p. Expressions for the total tangential, $S_{\theta\theta}$ and the total axial, S_{yy} stresses (from Eq. 3.2 and 3.3 without the p_p term subtracted) are inserted into Eq. 3.7 – the expression for $\sigma_{\theta\theta}$ modified for porous-permeable media with fluid infiltration. For a horizontal wellbore aligned with S_{hmin} (y-axis on Figure 3.4) and perforation pressurized uniformly at p_w, the tangential stress around the base of a cylindrical perforation, $\sigma_{\theta\theta_p}$, takes the form:

$$\sigma_{\theta\theta_p} = S_{yy} + S_{\theta\theta} - 2(S_{yy} - S_{\theta\theta})\cos 2\theta_p + A(p_w - p_p) - 2p_w \qquad (3.11)$$

where θ_p is the angle measured from y-axis (Figure 3.5); the coordinate axis parallel to the wellbore, which is assumed to be parallel to S_{hmin} to maximize the likelihood of transverse CIHF initiation to occur. Substituting Eq. 3.7 and 3.8 into Eq. 3.11 yields,

$$
\begin{aligned}
\sigma_{\theta\theta_p} = {} & (S_{Hmax} + S_{hmin} - 2v[S_v - S_{Hmax}]\cos 2\theta + S_v) \\
& + 2(S_{Hmax} + S_v - S_{hmin} + 2v[S_v - S_{Hmax}]\cos 2\theta)\cos 2\theta_p \\
& - 2(S_v - S_{Hmax})(\cos 2\theta + 2\cos 2\theta \cos 2\theta_p) \\
& - p_w(3 + 2\cos 2\theta_p) + A(p_w - p_p)
\end{aligned}
\qquad (3.12)
$$

For a perforation oriented parallel to the S_{Hmax} (Figure 3.4) in a porous-permeable medium, $\theta = 90°$, the tangential stress around the perforation base, $\sigma_{\theta\theta_p}$ is simplified to:

$$\sigma_{\theta\theta_p}\Big|_{\theta=90°} = S_{hmin} + ([4v-2]\cos 2\theta_p - 2v - 1)S_{Hmax}$$
$$+ ([6-4v]S_v - 2S_{hmin})\cos 2\theta_p + (2v+3)S_v \qquad (3.13)$$
$$+ 3A(p_w - p_p) - (3 + 2\cos 2\theta_p)p_w$$

Eq. 3.13 has two extreme values designated as the longitudinal fracturing stress, $\sigma_{\theta L}$ and the transverse fracturing stress, $\sigma_{\theta T}$ (Figure 3.5). A similar designation can be made for a perforation at the top of the hole ($\theta = 0°$). At $\theta_p = 0°$, $\sigma_{\theta\theta_p} = \sigma_{\theta L}$ and at $\theta_p = 90°$, $\sigma_{\theta\theta_p} = \sigma_{\theta T}$ such that,

$$\sigma_{\theta L} \equiv \sigma_{\theta\theta_p}\Big|_{\theta=90°,\theta_p=0°}$$
$$= 9S_v - 3S_{Hmax} - (S_{hmin} - 2v[S_{Hmax} - S_v]) \qquad (3.14)$$
$$+ A(p_w - p_p) - 5p_w$$

$$\sigma_{\theta T} \equiv \sigma_{\theta\theta_p}\Big|_{\theta=90°,\theta_p=90°}$$
$$= 3S_{hmin} - (2 - 6v)(S_v - S_{Hmax}) - S_v - S_{Hmax} \qquad (3.15)$$
$$+ A(p_w - p_p) - p_w$$
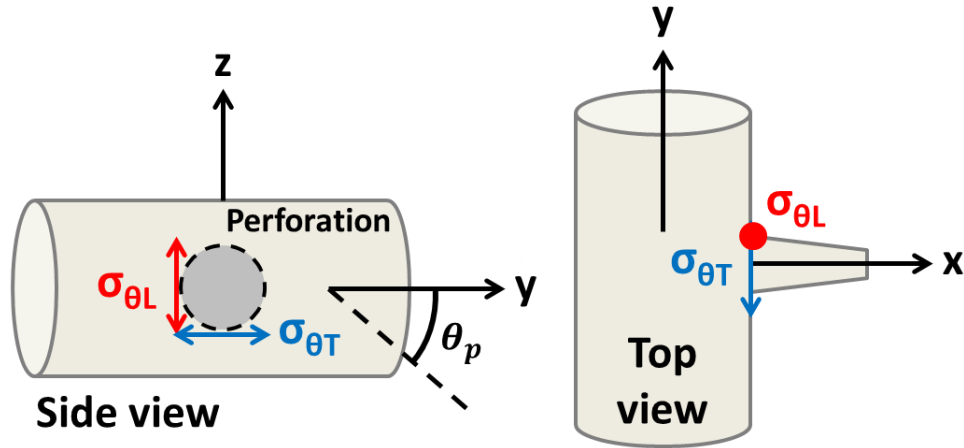
Figure 3.5. Configuration of the longitudinal $\sigma_{\theta L}$ ($\sigma_{\theta\theta_p}$ at $\theta_p = 0°$) and transverse $\sigma_{\theta T}$ ($\sigma_{\theta\theta_p}$ at $\theta_p = 90°$) fracturing stresses at the base of the perforation. The wellbore is assumed to be drilled parallel to the y-axis with perforations parallel to the x-axis.

Analytical approximations for $\sigma_{\theta L}$ and $\sigma_{\theta T}$ can be derived for any wellbore trajectory and perforation direction.

Incorporating tensile strength, T in the failure criterion requires, $\sigma_{\theta\theta_p}\big|_{\theta_p} < -T$, following a sign convention where compressive stresses are positive and tensile stresses negative. If the criterion is satisfied for $\theta_p = 0°$ and $\theta_p = 90°$, (Eq. 3.16, for $\sigma_{\theta T} < -T$), transverse CIHF initiation occurs if $\sigma_{\theta L}$ is more compressive/less tensile than $\sigma_{\theta T}$, such that $\sigma_{\theta T} < \sigma_{\theta L}$, giving a second condition for preferred transverse fracturing (Eq. 3.17), for $\sigma_{\theta T} = \sigma_{\theta L}$), which is the same as the corresponding expression derived for linearly elastic media after Hossain et al. (2000):

$$3S_{hmin} - (2 - 6v)(S_v - S_{Hmax}) - S_v - S_{Hmax} + (A - 1)p_w - p_p + T < 0 \quad (3.16)$$

$$S_{Hmax} + S_{hmin} - 3S_v + 2v(S_v - S_{Hmax}) + p_w < 0 \quad (3.17)$$

If the perforation is at the top of the hole (S_v direction), the S_v and S_{Hmax} terms are interchanged leading to the corresponding expressions for $\sigma_{\theta L}|_{\theta=0°}$ and $\sigma_{\theta T}|_{\theta=0°}$.

3.3.3 Initiation Pressures of DITFs and CIHFs

As mentioned in the previous section, in order for transverse DITFs to initiate from a non-perforated openhole wellbore, the following two conditions must be met at a specific position θ around the hole:

i. The wellbore axial stress is more tensile than the rock's tensile strength, (i.e., $\sigma_{yy} < -T$).

ii. The wellbore axial stress is more tensile than the wellbore tangential stress, (i.e., $\sigma_{yy} < \sigma_{\theta\theta}$).

For a horizontal well drilled parallel to S_{hmin} the initiation pressures for longitudinal and transverse DITFs, p_{iL} and p_{iT} respectively, can be calculated from a location θ by setting Eq. 3.7 and 3.8 equal to $-T$, respectively and solving for p_w. As the whole circumference of the borehole is exposed during drilling, there is an infinite number of potential DITF initiation locations. DITFs will initiate from the location around the borehole at which either p_{iL} or p_{iT} is minimized, such that

$$p_{iL}|_\theta = min\left(\frac{2(S_v - S_{Hmax})\cos 2\theta - S_v - S_{Hmax} + Ap_p - T}{A - 2}\right) \qquad (3.18)$$

$$p_{iT}|_\theta = min\left(\frac{2v(S_v - S_{Hmax})\cos 2\theta - S_{hmin} + Ap_p - T}{A - 1}\right) \qquad (3.19)$$

Similarly, expressions for p_{iL} and p_{iT} can also be derived for wellbores of different trajectories. The DITF initiation mechanism is identical to the mechanism of fracture initiation during the post-blowout capping stage in loss of well control situations (Michael and Gupta, 2018).

The p_w at CIHF initiation is approximated in the field as the breakdown pressure, p_b (the highest pressure reached during a hydraulic fracture treatment). Although studies (Zoback et al., 1977) have shown that fractures can initiate at p_w values narrowly below p_b, in this study we assume that CIHFs initiate at p_b. Analytical expressions (Eq. 3.20 and 3.21) are derived for p_b for longitudinal and transverse CIHF initiation, (p_{bL} and p_{bT}) by setting Eq. 3.14 and 3.15 equal to $-T$ and solving for p_w, respectively:

$$p_{bL}|_{\theta=90°} = \frac{Ap_p + 2v(S_v - S_{Hmax}) + 3S_{Hmax} - 9S_v + S_{hmin} - T}{A - 5} \qquad (3.20)$$

$$p_{bT}|_{\theta=90°} = \frac{Ap_p + S_v + S_{Hmax} - 3S_{hmin} + (2 - 6v)(S_v - S_{Hmax}) - T}{A - 1} \qquad (3.21)$$

Similar expressions are derived for p_b for CIHFs initiating from perforations at the top of the hole aligned parallel to S_v at ($\theta = 0°$), by interchanging all S_v and S_{Hmax} terms.

3.4 OILFIELD APPLICATION

3.4.1 Allowable Stress State Diagrams

The range of possible relative principal stresses can be visualized on a diagram of S_{Hmax}/S_v against S_{hmin}/S_v (Figure 3.6, after Nelson et al., 2005 and Zoback, 2014). The allowable region is bounded by the frictional limits and the line of horizontal isotropy ($S_{Hmax} = S_{hmin}$). The theory of frictional limits constrains the magnitude of the horizontal stresses by not allowing the ratio of the effective maximum to minimum stress $(S_1 - p_p)/(S_3 - p_p)$ to exceed the critical minimum value required for slippage on a pre-existing fault, which is ~3.12-4.33 (for rock friction factor, $\mu = 0.6$-0.8 after Byerlee, 1978). S_1 and S_3 are the greatest and least compressive principal stresses. The allowable region for possible subsurface stress states for a hydrostatic p_p gradient of 0.43 psi/ft, therefore becomes a region enclosed by the polygon shown in Figure 3.6.
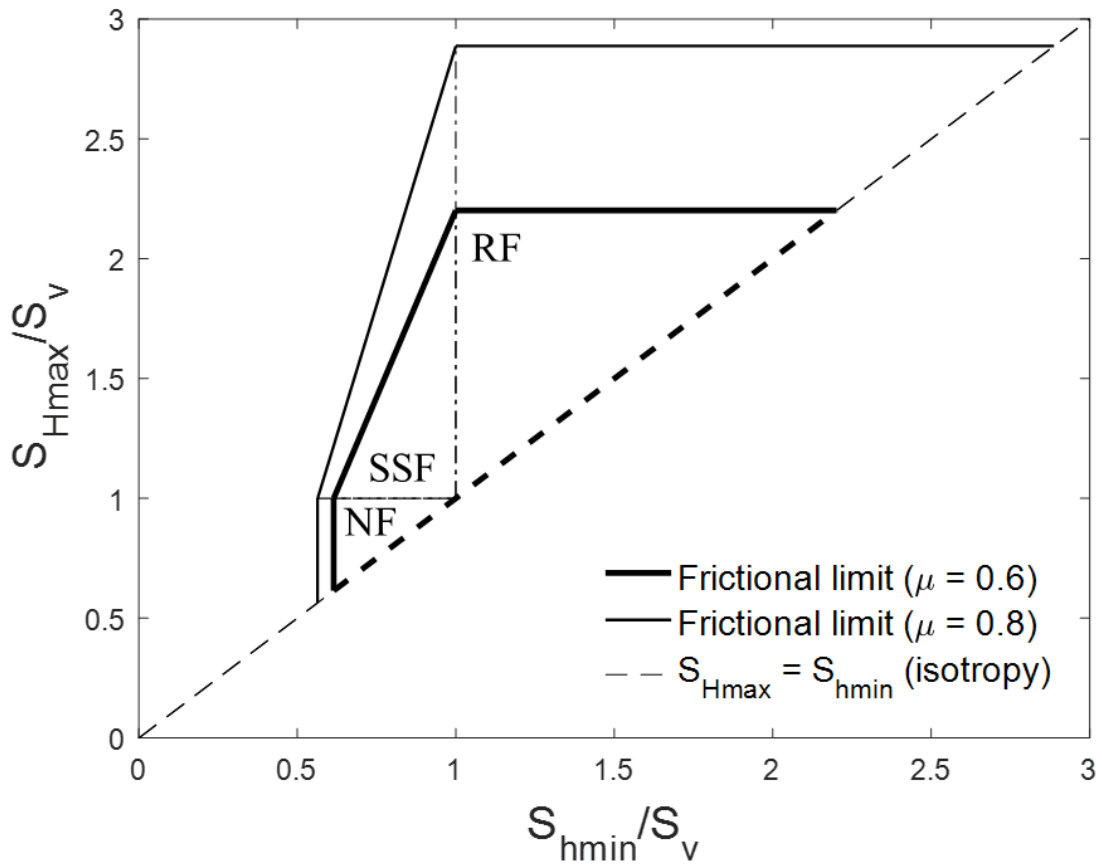
Figure 3.6.   Allowable region for *in-situ* stress states in the Earth subsurface for hydrostatic p_p (0.43 psi/ft). The dotted diagonal line represents horizontal isotropy ($S_{Hmax} = S_{hmin}$), the thicker solid lines represent the frictional limits at $\mu = 0.6$ and the thinner lines represent the frictional limits at $\mu = 0.8$. The region bounded by the solid lines and the horizontal isotropy diagonal, represents the region of possible subsurface stress states (NF: normal faulting, RF: reverse faulting and SSF: strike-slip faulting).

Following Nelson et al. (2005), the criteria for transverse DITF initiation in porous-permeable media can be presented on a single allowable *in-situ* stress diagram (Figure 3.7) as a cyan line representing $\sigma_{yy} = 0$ (Eq. 3.9) and a green line representing $\sigma_{yy} = \sigma_{\theta\theta}$ (Eq. 3.10) on the wellbore radius ($r = r_w$). The blue region shown on Figure 3.7 indicates the

range of *in-situ* stress states, which promote transverse DITFs from the side of the hole

($\theta = 90°$, along S_{Hmax}) for hydrostatic p_p, p_w gradient equal to 0.5 psi/ft and $T = 0$, in

horizontal wells drilled parallel to S_{hmin}. The diagram shows that under most *in-situ*

conditions, longitudinal DITFs should be expected rather than transverse DITFs.
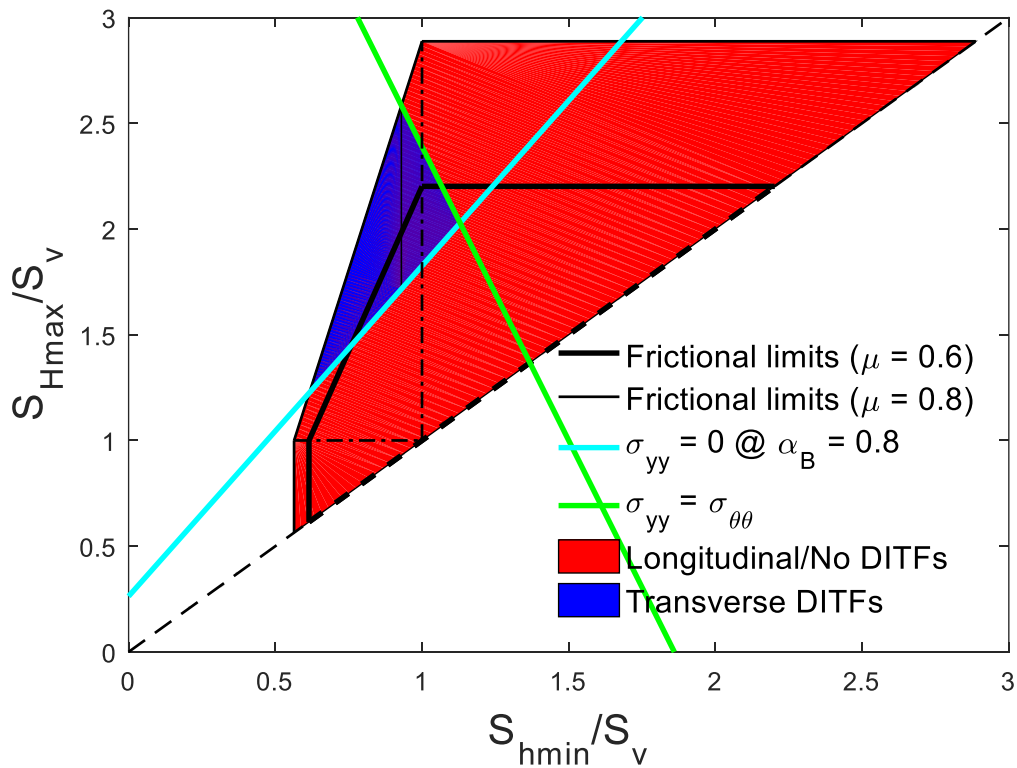
Figure 3.7. Allowable *in-situ* stress diagram for DITF initiation at $\alpha_B = 0.8$ from the side of the hole ($\theta = 90°$) of horizontal wells drilled parallel to S_{hmin}. The blue region indicates the stress states in which transverse DITFs are promoted at a given p_w (0.5 psi/ft in this example) and $T = 0$.

Allowable *in-situ* stress diagrams can also be used to demonstrate the stress states

for transverse CIHF initiation. For examining CIHF initiation for horizontal wells parallel

to S_{hmin} with perforations parallel to S_{Hmax} ($\theta = 90°$) using the stress polygon, two new lines are used (Figure 3.8); a solid cyan line for $\sigma_{\theta T} = 0$ (Eq. 3.16) and a green line for $\sigma_{\theta T} = \sigma_{\theta L}$ (Eq. 3.17) assuming p_p gradient 0.43 psi/ft. The region between the two lines (where $\sigma_{\theta T} < 0$ and $\sigma_{\theta T} < \sigma_{\theta L}$) represents the stress states where transverse CIHF initiation occurs for the given p_w gradient. A dash-dotted and dotted cyan line is used to provide comparisons with older models neglecting p_p (Hossain et al., 2000) and fluid infiltration (Michael et al., 2018), respectively. Both older models clearly yield smaller blue region on the diagram (Figure 3.8) than using the model that considers infiltration of the injected fluid into the porous-permeable rock.
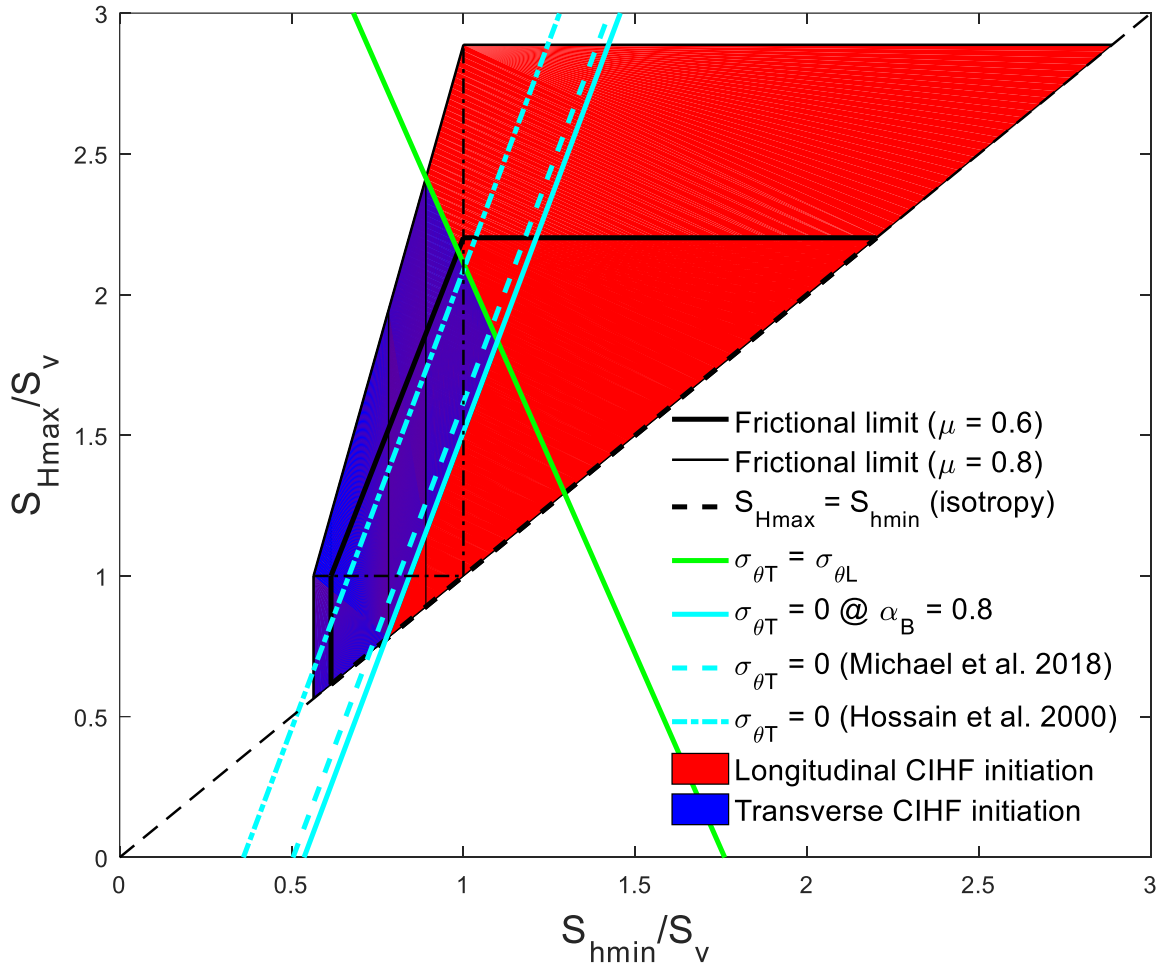
Figure 3.8.   Allowable *in-situ* stress diagram for CIHF initiation at $\alpha_B = 0.8$ for perforations parallel to S_{Hmax} ($\theta = 90°$) in horizontal wells parallel to S_{hmin}. The blue region indicating transverse CIHF initiation is much larger than the corresponding blue region for transverse DITF on Figure 3.7.

3.4.2   Using DITF Observations to Constrain S_{Hmax}

Nelson et al. (2005) used the linear elasticity theory along with the observation of transverse DITFs on image logs from vertical wells in West Tuna area, in the Gippsland basin, offshore southeastern Australia to constrain the magnitude of the local S_{Hmax}. The

extended criterion for porous-permable media allowing fluid infiltration from the wellbore to the surrounding formation is applied to a hypothetical case of a horizontal well drilled parallel to S_{hmin}. Assuming transverse DITFs were observed at a p_w gradient within 0.6-0.8 psi/ft, the magnitude of S_{Hmax} can be constrained by adding another line to the allowable *in-situ* stress diagram for the value of S_{hmin} (the magenta line). The value of S_{hmin} can be estimated from a leak-off test (Zoback, 2014) and for this hypothetical case we assume that $S_{hmin} = \sim S_v$. The three lines ($\sigma_{yy} = 0$, $\sigma_{yy} = \sigma_{\theta\theta}$, and $S_{hmin}/S_v = 1$) enclose a smaller yellow region within the blue, transverse DITF-promoting region (Figure 3.9). Using the vertical bounds of the yellow region, the range of S_{Hmax} is constrained to $\sim$1.8-2.4S_v. Due to their rarer occurrence, transverse DITFs when observed can constrain the stress tensor more effectively than longitudinal DITFs.
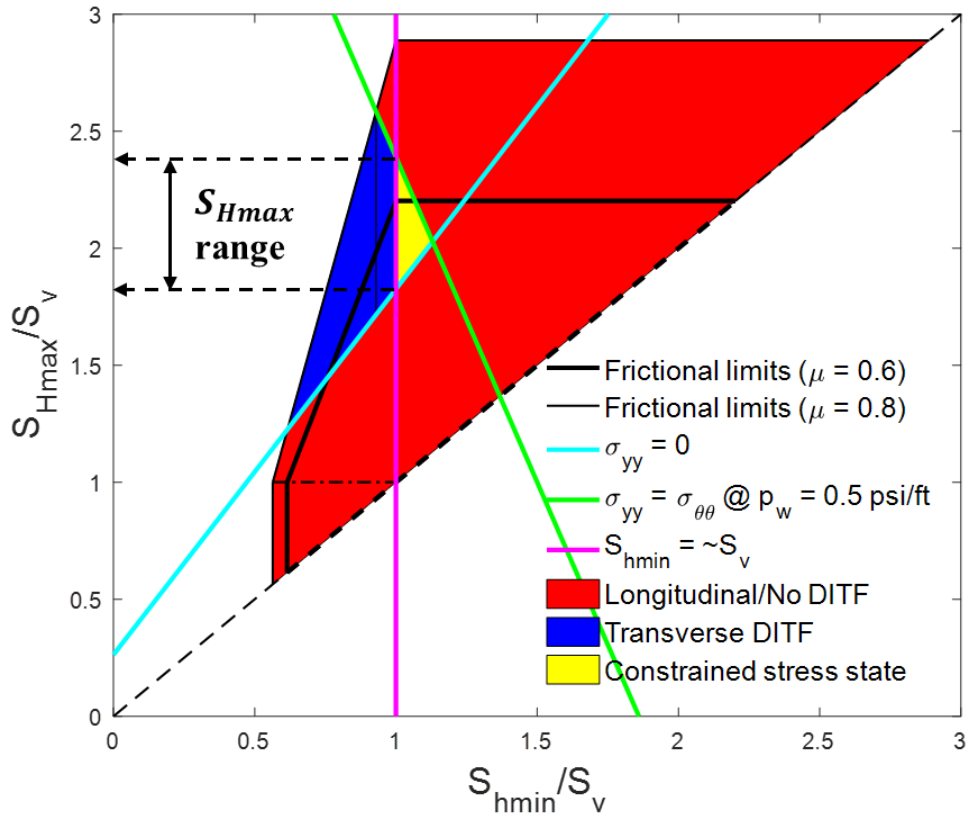
Figure 3.9. Region (yellow) of possible *in-situ* stress states for a hypothetical case of transverse DITF occurrence. The range of possible magnitudes for S_{Hmax}/S_v is subsequently constrained to ~1.8-2.4. Similar analyses can be performed to constrain S_{Hmax} for wells aligned with one of the principal stress direction, or some components of the *in-situ* stress tensor for wells, which are not aligned with the direction of one of the principal stresses.

3.4.3 Orientation Prediction of CIHF Initiation

In order for transverse CIHF initiation to be induced from a perforated wellbore, the following conditions must be met at $p_w = p_b$:

i. The transverse fracturing stress is more tensile than the tensile strength of the rock formation (i.e., $\sigma_{\theta T} < -T$).

ii.   The transverse fracturing stress is more tensile than the corresponding longitudinal fracturing stress (i.e., $\sigma_{\theta T} < \sigma_{\theta L}$).

3.4.3.1 Breakdown Pressure Window

According to the analytical fracture initiation criterion, transverse CIHF initiation occurs at p_w lower than longitudinal CIHF initiation (Figure 3.10, for parameters from the Barnett Shale), so that $\sigma_{\theta T}$ is more tensile (negative) than $\sigma_{\theta L}$. As p_w increases $\sigma_{\theta T}$ (blue line), which starts from a small tensile value at $p_w = 0$, becomes more and more tensile. However, $\sigma_{\theta L}$ (red line) which starts from a compressive (positive) value at $p_w = 0$, becomes tensile at a much higher rate (higher slope) than $\sigma_{\theta T}$. This creates a "breakdown pressure window" for transverse CIHF initiation (yellow region in Figure 3.10), which would occur only if the breakdown p_b is lower than the p_w value at the intersection point of the $\sigma_{\theta L}$ and $\sigma_{\theta T}$ lines, which is the upper-bound of the p_b window, $p_{b,upper}$. Eq. 3.17 can be rearranged to solve for p_w, giving us an expression for $p_{b,upper}$:

$$p_{b,upper}\big|_{\theta=90°} = 3S_v - S_{Hmax} - S_{hmin} + 2v(S_{Hmax} - S_v) \tag{3.22}$$

for perforations in the direction of S_{Hmax}, for a well drilled parallel to S_{hmin} in a normal faulting stress regime. For perforations in the direction of S_v (top of the hole), $p_{b,upper}$ is calculated by interchanging the S_v terms with S_{Hmax} in Eq. 3.22. Although largely dependent on the *in-situ* conditions, p_b can to some extent be controlled by the practitioner on the surface. Low pressurization rates have been shown to suppress p_b (Zoback et al.,

1977; Weijers, 1995) and thus low injection rates can be premeditated to ensure that $p_b <$

$p_{b,upper}$.
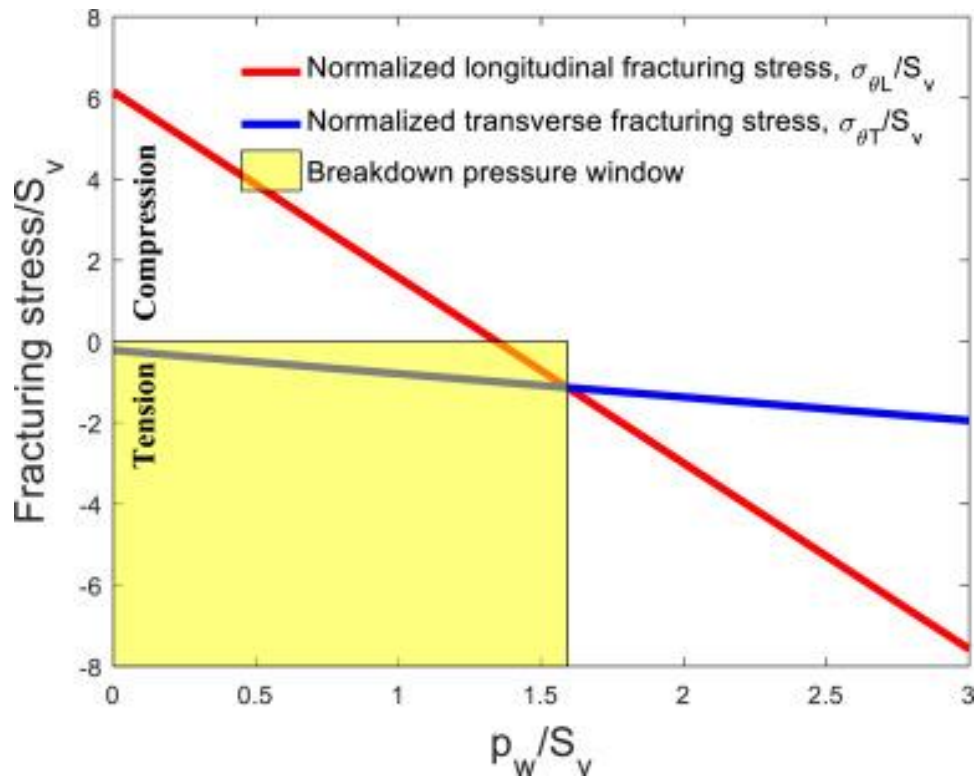
Figure 3.10. Graphical solution of $\sigma_{\theta L}$ and $\sigma_{\theta T}$ against p_w for parameters of the Barnett Shale (Table 3.1) with the breakdown pressure window indicated for $\alpha_B = 0.8$ by the width of the yellow region. The p_b window is 0-11,489 psi.

3.4.3.2 Preferred Perforation Alignment (PPA)

For linearly elastic rocks under normal faulting stress regime, $p_{b,upper}$ values are maximized when perforations are parallel to S_{Hmax}, making those perforations most likely to generate transverse CIHF initiation (Michael et al., 2018; Michael and Gupta, 2019e; Michael, 2019a). The same is true for porous-permeable media, because $p_{b,upper}$ is independent of the α_B value (Eq. 3.22) making the S_{Hmax} direction the preferred

perforation alignment (PPA) for normal faulting stress states (PPA depending solely on the stress state). Perforations parallel to PPA thus yield the best chance for generating transverse CIHF initiation (Figure 3.11, for the Barnett Shale). For strike-slip faulting stress states, S_v is the PPA (Figure 3.12, for the Marcellus Shale).
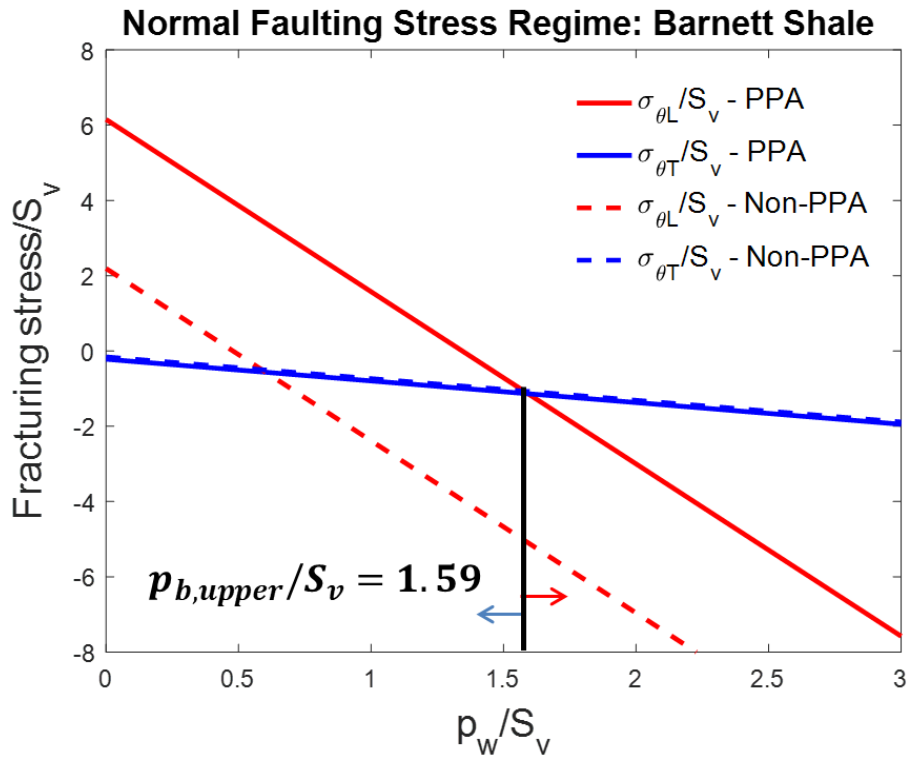
Figure 3.11. The fracturing stresses for PPA and non-PPA oriented perforations for a normal faulting stress regime example (the Barnett Shale; see Table 3.1 for the in-situ stress state), yielding a maximum $p_{b,upper}$ of $1.59S_v$. The solid lines for PPA perforations yield larger p_b windows. For normal faulting stress states, PPA is parallel to S_{Hmax} ($\theta = 90°$, side of the hole).

Strike-slip Faulting Stress Regime: Marcellus Shale
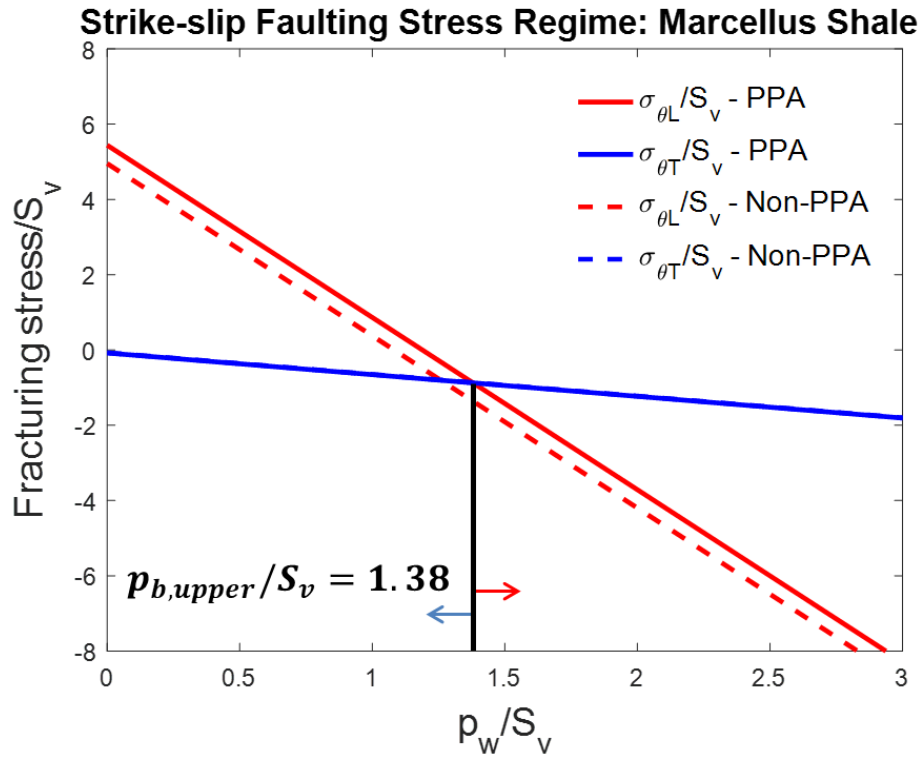
Figure 3.12. The fracturing stresses for PPA and non-PPA oriented perforations for a strike-slip faulting stress regime example (the Marcellus Shale – see Table 3.1 for the *in-situ* stress state), yielding a maximum $p_{b,upper}$ of $1.38S_v$. Similar with normal faulting stress states, the solid lines for PPA perforations yield larger p_b windows. However, for strike-slip faulting stress states PPA is parallel to S_v (top of the hole).

If a wellbore is drilled parallel to the least principal stress, the PPA direction – which is dictated by the stresses orthogonal to the wellbore – is parallel to the least of the two stresses acting orthogonal to the wellbore (Figure 3.13). For horizontal wells drilled along S_{hmin}, PPA is always contained within the preferred fracture plane (PFP), which is orthogonal to the wellbore according to Hubbert and Willis (1957). For a reverse faulting regime, determining PPA is more complex because the PFP is horizontal, perpendicular to

S_v. For a horizontal well along S_{hmin}, the PPA is in the direction of the least compressive of S_v and S_{Hmax}. This is useful for completion engineers – when targeting "sweet spots" strategically oriented perforations (Kurdi, 2018) along PPA can be used to enhance the promotion of transverse CIHF initiation by maximizing $p_{b,upper}$.
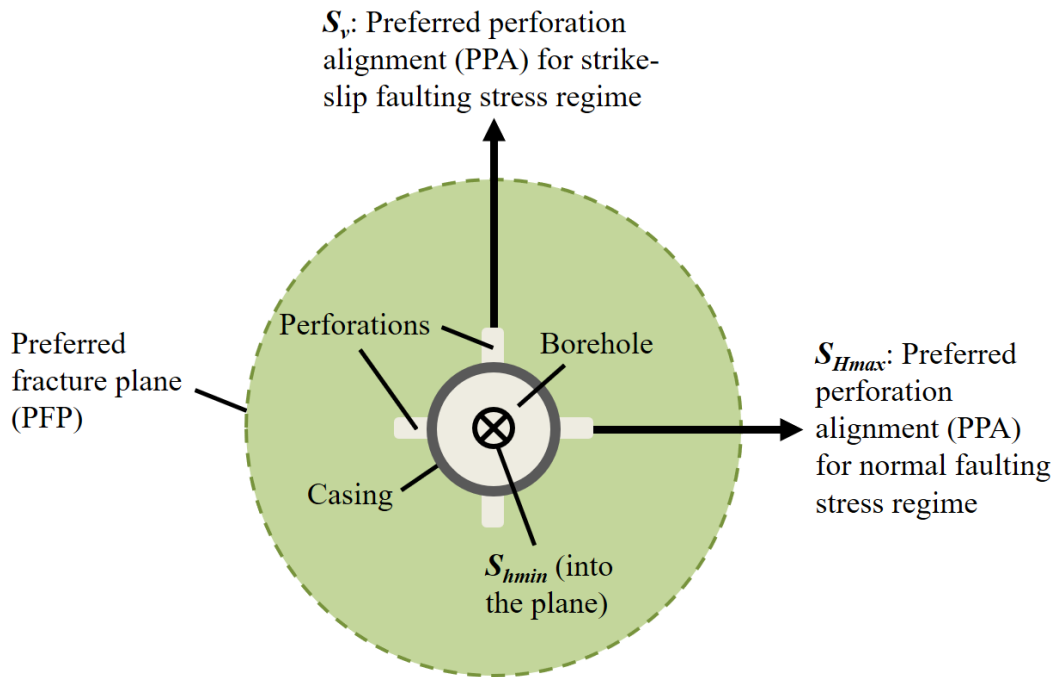
Figure 3.13. The preferred perforation alignment (PPA) configurations for horizontal wellbores drilled parallel to S_{hmin} under normal and strike-slip faulting stress regimes.

As the fracture propagates away from the wellbore, the *in-situ* stresses become more dominant over the near-wellbore stresses and dictate PFP. Thus, if a fracture initiates at an orientation plane different to the PFP, reorientation is expected to occur in the near-wellbore region, aligning the fracture propagation plane with the PFP. For instance,

longitudinal CIHF initiation from a horizontal well parallel to S_{hmin}, is expected to lead to reorientation as the fracture moves away from the wellbore aligning the fracture transversely to the wellbore.

3.4.3.3 Effect of the Wellbore Pressure

High p_w hinders transverse CIHF initiation for a given stress state as previously shown on Figure 3.10. Transverse CIHF initiation will occur if $p_b \leq p_{b,upper}$. Low p_w at breakdown makes more *in-situ* stress states to promote transverse CIHF initiation by enlarging the blue region as seen on Figure 3.14. Increasing p_w from 0.5 psi/ft to 0.7 psi/ft, reduces the range of stress states, yielding transverse CIHF initiation. The $\sigma_{\theta L}$ expression is more sensitive to p_w compared to the $\sigma_{\theta T}$ expression, with the former becoming more tensile (negative) than the latter as p_w increases.
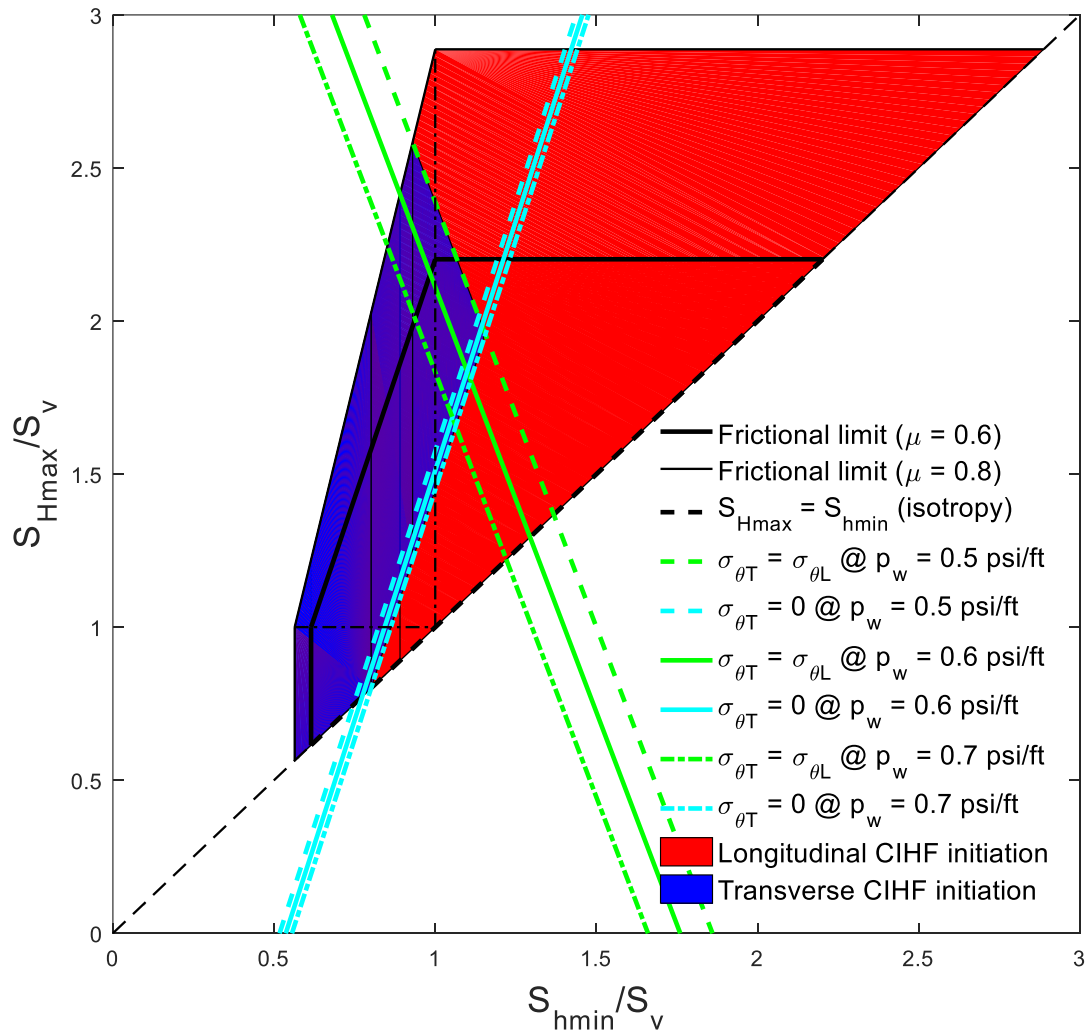
Figure 3.14. The effect of p_w on the orientation of CIHF initiation; as p_w gradient increases the blue region representing the stress states where transverse CIHF initiation will be promoted, shrinks.

3.4.3.4 Effect of the Biot's Poroelastic Coefficient

For a specific *in-situ* stress state, $p_{b,upper}$ is independent of the Biot's poroelastic coefficient, α_B as Eq. 3.22 dictates. Hence, as α_B decreases from 1.0 (soft rock) to 0.6

81

(stiffer rock) the p_b window range remains the same (Figure 3.15, for the Barnett Shale parameters).
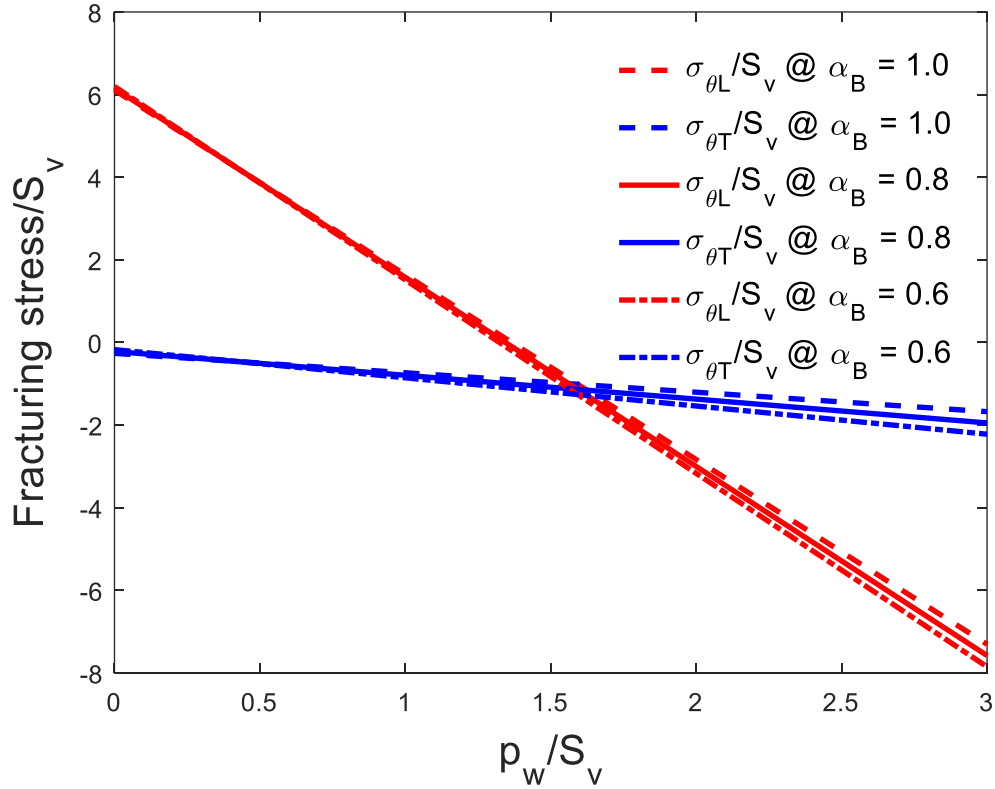
Figure 3.15. The effect of Biot's poroelastic coefficient, α_B on $\sigma_{\theta L}$ and $\sigma_{\theta T}$ for parameters of the Barnett Shale (Table 3.1).

Nevertheless, Figure 3.16 shows that at a given p_w gradient (0.6 psi/ft), smaller α_B values yield a slightly larger range of *in-situ* stress states (indicated by the blue region) where transverse CIHF initiation is promoted as opposed to the red region indicating the stress states in which longitudinal CIHF initiation will be promoted.
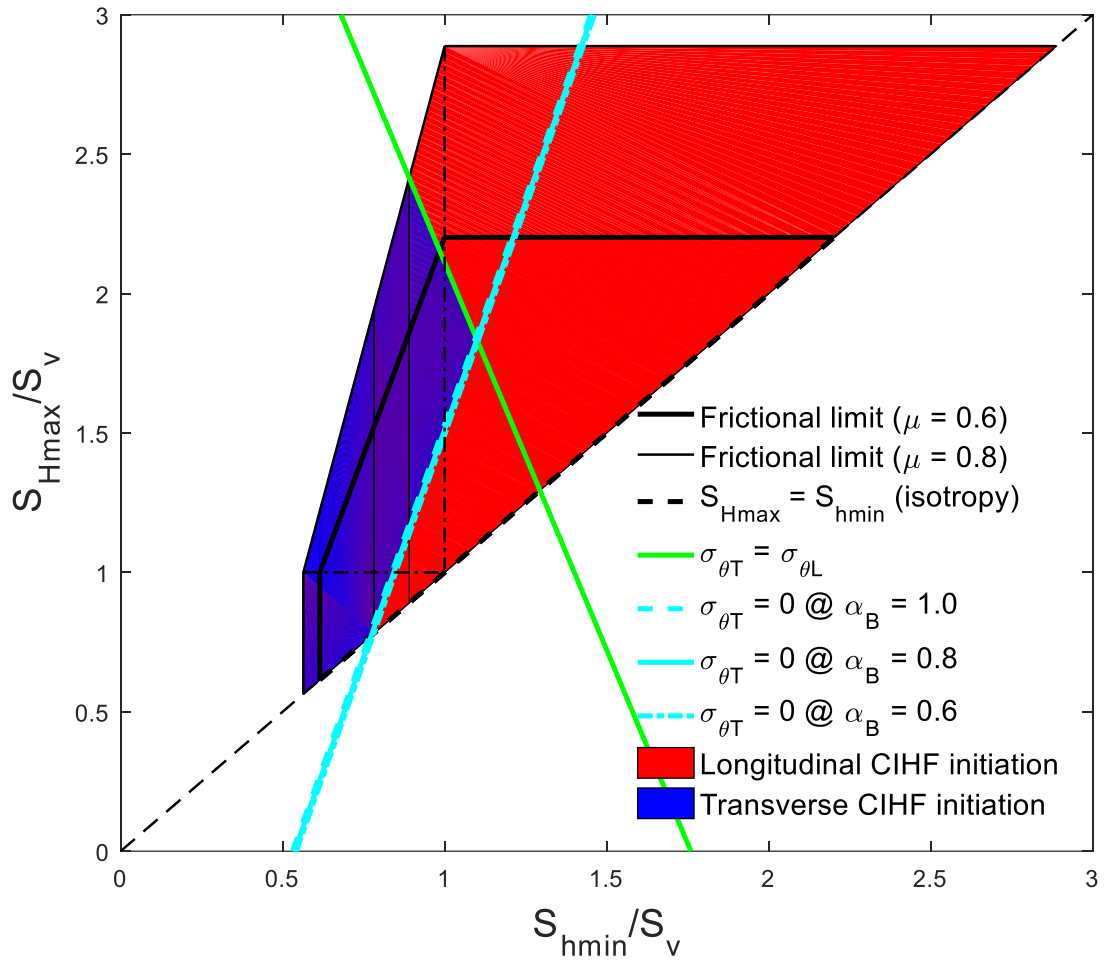
Figure 3.16. As α_B increases the blue region indicating the stress states in which transverse CIHF initiation is promoted shrinks.

3.4.3.5 Effect of the Poisson's Ratio

The formation's Poisson's ratio, v impacts the p_b window by affecting the value of $p_{b,upper}$. Both expressions for $\sigma_{\theta L}$ and $\sigma_{\theta T}$ contain v terms which makes the result more tensile (negative). The impact of v however, depends on the stress anisotropy between the two stresses acting orthogonally to the well (S_v and S_{Hmax} for wells drilled parallel to

S_{hmin}). The higher this stress anisotropy, the smaller $p_{b,upper}$ becomes. Subsequently, for the stress state and formation properties of the Barnett Shale, the p_b window for transverse CIHF initiation shrinks by pushing the intersection point of the $\sigma_{\theta T}$ and $\sigma_{\theta L}$ lines to the left (Figure 3.17).
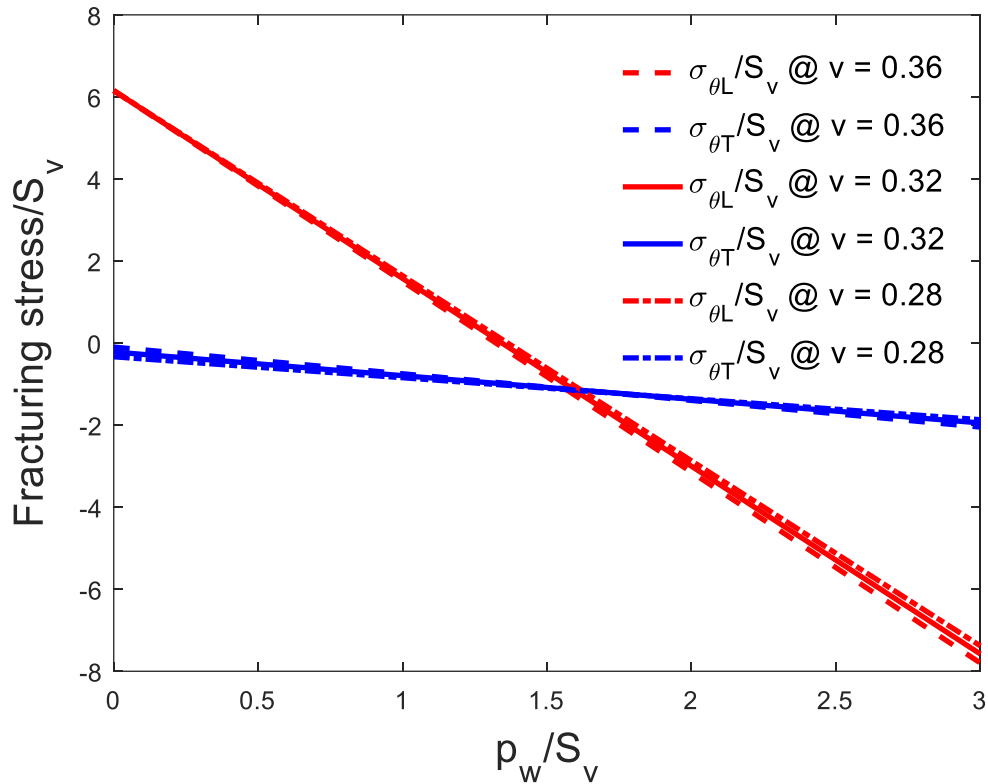
Figure 3.17. The effect of Poisson's ratio, v on $\sigma_{\theta L}$ and $\sigma_{\theta T}$ for parameters of the Barnett Shale (Table 3.1).

Nonetheless, at a given p_w gradient, a higher v value increases the range of *in-situ* stress states, which promote transverse CIHF initiation as indicated by the blue region in Figure 3.18 for a given p_w gradient of 0.6 psi/ft.
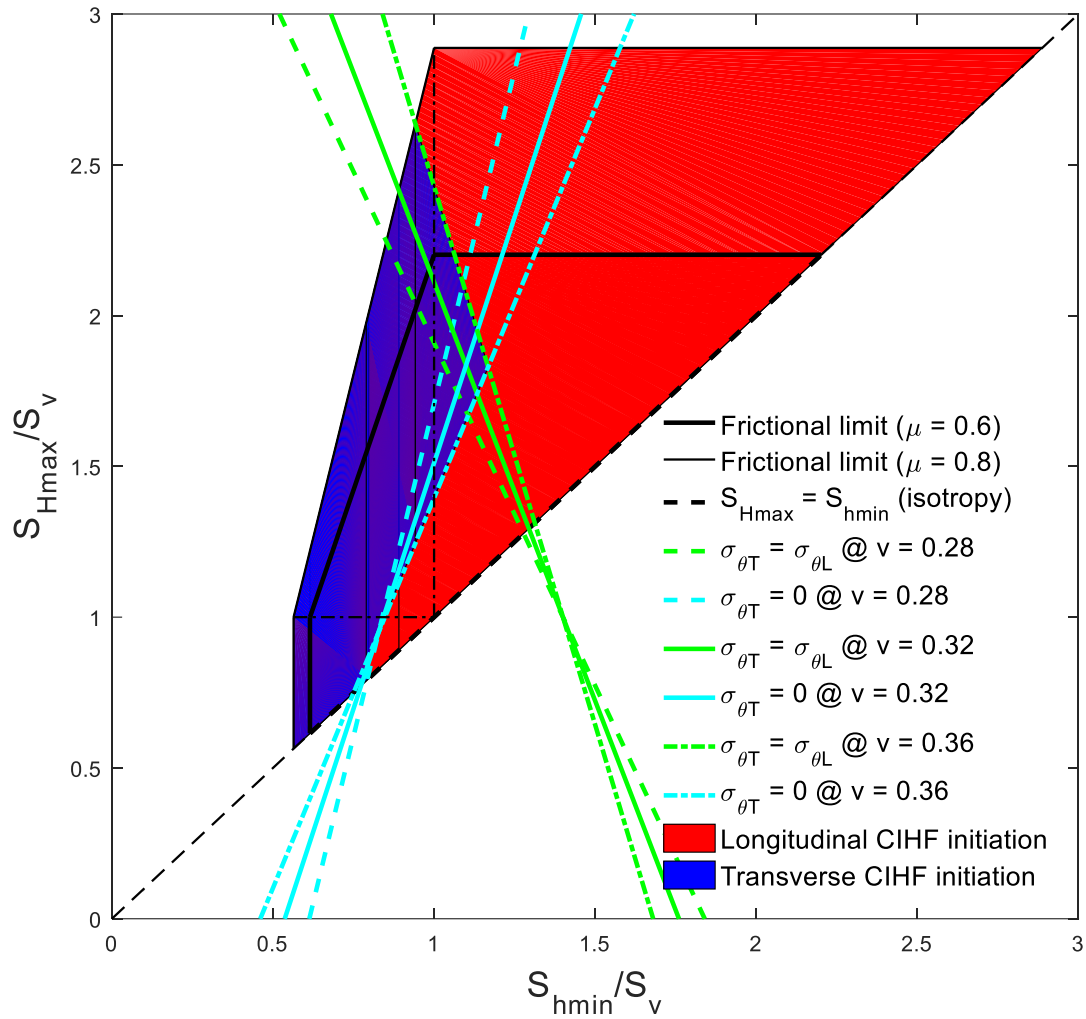
Figure 3.18. As *v* increases, the blue region indicating the range of *in-situ* stress states in which transverse CIHF is promoted is enlarged.

3.4.4 Shale Play Case Studies

Seven shale plays are studied; five under normal faulting (Barnett, Bakken, Fayetteville, Haynesville and Niobrara) and two under strike-slip faulting stress regime (Marcellus and Vaca Muerta). The calculation of the p_b window range for each of the seven

shale plays is performed using the appropriate expression for $p_{b,upper}$ per given *in-situ* stress regime. Table 3.1 summarizes the *in-situ* stress states of the seven shale plays, which are illustrated on the allowable *in-situ* stress diagram on Figure 3.19. The p_b window range is calculated for perforations parallel to PPA for each play (Table 3.2) and a prediction is made for the orientation of CIHF initiation using p_b values from the literature (Table 3.3).
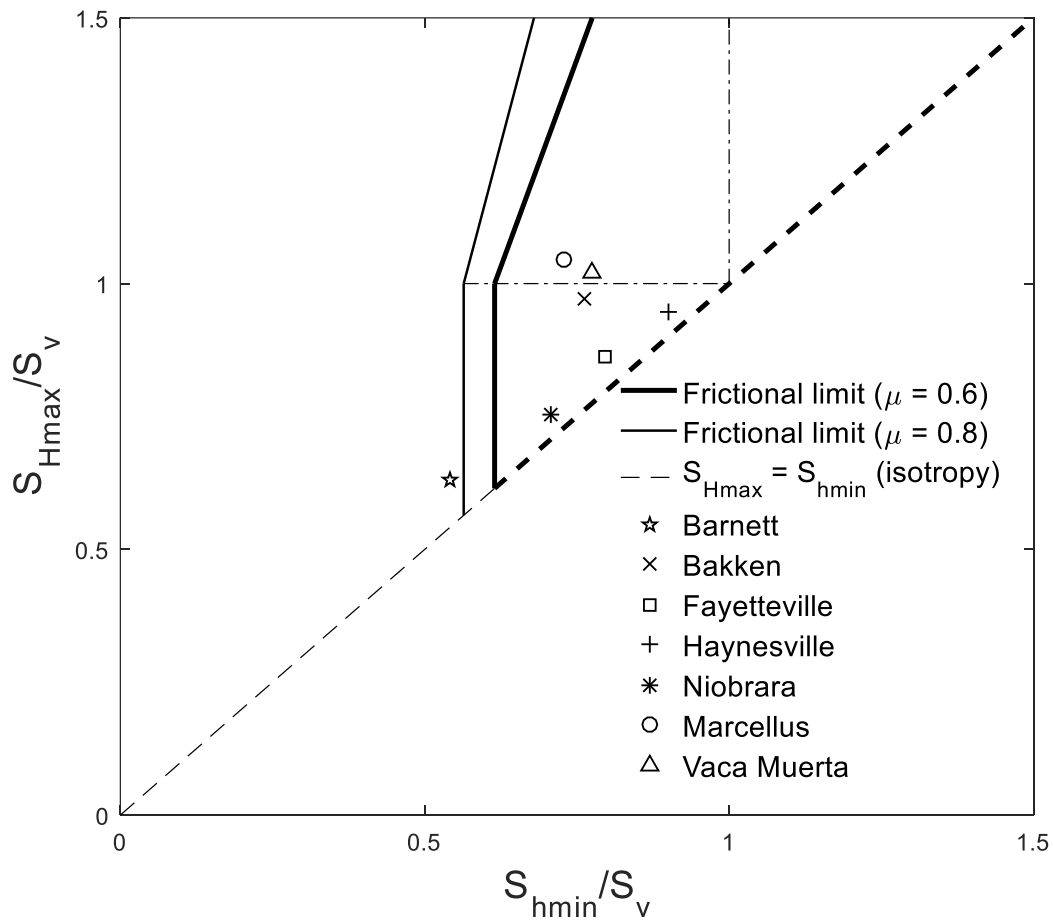
Figure 3.19. *In-situ* stress states of the seven shale plays on an allowable stress diagram.

Table 3.1. Summary of the *in-situ* stresses and pore pressure of the seven shale plays.

Shale play	Location	S_v (psi)	S_{hmax} (psi)	S_{hmin} (psi)	p_p (psi)	Source
Barnett	TX	7,215	4,550	3,900	3,055	Moos (2012)
Bakken	MN, ND and Canada	10,605	10,302	8,080	6,666	Yang and Zoback (2014)
Fayetteville	AR and OK	5,085	4,388	4,050	1,913	Prioul et al. (2011)
Haynesville	AR, LA and TX	13,320	12,600	12,000	10,200	Prioul et al. (2011)
Niobrara	CO, KS, NE and WY	7,102	~5,360	5,025	3,283	Koskella et al. (2015)
Marcellus	NY, MD, NJ, OH, PA, VA and WV	9,152	9,568	6,656	4,576	Kowan and Ong (2016)
Vaca Muerta	Argentina	8,692	8,856	6,724	5,330	Kosset (2014)

Table 3.2. The p_b window ranges for perforations parallel to PPA for the seven shale plays studied. Based on p_b values reported in the literature (Table 3.3), predictions are made for the orientation of CIHF initiation for each shale play.

Shale play	PPA	p_b window @ PPA	Predicted orientation of CIHF initiation
Barnett	S_{Hmax} ($\theta = 90°$)	0-11,489	Transverse
Bakken	S_{Hmax} ($\theta = 90°$)	0-13,239	Transverse
Fayetteville	S_{Hmax} ($\theta = 90°$)	0-6,371	Transverse
Haynesville	S_{Hmax} ($\theta = 90°$)	0-14,899	Transverse
Niobrara	S_{Hmax} ($\theta = 90°$)	0-9,806	Transverse
Marcellus	S_v ($\theta = 0°$)	0-12,630	Transverse
Vaca Muerta	S_v ($\theta = 0°$)	0-11,047	Longitudinal

Table 3.3. Summary of the p_b estimations used for predicting the orientation of CIHF initiation (Table 3.2).

Shale play	Average depth (ft)	Fracture gradient (psi/ft)	Estimated p_b (psi)	Source
Barnett	6,500	0.60	3,900	Ketter et al. (2006)
Bakken	10,070	0.90	9,063	Schlumberger (2014)
Fayetteville	5,000	1.10	5,500	Lynk et al. (2017)
Haynesville	13,000	1.00	13,000	Hammes et al. (2011)
Niobrara	7,500	0.85	6,375	Koskella et al. (2015)
Marcellus	6,250	1.10	6,875	Barth et al. (2012)
Vaca Muerta	9,500	1.18	11,210	Kosset (2014)

Using the p_b values from the literature (Table 3.3, ranging from 0.60-1.18 psi/ft), we see that transverse CIHF initiation is a likely occurrence in six of the seven shale plays studied assuming porous-permeable formations with $\alpha_B = 0.8$ and $\nu = 0.32$. The only shale play where longitudinal CIHF initiation may dominate is the Vaca Muerta Shale in Argentina, because the p_b reported in the literature is higher than the p_b window estimated using the analytical approximations. This is a surprising result as conventional analytical models either neglecting p_p (Hossain et al., 2000) or fluid infiltration (Michael et al., 2018) are more conservative in their prediction of transverse CIHF initiation.

3.5   DISCUSSION

3.5.1   Analytical Model Validation

The orientation criterion for DITF initiation (Figure 3.7) was developed using fully analytical solutions, making a numerical follow-up study redundant. The derivation of the analytical criterion for the orientation of CIHF initiation in porous-permeable media

(Figure 3.8), however is based on approximations made and should not be considered fully exact. The Kirsch (1898) theory provides a solution for a simplified, 2D problem and in the development of our criterion this solution is used twice to approximate a three-dimensional (3D) problem, mirroring Hossain et al (2000) and Michael et al. (2018)'s approach. The higher promotion of transverse fracture initiation suggested by our criterion compared to older models for perforated wells (Figure 3.8), improves our confidence on our model's realism. Laboratory-scale experiments were performed in materials (such as rock or synthetic cement blocks), that did not contain fluid-filled pores, making it impossible to apply any p_p. In the absence of p_p, validation assessments using results from such experiments (Figure 3.20) is not straight-forward.

El Rabaa (1989) obtained transverse fracture initiation in his true triaxial tests on cement blocks, initiating fractures using motor oil injection. A highly anisotropic stress state was used that would not be stable against shear failure, thus not likely to occur in the Earth's subsurface (well outside the polygon if hydrostatic p_p is present). The stress state used by El Rabaa (1989) fulfills the criteria necessary for transverse fracture initiation if the tensile strength of the cement block is neglected; $\sigma_{\theta T} < 0$ and $\sigma_{\theta T} < \sigma_{\theta L}$. Feng and Sarmadivaleh (2019) performed true triaxial testing on synthetic samples of low tensile strength, using edible honey as fracturing fluid also achieving transverse fracture initiation. A highly anisotropic stress state, close to the stress state of El Rabaa (1989)'s experiments was used with a notably low pressurization rate. Figure 3.20 also shows the stress state of block experiments performed by Weijers (1995) yielding both longitudinal and transverse fracture initiation and by Alabbad (2014) yielding solely longitudinal fracture initiation, despite transverse fracture initiation being expected in these stress states. Fracturing fluid leakage around the wellbore, discussed in the next section, is the cause of this outcome.
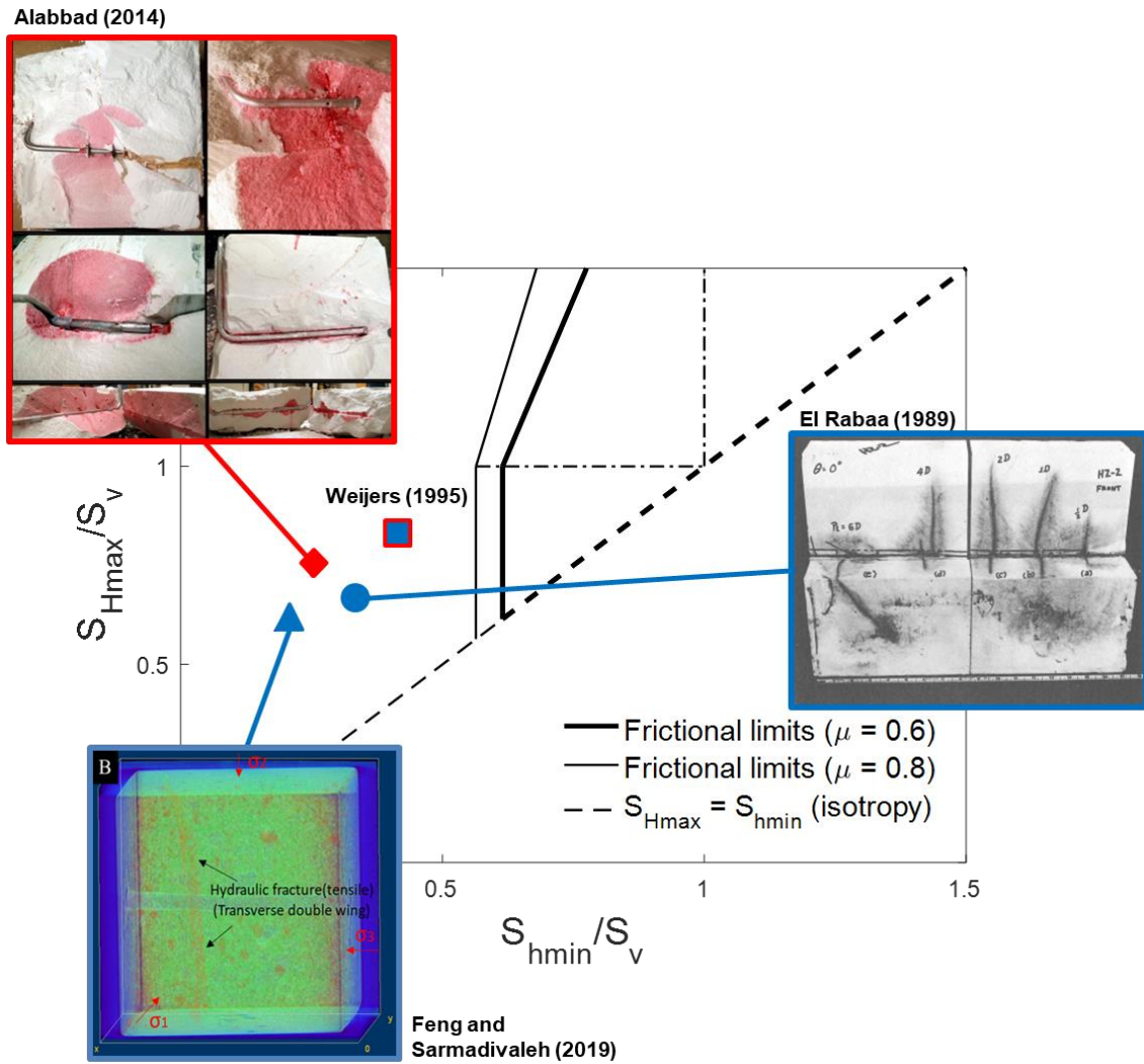
Figure 3.20. Stress states of three laboratory experiments illustrated on an allowable *in-situ* stress diagram; transverse fracture initiation by El Rabaa (1989) and Feng and Sarmadivaleh (2019) and longitudinal fracture initiation by Alabbad (2014). The stress state used by Weijers (1995) experiments is also illustrated, which yielded both longitudinal and transverse fracture initiation and will be discussed in the next section. For reference, the polygon for hydrostatic p_p (0.43 psi/ft) is shown, even though none of the experiments incorporated p_p.

3.5.2 Fracturing Fluid Leakage around the Wellbore

Evidence from laboratory testing (Weijers, 1995; Alabbad, 2014; Michael, 2016b) and from the field (Barree and Miskimins, 2015) showed that fracturing fluid can often leak from the perforation tunnel, all around the cross-section of the wellbore. This makes fracture initiation possible from all around the wellbore, not just from the perforation base.

The upside of this is that fluid leakage reduces the problem effectively to that of DITF initiation; one with a fully analytical solution. If the perforation is ignored, the axial and tangential stresses (σ_{yy} and $\sigma_{\theta\theta}$) determine the orientation of CIHF initiation taking the place $\sigma_{\theta T}$ and $\sigma_{\theta L}$ respectively, as the transverse and longitudinal-inducing fracturing stresses. The general effect of fluid leakage is that it shrinks the p_b window (Figure 3.21), suppressing transverse CIHF initiation. Furthermore, leakage decreases the range of stress states, which would promote transverse fracture initiation, as can be observed when comparing Figure 3.7 and Figure 3.8 (smaller blue region in Figure 3.7).

Weijers (1995) performing experiments (Figure 3.20) in cement blocks, observed sole transverse fracturing in the cases where fluid flow in the annulus was prevented. Nevertheless, a combination of longitudinal and transverse fracturing was observed in the cases where fluid flow leaked in the annulus. Alabbad (2014) presented several horizontal well design setups (Figure 3.20) attempted in hydrostone/gypsum plaster block samples. All those setups were deemed unsuccessful, because of leakage around the wellbore, attributed to the weak interface between the aluminum tube used and the surrounding gypsum plaster. Better adhesion between the tube and the surrounding gypsum plaster would have prevented leakage and generated transverse fracture initiation.
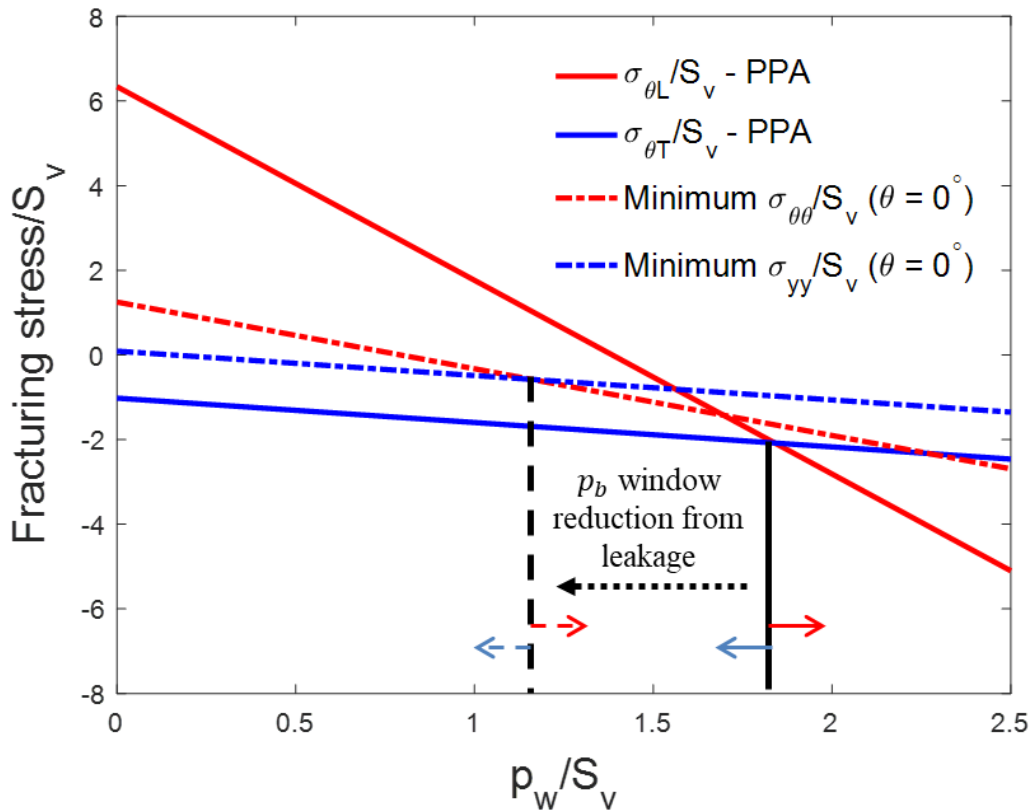
Figure 3.21. The stresses on the wellbore radius; longitudinal fracture-inducing $\sigma_{\theta\theta}$ and transverse fracture-inducing σ_{yy}, at S_v (dashed-dotted lines) which is where these stresses are the most tensile for the stress state used in Alabbad (2014)'s hydrostone/gypsum plaster block experiments (Figure 3.20). These two stresses determine the orientation of fracture initiation instead of $\sigma_{\theta L}$ and $\sigma_{\theta T}$ when fracturing fluid leaks along the wellbore, shrinking the p_b as a result.

3.5.3   The Effect of the Cemented Casing on CIHF Initiation

As mentioned by Fallahzadeh et al. (2017) and Michael et al. (2018), the presence of a cemented casing in the borehole shields the impact of p_w on the surrounding rock formation. In the case of a good cement job, the higher Young's modulus, E of the casing is expected to suppress the stress changes caused by p_w. The higher value of E of the steel

casing and the cement layers compared to the formation's suggests that the radial displacement the wellbore experiences will be smaller compared to an openhole configuration at the same pressure.

Re-computing the analytical results assuming the extreme case where the tangential stresses around the wellbore are fixed at the point of cement curing can mimic these effects. We assume this to be a balanced condition, $p_w = p_p$. These wellbore stresses constitute the "remote" loading at the perforation base and we use the perforation pressure as the pressure at the perforation base, which acts as a fracturing pressure. The shielding effect of the cemented casing results in an increase in $p_{b,upper}$, suggesting that good cement jobs without annular leakage are an important aid for transverse CIHF initiation. The range of *in-situ* stress states promoting transverse CIHF initiation expands (Figure 3.22) as the cyan line for $\sigma_{\theta T} = 0$ shifts to the right, increasing size of the blue region.
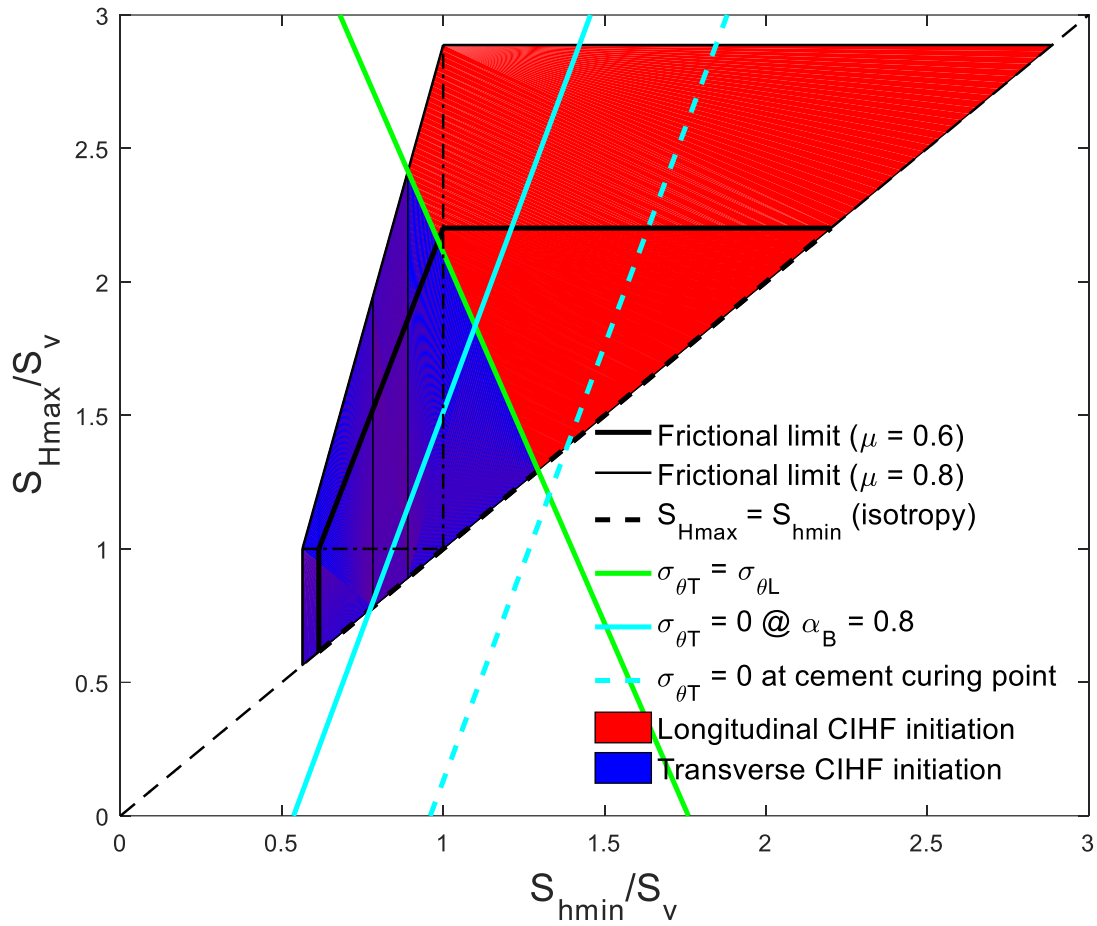
Figure 3.22. Allowable *in-situ* stress diagram for the extreme case of cement curing indicated by the dotted cyan ($\sigma_{\theta T} = 0$) line, compared to the case neglecting the cemented casing presence with the solid cyan line for $p_w = 0.6$ psi/ft. The size of the blue region remains unaffected for this p_w value.

3.6   CONCLUSIONS

Analytical criteria are presented for the orientation of fracture initiation from perforated and non-perforated wellbores in porous-permeable media, enhancing our understanding of the initiation mechanisms of drilling-induced tensile fractures and

completion-induced hydraulic fractures. Based on the preceding analysis, the following conclusions are made:

- The presence of perforation tunnels aids transverse CIHF initiation. It is more likely for transverse CIHF initiation to occur, compared to transverse DITFs. Orientation criteria are developed for CIHF initiation from perforated horizontal wellbores in porous-permeable media, considering fluid infiltration into the surrounding rock based on analytical approximations for $\sigma_{\theta L}$ and $\sigma_{\theta T}$.

- A p_b window exists for transverse CIHF initiation, which occurs within a low p_w range, whereas longitudinal CIHF initiation occurs at higher p_w values. For horizontal wells parallel to S_{hmin}, this p_b window is larger for perforations parallel the direction of the least of either S_v, or S_{Hmax}, making this direction the preferred perforation alignment for transverse CIHF initiation.

- Transverse CIHF initiation is a more likely event in porous-permeable media with fluid infiltration. Out of seven prolific shale plays studied, transverse CIHF initiation appears to be the most likely event in six, with the Vaca Muerta Shale in Argentina the only one exception.

- Low α_B values and high v values increase the range of *in-situ* stress states, which promote transverse CIHF initiation at a given p_w gradient. Contrary, higher p_w gradients hinder transverse CIHF initiation.

The following recommendations are made to practitioners for enhanced promotion of transverse CIHF initiation from perforated horizontal wells:

1. Slow pumping. Strategic use of slow pumping during the fracture treatment can keep p_b within the window for transverse CIHF initiation.

2. Strong casing-cement sheath and if possible cement sheath-rock formation interface bonding. This will suppress leakage of the fracturing fluid around the wellbore during the treatment, bypassing the perforations. This negates the impact of the perforation tunnels in promoting transverse CIHF initiation.

3. Using an oriented perforation strategy can under ideal circumstances, promote transverse CIHF initiation by expanding the p_b window.

Chapter 4. Numerical Evaluation of Fracture Initiation from Perforated Wells

For maximum productivity enhancement when targeting low permeability formations, horizontal wells must be made to induce multiple transverse fractures. In this chapter, an orientation criterion for fracture initiation is developed using analytically-derived approximations for the longitudinal and transverse fracturing stresses for perforated wellbores from the literature. The validity of the criterion is assessed numerically and is found to overestimate transverse fracture initiation, which occurs under a narrow range of conditions; pertaining to low breakdown pressure and low formation tensile strength.

A 3D numerical model shows that contrary to existing approximations, the transverse fracturing stress from perforated horizontal wells becomes more compressive as wellbore pressure increases. This shrinks the "breakdown pressure window," which is the range of wellbore pressures over which transverse fracture initiation takes place. This creates a second constraint for transverse fracture initiation, which is the "critical tensile strength" value. This determines the maximum formation tensile strength at which transverse fracture initiation is possible for a given *in-situ* stress state and perforation direction.

Sensitivity analyses are performed based on data from seven unconventional shale reservoirs (Barnett, Bakken, Fayetteville, Haynesville, Niobrara, Marcellus and Vaca Muerta) for horizontal wells drilled parallel to S_{hmin}. The frequent longitudinal fracture initiation occurrence indicated suggests fracture reorientation in the near-wellbore region

to be a common event, through which the propagating fractures become aligned with the preferred fracture plane (perpendicular to the least compressive principal stress). This induces near-wellbore fluid tortuosity, which in turn can lead to completions and production-related problems, such as early screenouts and post-stimulation well underperformance.

4.1 INTRODUCTION

Hydraulic fracture orientation impacts well productivity from hydrocarbon reservoirs. Productivity from low permeability formations is significantly improved having multiple fractures oriented transversely rather than longitudinally relative to a horizontal wellbore. This is useful for completion design; when targeting low permeability formations, horizontal wells should be made to induce multiple transverse fractures, as opposed to longitudinal fractures, which are more effective in higher permeability formations (Deimbacher et al., 1993; Economides and Nolte, 2000; Economides and Martin, 2010).

Fluid-driven fracture initiation depends primarily on (i) the subsurface stress state, (ii) the formation's mechanical properties, and (iii) perforation geometry. Knowledge of these three primary factors can be used to determine *a-priori* the orientation of a fractured induced from a pressurized wellbore. Additional, secondary factors of fracture initiation fluid-related properties include, (iv) the injection rate, and (v) the fracturing fluid viscosity (Fallahzadeh et al., 2017).

Fracture initiation often follows a plane different than the final fracture propagation plane. Stress reorientation in the near-wellbore region may promote fracture initiation of different orientation than the one dictated by the far-field stresses. Barree and Miskimins

98

(2015) concluded that under many facture initiation conditions a longitudinal component occurs at some level during fracture propagation, parallel to the wellbore. These longitudinal fracture components generate near-wellbore tortuosity, which is the cause of common post-stimulation problems, such as early screenouts and poor well productivity.

A number of authors (El Rabaa, 1989; King, 1989; Behrmaan and Elbel, 1991; Hallam and Last, 1991; Pearson et al., 1992) showed that the performance of the perforations is optimized when they are aligned with the anticipated fracture direction. This occurs when fractures initiate and propagate along the path of least resistance, known as the preferred fracture plane (PFP), which is dictated from the remote (*in-situ*) stress state (Economides and Nolte, 2000). Fractures not aligned with the PFP generate tortuous flow paths around them near the wellbore during post-treatment periods. Laboratory experiments showed fractures generated from cylindrical cavities, such as cased wellbores, having the tendency to be initiated in a longitudinal-to-the-wellbore orientation ignoring shallow crack notches (Weijers et al., 1994; Weijers, 1995; Alabbad, 2014; Michael, 2016b) and thus provide further motivation for extensive analysis of the mechanisms controlling the orientation of fracture initiation.

A 3D numerical analysis is conducted to assess an orientation criterion developed for fracture initiation from perforated wellbores. This is done by considering the tangential stresses on two points (extremes) around the perforation base: one for the initiation of transverse fractures and another for the initiation of longitudinal fractures. Critical parameters controlling the orientation of fracture initiation from perforated horizontal wellbores are investigated. The case where a micro-annulus exists between cement and the formation is included, which can be modeled as if the completion is openhole with a cylindrical perforation. *In-situ* stress state, wellbore pressure, perforation geometry and the rock formation's mechanical properties are independent variables that are shown to

99

determine the orientation of the initiated fractures; the dependent variable. Breakdown pressures reported in the literature from each shale play suggest that longitudinal fracture initiation may be common, increasing the chance of completion and production-related problems.

4.2 THEORETICAL BACKGROUND

The final propagation plane of fractures (far from the wellbore) is along PFP, which is orthogonal to the minimum principal stress (Hubbert and Willis, 1957). The disturbance of the stress field in the near-wellbore region from the presence of the pressurized wellbore (Kirsch, 1898) may cause the fracture to initiate in a plane different from the final fracture propagation plane (Weijers et al., 1994 and Michael et al., 2018).

4.2.1 Orientation of Fracture Initiation: Longitudinal vs. Transverse

For the limiting case of horizontal wellbores, initiated fractures can assume arbitrary orientations with the two main extreme configurations with respect to the wellbore being longitudinal and transverse (Figure 4.1). Longitudinal, or "axial" fractures, propagate in a plane parallel to the axis of the wellbore and are promoted by horizontal wells drilled along the direction of the larger horizontal principal stress, S_{Hmax}. Transverse, or "lateral" fractures, propagate in planes orthogonal to the wellbore axis and are promoted when a horizontal wellbore is drilled parallel to the minimum horizontal principal stress, S_{hmin}.
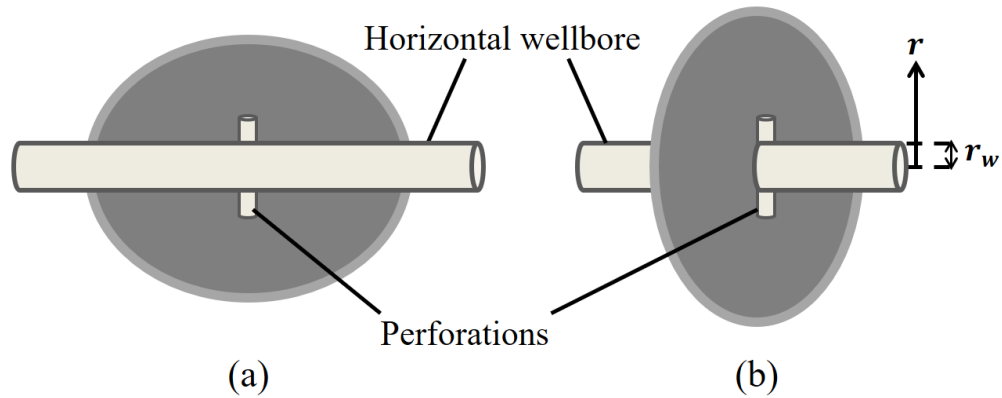
Figure 4.1. Fracture orientation configurations, (a) longitudinal and (b) transverse-to-the-wellbore. The wellbore radius is r_w and r is the radial distance from the center of the wellbore (modified from Michael and Gupta, 2020).

Numerous studies have compared the relative performance of the two main fracture orientations (Deimbacher et al., 1993; Economides and Martin, 2010; Economides et al., 2010). A single longitudinal fracture outperforms a single transverse fracture in terms of well productivity enhancement. This is because the flow inside the transverse fracture reverts from linear to radial in the near-wellbore region, reducing the flowrate as compared to a longitudinal fracture. However, the total flowrate from multiple transverse fractures in a horizontal well is much higher than from a single large longitudinal fracture. This makes transversely-oriented fractures more desired for applications in low permeability formations such as shale. Longitudinal fractures are still desired for some formations of higher permeability formations as well as frack-and-pack operations where transverse fractures tend to underperform (Economides and Martin, 2010; Economides et al., 2010).

4.2.2   Near-Wellbore Stress State

The equations for the magnitude of the stresses on a uniform plate with a circular hole under uniform tension were derived by Kirsch (1898) and were modified to include biaxial stresses and fluid pressure inside the hole (Hubbert and Willis, 1957). For a horizontal well of radius, r_w, drilled parallel to the y-axis, with the z-axis parallel to the vertical, the polar stress components at a radius, r, from the center of the well ($r \geq r_w$) in a homogeneous, isotropic, linearly elastic rock are analytically defined (Zoback, 2014) as

$$\sigma_{rr} = \frac{1}{2}(S_v + S_{Hmax})\left(1 - \frac{r_w^2}{r^2}\right) + \frac{1}{2}(S_v - S_{Hmax})\left(1 - 4\frac{r_w^2}{r^2} + 3\frac{r_w^4}{r^4}\right)\cos 2\theta$$
$$+ \frac{r_w^2}{r^2}\left(p_w - p_p\right) \tag{4.1}$$

$$\sigma_{\theta\theta} = \frac{1}{2}(S_v + S_{Hmax})\left(1 + \frac{r_w^2}{r^2}\right) - \frac{1}{2}(S_v - S_{Hmax})\left(1 - 4\frac{r_w^2}{r^2} + 3\frac{r_w^4}{r^4}\right)\cos 2\theta$$
$$- \frac{r_w^2}{r^2}\left(p_w - p_p\right) \tag{4.2}$$

$$\sigma_{yy} = S_{hmin} - 2\nu(S_v - S_{Hmax})\frac{r_w^2}{r^2}\cos 2\theta - \frac{r_w^2}{r^2}p_p \tag{4.3}$$

$$\sigma_{r\theta} = \frac{1}{2}(S_v - S_{Hmax})\left(1 + 2\frac{r_w^2}{r^2} - 3\frac{r_w^4}{r^4}\right)\sin 2\theta \tag{4.4}$$

where $\boldsymbol{\sigma_{rr}}$ is the radial stress, $\boldsymbol{\sigma_{\theta\theta}}$ is the "hoop" (or circumferential/tangential: normal stress in the tangential direction) stress, $\boldsymbol{\sigma_{yy}}$ is the out-of-plane stress parallel to the wellbore, and $\boldsymbol{\sigma_{r\theta}}$ is the shear tangential stress. $\boldsymbol{S_{Hmax}}$, $\boldsymbol{S_{hmin}}$, and $\boldsymbol{S_v}$ are the stress components parallel to the x, y, and z-axis respectively, with $\boldsymbol{\theta}$ the azimuth measured from $\boldsymbol{S_v}$ in the $(\boldsymbol{S_v} - \boldsymbol{S_{Hmax}})$ plane. The formation pore pressure is indicated by $\boldsymbol{p_p}$ and $\boldsymbol{p_w}$ is

the fluid pressure in the borehole.

4.3   ANALYTICAL APPROACH

Using the stresses on the wellbore radius, closed-form analytical criteria can be derived for the determination of the orientation of fracture initiation from non-perforated (i.e., during drilling) and perforated (i.e., during reservoir stimulation) wellbores.

4.3.1   Non-Perforated Wellbores

Incorporating formation tensile strength, T, in the tensile failure criterion requires, $\sigma_{yy}\big|_{r=r_w} < -T$, following a sign convention where compressive stresses are positive and tensile stresses negative. Hence, if σ_{yy} at $r = r_w$ and any θ becomes more negative than $-T$, a transverse fracture will initiate at that particular position on the wellbore indicated by θ, where the axial stress is more tensile than the tangential stress, such that $\sigma_{yy}\big|_{r=r_w} < \sigma_{\theta\theta}\big|_{r=r_w}$.

Substituting the full expressions (Eq. 4.2 and 4.3) for the wellbore stresses in these two conditions, two sets of closed-form, analytical criteria are derived for the initiation of transverse fractures. Appendix C demonstrates a simple 2D application of the criteria for fracture initiation and orientation from non-perforated wells using results from laboratory testing performed by AlTammar et al. (2018). For the top of the hole ($\theta = 0°$), a transverse fracture will initiate if the following conditions are true

$$S_{hmin} + 2v(S_v - S_{Hmax}) - p_p + T < 0 \qquad (4.5)$$

$$S_{hmin} + (1 - 2v)S_v + (2v - 3)S_{Hmax} + p_w < 0 \qquad (4.6)$$

103

For the side of the hole (S_{Hmax} direction), the S_v and S_{Hmax} terms are interchanged leading to the conditions for transverse fracture initiation taking the following form,

$$S_{hmin} + 2\nu(S_{Hmax} - S_v) - p_p + T < 0 \tag{4.7}$$

$$S_{hmin} + (1 - 2\nu)S_{Hmax} + (2\nu - 3)S_v + p_w < 0 \tag{4.8}$$

4.3.2   Perforated Wellbores

The presence of a perforation tunnel intersecting the cylindrical wellbore increases the geometric complexity of the problem, making derivation of an analytical solution extremely challenging. Hossain et al. (2000) applied three assumptions to reduce the problem to a more simplified form, for which closed-form analytical solutions can be derived:

i.   A micro-annulus existing between the cement and the rock formation, allowing modeling the wellbore as an openhole completion.

ii.   The pressure in the perforation tunnel, p_{perf} is equal to p_w.

iii.   Fractures initiate at the perforation base, which is cylindrical.

Using a second "Kirsch analysis," Hossain et al. (2000) derived closed-form analytical approximations for the longitudinal and transverse fracturing stresses from a perforated wellbore. For a perforation located on the side of a horizontal well (Figure 4.2), the tangential stress around the perforation base, $\sigma_{\theta\theta_p}$, has two extreme values designated as the longitudinal fracturing stress, $\sigma_{\theta L}$, and the transverse fracturing stress, $\sigma_{\theta T}$. A similar designation can be made for a perforation at the top of the hole.

104
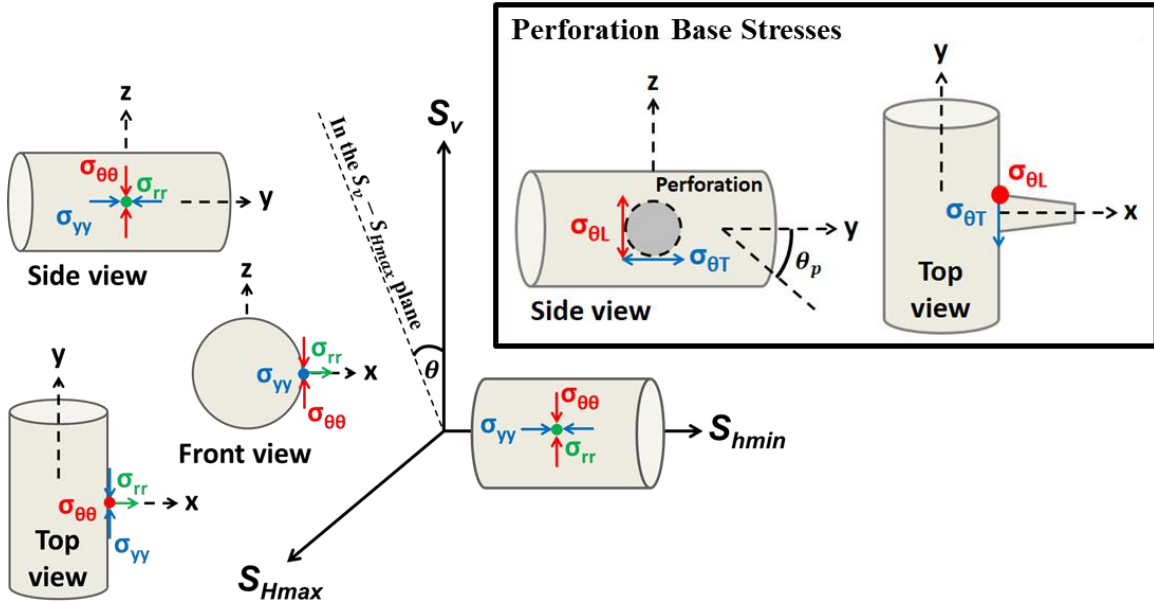
Figure 4.2. Configuration of the stresses on the wellbore radius ($\sigma_{\theta\theta}$, σ_{yy}, and σ_{rr}) for a well parallel to S_{hmin} (y-axis) and the stresses on the perforation base ($\sigma_{\theta L}$ and $\sigma_{\theta T}$) for perforations on the side of the hole (x-axis, $\theta = 90°$). At $r = r_w$, $\sigma_{r\theta} = 0$ (not shown).

The derivation of $\sigma_{\theta\theta_p}$ is shown in Appendix D, after Hossain et al. (2000) and modified by Michael et al. (2018) to incorporate the effects of p_p. Eq. B.3 is an expression for $\sigma_{\theta\theta_p}$ for a horizontal well parallel to S_{hmin} and a perforation aligned with S_{Hmax} (side of the hole, $\theta = 90°$), which for $p_{perf} = p_w$ is modified into

$$
\begin{aligned}
\sigma_{\theta\theta_p}\big|_{\theta=90°} = {}& S_{hmin} + \left([4v-2]\cos 2\theta_p - 2v - 1\right)S_{Hmax} \\
& + \left([6-4v]S_v - 2S_{hmin}\right)\cos 2\theta_p + (2v+3)S_v \qquad (4.9) \\
& - p_w\left(2\cos 2\theta_p + 2\right) - p_p
\end{aligned}
$$

105

where θ_p is the angle around the perforation measured from the σ_{yy} direction. At $\theta_p = 0°$, $\sigma_{\theta\theta_p} = \sigma_{\theta L}$ and at $\theta_p = 90°$, $\sigma_{\theta\theta_p} = \sigma_{\theta T}$ such that,

$$\sigma_{\theta L} \equiv \sigma_{\theta\theta_p}\Big|_{\theta=90°,\theta_p=90°}$$
$$= 9S_v - 3S_{Hmax} - (S_{hmin} - 2v[S_{Hmax} - S_v]) - 4p_w - p_p \tag{4.10}$$

$$\sigma_{\theta T} \equiv \sigma_{\theta\theta_p}\Big|_{\theta=90°,\theta_p=0°}$$
$$= 3S_{hmin} - (2 - 6v)(S_v - S_{Hmax}) - S_v - S_{Hmax} - p_p \tag{4.11}$$

If the perforation is at the top of the hole (S_v direction), the S_v and S_{Hmax} terms are interchanged in Eq. 4.9, leading to the expressions for $\sigma_{\theta L}$ and $\sigma_{\theta T}$ becoming

$$\sigma_{\theta L} \equiv \sigma_{\theta\theta_p}\Big|_{\theta=0°,\,\theta_p=90°}$$
$$= 9S_{Hmax} - 3S_v - (S_{hmin} - 2v[S_v - S_{Hmax}]) - 4p_w - p_p \tag{4.12}$$

$$\sigma_{\theta T} \equiv \sigma_{\theta\theta_p}\Big|_{\theta=0°,\,\theta_p=0°}$$
$$= 3S_{hmin} - (2 - 6v)(S_{Hmax} - S_v) - S_{Hmax} - S_v - p_p \tag{4.13}$$

The tensile failure criterion requires, $\sigma_{\theta\theta_p}\Big|_{\theta_p} < -T$. For perforations parallel to S_{Hmax} (side of the hole, $\theta = 90°$), the criteria for longitudinal and transverse fracture initiation, respectively, become

$$(9 - 2v)S_v + (2v - 3)S_{Hmax} - S_{hmin} - 4p_w - p_p + T < 0 \tag{4.14}$$

$$3S_{hmin} + (6v - 3)S_v + (1 - 6v)S_{Hmax} - p_p + T < 0 \qquad (4.15)$$

If both criteria are satisfied, we assume transverse fracture initiation will only occur if $\sigma_{\theta L}$ is more compressive/less tensile than $\sigma_{\theta T}$, such that $\sigma_{\theta T} < \sigma_{\theta L}$, giving a condition for preferred transverse fracture initiation of

$$S_{Hmax} + S_{hmin} - 3S_v + 2v(S_v - S_{Hmax}) + p_w < 0 \qquad (4.16)$$

4.3.3 Breakdown Pressure Window

According to the analytical fracture initiation criteria (Eq. 4.14 and 4.15), transverse fracture initiation is favored at lower p_w than longitudinal fracture initiation. Figure 4.3 shows $\sigma_{\theta T}$ (blue line) and $\sigma_{\theta L}$ (red line) variation with p_w for *in-situ* stress state parameters typical to the Barnett Shale (Table 3.1). As p_w increases, $\sigma_{\theta T}$ stays constant, while $\sigma_{\theta L}$ becomes more tensile (negative). This creates a "breakdown pressure window" for the initiation of transverse fractures; if the breakdown pressure, p_b is lower than a certain finite value, transverse fracture initiation occurs, as opposed to longitudinal. While the lower bound of the p_b window is always zero, the upper-bound ($p_{b,upper}$) can be calculated by rearranging Eq. 4.16 for p_w, such that

$$p_{b,upper}\big|_{\theta=90°} = 3S_v - S_{Hmax} - S_{hmin} + 2v(S_v - S_{Hmax}) \qquad (4.17)$$

for perforations in the S_{Hmax} direction, for the case of a well drilled parallel to S_{hmin} in a normal faulting stress regime. For perforations in the S_v direction (top of the hole), $p_{b,upper}$ is given by interchanging the S_v terms with S_{Hmax} in Eq. 4.17.
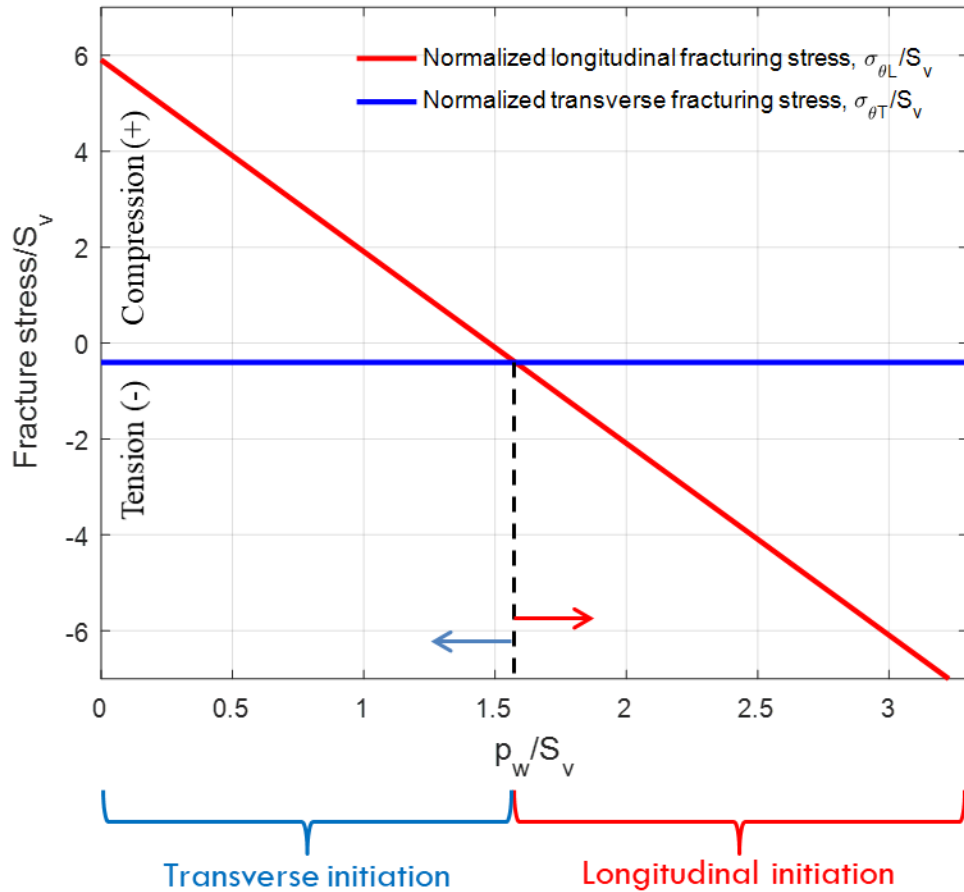
Figure 4.3. Variation of $\sigma_{\theta L}$ (red line) and $\sigma_{\theta T}$ (blue line) with p_w for horizontal wells parallel to S_{hmin} and perforated in the S_{Hmax} direction, for stress state parameters of the Barnett Shale. For p_b values smaller than p_w at the intersection point of the red and blue lines, transverse fracture initiation is promoted, whereas higher p_b yield longitudinal fracture initiation.

This is an important condition as the practitioners to an extent can have an impact p_b. Low pressurization rates were shown to suppress p_b (Zoback et al., 1977; Weijers, 1995) and can be used strategically to ensure $p_b \leq p_{b,upper}$.

4.3.4 Fracturing Fluid Leakage around the Wellbore

In the possibility of fracturing fluid leakage along the wellbore, due to cementing defects, or openhole completions, $\sigma_{\theta\theta}|_{r=r_w}$ and $\sigma_{yy}|_{r=r_w}$ should also be considered for fracture initiation, similar to the case of drilling-induced tensile fractures (DITF), from non-perforated openhole wellbores. Nelson et al. (2005) investigated transverse versus longitudinal DITF initiation from vertical wellbores. Figure 4.4 shows that in the case of leakage, $\sigma_{\theta T}$ caused by the wellbore is more tensile than that from the perforations, so it seems unlikely the perforations would be responsible for fracture initiation.
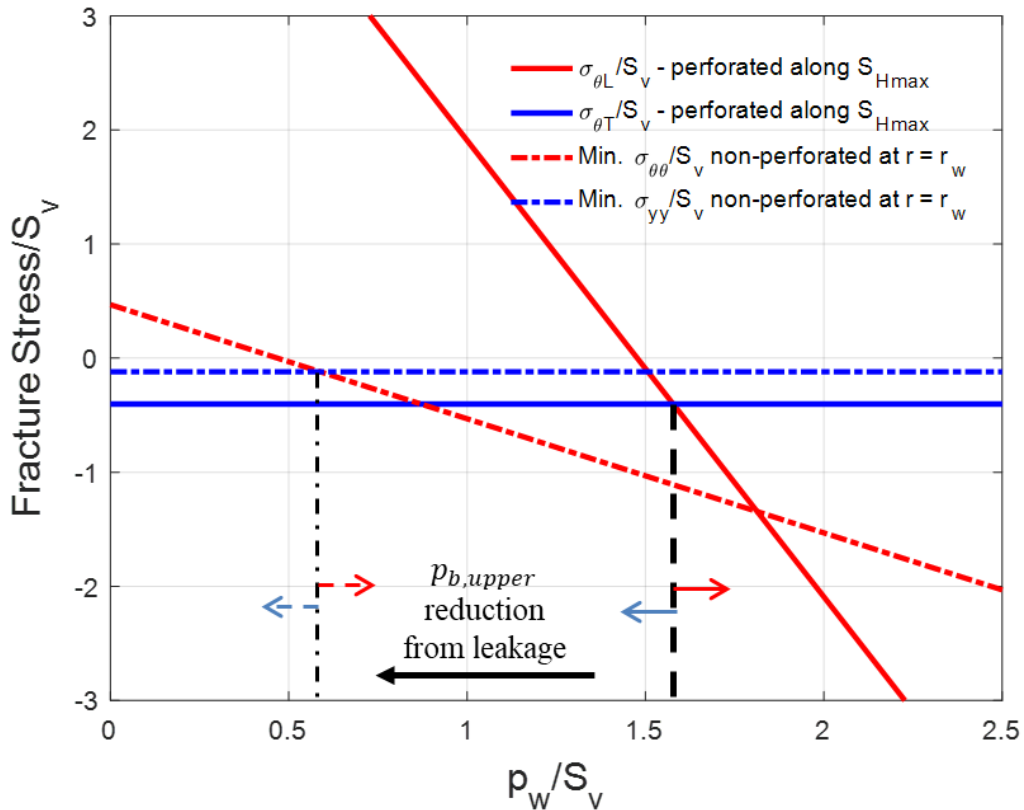
Figure 4.4. Longitudinal fracture-inducing $\sigma_{\theta\theta}|_{r=r_w}$ and transverse fracture-inducing $\sigma_{yy}|_{r=r_w}$, at S_v (dashed-dotted lines), compared with $\sigma_{\theta L}$ and $\sigma_{\theta T}$ (solid lines) at the locations where each of these stresses are the most tensile.

The p_b window for transverse fracture initiation from perforations parallel to S_{Hmax} (solid lines) is much wider (higher $p_{b,upper}$) than that for the two stresses around the perforation base, indicated by the solid lines on Figure 4.4 (same as in Figure 4.3). The wellbore stresses; $\sigma_{\theta\theta}|_{r=r_w}$ and $\sigma_{yy}|_{r=r_w}$, shown with the dash-dotted lines indicate a narrower p_b window for transverse fracture initiation, than the corresponding p_b window determined by $\sigma_{\theta L}$ and $\sigma_{\theta T}$. The p_b window for a perforation at the top of the hole (S_v direction), not shown on Figure 4.4, will be still wider than the p_b window determined by $\sigma_{\theta\theta}|_{r=r_w}$ and $\sigma_{yy}|_{r=r_w}$. Hence, leakage of fracturing fluid makes the initiation of longitudinal fractures occur at lower p_w than without leakage regardless of the location of the perforation.

4.3.5   Allowable Stress State Diagrams

The allowable range of possible relative principal stresses can be visualized on a diagram of S_{Hmax}/S_v against S_{hmin}/S_v (Figure 4.5, after Nelson et al., 2005). The allowable region is bound by the frictional limits of slip on a fault and the line of horizontal isotropy ($S_{Hmax} = S_{hmin}$). Critically-stressed faulting theory constrains the ratio of the effective maximum to minimum stress, $(S_1 - p_p)/(S_3 - p_p)$, to be less than the critical minimum value required for slippage on a pre-existing fault as

$$\frac{S_1 - p_p}{S_3 - p_p} \leq \left(\mu + \sqrt{(1 + \mu^2)} \right)^2 \tag{4.18}$$

where μ is the friction coefficient of the fault and, S_1 and S_3 are the greatest and least compressive principal stresses, respectively. According to Anderson (1951), $S_1 = S_v$ and $S_3 = S_{hmin}$ for a normal faulting stress state, $S_1 = S_{Hmax}$ and $S_3 = S_v$ for reverse faulting

and $S_1 = S_{Hmax}$ with $S_3 = S_{hmin}$ for strike-slip faulting. Typical friction values for rocks are ~0.6 (Byerlee, 1978), which puts the ratio $(S_1 - p_p)/(S_3 - p_p)$ at 3.12; if the ratio reaches this point fault slippage will occur. Assuming a hydrostatic gradient for $p_p = 0.433$ psi/ft, then the allowable region for a stress state becomes a region enclosed by the polygon shown in Figure 4.5.
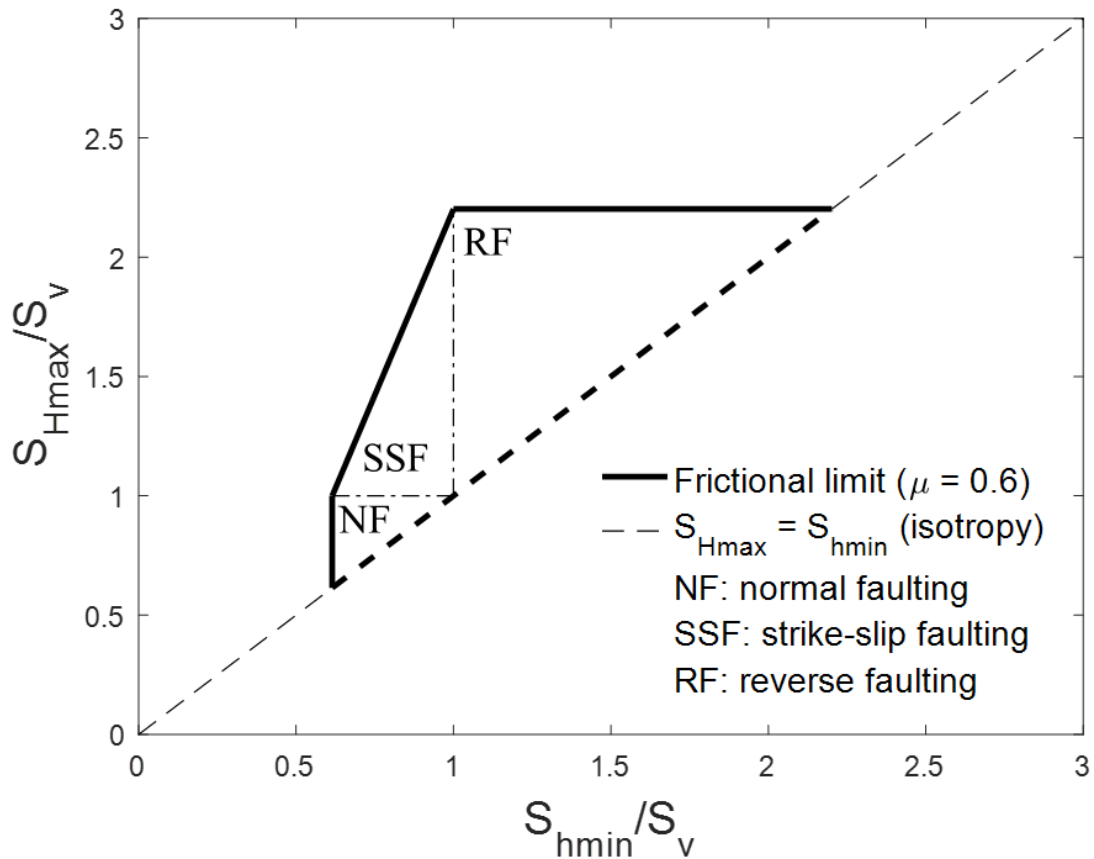
Figure 4.5. *In-situ* stress states possible in the Earth's subsurface. The dotted line represents horizontal isotropy ($S_{Hmax} = S_{hmin}$) and the solid line represent the frictional limits at $\mu = 0.6$ (Byerlee, 1978). The region bounded by the solid lines and the horizontal isotropy line represents the range of possible subsurface stress states.

Following Nelson et al. (2005), the criteria for transverse fracture initiation from non-perforated wells, can be demonstrated on allowable stress state diagrams as the area between the lines of $\sigma_{yy} = 0$ and $\sigma_{yy} = \sigma_{\theta\theta}$ at $r = r_w$ drawn using Eq. 4.5 through 4.8. Figure 4.6 shows that for the top and side of the hole (S_v and S_{Hmax} direction, respectively) with p_p and p_w gradients equal to 0.433 psi/ft. The figure shows that under virtually all stress conditions, longitudinal fracture initiation is expected before transverse fracture initiation. However, transverse fracture initiation is more likely for the side of the hole (S_{Hmax} direction) than the top (S_v direction).
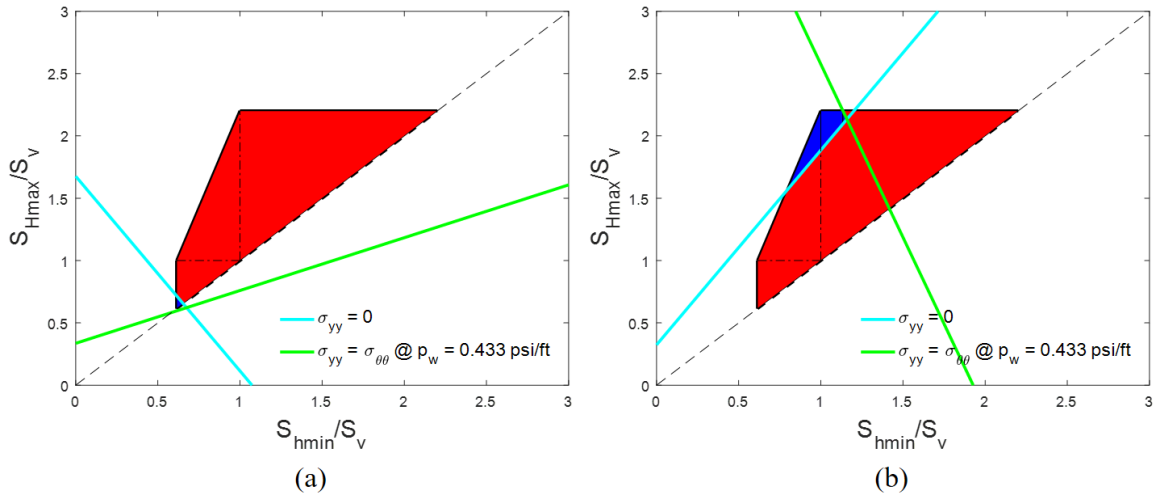
Figure 4.6.   Allowable *in-situ* stress state diagram for fractures initiated from non-perforated wellbores for a horizontal well parallel to S_{hmin} from, (a) the top of the hole (S_v direction), and (b) the side of the hole (S_{Hmax} direction). The blue region indicates the stress states promoting transverse fracture initiation, while the red indicates the stress states promoting longitudinal fracture initiation.

Allowable stress state diagrams can also be used to demonstrate the transverse fracture initiation criteria from perforated wells. Using Eqs. 4.10 and 4.11, two lines are

added to the stress polygon; one for $\sigma_{\theta T} = 0$ and another for $\sigma_{\theta T} = \sigma_{\theta L}$ assuming a p_p gradient 0.433 psi/ft (Figure 4.7). The region between the two lines (where $\sigma_{\theta T} < 0$ and $\sigma_{\theta T} < \sigma_{\theta L}$) represents the stress state where transverse fracture initiation occurs for a given p_w gradient. Increasing the p_w gradient from 0.6 psi/ft to 0.9 psi/ft, reduces the stress state range that would yield transverse fracture initiation. This is comparable with the effect of p_w within a specific stress state (Figure 4.3) where its increase causes a gradual shift from transverse to longitudinal fracture initiation.
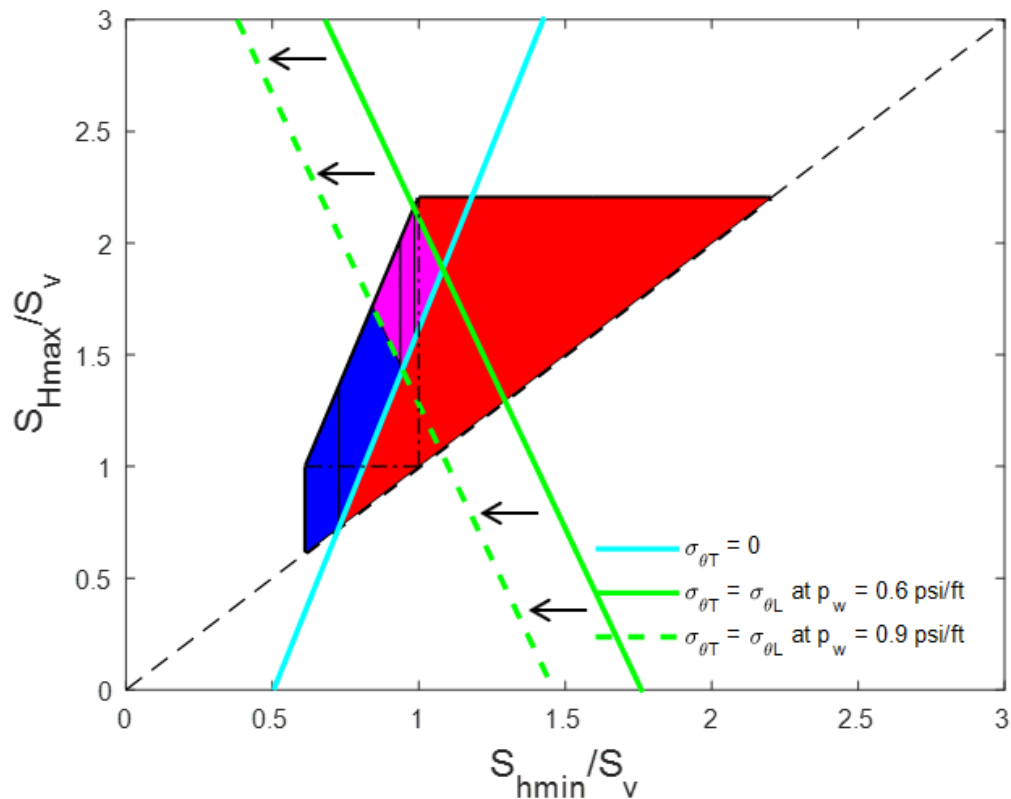
Figure 4.7. Analytically-approximated orientation criterion for fracture initiation from perforated horizontal wells drilled parallel to S_{hmin} and perforated along S_{Hmax}. The red region indicates longitudinal fracture initiation, while the blue region indicates transverse fracture initiation. The magenta region shows the stress states where transverse fracture initiation does not take place following a p_w increase from 0.6 to 0.9 psi/ft.

113

4.3.6   Practical Problems Caused by Longitudinal Fracture Initiation

The PFP of a horizontal well parallel to S_{hmin} is transverse to the wellbore (Hubbert and Willis, 1957). Therefore, longitudinal fracture initiation from such wells, which is a non-PFP orientation, is expected to lead to fracture reorientation (El Rabaa, 1989; Weijers, 1992; Olson, 1995) at some point as the fracture propagates away from the wellbore, to align the fracture transversely to the well along PFP. This reorientation is forced by the magnitudes of the far-field, *in-situ* principal stresses (S_v, S_{Hmax} and S_{hmin}), which while moving away from the well, become more dominant as the near-wellbore stresses (Kirsch, 1898 modified by Hubbert and Willis, 1957) diminish (El Rabaa, 1989; Hallam and Last, 1991; Owens et al., 1992; Weijers, 1992; Olson, 1995).

Fracture reorientation generates tortuosity in the near-wellbore region, which can cause serious completion-related problems like early screenouts. The point of reorientation restricts the flow of proppant carried in the treatment fluid, something observed at the surface as a sudden rise in pump pressure. Another problem caused by the near-wellbore tortuosity is fracture fluid leakages across adjacent stages during multi-stage fracture treatments. The results of a tracer test (Barree and Miskimins, 2015) show fluid used in the stimulation of a stage appearing in adjacent stages, despite all stages separated from each other using packers. Barree and Miskimins (2015) explain this by longitudinal fractures, which penetrate an as of yet untreated stage, providing possible paths of low resistance for fluid entry.

The aforementioned completion-related issues suppress the efficiency of a hydraulic fracture treatment, giving rise to production-related problems, such as poor, below expectations post-treatment well performance. As a result, the overall net present

value (NPV) of the fracture treatment is negatively impacted (Balen et al., 1988; Michael, 2019b).

4.4 TRUE-3D MODEL DEVELOPMENT

Numerical modeling was performed using *FLAC³D* (*Fast Lagrangian Analysis of Continua in 3 Dimensions*, Itasca Consulting Group), which utilizes an explicit finite volume formulation that can simulate the complex behavior of non-linear or unstable models exhibiting high degrees of strain. We studied a rectangular body with a cylindrical wellbore in the middle (Figure 4.8). A perforation of radius significantly smaller than that of the wellbore was placed perpendicular to the wellbore central axis at the top and side of the hole ($\theta = 90°$).

The block was modeled as a homogeneous, linear elastic continuum with a Young's modulus, E and a Poisson's ratio, v. Constant stress or no displacement boundary conditions were used appropriately to set up the simulation model and p_{perf}, was set equal to p_w. Explicit modeling of the casing and cement was excluded to simplify the model. This was justified by assuming the existence of a micro-annulus between cement and the formation prior to fracture initiation. Use of capsule guns, small gun-to-casing clearance, and presence of liquid in the wellbore during the perforation process promote the micro-annulus formation (Behrmann and Nolte, 1998).
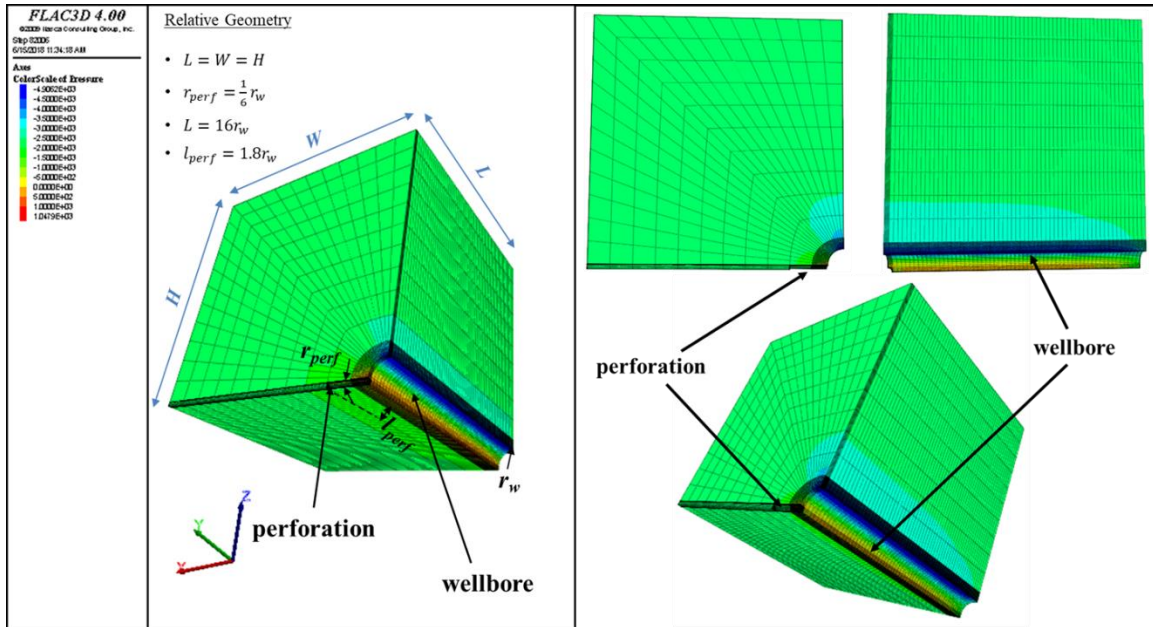
Figure 4.8.   The *FLAC³D* model mesh, with 174,496 grid points in total. A grid refinement study was performed to optimize computational time without affecting the output accuracy.

4.4.1   Variation of the Wellbore Stresses in the Absence of Perforations

The model was verified against the plane strain analytical solution of the elastic stresses around a circular hole (Kirsch, 1898). A point on the wellbore far away from the perforation (10 perforation radii) was chosen for verification of the polar stress components around the wellbore radius (σ_{yy}, $\sigma_{\theta\theta}$, σ_{rr}, and $\sigma_{r\theta}$), where the effects of its presence are diminished. The *FLAC³D* solutions of σ_{yy}, $\sigma_{\theta\theta}$, σ_{rr}, and $\sigma_{r\theta}$ show excellent agreement with the analytical solutions for the same stresses at distance $r = 1.02r_w$ from the center of the wellbore (Figure 4.9).
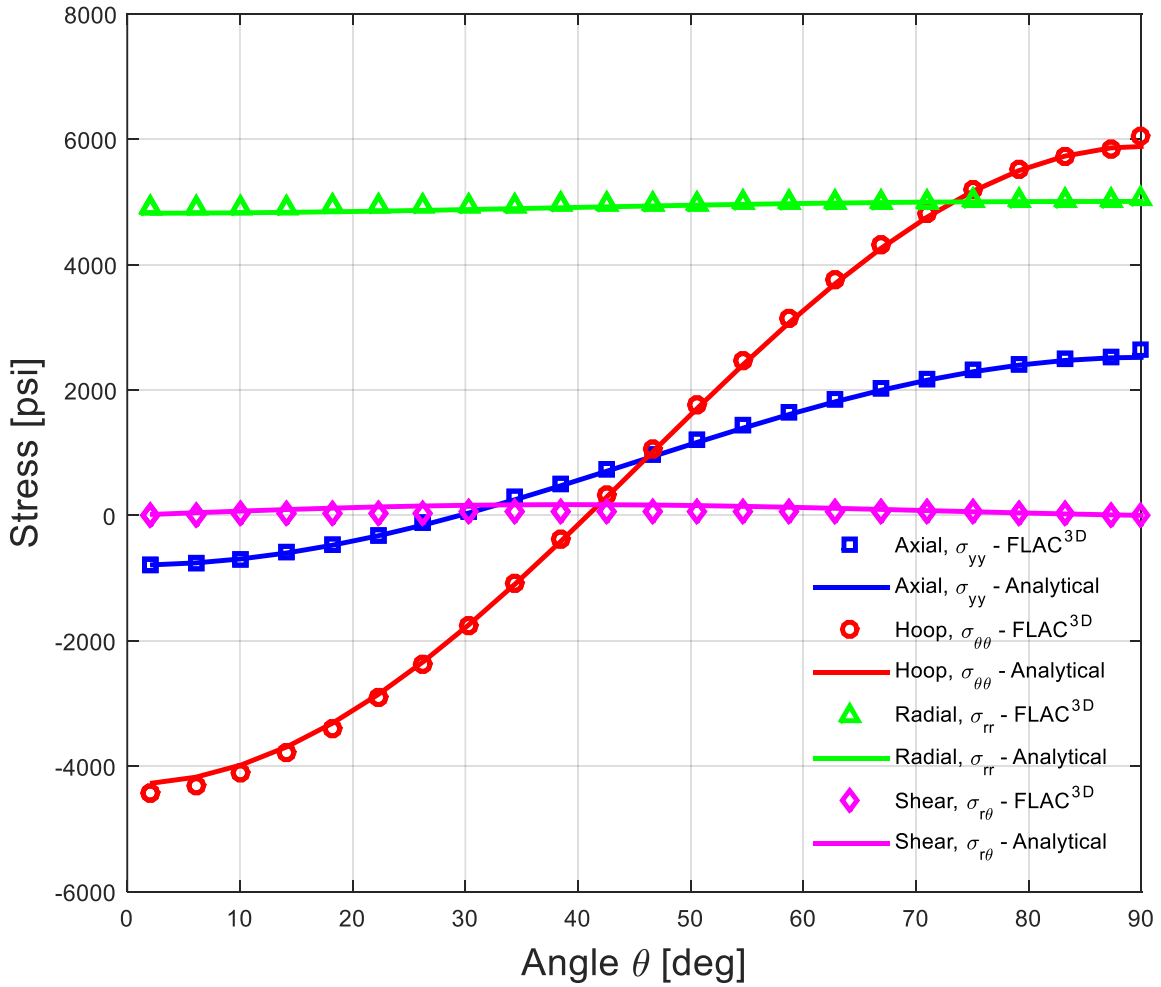
Figure 4.9. Comparison between the stress components around the wellbore, predicted by the true-3D numerical (*FLAC³ᴰ*) model and the analytical solutions of Kirsch (1898). Barnett Shale stress state parameters were used, with p_w fixed at 5,000 psi and all stresses calculated at a distance $r = 1.02r_w$ from the center of the wellbore and $10r_w$ away from the perforation.

The variation of $\sigma_{\theta\theta}$ and σ_{yy} around the wellbore radius with variable p_w was also verified. The stress state of the Barnett Shale (Table 3.1) was used with p_w ranging from 0 to 10,000 psi (Figure 4.10). The *FLAC³ᴰ* model maintains an excellent agreement with the

corresponding analytical solutions (from Kirsch, 1898) of these stresses across the p_w range giving confidence in our numerical wellbore mesh and boundary conditions.
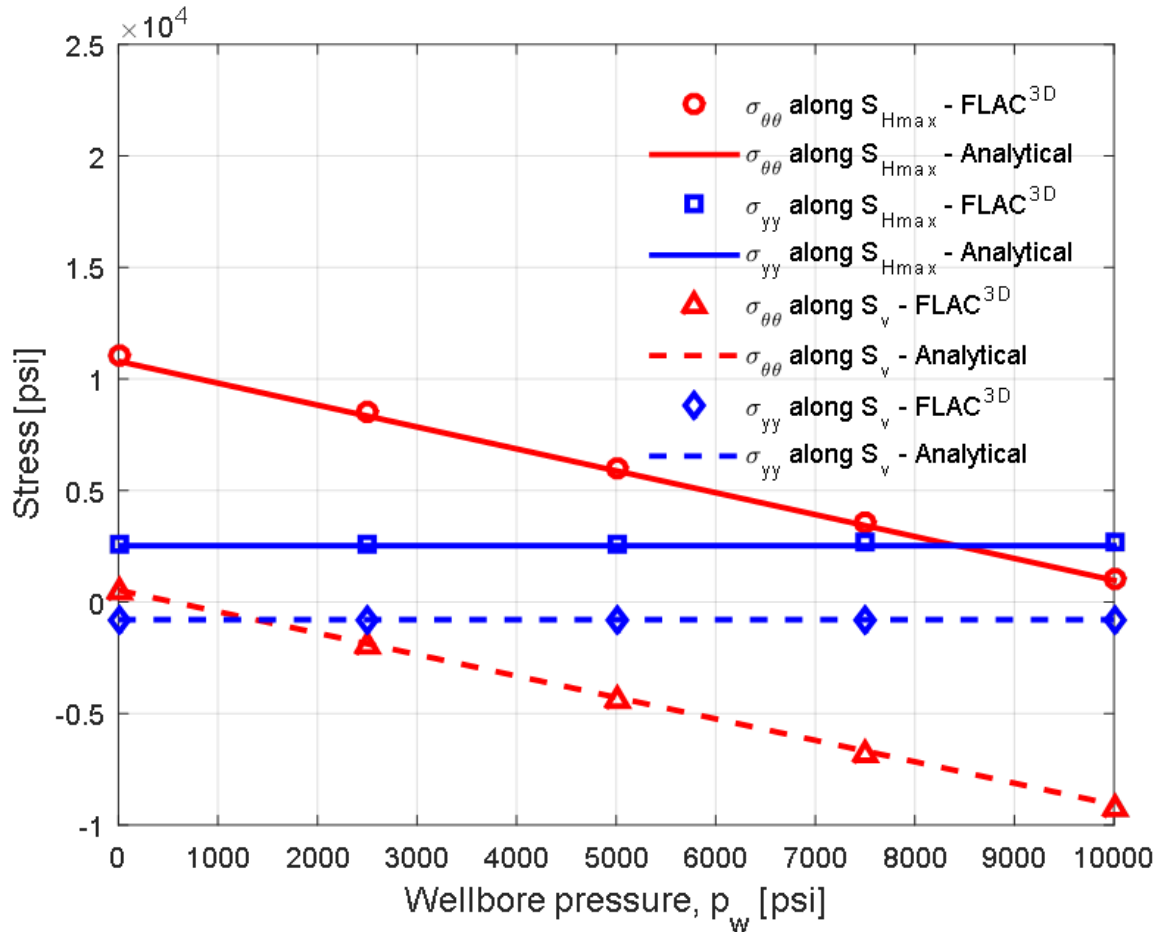
Figure 4.10. Stresses on the wellbore radius ($\sigma_{\theta\theta}$ and σ_{yy}) along S_v and S_{Hmax}, for varying p_w as predicted by the true-3D numerical ($FLAC^{3D}$) model (points) and the corresponding analytical solutions (lines) for the *in-situ* stress state of the Barnett Shale. The stresses are calculated at a distance $r = 1.02r_w$ from the center of the wellbore and $10r_w$ away from the perforation.

4.4.2 Perforation Geometry

A series of simulations was performed to investigate the effect of the perforation geometry on $\sigma_{\theta\theta_p}$. The length of the perforation, l_{perf}, was found to have only a minor impact on the stresses around the perforation base compared to the perforation radius, r_{perf}. Subsequently, the perforation length, $l_{perf} = 16r_w/9$, and perforation radius, $r_{perf} = r_w/6$, used in this study were kept unchanged to ensure a fair assessment and accurate conclusions.

4.4.3 Numerical Solutions of the Longitudinal and Transverse Fracturing Stresses

A weakness in the analytical approach for the perforated wellbore is that the analytical equations cannot explicitly reproduce the real geometry. The approximations (Hossain et al., 2000; Michael et al., 2018) simply superpose two plane strain cylindrical hole solutions using the wellbore stresses (first hole) for boundary conditions on the perforation (second hole). Numerically-obtained solution of the perforated wellbore problem using the true-3D model, which can explicitly represent the complex 3D geometry, demonstrates the shortcomings of the superposed approximate model.

Numerical simulations performed using the true-3D numerical model (written on *FLAC^{3D}*) show that the stresses at the perforation base with variation in the p_w differ considerably to the values predicted analytically (Figures 4.11 and 4.12). Unlike the analytical prediction given by Hossain et al. (2000) modified for p_p by Michael et al. (2018), $\sigma_{\theta T}$ does not remain constant as p_w increases. *FLAC^{3D}* outputs showed instead a positive relationship between the $\sigma_{\theta T}$ and p_w.
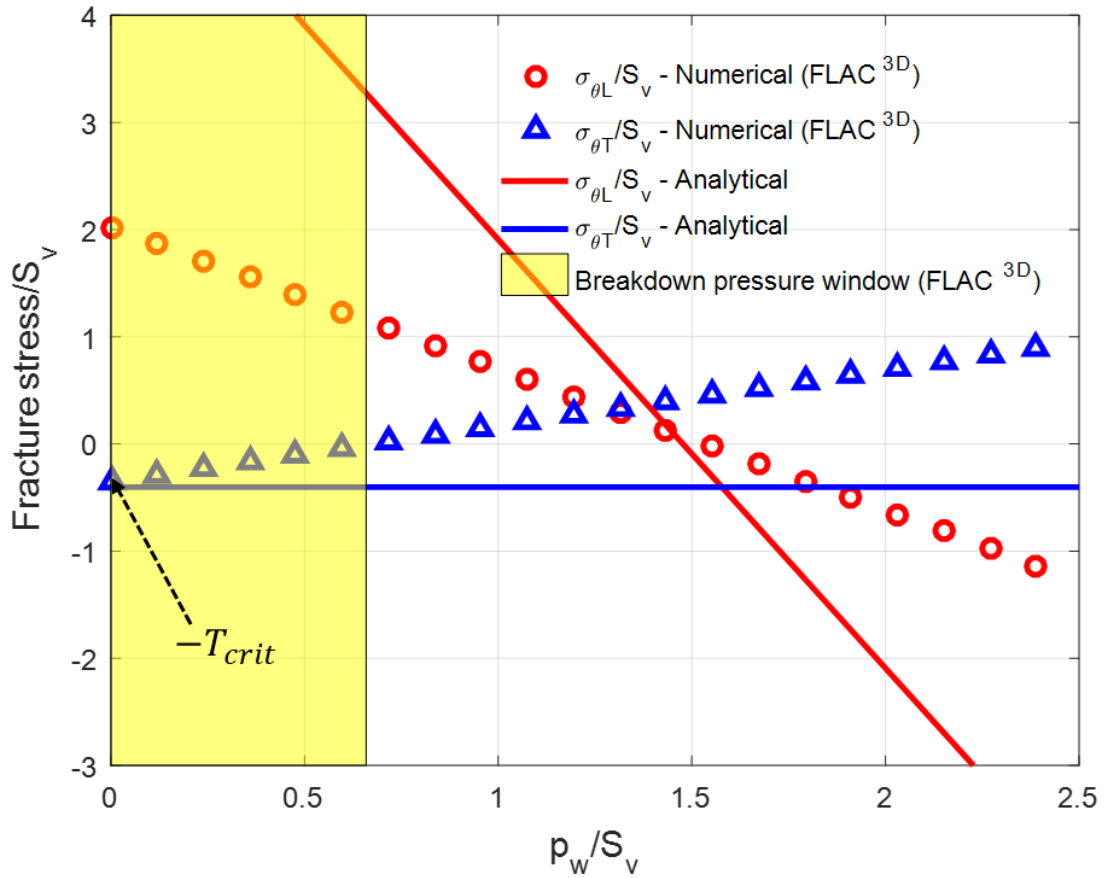
Figure 4.11. Comparison between the $FLAC^{3D}$ model and the modified Hossain et al. (2000) approximations for $\sigma_{\theta L}$ and $\sigma_{\theta T}$ on Barnett Shale parameters with perforations parallel to S_{Hmax}. The yellow-shaded region represents the p_b window for transverse fracture initiation (0-4,754 psi). The intercept of the $\sigma_{\theta T}$ line at $p_w = 0$ represents the critical tensile strength, T_{crit}, which is 2,482 psi.
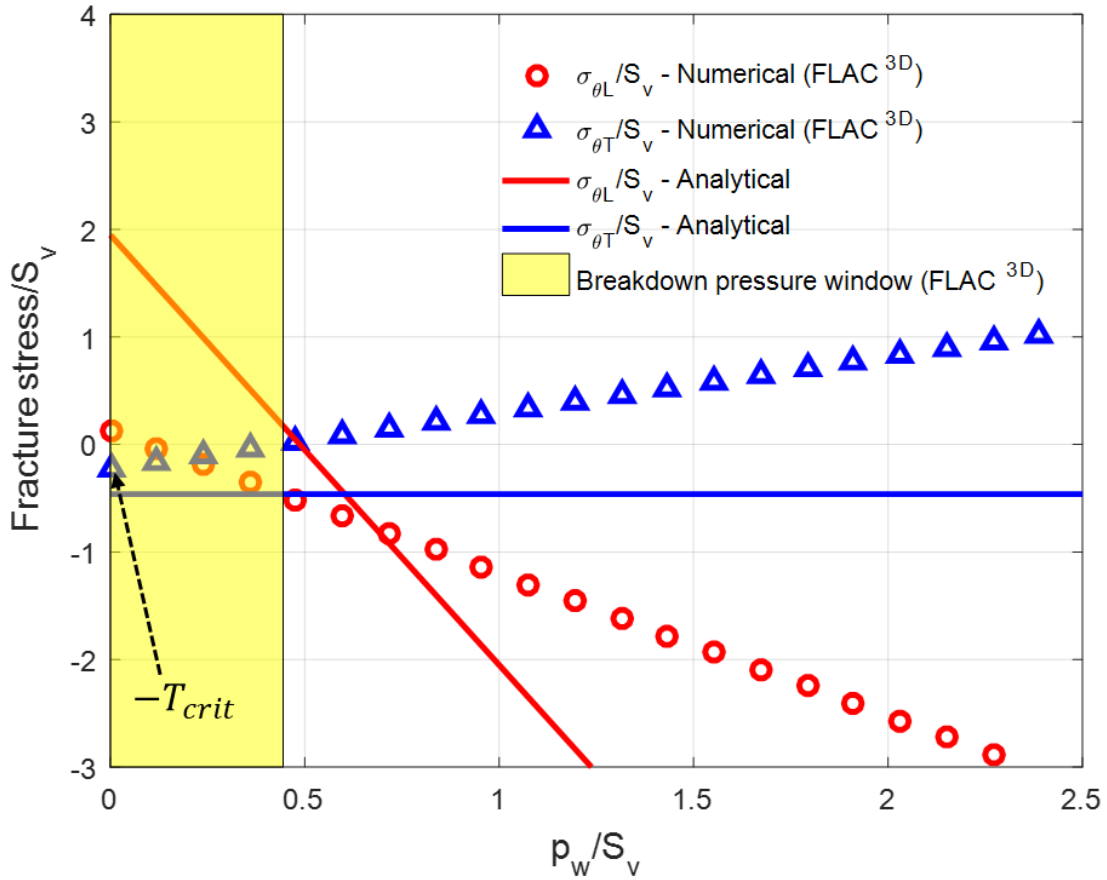
Figure 4.12.   Comparison between the $FLAC^{3D}$ model and the modified Hossain et al. (2000) approximations for $\sigma_{\theta L}$ and $\sigma_{\theta T}$ on Barnett Shale parameters, with perforations parallel to S_v. The yellow-shaded region represents the p_b window (0-3,206 psi) for transverse fracture initiation, which is significantly narrower than the p_b window for perforations parallel to S_{Hmax} (Figure 4.11). T_{crit} is 1,676 psi.

The main implication of this is that the p_b window decreases significantly what the analytical approximation predicts, because $\sigma_{\theta T}$ increases as p_w increases, eventually becoming compressive before the $\sigma_{\theta T}$ line meets the $\sigma_{\theta L}$ line as seen on Figures 4.11 and 4.12. For the stress state and formation properties of the Barnett Shale and perforations aligned with S_{Hmax}, the transverse fracture initiation window ends at 4,754 psi, making it

60% smaller than the 11,490 psi prediction from the analytical equations. For perforations aligned with S_v the window ends at 3,206 psi, which is 24% shorter than the analytically-approximated criterion's prediction. As p_w increases, $\sigma_{\theta L}$ still becomes more tensile but at a shallower slope than the analytical solution. Another implication of $\sigma_{\theta T}$ correlating positively with p_w, is that a region is created where both $\sigma_{\theta L}$ and $\sigma_{\theta T}$ are compressive and thus no fracture initiation is predicted for in that p_w range. Nevertheless, longitudinal fracture initiation is expected at higher p_w values, since if the p_w is in this range, it has already exceeded the p_b window for transverse fracture initiation.

To explain the perforation stress dependence on p_w one has to look at the 3D geometry of the combined wellbore and perforation. When either of the two cavities (wellbore or perforation) are pressurized, a radial stress is experienced on its wall, causing some degree of radial displacement. The presence of the pressurized wellbore so close to the perforation means that at the point of attachment; the perforation base, the radial stresses of the wellbore and the perforation act against each other. From this interaction, the magnitudes of $\sigma_{\theta\theta}|_{r=r_w}$ and $\sigma_{yy}|_{r=r_w}$ is altered. This in turn, affects the magnitude of the tangential stress at the perforation base, $\sigma_{\theta\theta_p}\big|_{\theta_p}$. Lower radial stress leads to a higher $\sigma_{\theta\theta}$ at that point, which translates to a change in $\sigma_{\theta\theta_p}$ of some sort. At $\theta_p = 90°$, the magnitude of $\sigma_{\theta\theta_p}$ increases as p_w rises, yielding a more compressive $\sigma_{\theta T}$. At $\theta_p = 0°$, $\sigma_{\theta\theta_p}$ decreases leading to $\sigma_{\theta L}$ becoming more tensile as p_w increases, as the modified Hossain et al. (2000) approximation suggested. However, the magnitude of $\sigma_{\theta L}$ predicted by the analytical approximation per se, is always smaller than true 3D, numerically-computed value.

Expanding the simulation over a range of stress states, we see that for a fixed p_w value, the region of stress states promoting transverse fracture initiation as predicted by the

true-3D numerical model is smaller compared to what the analytically-approximated model predicts. Figure 4.13a indicates the stress states, which promote transverse (versus longitudinal) fracture initiation according to the orientation criterion developed using the modified Hossain et al. (2000) analytical approximations for $\sigma_{\theta L}$ and $\sigma_{\theta T}$, while Figure 4.13b shows the same criterion developed using the true-3D numerical model constructed by plotting specific points. The blue region of the stress states expected to generate transverse fracture initiation in Figure 4.13b is visibly smaller and narrower than the corresponding blue region in Figure 4.13a, highlighting the extent to which the analytical approximations for the fracturing stresses overestimate transverse fracture initiation.

While the analytically-approximated orientation criterion (Figure 4.13a) can be applied to virtually any stress state, even outside the polygon, the applicability range of the numerically-developed criterion is restricted to the range of stress states for which simulations were performed (Figure 4.13b). Nevertheless, the true-3D numerical model enables the possibility of the model's use for the development of correlations for predicting the orientation of fracture initiation from perforated wells, based on the *in-situ* conditions. This can be achieved by using the true-3D numerical model to derive correction factors to the existing analytical approximations (Hossain et al., 2000; Michael et al., 2018; Michael, 2019a) for specific cases, at different p_w values.
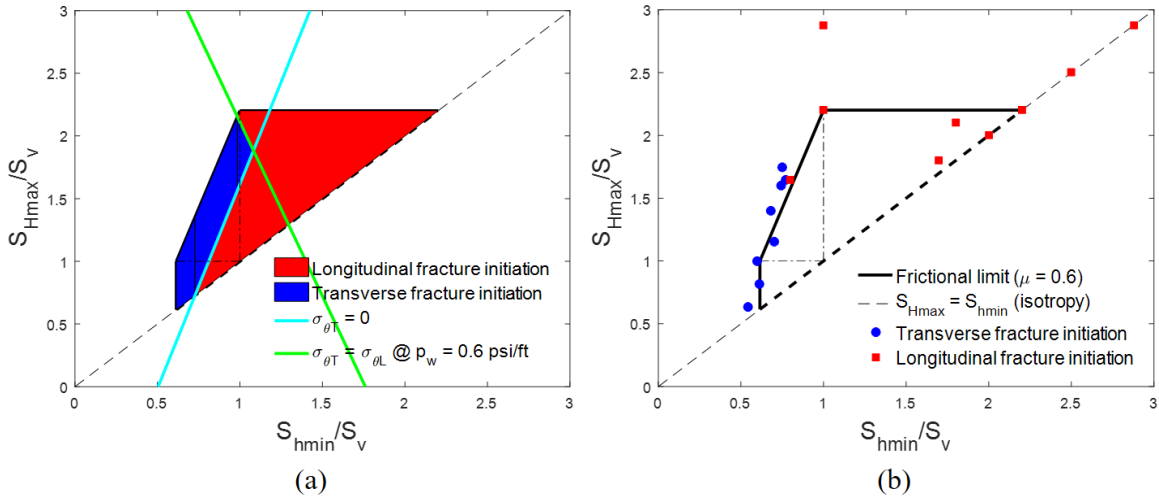
Figure 4.13. Allowable stress state diagrams indicating the orientation of fracture initiation as predicted at $p_w = 0.6$ psi/ft by, (a) the criterion developed using the modified Hossain et al.'s (2000) analytical approximations for the fracturing stresses and (b) the true-3D numerical model.

4.4.3.1 Critical Tensile Strength

The positive slope of $\sigma_{\theta T}$ with p_w indicated by the true-3D numerical model creates an additional constraint for transverse fracture initiation. The $\sigma_{\theta T}$ value at $p_w = 0$ (Figures 4.11 and 4.12) represents the critical tensile strength, T_{crit}. If $|T| > |T_{crit}|$, transverse fracture initiation is impossible, regardless of how low p_b is. Defined as a quantity evaluated at $p_w = 0$, T_{crit} depends solely on the rock properties and *in-situ* stress state. Thus, contrary to the p_b window constraint, there is no way with which the practitioner can decrease T_{crit} to promote transverse fracture initiation.

Consequently, for transverse fracture initiation to be generated from a perforated well (assuming no fracturing fluid leakages), three criteria must be met in the following order:

i. $|T| < |T_{crit}|$.

ii. The value of p_b falls within a "window" for transverse fracture initiation (i.e. $\sigma_{\theta T} < -T$).

iii. The longitudinal fracturing stress is less tensile than the transverse fracturing stress at $p_w = p_b$ (i.e. $\sigma_{\theta T} < \sigma_{\theta L}$).

4.4.3.2 Preferred Perforation Alignment (PPA)

The values of T_{crit} and $p_{b,upper}$ are higher for perforations parallel to S_{Hmax} in a normal faulting stress regime compared to the subsequent values for perforations parallel to S_v (Michael and Gupta, 2019e; 2020b; Michael, 2019a). This makes the S_{Hmax} direction the preferred perforation alignment (PPA) for normal faulting stress states, since this perforation alignment is the best for generating transverse fracture initiation. For strike-slip faulting stress states, S_v is the PPA. If a wellbore is drilled parallel to the least principal stress (Figure 4.14), any possible PPA direction, which is dictated by the stresses orthogonal to the wellbore, will be contained within the PFP.
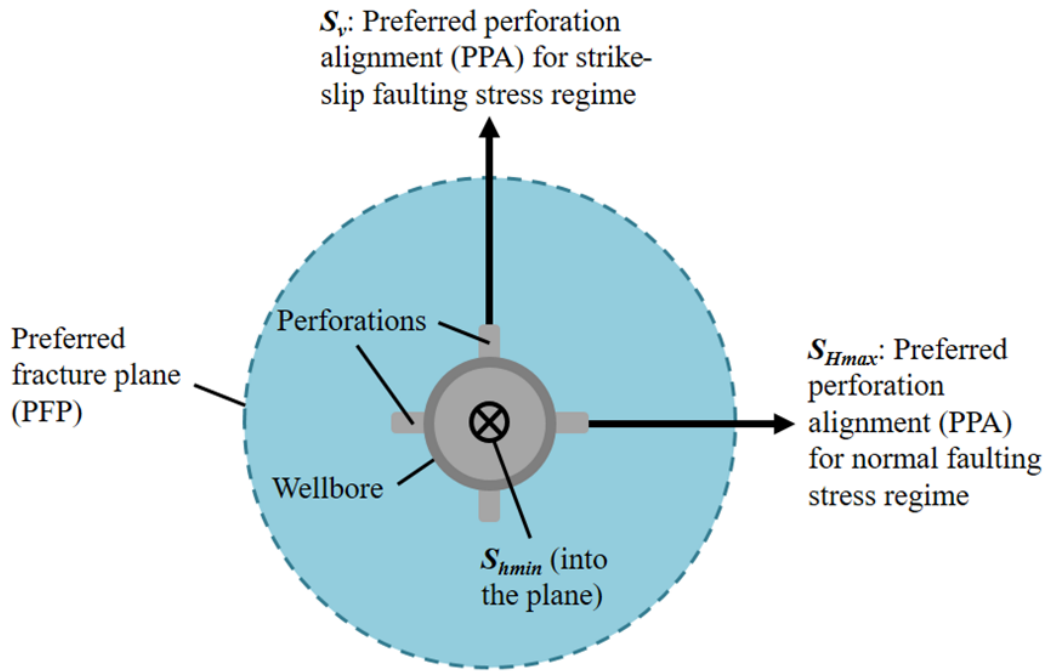
Figure 4.14. The preferred perforation alignment (PPA) configurations for horizontal wells drilled parallel to S_{hmin} under normal and strike-slip faulting stress regimes (from Michael, 2019a).

It is worth mentioning that the modified Hossain et al. (2000) analytical approximations for $\sigma_{\theta L}$ and $\sigma_{\theta T}$ predicted correctly which perforation alignment (PPA) is the most favored for yielding transverse fracture initiation. PPA is the alignment with the highest T_{crit} and largest p_b window according to the analytical approximation and is validated by the numerical model. This is useful for completion engineers; when targeting "sweet spots" strategically oriented perforations (Kurdi, 2018) along PPA can be used to enhance the promotion of transverse fracture initiation by maximizing $p_{b,upper}$ and T_{crit}.

4.5 SHALE PLAY (NUMERICAL) CASE STUDIES

Seven unconventional shale formations under current development (Barnett, Bakken, Fayetteville, Haynesville, Niobrara, Marcellus and Vaca Muerta) are used to assess and compare the analytical orientation criterion with the numerical model when it comes to field-scale application. The values of $\sigma_{\theta L}|_{p_w}$ and $\sigma_{\theta T}|_{p_w}$ were calculated using published *in-situ* stress state data (Prioul et al., 2011; Moos, 2012; Yang and Zoback, 2014; Koskella et al., 2015; Kowan and Ong, 2016) shown on Figure 4.15 and summarized on Table 3.1. For all simulations $p_{perf} = p_w$.
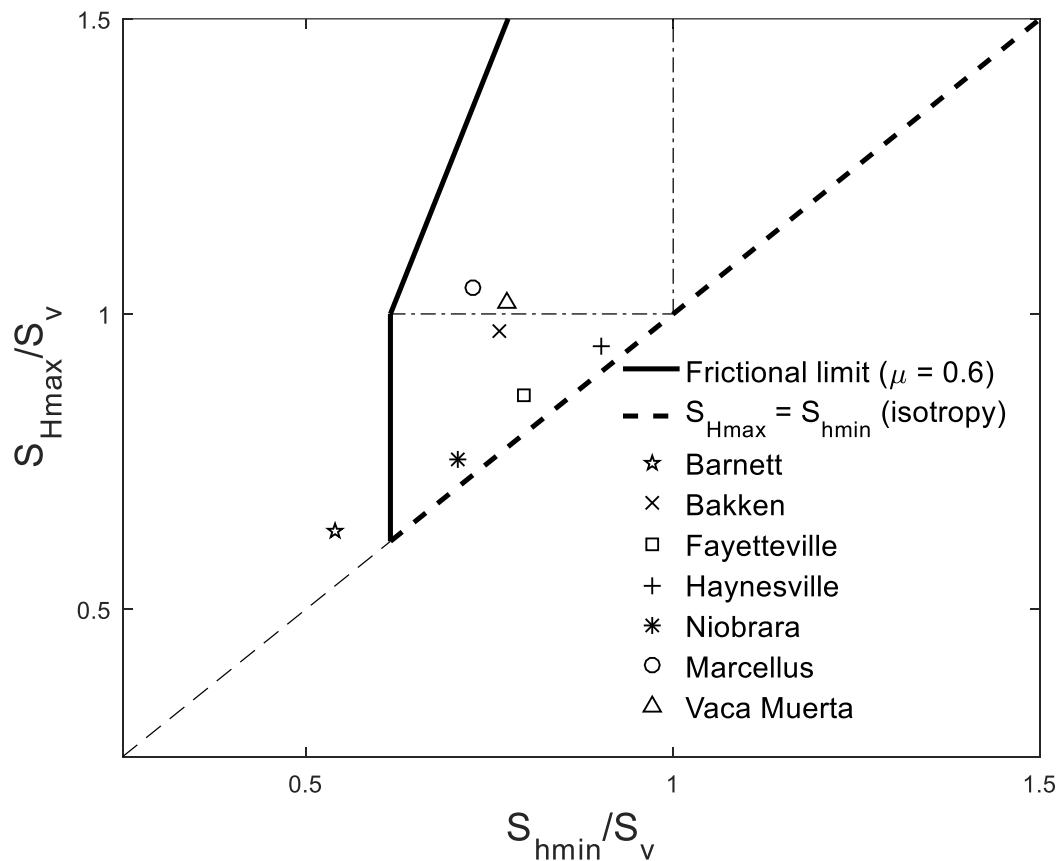
Figure 4.15. *In-situ* stress state of the seven shale plays on an allowable stress diagram.

The Barnett, Bakken, Fayetteville, Haynesville and Niobrara (Figure 4.16) are shale formations located in the United States that are under normal faulting *in-situ* stress states where $S_v > S_{Hmax} > S_{hmin}$. The PPA for those formations is thus in the S_{Hmax} direction, for which $p_{b,upper}$ and T_{crit} are maximized.
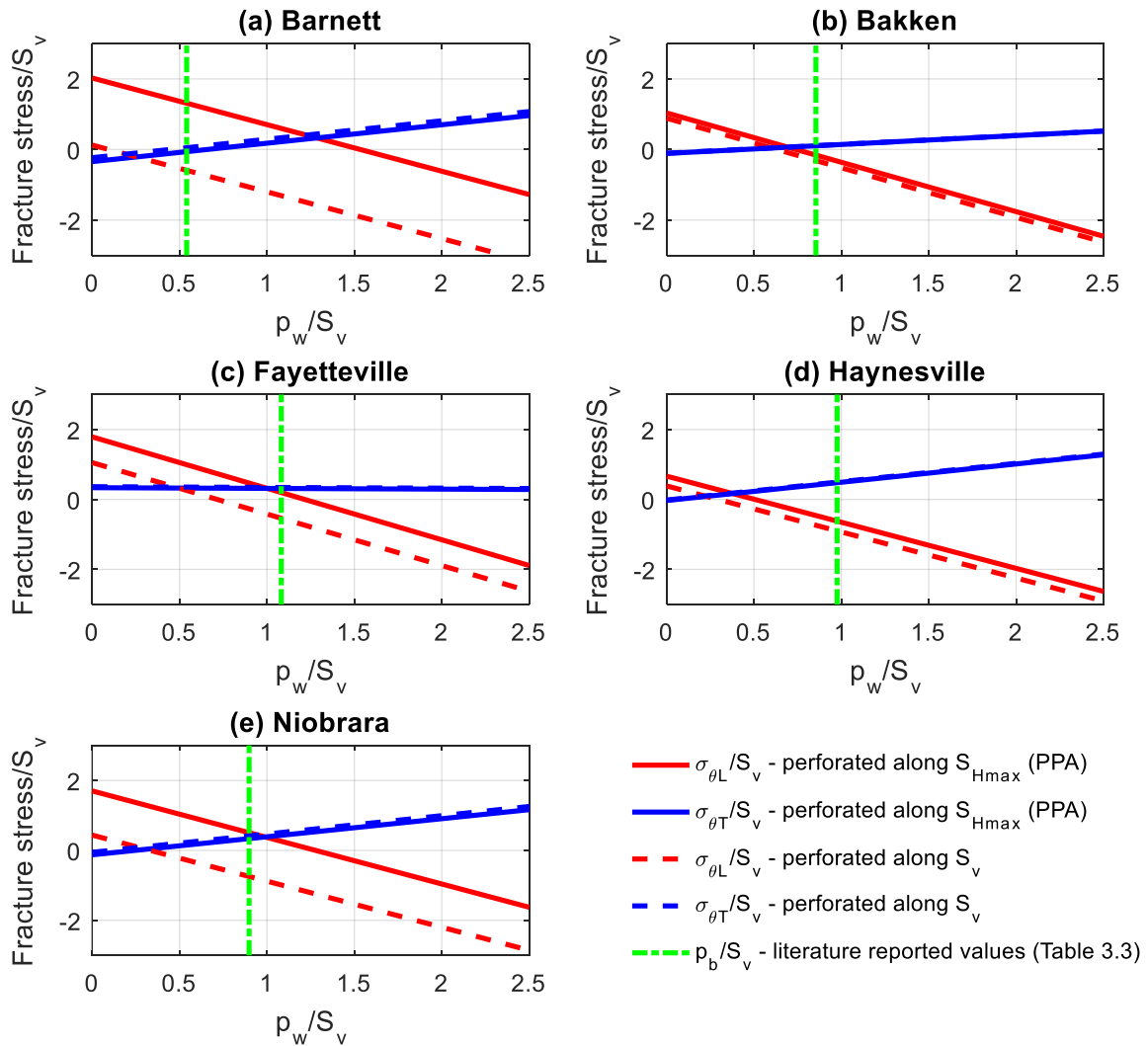
Figure 4.16. Numerically-calculated $\sigma_{\theta L}$ and $\sigma_{\theta T}$ relationship with p_w for the five shale plays under normal faulting stress regime.

The Marcellus in the United States and Vaca Muerta in Argentina (Figure 4.17) are two shale formations where the *in-situ* stress state is strike-slip faulting with $S_{Hmax} > S_v > S_{hmin}$. The PPA for horizontal wells aligned with S_{hmin} in these plays is parallel to S_v.
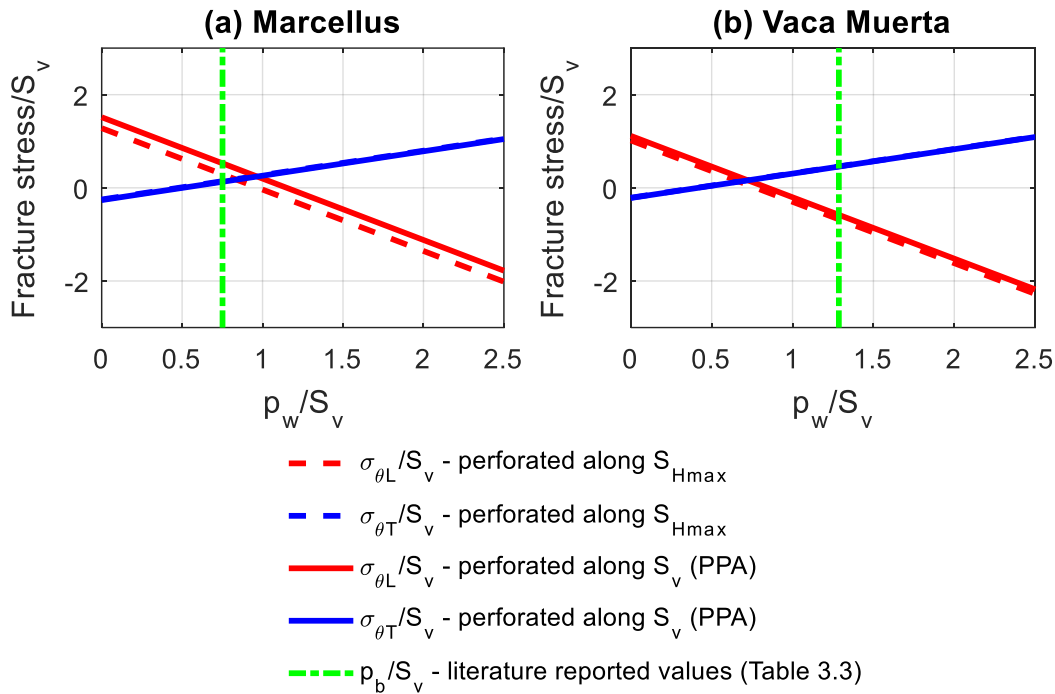
Figure 4.17. Numerically-calculated $\sigma_{\theta L}$ and $\sigma_{\theta T}$ relationship with p_w for two shale plays under strike-slip faulting stress regime.

For comparison purposes, p_b estimates for the seven shale plays were calculated using fracture gradient values from the literature (Ketter et al., 2006; Hammes et al., 2011; Barth et al., 2012; Schlumberger, 2014; Kosset, 2014; Koskella et al., 2015 and Lynk et al., 2017). These p_b estimates can be found on Table 3.3. Analytical estimation of p_b can be done, however that value depends on the fracture orientation (Barree and Miskimins,

2015). Because orientation is the dependent variable in this study it was deemed more reliable to estimate p_b independently using actual field-reported values.

Table 4.1 indicates PPA as the best perforation direction for transverse fracture initiation, yielding the highest $p_{b,upper}$ and T_{crit} values, with the non-PPA direction (perpendicular to PPA) the least. It is surprising that the numerical model predicts transverse fracture initiation only for the Barnett Shale for perforations parallel to PPA.

Table 4.1.   Calculation summary of the p_b window and T_{crit} for transverse fracture initiation, and hence the orientation prediction for the fracture initiation for perforations aligned with PPA and orthogonal (non-PPA). All numbers are in "psi" units.

Shale play	p_b window PPA[a]	p_b window non-PPA[b]	T_{crit} PPA	T_{crit} non-PPA	Fracture initiation PPA	Fracture initiation non-PPA
Barnett	0-4,754	0-3,206	2,482	1,676	Transverse	Longitudinal
Bakken	0-4,691	0-4,481	3,485	1,126	Longitudinal	Longitudinal
Fayetteville	No window	No window	< 0	< 0	–	Longitudinal
Haynesville	0-780	0-397	62	209	Longitudinal	Longitudinal
Niobrara	0-1,735	0-741	531	389	–	Longitudinal
Marcellus	0-4,615	0-4,376	3,411	2,292	–	–
Vaca Muerta	0-3,627	0-3,535	2,719	1,850	Longitudinal	Longitudinal

[a] PPA: along S_{Hmax} and S_v for a well drilled parallel to S_{hmin} in a normal and strike-slip faulting stress regime, respectively. Location where transverse fracture initiation is promoted the most.

[b] Non-PPA: along S_v and S_{Hmax} for a well drilled parallel to S_{hmin} in a normal and strike-slip faulting stress regime, respectively. Location where transverse fracture initiation is least promoted.

For the Barnett Shale example, the value of T_{crit} given by the true-3D numerical model is 2,482 psi for perforations along S_{Hmax}, which is the PPA direction (Figure 4.11). Published data on the Barnett Shale by Rybacki et al. (2015) indicates a maximum tensile

strength of ~2,500 psi, so following the modified Hossain et al. (2000)'s approximation for $\sigma_{\theta L}$ and $\sigma_{\theta T}$ (Eqs. 4.10 and 4.11), the fracture initiation observed in the Barnett Shale would most likely be transverse if p_b is kept under 4,574 psi. The Barnett Shale seems to be a special case among the seven shale plays studied, which is the only play with stress state slightly outside the allowable region for $\mu = 0.6$ (Figure 4.15) and highly favorable to transverse fracture initiation (Figure 4.13b). Furthermore, the Barnett Shale's low fracture gradient (0.6 psi/ft) ensures the p_b falls within the window of transverse fracture initiation.

For the Marcellus Shale $\sigma_{\theta T}$ and $\sigma_{\theta L}$ for both PPA and non-PPA are compressive at the reported p_b, making it impossible to determine the orientation of fracture initiation from our analysis. However, transverse initiation is more likely to occur first, because $\sigma_{\theta T}$ is less compressive than $\sigma_{\theta L}$ for $0 \leq p_w \leq p_b$ (Figure 4.17). Fayetteville Shale presents an interesting case, as $\sigma_{\theta T}$ is compressive there for the p_w range examined.

4.6   DISCUSSION

4.6.1   Effect of the Cemented Casing

As mentioned by Fallazadeh et al. (2017) and Michael et al. (2018) the presence of a cemented casing in the borehole shields the impact of the p_w on the surrounding rock formation. In the case of a good cement job, the higher Young's modulus, E of the casing is expected to suppress the stress changes caused by the p_w. The higher value of E of the steel casing and the cement layers compared to the formation's suggests that the radial displacement the wellbore experiences will be smaller compared to an openhole configuration at the same pressure.

We tried to mimic this effect by re-computing the analytical results assuming the extreme case where the hoop stresses around the wellbore are fixed at the point of cement curing. We assume this to be a balanced condition, $p_w = p_p$. These wellbore stresses still act as the "remote" loading at the perforation base with p_{perf} acting as the fracturing pressure. Using parameters of the Barnett Shale (Figure 4.18), it is apparent that the shielding effect of the cemented casing causes both $\sigma_{\theta L}$ and $\sigma_{\theta T}$ at the perforation base to become more tensile as p_{perf} increases. This implies that good cement jobs without annular leakage will be an important aid for transverse fracture initiation.
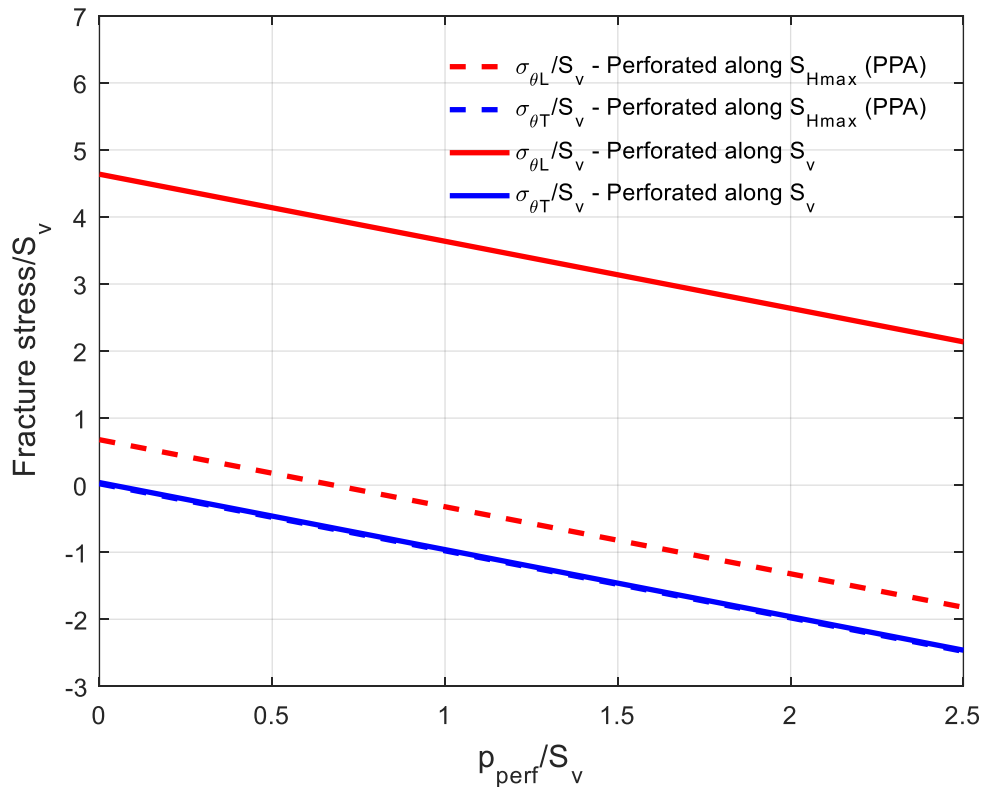
Figure 4.18. Extreme case of perfectly-cemented boreholes, showing both $\sigma_{\theta L}$ and $\sigma_{\theta T}$ becoming more tensile (at the same slope) as p_{perf} increases (for the Barnett Shale). In this case, transverse fracture initiation would always be promoted regardless of p_{perf}.

4.6.2 Impact of Natural Fractures

Interactions between induced hydraulic fractures with natural fractures were examined in experimental and numerical studies (Lee et al., 2015). The presence of a propagating hydraulic fracture may lead to either (i) crossing, (ii) divergence, or (iii) step-over, depending on various parameters such as the angle at which the fractures meet and the minerals present in the natural fracture, for instance calcite. Nonetheless, this falls into topics related to fracture propagation, beyond the scope of this study, which focuses on initiation.

Concerning fracture initiation *per se*, a natural fracture will have an impact only if it intersects the wellbore and thus the fracture initiation location. This is a rare, but possible situation and numerical modeling can be used to predict the outcome of such a unique occurrence. Nevertheless, heterogeneities in the medium, such as natural fractures should be put into consideration, especially if an unexpected result is observed. Heterogeneities induced by the presence of natural fractures, can diminish the advantages of using PPA-oriented perforations rather than a conventional phase perforation technique.

4.7 CONCLUSIONS

An orientation criterion was developed for fracture initiation from perforated wells using analytical approximations from the literature modified for porous media. The criterion was then assessed using a true-3D numerical model. The following general conclusions are reached:

- Transverse fracture initiation is a rarity occurring if p_b is within a "window," such $p_b \leq p_{b,upper}$. Numerical analysis showed that the developed orientation criterion overestimates transverse fracture initiation. The frequent occurrence of longitudinal

fracture initiation, suggests that fracture reorientation as it propagates away from the wellbore is likely field scenario.

- As p_w increases, $\sigma_{\theta T}$ is shown to become more compressive. A critical tensile strength, T_{crit} exists determining whether transverse fracture initiation is possible regardless of p_w in a given stress state. T_{crit} and $p_{b,upper}$ are maximized for perforations parallel to PPA (S_{Hmax} for normal faulting and S_v for strike-slip faulting cases).

- Application of the true-3D numerical model on seven shale plays showed transverse fracture initiation likely to occur in only one of the plays, the Barnett Shale. Values predicted by the model for the $p_{b,upper}$ and T_{crit} are given for each shale play.

- Fracturing fluid leakages around the wellbore hinder transverse fracture initiation by decreasing the p_b window. This infers that correctly performed perforations aid transverse fracture initiation.

The following recommendations are made to practitioners for enhanced promotion of transverse fracture initiation from perforated horizontal wells:

1. Slow pumping. Strategic use of slow pumping during the fracture treatment can keep $p_b \leq p_{b,upper}$.

2. Strong casing-cement sheath and cement sheath-rock formation interface bonding. This will suppress leakage of the fracturing fluid around the wellbore during the treatment, bypassing the perforations. Hence, strong interface bonding negates the impact of the perforation tunnels in promoting transverse fracture initiation.

3. An oriented perforation strategy can, under ideal circumstances, promote transverse fracture initiation by expanding the p_b window.

4. In laboratory experiments, using reservoir analogue material of low T improves the possibility of generating transverse fracture initiation.

Chapter 5. A Semi-Analytical Model for Fractures Initiated from Perforated Wells

Accurate prediction of fracture initiation pressure and orientation is paramount to the design of a hydraulic fracture stimulation treatment and is a major factor in the treatment's eventual success. In this study, closed-form analytical approximations of the fracturing stresses are used to develop orientation criteria for relative-to-the-wellbore (longitudinal or transverse), fracture initiation from perforated wells. These criteria were assessed numerically and found to overestimate the occurrence of transverse fracture initiation, which only takes place under a narrow range of conditions where the tensile strength of the rock formation is lower than a critical value and the breakdown pressure falls within a "window". For a case study performed on the Barnett Shale, transverse fracture initiation is shown to take place for breakdown pressures below 4,762 psi, provided that the formation's tensile strength is below 2,482 psi.

A robust 3D finite volume numerical model is used to evaluate solutions for the longitudinal and transverse fracturing stresses for a variable wellbore pressure, hence developing correction factors for the existing closed-form approximations. Geomechanical inputs from the Barnett Shale are considered for a horizontal well aligned parallel to the direction of the least compressive horizontal principal stress. The corrected numerically-derived expressions can predict initiation pressures for a specific orientation of fracture initiation. Similarly, at known breakdown pressures, the corrected expressions are used to predict the orientation of fracture initiation. Besides wellbore trajectory, the results depend on the perforation direction. For the Barnett Shale case study, which is under a normal faulting stress regime, the perforations on the side of the borehole yield a wider breakdown

---

Parts of this Chapter were presented in the following conference article: Michael, A., and Gupta, I. (2020a). A Semi-Analytical Modeling Approach for Hydraulic Fracture Initiation and Orientation in Shale Reservoirs. Unconventional Resources Technology Conference. Jul 20, doi:10.15530/urtec-2020-3137.

pressure window by 71% and higher critical tensile strength by 32.5%, compared to perforations on top of the borehole, implying better promotion of transverse fracture initiation. Leakage of fracturing fluid around the wellbore, between the cemented casing and the surrounding rock, reduces the breakdown pressure window by 11% and the critical tensile strength by 65%.

Dimensionless plots are employed to present the range of *in-situ* stress states where longitudinal or transverse hydraulic fracture initiation is promoted. This is useful for completion engineers; when targeting low permeability formations such as shale reservoirs, multiple transverse fractures must be induced from the horizontal wells, as opposed to longitudinal fracture initiation, which is desired in higher permeability reservoirs or frac-and-pack operations.

5.1   INTRODUCTION

Exploitation of tight shale reservoirs is made possible by the generation of multiple transverse fractures from horizontal wells during stimulation treatments. The primary objective of this treatment is to create high permeability/high surface area conduits for reservoir fluids to flow into the wellbore (Clark, 1949). The resultant fracture geometric dimensions are primarily dependent on the *in-situ* stress state (Li et al., 2018; 2020) with fracture propagation being significantly influenced from interactions with natural fractures (Zhang et al., 2019) weak bedding planes in multi-layered formations (Tang et al., 2018; 2019). The high cost of hydraulic fracture treatments encourages operators in seeking the maximum possible productivity from their wells in the post-stimulation period. Accurate prediction of fracture initiation pressure, p_i and the orientation of fracture initiation are paramount for engineering an efficient fracture treatment achieving maximum well

productivity at the lowest cost. Current models involving closed-form analytical approximations have however not effectively estimated p_i, failing to match observations from laboratory and field-scale studies.

In this study, a 3D finite volume numerical model is employed to evaluate correction factors for analytical approximations from the literature (Hossain et al., 2000, later modified by Michael et al., 2018). Tangential stresses at two extreme points around the base of the perforation are evaluated for transverse and longitudinal fracture initiation with respect to the wellbore. Considering the presence of a microannulus between the cement layer and the formation prior to fracture initiation (Behrmann and Elbel, 1991; Zhang et al., 2018), the well is modeled as an openhole completion intersected by one cylindrical-shaped perforation. Brittleness is an important rock feature, related to its mechanical behavior. An accurate evaluation of rock brittleness places an analytical foundation of drilling and reservoir stimulation via hydraulic fracturing. The independent variables are the far-field (*in-situ*) principal stresses, wellbore pressure, p_w and the rock formation's mechanical properties that control its brittleness (Li et al., 2017) with all influencing p_i, which is the p_w at which the tensile failure criterion is exceeded by the tangential stress on the perforation base, which is the presumed location of fracture initiation. This is supported by observations from laboratory studies from Behrmann and Elbel (1991) and Zhang et al. (2018).

The semi-analytical modeling approach developed in this work is then applied on a case study for the Barnett Shale, which is under a strong normal faulting stress state. A true-3D numerical model is used to evaluate correction factors for fracture treatments in perforated horizontal wells. Subsequently, breakdown pressure, p_b, values from the literature are used for predicting p_i and the orientation of fracture initiation (longitudinal or transverse). Besides wellbore trajectory, which for this study is set parallel to the least

compressive (minimum) horizontal stress, S_{hmin}, the results are dependent on the perforation direction. For horizontal wells drilled parallel to S_{hmin} in normal faulting regimes, the preferred perforation alignment ("PPA", after Michael and Gupta, 2019) for promoting transverse fracture initiation is parallel to S_{Hmax} on the side of the borehole.

Finally, following stimulation, fracture orientation controls the resulting productivity from tight shale reservoirs. Transverse fracture initiation, although a rarity, bears some significant advantages over longitudinal fracture initiation regarding post-stimulation well productivity (Economides and Martin, 2010). Contrary, longitudinal fracture initiation leads to higher productivity in higher permeability zones and frac-and-pack operations (Economides and Martin, 2010). The fracture initiation plane is often dissimilar to the final fracture propagation plane (Daneshy, 1973; Weijers, 1995; Alabbad, 2014; Michael, 2016b). Stress interference in the near-wellbore region caused by the presence of the wellbore may lead to fracture initiation at a different orientation plane than the one dictated by the far-field stresses. Thus, favorable well trajectory (parallel to S_{hmin}) does not guarantee transverse fracture initiation (Hossain et al., 2000; Michael, 2019a; Michael and Gupta, 2020b).

The presented semi-analytical modeling approach is also used to indicate the range of conditions for which transverse fracture initiation will be promoted for the *in-situ* stress conditions under consideration. Fracture reorientation, which is promoted from longitudinal fracture initiation in wells aligned with the minimum horizontal *in-situ* principal stress (El Rabaa, 1989; Hallam and Last, 1991; Owens et al., 1992; Weijers, 1992; Olson, 1995) causes near-wellbore tortuosity (Huang et al., 2020; Michael et al., 2020). This in turn triggers completion and production-related problems (Barree and Miskimins, 2015; Michael et al., 2020), such as early screenouts and poor well productivity following the stimulation treatment.

5.2 THEORETICAL BACKGROUND

5.2.1 Fracture Initiation and Orientation

During a hydraulic-fracture treatment, the bottomhole pressure (BHP) and injection flowrate are monitored (Zoback et al., 2003; Huang et al., 2020). At a steady injection flowrate, BHP increases linearly with time until a point where the increase becomes non-linear when the injected fracturing fluid begins leaking into the formation (Figure 5.1). The pressure at which the fluid leakage into the rock starts is called the leak-off pressure (LOP) and can be measured at the field reliably using data from "leak-off tests" (Dontsov, 2016; Huang et al., 2020). Despite the leak-off, the BHP carries on building up until the breakdown which is manifested as a sudden, distinct drop (Figure 5.1) from the p_b of the rock which is the maximum pressure attained during a fracture treatment. Fracture initiation occurs at p_i once the crack starts forming in the $LOP \leq p_i \leq p_b$ range. Any further injection beyond breakdown, makes a fracture propagate from the induced crack.

In horizontal wells, the fractures initiated can assume two bounding orientations with respect to the wellbore axis – longitudinal (or "axial"), which is parallel to the axis, or transverse (or "lateral"), orthogonal to the axis (Figure 5.2a). This study focuses on fracture orientation in the early initiation stages, within a small region near the wellbore, which is more challenging to predict than the fracture orientation in the later propagation stages outside this near-wellbore region, which is dominated by the well trajectory compared to the *in-situ* stress state.
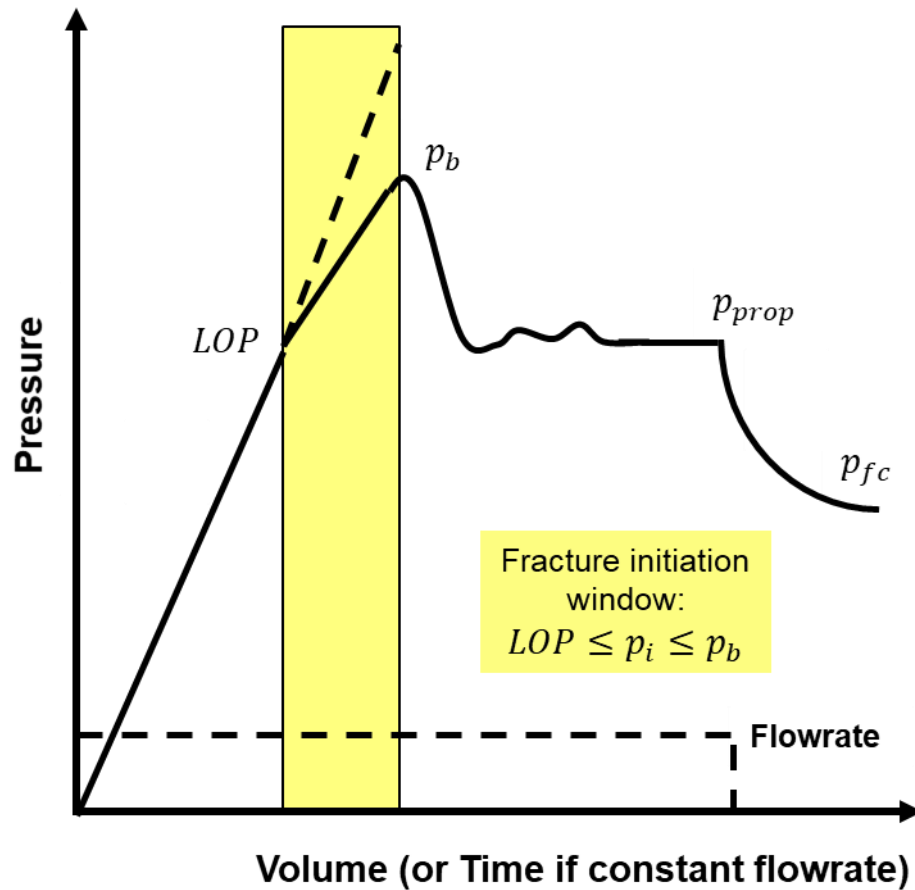
Figure 5.1.   BHP variation during time during a typical fracture treatment (modified from Zoback et al., 2003).

Hubbert and Willis (1957) famously concluded that the final fracture propagation plane is perpendicular to the least compressive stress, known as the preferred fracture plane (PFP), which solely depends on the well trajectory compared to the *in-situ* principal stresses. Hence, a well parallel to the least compressive horizontal stress S_{hmin} (a common industry practice), is expected to yield transverse final fracture propagation. Nevertheless, drilling the well along S_{hmin} does not guarantee that the fracture initiation plane will also be transverse-to-the wellbore.

141

Localized stress changes in the near-wellbore region induced from the presence of the borehole, means that the fracture initiation plane is not always parallel to PFP (Daneshy, 1973; Barree and Miskimins, 2015; Michael et al., 2018; Michael, 2019a). Potential longitudinal fracture initiation from a horizontal well in a tight shale reservoir bears significant practical problems, which can alter the outcome of a hydraulic fracture treatment. First, fracture reorientation can occur away from the wellbore influenced by the far-field principal stresses (El Rabaa, 1989; Hallam and Last, 1991; Owens et al., 1992; Weijers, 1992; Olson, 1995). This in turn increases the tortuosity (Huang et al., 2020) in the near-wellbore region (Figure 5.2a) leading to completion-related problems such as early screenouts (Michael et al., 2020).

Additionally, results from tracer testing performed during a multi-stage fracture treatment (Barree and Miskimins, 2015) have indicated presence of fracturing fluid from neighboring stages despite stage isolation with packers (Figure 5.2b). Barree and Miskimins (2015) interpreted this by the presence of longitudinal fractures that extended beyond the stage lengths. The aforementioned completion-related problems result in poor stimulated-well productivity and thus loss of net present value (NPV) for the hydraulic fracture treatment (Balen et al., 1988; Michael, 2019b).
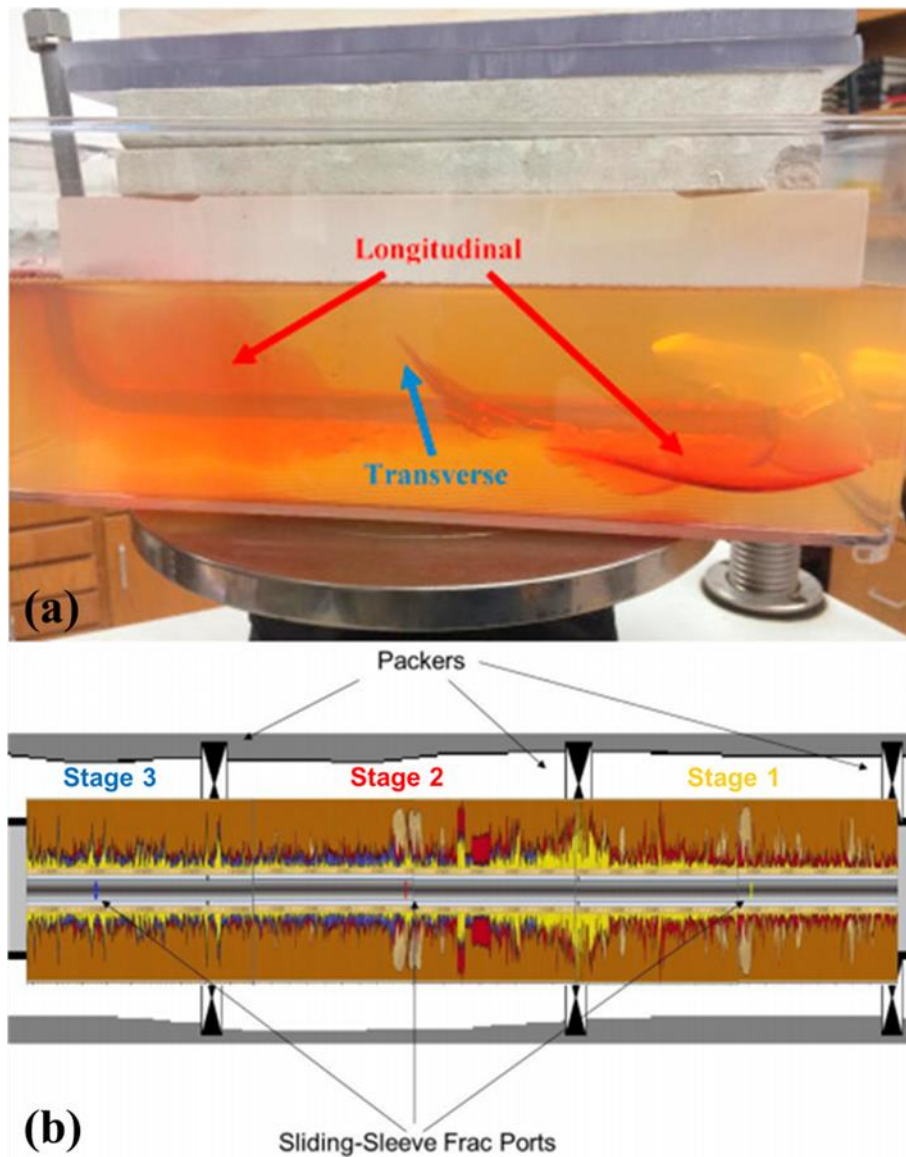
Figure 5.2. (a) Longitudinal and transverse fractures initiated from a perforated horizontal well during scaled laboratory experiments in highly concentrated gelatin polymer, with visible tortuosity in the near-wellbore region (modified from Michael, 2016b). (b) Schematic showing the results of a tracer test during a multi-stage fracture treatment. Fracturing fluid from each of the three stages was detected in neighboring stages, despite all stages being isolated from each other with packers (modified from Barree and Miskimins, 2015). This is attributed to longitudinal fracture initiation – prior to reorientation to transverse – where the longitudinal fractures initiated extend beyond the stage length.

143

5.2.2 Stresses around a Horizontal Well

Kirsch (1898) derived analytical solutions for the stress concentrations on a 2D plate, with a circular cavity under uniform tension in a linearly elastic medium. Hubbert and Willis (1957) modified those solutions to incorporate biaxial stress loading and fluid pressure inside the hole. For a horizontal well drilled parallel to the y-axis, along S_{hmin} and perpendicular to the overburden and most compressive (maximum) horizontal principal stress (S_v and S_{Hmax}, respectively) in a homogeneous, isotropic rock, the stresses on the wellbore radius, $r = r_w$, with r being the radial distance from the center of the wellbore, are defined analytically (after Zoback, 2007) by

$$\sigma_{yy}\big|_{r=r_w} = S_{hmin} - 2\nu(S_v - S_{Hmax})\cos 2\theta - p_p \tag{5.1}$$

$$\sigma_{\theta\theta}\big|_{r=r_w} = S_{Hmax} + S_v - 2(S_v - S_{Hmax})\cos 2\theta - p_p - p_w \tag{5.2}$$

$$\sigma_{rr}\big|_{r=r_w} = p_w - p_p \tag{5.3}$$

$$\sigma_{r\theta}\big|_{r=r_w} = 0 \tag{5.4}$$

where θ is the angle measured clockwise from the S_v orientation, σ_{yy} is the axial stress parallel to the wellbore, $\sigma_{\theta\theta}$ is the tangential (also called circumferential or "hoop") stress, σ_{rr} is the radial stress, and $\sigma_{r\theta}$ is the shear stress, which is zero on the wellbore radius (Figure 5.3).

144
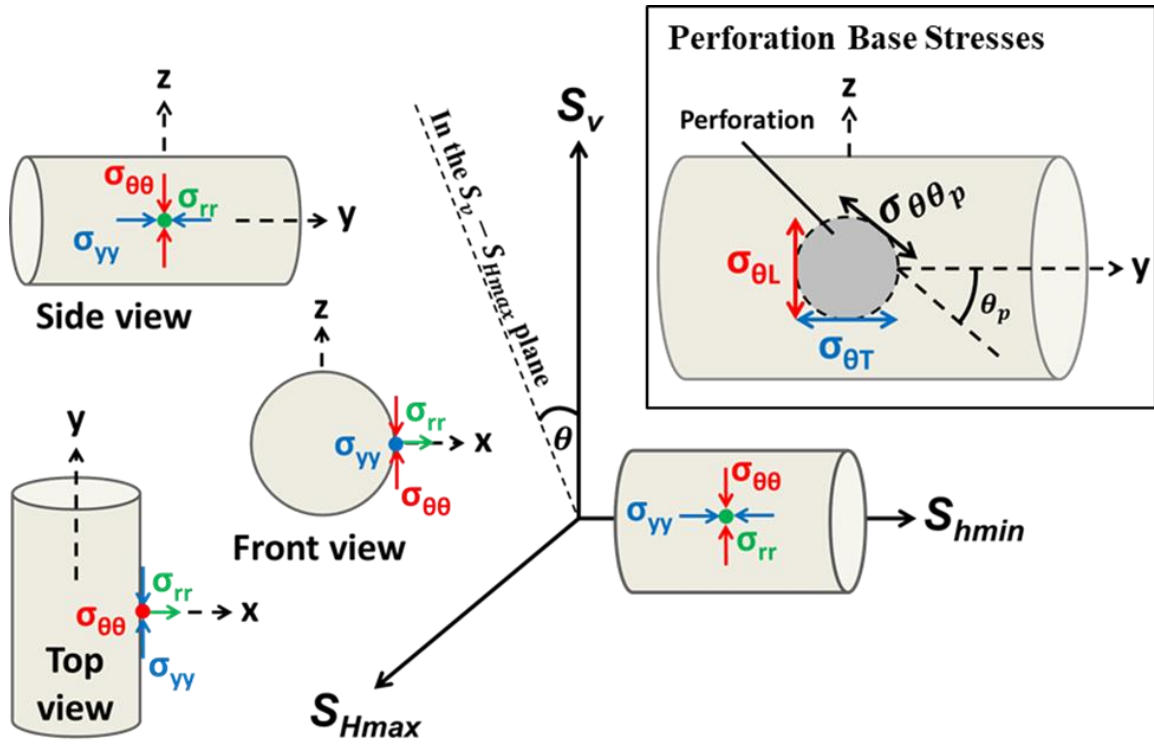
Figure 5.3. Visual representation of the main parameters and symbols used in equations in this study. The configuration of the stresses on the wellbore radius ($\sigma_{\theta\theta}$, σ_{yy}, and σ_{rr}) of a horizontal well parallel to S_{hmin} (y-axis) and the stresses on the perforation base ($\sigma_{\theta L}$ at $\theta_p = 90°$ and $\sigma_{\theta T}$ at $\theta_p = 0°$) for perforations on the side of the borehole (x-axis, $\theta = 90°$) is shown. At $r = r_w$, $\sigma_{r\theta} = 0$, which is not shown on the schematic (from Michael et al., 2020).

5.3   MODEL DEVELOPMENT

5.3.1   Analytical Derivation

Assuming that fracture initiation occurs at the perforation base (after Behrmann and Nolte, 1998) and that a microannulus exists along the cement sheath-rock formation interface (after Behrmann and Elbel, 1991; Zhang et al., 2018), Hossain et al. (2000) derived closed-form expressions for the longitudinal and transverse fracturing stresses ($\sigma_{\theta L}$

145

and $\sigma_{\theta T}$, respectively) for perforated wells. The pressure in the perforation tunnel is assumed to be equal to p_w.

Considering the perforation as a pressurized cylindrical cavity, which orthogonally intersects the wellbore – a bigger pressurized cylindrical cavity – Hossain et al. (2000) used a second "Kirsch analysis" to approximate the tangential stress on the perforation base, $\sigma_{\theta\theta_p}$. Michael et al. (2018) modified the $\sigma_{\theta\theta_p}$ expression to incorporate p_p effects. Using the expressions of σ_{yy} and $\sigma_{\theta\theta}$ at $r = r_w$ (Eqs. 5.1 and 5.2) yields

$$\sigma_{\theta\theta_p} = \sigma_{\theta\theta}|_{r=r_w} + \sigma_{yy}\big|_{r=r_w} - 2\left(\sigma_{yy}\big|_{r=r_w} - \sigma_{\theta\theta}|_{r=r_w}\right)\cos 2\theta_p + p_p - p_w \quad (5.5)$$

where θ_p is the angle on the perforation base measured from the σ_{yy} direction (Figure 5.3). The magnitude of $\sigma_{\theta\theta p}$ at $\theta_p = 0°$ (Figure 5.3) represents the stress needed to be overcome in tension for longitudinal fracture initiation to take place and is hence known as the longitudinal fracturing stress, $\sigma_{\theta L}$ (Eq. 5.6). Similarly, the magnitude of $\sigma_{\theta\theta p}$ at $\theta_p = 90°$ (Figure 5.3) represents the stress necessary for transverse fracture initiation to take place and is called the transverse fracturing stress, $\sigma_{\theta T}$ (Eq. 5.7). If the horizontal well is perforated along S_{Hmax}, then $\theta = 90°$, the expressions for $\sigma_{\theta L}$ and $\sigma_{\theta T}$ simplify to

$$\sigma_{\theta L} \equiv \sigma_{\theta\theta_p}\Big|_{\theta=90°,\theta_p=0°}$$
$$= 9S_v - 3S_{Hmax} - S_{hmin} + 2v(S_{Hmax} - S_v) - p_p - 4p_w \quad (5.6)$$

$$\sigma_{\theta T} \equiv \sigma_{\theta\theta_p}\Big|_{\theta=90°,\theta_p=90°}$$
$$= 3S_{hmin} - S_{Hmax} - S_v - (2 - 6v)(S_v - S_{Hmax}) - p_p \quad (5.7)$$

146

A parallel designation can be made for a perforation at the top of the borehole (at $\theta = 0°$, parallel to S_v), by interchanging the S_v and S_{Hmax} terms in Eqs. 5.6 and 5.7.

The Barnett Shale is a gas formation of Mississippian age located in the Fort Worth Basin of Texas. The payzone is located at an average depth of 6,500 ft and is characterized as having a normal faulting stress regime (Moos, 2012). Table 5.1 summarizes the stress parameters and mechanical properties of the Barnett Shale, used as an application example throughout this study.

Table 5.1.   Input parameters for the Barnett Shale in Texas.

Parameter	Symbol	Value
Payzone depth	D_{pay}	5,000-8,000 ft
Overburden stress	S_v	7,215 psi
Maximum horizontal principal stress	S_{Hmax}	4,550 psi
Minimum horizontal principal stress	S_{hmin}	3,900 psi
Formation pore pressure	p_p	3,055 psi
Elastic Young's modulus	E	2×10^5 psi
Poisson's ratio	v	0.23-0.32
Tensile strength	T	~ 0

The variation of the two fracturing stresses, $\sigma_{\theta L}$ and $\sigma_{\theta T}$, with p_w (which by the second assumption is equal to p_{perf}) is considered. Hossain et al.'s (2000) analytical approximation – followed by Michael et al.'s (2018) modification – shows $\sigma_{\theta T}$ being independent from p_w, remaining at a constant value as p_w increases (Eq. 5.7), contrary to $\sigma_{\theta L}$ which becomes more tensile (negative) as p_w increases (Eq. 5.8). Assuming that the rock formation's tensile strength, $T = 0$, and $\sigma_{\theta T}$ independent from p_w, transverse fracture initiation occurs as $\sigma_{\theta T} < 0$ and $\sigma_{\theta T} < \sigma_{\theta L}$, conditions which exist between $p_w = 0$ and

the finite p_w value at which $\sigma_{\theta T} = \sigma_{\theta L}$. This p_w range was defined as the "breakdown pressure window" first by Michael et al. (2018). The upper-limit of the p_b window is indicated by $p_{b,upper}$. A pair of expressions for calculating $p_{b,upper}$ is presented later (Eqs. 5.10a or 5.10b), depending on the *in-situ* stress state in question. If $p_b < p_{b,upper}$, transverse fracture initiation is promoted. This is a paramount constraint, because the practitioners on the surface can, to an extent, impact p_b. Lower pressurization rates suppress p_b for a given *in-situ* state, compared to higher pressurization rates (Zoback et al., 1977; Weijers, 1995). Thus, low pressurization rates can be strategically used to ensure $p_b \leq p_{b,upper}$ and that transverse fracture initiation is promoted.

The Kirsch's (1898) theory is a purely 2D theory, developed assuming a state of plane strain. Hossain et al.'s (2000) idea of applying the Kirsch analysis twice in an attempt to simulate a 3D problem could not yield exact solutions for $\sigma_{\theta L}|_{p_w}$ and $\sigma_{\theta T}|_{p_w}$. Based on this, Hossain et al.'s (2000) closed-form analytical expressions (Eqs. 5.6 and 5.7) are referred to as the "approximated" solutions of the two fracturing stresses ($\sigma_{\theta L}$ and $\sigma_{\theta T}$). Numerical assessment performed using finite volume modeling (Michael et al., 2018; 2020; Michael, 2019a) however, found these approximated solutions to be insufficient in predicting the actual 3D solutions for $\sigma_{\theta L}|_{p_w}$ and $\sigma_{\theta T}|_{p_w}$.

5.3.2   Perforation Direction and Preferred Perforation Alignment

The preferred perforation alignment (PPA) is a concept introduced by Michael and Gupta (2019), referring to the perforation direction which is optimal for the promotion of favorable orientation of fracture initiation (along PFP). For a horizontal well drilled parallel to S_{hmin}, this favorable orientation would be transverse to the wellbore. For a given *in-situ* stress state, the p_b window is maximized for perforations parallel to the PPA direction. The

PPA direction (Figure 5.4a) was shown (Michael and Gupta, 2019; 2020) to depend solely on the *in-situ* stress regime (Anderson, 1951). For normal faulting stress states as the Barnett Shale, PPA is parallel to S_{Hmax} (side of the borehole, at $\theta = 90°$), whereas for strike-slip faulting stress states as the Marcellus Shale (Michael and Gupta, 2019; 2020), PPA is parallel to S_v (top of the borehole at $\theta = 0°$).

The preferred perforation alignment (PPA) is a concept introduced by Michael and Gupta (2019), referring to the perforation direction which is optimal for the promotion of favorable orientation of fracture initiation (along PFP). For a horizontal well drilled parallel to S_{hmin}, this favorable orientation would be transverse to the wellbore. For a given *in-situ* stress state, the p_b window is maximized for perforations parallel to the PPA direction. The PPA direction (Figure 5.4a) was shown (Michael and Gupta, 2019; 2020) to depend solely on the *in-situ* stress regime (Anderson, 1951). For normal faulting stress states as the Barnett Shale, PPA is parallel to S_{Hmax} (side of the borehole, at $\theta = 90°$), whereas for strike-slip faulting stress states as the Marcellus Shale (Michael and Gupta, 2019; 2020), PPA is parallel to S_v (top of the borehole at $\theta = 0°$).

S_v: Preferred perforation alignment (PPA) for the Marcellus Shale at which $p_{b,upper}$ and T_{crit} are maximized and at which p_i is the lowest.

Perforations

Wellbore

S_{hmin} (into the plane)

Preferred fracture plane (PFP)

S_{Hmax}: Perforation direction (non-PPA) at which $p_{b,upper}$ and T_{crit} are minimum and at which p_i is the highest for the Marcellus Shale.

Vertical section

S_v

S_{hmin}

S_{Hmax}

(i) Oriented perforating on the top of the borehole (along $S_v, \theta = 0°$)

(ii) Oriented perforating on the side of the borehole (along $S_{Hmax}, \theta = 90°$)

(a)　　　　　　　　　　　　　　　(b)

Figure 5.4.　(a) Configurations for the preferred perforation alignment (PPA) in horizontal wells drilled parallel to S_{hmin} under normal or strike-slip faulting stress regime (from Michael and Gupta, 2020). The PFP for a horizontal well drilled parallel to S_{hmin} is orthogonal to the wellbore. (b) Oriented perforating configurations for horizontal wells drilled parallel to S_{hmin} in locations under stress regimes that honor Anderson's (1951) theory.

For reverse faulting stress regime, where $S_{Hmax} > S_{hmin} > S_v$, the PFP is perpendicular to the least compressive stress, which is S_v. This implies that transverse fracture initiation in reverse faulting stress states is best promoted from vertical wells with the PPA direction being that of S_{hmin}. Nevertheless, multiple transverse fractures is generally not an objective in vertical wells, drilled through horizontal geologic formation layers, where longitudinal fractures are the most efficient stimulation option (Economides and Martin, 2010; Yang, 2014).

5.3.3 Numerical Correction

A "true-3D" numerical model based on those from Michael et al. (2018; 2020) and Michael (2019a) was used to calculate solutions for $\sigma_{\theta L}|_{p_w}$ and $\sigma_{\theta T}|_{p_w}$. The model (Figure 5.5) was built on *FLAC³D* (*Fast-Lagrangian Analysis of Continua in 3 Dimensions*) which uses explicit finite volume formulations to simulate non-linear mechanical behavior involving high degrees of displacement (Itasca Consulting Group, 2009 for Version 4.0) The mechanics of the modeled solid medium are derived from definitions of stress and displacement (strain) with constitutive relationships describing the behavior of the material. The resulting partial differential equations (PDEs) relate mechanical stress to induced strain and vice versa and are solved under the specified boundary and initial conditions.

The true-3D numerical model consists of a $1/8^{\text{th}}$ square block of length, L, height, H, and width, W, which are 16 times larger than r_w, where r_w is 6 times larger than the perforation radius r_{perf}. The perforation tunnel length, l_{perf}, is 1.8 times larger than r_w (Figure 5.5). The true-3D numerical model is designed to model blocks of dimensions fixed at the aforementioned relative geometry and is applicable to any multiples of the example set of geometric dimensions summarized on Table 5.2 for a case of a block model with $r_w = 4$ in. Michael et al. (2018) found $\sigma_{\theta\theta_p}$ (and subsequently $\sigma_{\theta L}$ and $\sigma_{\theta T}$) to be more sensitive to r_{perf} than l_{perf}, unlike Hossain et al's (2000) approximations, where $\sigma_{\theta\theta_p}$ was completely independent of the perforation's geometry as long as the perforation cavity is cylindrical. Hence, both r_{perf} than l_{perf} were fixed such that their ratio with r_w is comparable to field-scale operations.
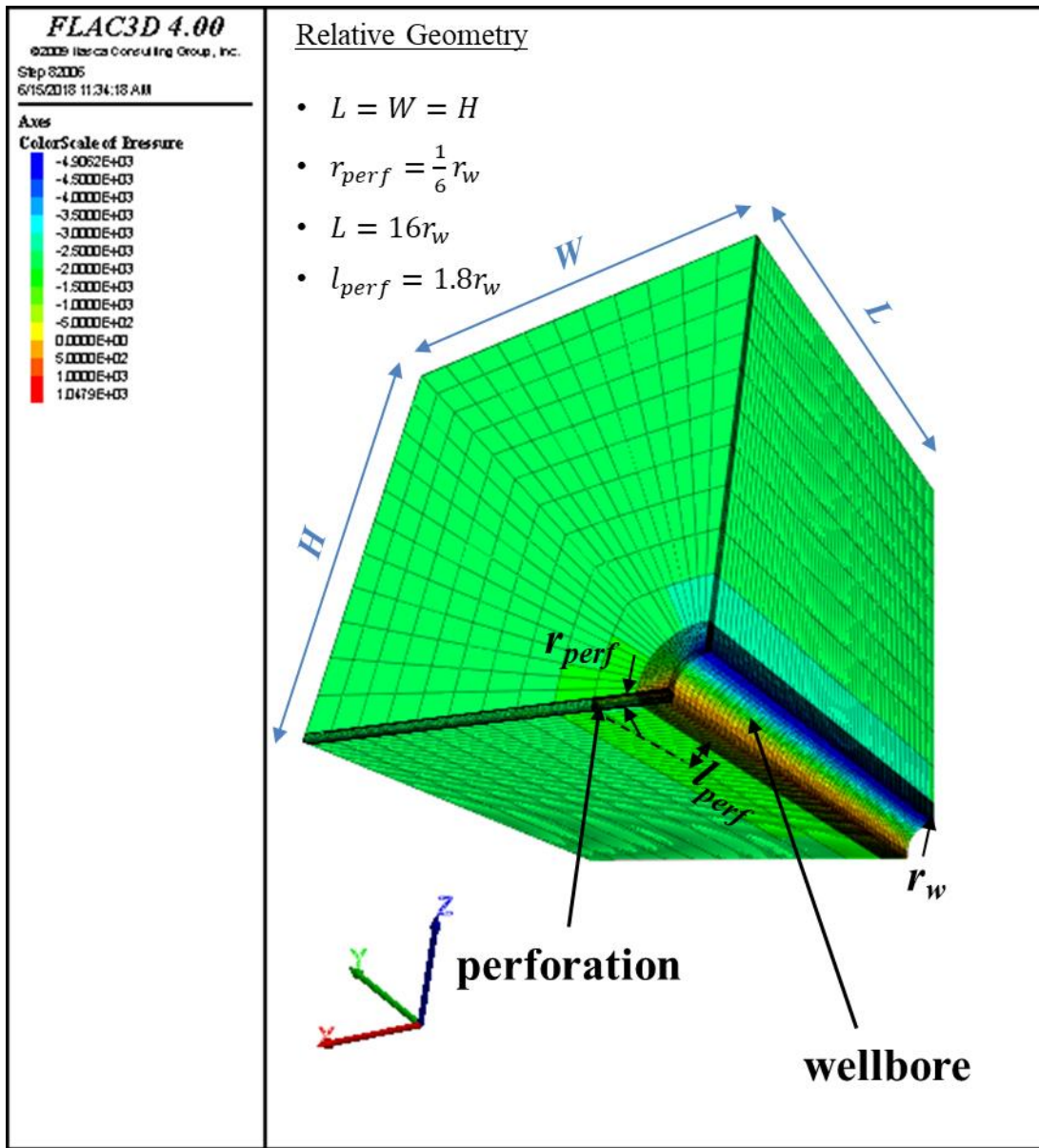
Figure 5.5. The true-3D numerical model written in *FLAC³ᴰ* and based on those from Michael et al. (2018; 2020) was used to calculate $\sigma_{\theta L}|_{p_w}$ and $\sigma_{\theta T}|_{p_w}$ for the Barnett Shale.

The fundamental assumptions of Hossain et al. (2000) are honored, thus the well is modeled as an openhole completion intersected orthogonally by a single perforation tunnel

which is pressurized at p_w. The stress field on the perforation base is evaluated at a varying p_w for the *in-situ* parameters on Table 5.1. The verification of the true-3D numerical model against analytical solutions was presented by Michael et al. (2018).

Table 5.2.   Absolute geometric dimensions of the true-3D numerical model for a presumed $r_w = 4$ in.

Parameter	Symbol	Value
Wellbore radius	r_w	4 in
Perforation radius	r_{perf}	$\frac{2}{3}$ in
Perforation length	l_{perf}	$7\frac{1}{5}$ in
Block height	H	$5\frac{1}{3}$ ft
Block length	L	$5\frac{1}{3}$ ft
Block width	W	$5\frac{1}{3}$ ft

Numerical simulations from Michael (2019a) showed that for the same p_w range, the stresses at the base of the perforation (i.e., the fracturing stresses, $\sigma_{\theta L}$ and $\sigma_{\theta T}$) differ considerably from the values calculated using the closed-form analytical approximations from Hossain et al. (2000), later modified for incorporating p_p effects by Michael et al. (2018). Unlike the predictions of the closed-form analytical approximations, $\sigma_{\theta T}$ is not independent from p_w variations. The numerical solutions suggest a positive relationship between $\sigma_{\theta T}$ and p_w (Figure 5.6a and 5.6b), with $\sigma_{\theta L}$ still becoming more tensile as p_w increases, but at a shallower slope compared to the prediction of the closed-form analytical approximation (Hossain et al., 2000).
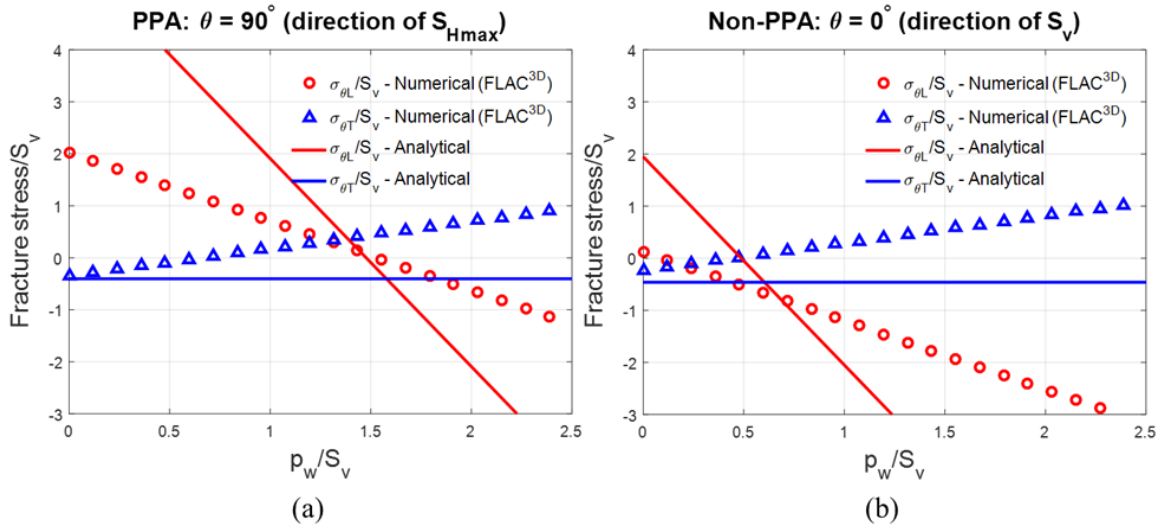
Figure 5.6. Comparison between the solutions of the two fracturing stresses ($\sigma_{\theta L}$ with red and $\sigma_{\theta T}$ with blue) according to the modified analytical expressions (Hossain et al., 2000 modified by Michael et al., 2018 to incorporate p_p effects) shown by the solid lines, against the true-3D numerical solutions shown by the triangular and circular points.

Hossain et al.'s (2000) model was based on closed-form approximations and did not involve a full 3D analysis. It considered the wellbore and the perforation as pressurized cylinders with the stress field around the wellbore not affected by the stress field around the perforation and vice versa. This rendered the resulting expressions (Eqs. 5.6 and 5.7) to be heavily approximated. Additionally, unlike the true-3D numerical model, the Hossain et al.'s (2000) model was independent of the dimensions of the perforation tunnel (r_{perf} and l_{perf}), barring its cylindrical shape. The verification process of the true-3D numerical model, presented by Michael et al. (2018; 2020) and Michael (2019), enhances our confidence on our numerical results. Increased compression with increasing p_w for $\sigma_{\theta T}$ was interpreted to be induced by the strong interaction between the radial stresses around the wellbore and around the perforation (Michael et al., 2020). The way those radial

154

stresses mutually interact alters the stress field around the wellbore, which in turn affects the magnitude of $\sigma_{\theta\theta_p}\big|_{\theta_p}$ from which $\sigma_{\theta L}$ and $\sigma_{\theta T}$ are calculated.

Using the results of the true-3D numerical simulations for the Barnett Shale case study (Figure 5.6a and 5.6b), the linear correction factors shown on Table 5.3 are derived. C_m is the correction factor for the slope of the $\sigma_{\theta L}$ or $\sigma_{\theta T}$ line versus p_w, and C_c is the correction factor on the vertical intercept at $p_w = 0$.

$$
\sigma_{\theta L}\big|_{\theta=90°} = 9S_v - 3S_{Hmax} - S_{hmin} + 2\nu(S_{Hmax} - S_v) - p_p - 4p_w
$$
$$
+ [C_m]_{\sigma_{\theta L}|_{\theta=90°}} p_w + [C_c]_{\sigma_{\theta L}|_{\theta=90°}}
\tag{5.8}
$$

$$
\sigma_{\theta T}\big|_{\theta=90°} = 3S_{hmin} - S_{Hmax} - S_v - (2 - 6\nu)(S_v - S_{Hmax}) - p_p
$$
$$
+ [C_m]_{\sigma_{\theta T}|_{\theta=90°}} p_w + [C_c]_{\sigma_{\theta T}|_{\theta=90°}}
\tag{5.9}
$$

where $[C_m]_{\sigma_{\theta L}|_{\theta=90°}}$ and $[C_c]_{\sigma_{\theta L}|_{\theta=90°}}$ are the correction factors for $\sigma_{\theta L}|_{p_w}$ and $[C_m]_{\sigma_{\theta T}|_{\theta=90°}}$ and $[C_c]_{\sigma_{\theta T}|_{\theta=90°}}$ are the correction factors for $\sigma_{\theta T}|_{p_w}$ for a horizontal well parallel to S_{hmin}, perforated along $\theta = 90°$. Similar expressions with their respective correction factors C_m or C_c can be written for any well trajectory, as well as perforation direction; corresponding $\sigma_{\theta L}|_{p_w}$ and $\sigma_{\theta T}|_{p_w}$ expressions for $\theta = 0°$ are obtained by interchanging S_v and S_{Hmax} in Eqs. 5.8 and 5.9. In all shale play case studies presented by Michael et al. (2020), the exact numerical solutions of $\sigma_{\theta L}$ and $\sigma_{\theta T}$ calculated were found to vary linearly with p_w. Nevertheless, due to the non-linear nature of the stress interactions between the wellbore and the perforation, linear correction factor sets as used in Eqs. 5.8 and 5.9 may not be sufficient in adequately describing the $\sigma_{\theta L}|_{p_w}$ and $\sigma_{\theta T}|_{p_w}$ relationships. However, for the scope of this study, which centers on the development of a modeling approach, Eqs. 5.8 and 5.9 modified using the correction factor set on Table 5.3 yields 100% match with the exact numerical solutions for the Barnett Shale as per Michael et al. (2020).

Table 5.3. Correction factor set (*vis-à-vis* Eqs. 5.8 and 5.9) developed for the Barnett Shale.

	C_m	C_c	Perforation direction
$\sigma_{\theta L}\|_{\theta=0°}$	2.6752	-41,726.3	Non-PPA
$\sigma_{\theta T}\|_{\theta=0°}$	0.5226	1,657.6	Non-PPA
$\sigma_{\theta L}\|_{\theta=90°}$	2.6794	-28,013.4	PPA
$\sigma_{\theta T}\|_{\theta=90°}$	0.5221	851.2	PPA

5.4   PRACTICAL UTILITY AND LIMITATIONS OF THE SEMI-ANALYTICAL MODEL

5.4.1   Application Case Study on the Barnett Shale

The semi-analytical model presented in the previous section, can be used for predicting p_i and the associated orientation of fracture initiation in a given basin. The following subsections demonstrate an example application of the model on the Barnett Shale.

5.4.1.1 Orientation Prediction for Fracture Initiation

Numerical simulations using the true-3D model (Figure 5.6 and 5.7) indicated $\sigma_{\theta T}$ becoming more compressive (positive using the convention followed in this study) with increasing p_w. Starting from a tensile (negative) value at $p_w = 0$, $\sigma_{\theta T}$ increases linearly with p_w yielding narrower p_b windows (yellow-shaded regions on Figures 5.7a and 5.7b) than what the modified Hossain et al.'s (2000) analytical approximations (Eqs. 5.6 and 5.7) yield. Quantitative comparisons between the modified Hossain et al.'s (2000) approximations and exact numerical solutions are discussed in Michael et al. (2018; 2020).
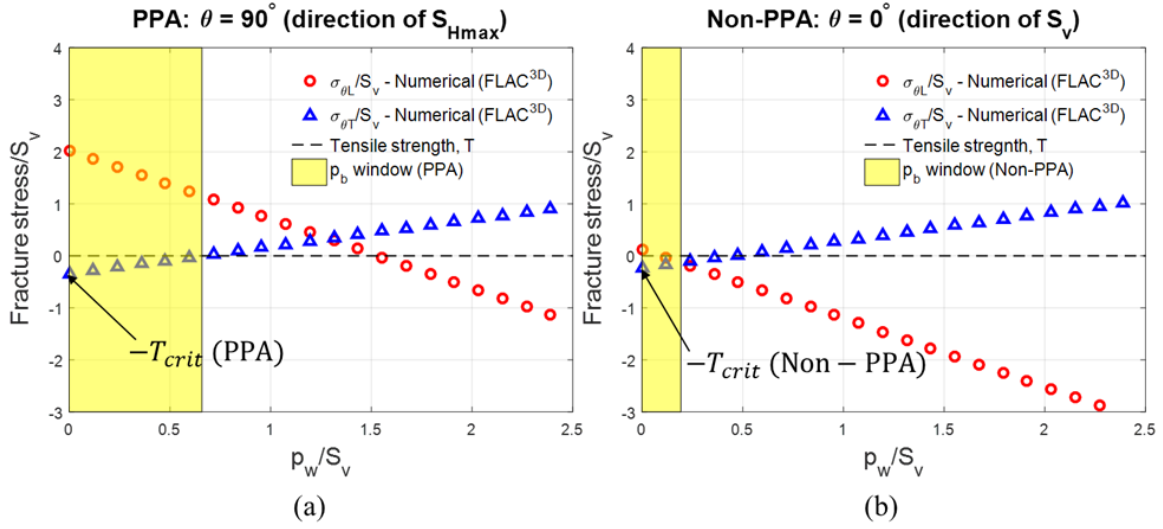
Figure 5.7. The two constraints to transverse fracture initiation; breakdown pressure window and critical tensile strength for two extreme perforation directions (PPA and non-PPA) from a horizontal well in the Barnett Shale drilled parallel to S_{hmin}. The p_b window is represented by the yellow-shaded region, while T_{crit} is given by the intercept of $\sigma_{\theta T}$ with the vertical axis. Both p_b window T_{crit} are maximized for perforations parallel to PPA and are minimized for perforations orthogonal to that in the non-PPA direction.

The p_b breakdown window for perforations parallel to PPA (Figure 5.7a) is wider than those for perforations in other directions. The p_b breakdown window is minimum for perforations perpendicular to PPA ("non-PPA" shown in Figure 5.7b). The upper-bound of the p_b breakdown window, $p_{b,upper}$, can be calculated by rearranging Eq. 5.9 to solve for $p_{b,upper}\big|_\theta = p_w$ at $\sigma_{\theta T} = -T$. For perforations along $\theta = 90°$ (PPA for normal faulting stress states), $p_{b,upper}$ is given by

$$p_{b,upper}\big|_{\theta=90°} = \frac{S_{Hmax} + S_v - 3S_{hmin} + (2 - 6v)(S_v - S_{Hmax}) + p_p - T - [C_c]_{\sigma_{\theta T}|_{\theta=90°}}}{[C_m]_{\sigma_{\theta T}|_{\theta=90°}}} \quad (5.10a)$$

where for a given *in-situ* stress state, transverse fracture initiation is promoted at $0 \leq p_b \leq p_{b,upper}$. Using the *in-situ* parameters from the Barnett Shale (Table 5.1), $p_{b,upper} = 4,762$ psi in the PPA direction (Figure 5.7a) and $p_{b,upper} = 1,393$ psi in the non-PPA direction (Figure 5.7b). For $T > 0$, the p_b window shrinks suppressing the likelihood of transverse fracture initiation for a specific stress state. Published data on the Barnett Shale by Rybacki et al. (2015) indicates an average T of ~580 psi, which would shrink the p_b windows, yielding a $p_{b,upper}$ of 3,651 psi and 283 psi from perforations in the PPA and non-PPA direction, respectively.

Nevertheless, there is a possibility that $\sigma_{\theta T}$ and $\sigma_{\theta L}$ become equal at a tensile (i.e. negative at $T = 0$) value. If this is true, then $p_{b,upper}$ is calculated by solving for the p_w at which $\sigma_{\theta T} = \sigma_{\theta L}$ (Eqs. 5.8 and 5.9) yielding

$$p_{b,upper}\big|_{\theta=90°} = \frac{[C_c]_{\sigma_{\theta T}|_{\theta=90°}} - [C_c]_{\sigma_{\theta L}|_{\theta=90°}} + 8\nu(S_v - S_{Hmax}) + 4(S_{Hmax} + S_{hmin}) - 12S_v}{[C_m]_{\sigma_{\theta T}|_{\theta=90°}} - [C_m]_{\sigma_{\theta L}|_{\theta=90°}} - 4} \qquad (5.10b)$$

for perforations along $\theta = 90°$. Unlike Eq. 5.10a, Eq. 5.10b shows no dependency of $p_{b,upper}$ on T, as it cancels out in the process of equating Eq. 5.8 and 5.9.

Furthermore, the positive slope of $\sigma_{\theta T}$ with p_w creates a second constraint to transverse fracture initiation, besides the p_b window. The intercept of $\sigma_{\theta T}$ with the vertical axis indicates the critical tensile strength, T_{crit}, defined first by Michael et al. (2018). T_{crit} represents the highest magnitude of T for the rock formation, at which transverse fracture initiation is possible; at $T > T_{crit}$, transverse fracture initiation is impossible at any p_b value. For perforations in the PPA direction ($\theta = 90°$ for a normal faulting stress regime), T_{crit} is given as

$$T_{crit}|_{\theta=90°} \equiv \sigma_{\theta T}|_{p_w=0,\theta=90°}$$
$$= 3S_{hmin} - S_{Hmax} - S_v - (2 - 6v)(S_v - S_{Hmax}) - p_p + [C_c]_{\sigma_{\theta T}|_{\theta=90°}} \quad (5.11)$$

which for the *in-situ* stresses of the Barnett Shale (Table 5.1), T_{crit} is 2,482 psi (Figure 5.7a) and 1,676 psi (Figure 5.7b) for perforations in the PPA and non-PPA directions, respectively.

For perforations parallel to PPA, both the p_b window (i.e. $p_{b,upper}$) and T_{crit} constraints are maximized, while for perforations in the non-PPA, both constraints are minimized. This enforces confidence in employing oriented perforating (Zeng et al., 2019; Huang et al., 2020) solely along S_{Hmax} in the Barnett Shale as a strategy to promote transverse fracture initiation (Figure 5.4b).

5.4.1.2 Fracture Initiation Pressure Prediction

During a fracture treatment, the pressure increases with LOP and p_b being easily distinguishable by the engineers on the surface, a range within which fracture initiation takes place. A close examination of $\sigma_{\theta L}|_{p_w}$ and $\sigma_{\theta T}|_{p_w}$ for PPA and non-PPA directions, plotted on the same graph (Figure 5.8) can help indicate the exact values of p_i. The "fracture initiation window" is defined as the p_w window within which fracture initiation takes place, such $p_p \leq p_i \leq p_b$, where p_p denotes LOP. This is separate from the definition of p_b window, which is the range of p_b values ($0 - p_{b,upper}$) within which transverse fracture initiation occurs.

For the *in-situ* state of the Barnett Shale (Table 5.1), the fracture initiation window is indicated by the yellow-shaded region on Figures 5.7a and 5.7b. Assuming that $T = 0$, pressurization of the wellbore under balanced conditions at $p_p/S_v = 0.42$, a transverse fracture(s) will initiate from the side of the borehole (parallel to S_{Hmax}, $\theta = 90°$ – the PPA

159

direction) at up to the theoretical p_w/S_v value of 0.66 (0.73 psi/ft), which is the p_w at which $\sigma_{\theta T} = 0$. Due to $p_b/S_v \cong 0.54$ (0.6 psi/ft, according to Ketter et al., 2006), the fracture initiation window is restricted within $0.42 \leq p_i/S_v \leq 0.54$ (Figure 5.8). From perforations on the top of the borehole (parallel to S_v, $\theta = 0°$ – the non-PPA direction) longitudinal fracture initiation(s) is expected all throughout the fracture initiation window ($0.42 \leq p_i/S_v \leq 0.54$), as $\sigma_{\theta L} = 0$ at $p_w/S_v = 0.09$ (0.10 psi/ft), a value much smaller than p_p (Figure 5.8).
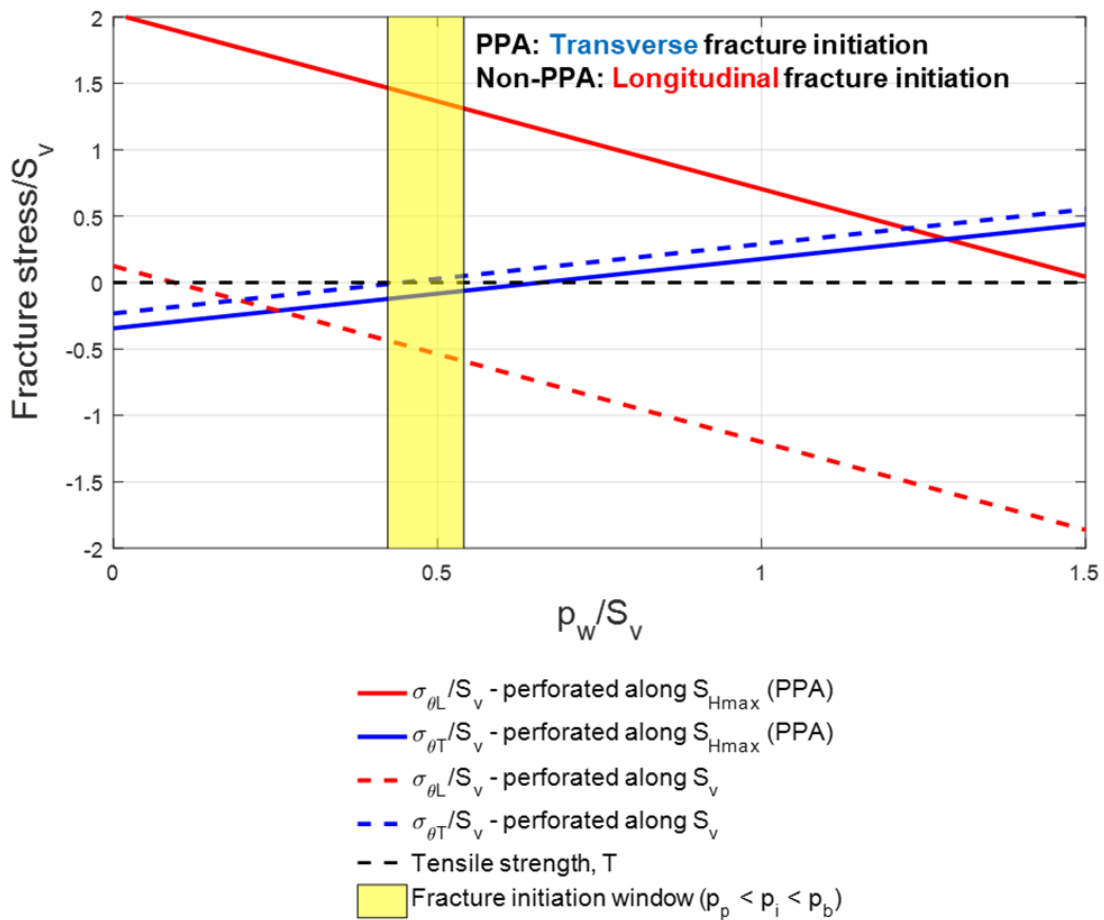
Figure 5.8.   Variation of $\sigma_{\theta L}$ and $\sigma_{\theta T}$ with p_w for the *in-situ* conditions of the Barnett Shale calculated by the true-3D numerical model. The yellow-shaded region indicates the $p_p - p_b$ range in within which p_i lies.

160

The aforementioned results agree with Kurdi (2018) for the Barnett Shale, which is under a strong normal faulting stress state (Table 5.1). Oriented perforating (Kurdi, 2018; Huang et al., 2020) along S_{Hmax} ($\theta = 90°$ on Figure 5.4b; the PPA direction), seems to be ideal in promoting transverse fracture initiation. Nevertheless, the results of case study on a single shale play (the Barnett) are not sufficient general conclusions on optimal perforating direction, considering that this may not be solely-dependent on the *in-situ* stress regime, as also concluded by Kurdi (2018).

5.4.2   Extension over a Range of *In-Situ* Stress States

The application of the true-3D numerical model can be expanded over a range of *in-situ* stress regimes. To demonstrate the results in a single plot, allowable stress state diagrams are employed (Figure 5.9). Allowable stress state diagrams, also known as "stress polygons," are simple 2D plots presenting the range of stable subsurface stress states, with S_{hmin} on the horizontal axis and S_{hmin} on the vertical axis. Both axes are normalized by S_v. The dotted diagonal is the line of horizontal isotropy, where $S_{Hmax} = S_{hmin}$ and the solid lines represent the frictional limits following

$$\frac{S_1 - p_p}{S_3 - p_p} \leq \left(\mu + \sqrt{1 + \mu^2} \right)^2 \tag{5.12}$$

where μ is the friction coefficient of the fault, and S_1 and S_3 are respectively the largest and least compressive principal stresses. In accordance with Anderson (1951), $S_1 = S_v$ and $S_3 = S_{hmin}$ for normal faulting, $S_1 = S_{Hmax}$ and $S_3 = S_v$ for reverse faulting, and $S_1 = S_{Hmax}$ with $S_3 = S_{hmin}$ for strike-slip faulting. Typically the value of friction factor for rocks ranges between 0.6-0.8 (Byerlee 1978), which puts the ratio $(S_1 - p_p)/(S_3 - p_p)$ between 3.12 and 4.33. If the ratio

exceeds this magnitude, shear fault slippage will occur. For a hydrostatic p_p gradient of 0.43 psi/ft, the allowable stress state region becomes the region enclosed by the polygon on Figure 5.9.
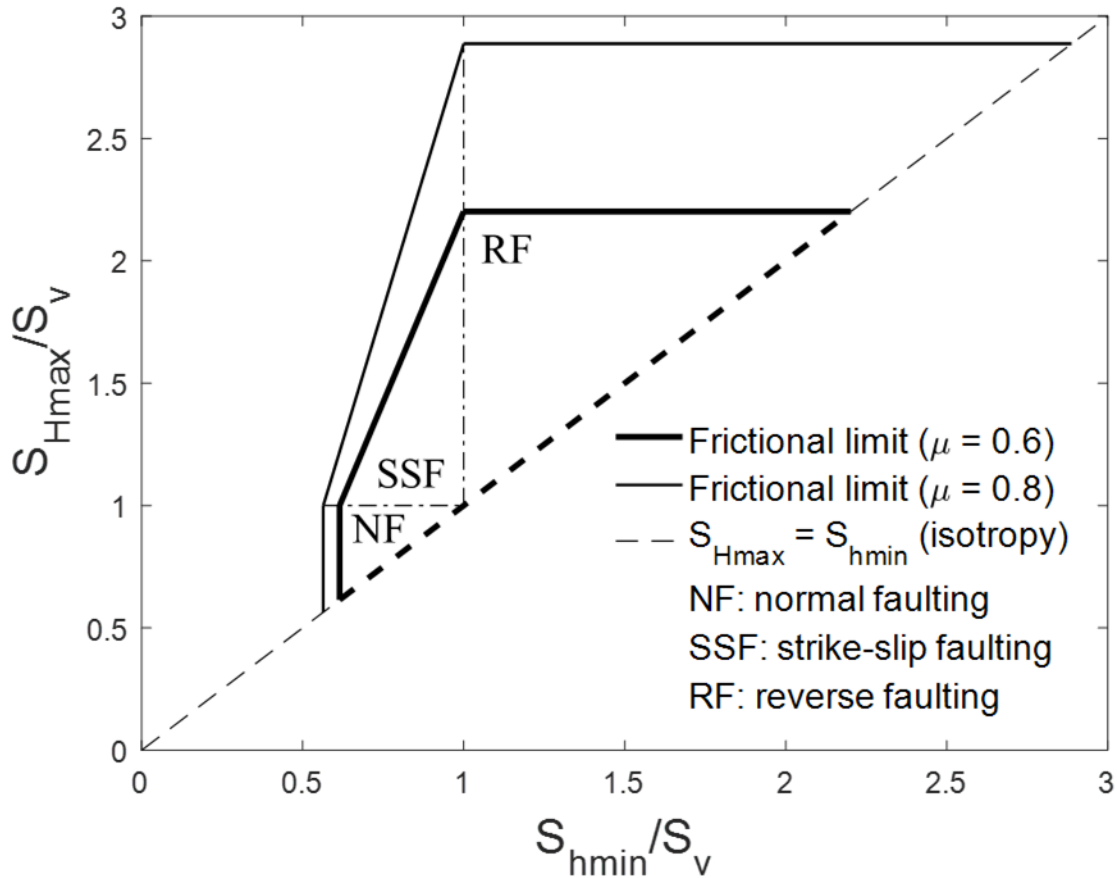
Figure 5.9: Allowable stress state diagram showing the range of stress states possible in the Earth's subsurface for $p_p/S_v = 0.43$. The dotted diagonal line represents horizontal isotropy ($S_{Hmax} = S_{hmin}$), the thicker and thinner solid lines represent the frictional limits for $\mu = 0.6$ and 0.8, respectively. The region enclosed by the frictional limits and the horizontal isotropy line, represents the range of possible subsurface stress states.

Nelson et al. (2005) used allowable stress state diagrams to identify the range of stress states which would promote transverse drilling-induced tensile fractures (DITFs)

162

from non-perforated wells by considering the "region" between two straight lines added on the allowable stress state diagram. The same approach is applied in this study for perforated wells to predict the orientation of fracture initiation at specific p_w, p_p, and v values. The range of stress states, where transverse fracture initiation is promoted can be visually displayed on an allowable stress state diagram, as the region behind both $\sigma_{\theta T}|_{r_w} = \sigma_{\theta L}|_{r_w}$ and $\sigma_{\theta T}|_{r_w} = -T$ lines (Michael et al., 2018; Michael, 2019a; Michael et al., 2020).

Figure 5.10 displays the range of stress states promoting longitudinal or transverse fracture initiation from horizontal wells parallel to S_{hmin} and perforated along S_{Hmax} at p_w of 0.6 psi/ft, the approximate p_b in the Barnett Shale (Ketter et al., 2006). The cyan and green lines represent the stress states where $\sigma_{\theta T} = 0$ (Eq. 5.8) and $\sigma_{\theta T} = \sigma_{\theta L}$ (Eq. 5.9) respectively, modified using the correction factor set developed for the Barnett Shale (Table 5.3). The blue points indicate stress states for which the true-3D numerical model predicts transverse fracture initiation at $p_b \leq 0.6$ psi/ft ($\sigma_{\theta T}|_{p_w=0.6\ psi/ft} < 0$ and $\sigma_{\theta T}|_{p_w=0.6\ psi/ft} < \sigma_{\theta L}|_{p_w=0.6\ psi/ft}$. The red points indicate stress states for which the true-3D numerical model predicts longitudinal fracture initiation at $p_b > 0.6$ psi/ft ($\sigma_{\theta T}|_{p_w=0.6\ psi/ft} > 0$ or $\sigma_{\theta T}|_{p_w=0.6\ psi/ft} > \sigma_{\theta L}|_{p_w=0.6\ psi/ft}$). Previous studies (Michael and Gupta, 2019; 2020) showed the "blue region" shrinking as p_w increases. For enhanced clarity, not all red points are shown on Figure 5.10, whereas the blue points displayed are to be considered representative of the full size of the blue region.
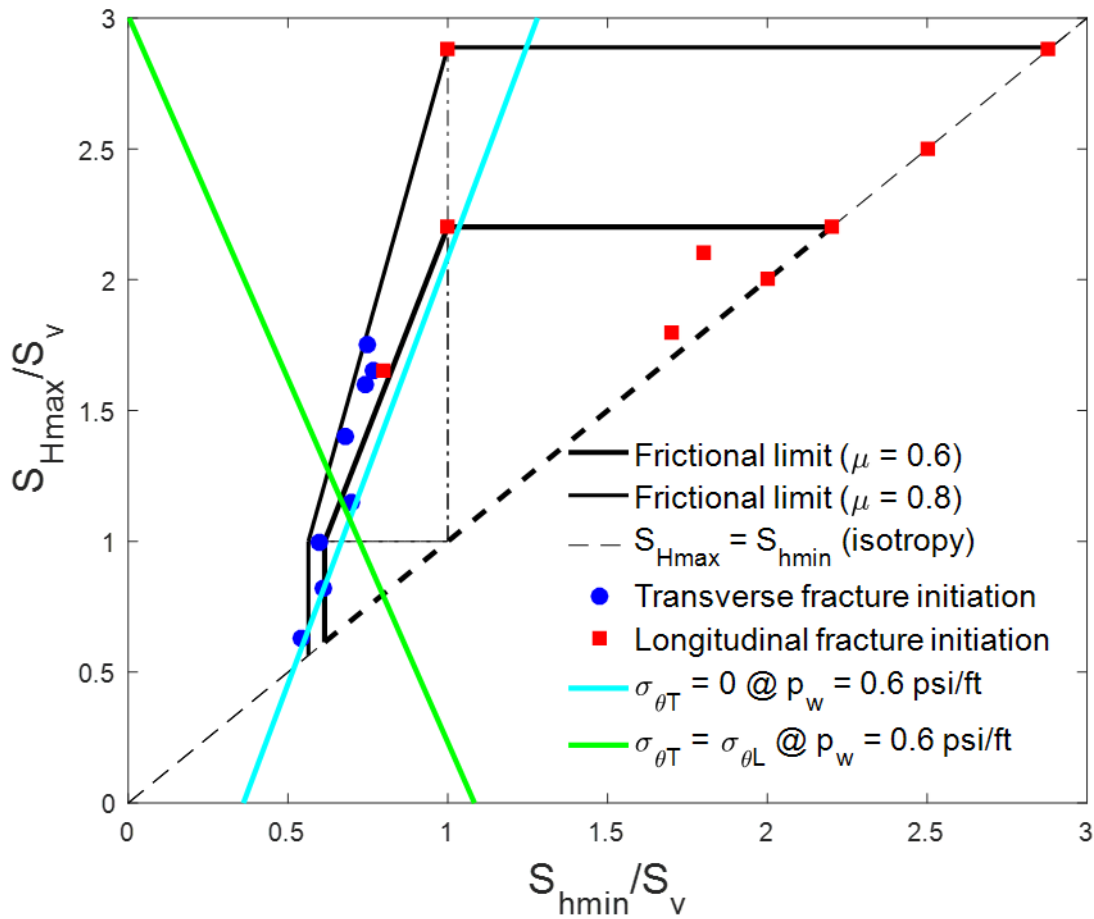
Figure 5.10. Allowable stress state diagrams indicating the orientation of fracture initiation at various points (red for longitudinal and blue for transverse) as predicted at $p_w = 0.6$ psi/ft and $p_p = 0.43$ psi/ft by the true-3D numerical model. The cyan and green lines ($\sigma_{\theta T} = 0$ and $\sigma_{\theta T} = \sigma_{\theta L}$, respectively) are drawn using Eq. 5.8 and 5.9 and the correction factors calculated for the Barnett Shale (Table 5.3).

Evidently from Figure 5.10, a more representative line-fit is possible between the blue and red regions, as the correction factor set for the Barnett Shale (Table 5.3) provides a conservative prediction for the S_{Hmax} while overestimating S_{hmin}. This is in regards to the range of stress states where transverse fracture initiation is promoted at the given conditions ($p_w = 0.6$ psi/ft, $p_p = 0.43$ psi/ft, and $v = 0.32$). Caution is advised as this

modeling approach requires using a correction factor set appropriate for the *in-situ* conditions in question.

The correction factor set developed for the Barnett Shale (Table 5.3), significantly decreases the range of stress states promoting transverse fracture initiation. Figures 5.11a and 5.11b show the allowable stress state diagrams without correction for perforations on $\theta = 90°$ and $\theta = 0°$ (along S_{Hmax} and S_v), respectively, while Figures 5.11b and 5.11d show the allowable stress state diagrams for $\theta = 90°$ and $\theta = 0°$ respectively, modified according to the numerically-developed correction factor set (Table 5.3). The blue region in Figures 5.11b and 5.11d is smaller than the blue region in Figures 5.11a and 5.11c, respectively, highlighting the extent to which the modified Hossain et. al's (2000) analytical approximations overestimate transverse fracture initiation. An allowable stress state diagram shows a range of stress states and thus the concept of PPA does not apply on the diagram *per se*, unless a specific stress state is considered, in which case the PPA concept applies (Figure 5.4a).
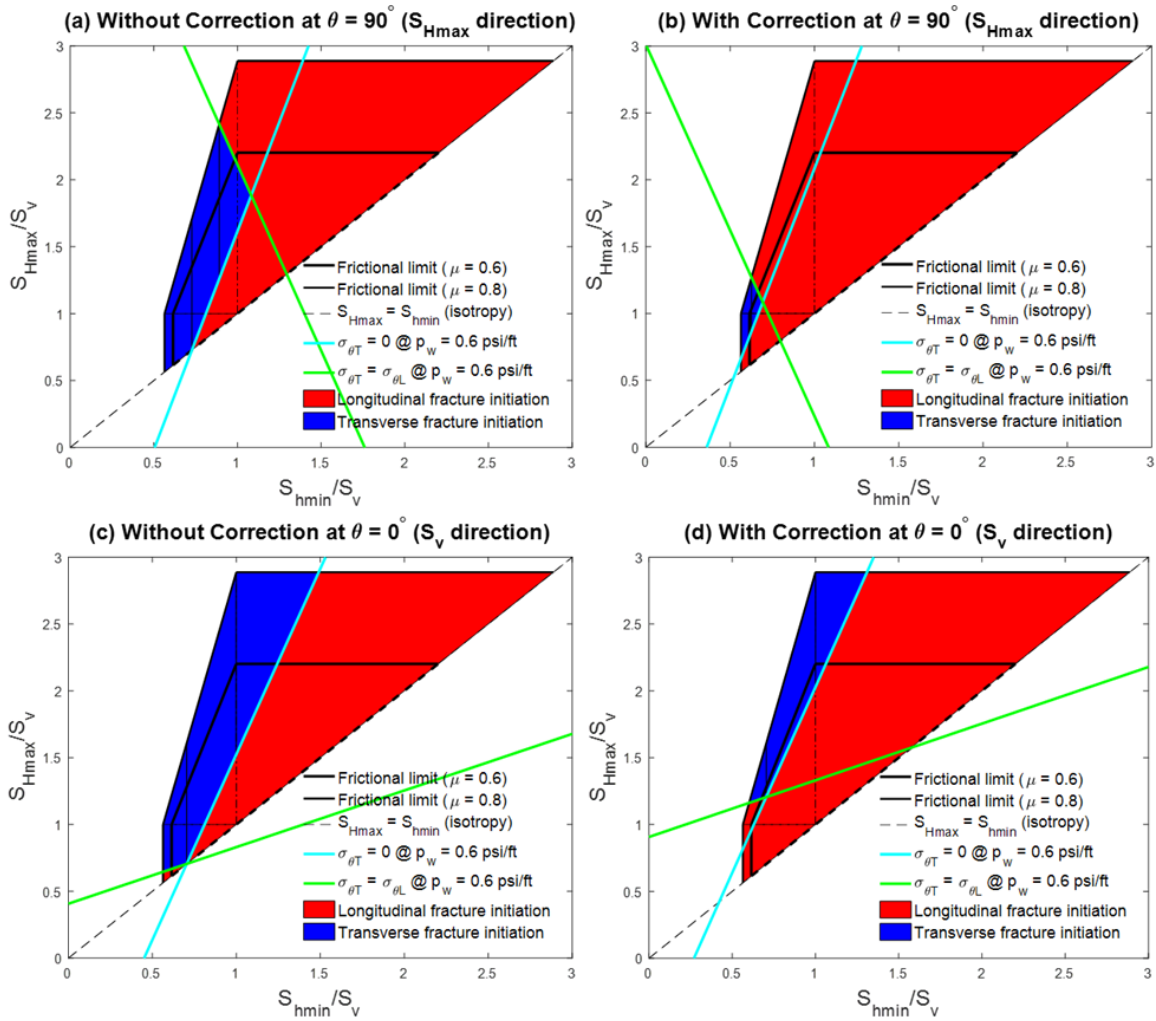
Figure 5.11. Comparison between the resulting allowable stress state diagrams for (a) perforations at $\theta = 90°$ and (b) $\theta = 0°$ without application of the correction factor set (Table 5.3), with (c) perforations at $\theta = 90°$ and (b) $\theta = 0°$ with the correction factors applied. The correction for both θ shrinks the blue regions suggesting the uncorrected modified Hossain et al's (2000) analytical approximations overestimate transverse fracture initiation. For all diagrams $p_w = 0.6$ psi/ft, $p_p = 0.43$ psi/ft, and $\nu = 0.32$.

5.5   DISCUSSION

5.5.1   Fracturing Fluid Leakage around the Wellbore

Fracture initiation can occur from all around the wellbore if fractures fluids leak (Alabbad, 2014; Barree and Miskimins, 2015; Michael, 2016b). In those situations, the presence of the perforation must be "ignored" and the problem's geometry is simplified to the extent at which a fully-analytical solution can be defined. This simplifies the problem to DITF initiation in linearly elastic rocks (Nelson et al., 2005), where p_i can be given only for longitudinal fracture initiation, as

$$p_i|_\theta = min[S_v + S_{Hmax} - 2(S_{Hmax} - S_v) \cos 2\theta - p_p] \qquad (5.12)$$

Inelastic rock models, which indicate dependency of σ_{yy} on p_w allow derivation of exact analytical solutions of p_i for transverse fracture initiation for situations of fluid leakage around the well. Nevertheless, following the theory of linear elasticity (Eq. 5.1), $\sigma_{yy} \neq f(p_w)$ rendering it impossible to derive an expression for p_i for transverse fracture initiation.

If the presence of the perforation tunnel is ignored, the fracture orientation will be determined by $\sigma_{yy}|_{r=r_w}$ and $\sigma_{\theta\theta}|_{r=r_w}$ substituting $\sigma_{\theta T}$ and $\sigma_{\theta L}$, respectively, as the transverse and longitudinal-inducing fracturing stresses. The resulting impact on T_{crit} and the p_b window varies depending on the perforation direction and the reference point on the wellbore.

Figure 5.12a demonstrates the impact of fracturing fluid leakage around a horizontal well in the Barnett Shale (Table 5.1), perforated along non-PPA ($\theta = 0°$, S_v direction). The $\sigma_{\theta L}|_{p_w}$ and $\sigma_{\theta T}|_{p_w}$ lines (dotted) at $\theta = 0°$ are compared with the $\sigma_{\theta\theta}|_{r=r_w,p_w}$ and $\sigma_{yy}|_{r=r_w,p_w}$ lines (dash-dotted) along the PPA direction, orthogonal to the

167

perforations. Figure 5.12a shows $\sigma_{\theta\theta}|_{r=r_w,p_w}$ and $\sigma_{yy}|_{r=r_w,p_w}$ becoming equal at a tensile value which corresponds to a p_w smaller than that at which $\sigma_{\theta T} = -T = 0$. The former intersection point therefore indicates $p_{b,upper}$ when no leakage has taken place (Eq. 5.10a). Fluid leakage makes both T_{crit} and p_b window vanish, as $\sigma_{yy}|_{r=r_w,p_w} > -T = 0$, making transverse fracture initiation impossible. Longitudinal fracture initiation is expected at a much higher p_i at 14,040 psi (Figure 5.12a).

Figure 5.12b displays the impact of fracturing fluid leakage for perforations oriented along PPA ($\theta = 90°$, S_{Hmax} direction) in a horizontal well in the Barnett Shale. For this configuration, the p_b window is shown to shrink by 11% from 0-4,762 psi to 0-4,241 psi. Also, T_{crit} decreases by 65% from 2,482 psi to 861 psi. This is demonstrated by comparing the $\sigma_{\theta\theta}|_{r=r_w,p_w}$ and $\sigma_{yy}|_{r=r_w,p_w}$ lines (dash-dotted) at $\theta = 0°$, with the $\sigma_{\theta L}|_{p_w}$ and $\sigma_{\theta T}|_{p_w}$ lines (solid) for perforations along PPA. The net impact of the changes in the p_b window and T_{crit} inhibits the promotion of transverse fracture initiation for wells perforated along PPA (Figure 5.12b). Specifically, at $4,241 < p_b < 4,762$ psi, fracturing fluid leakage induces longitudinal fracture initiation instead of transverse which is what happens expected in the no leakage scenario.
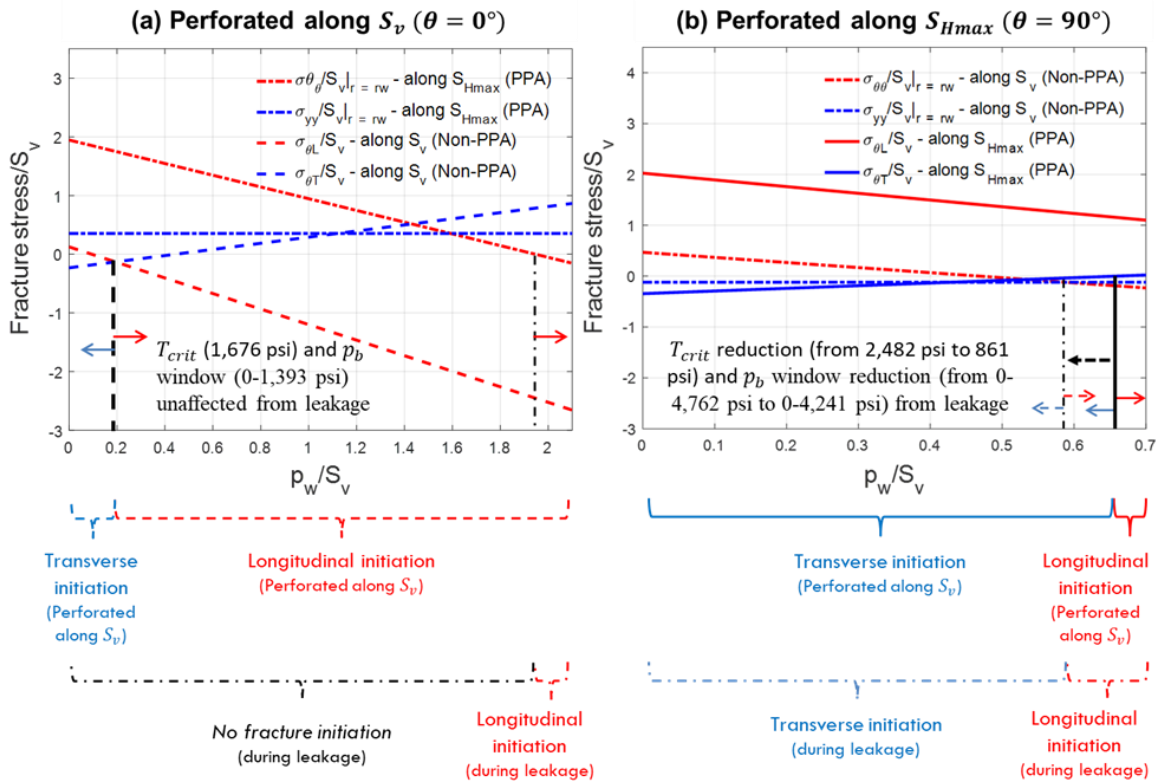
Figure 5.12. Longitudinal fracture-inducing $\boldsymbol{\sigma_{\theta\theta}}|_{r=r_w}$ and transverse fracture-inducing $\boldsymbol{\sigma_{yy}}|_{r=r_w}$ with dashed-dotted lines for the Barnett Shale (Table 5.1) along (a) non-PPA ($\theta = 0°$, S_v direction) compared with $\sigma_{\theta L}$ and $\sigma_{\theta T}$ (solid lines) along PPA ($\theta = 90°$, S_{Hmax} direction), and (b) $\boldsymbol{\sigma_{\theta\theta}}|_{r=r_w}$ and $\boldsymbol{\sigma_{yy}}|_{r=r_w}$ along PPA compared with $\sigma_{\theta L}$ and $\sigma_{\theta T}$ along non-PPA. The wellbore stresses ($\boldsymbol{\sigma_{\theta\theta}}|_{r=r_w}$ and $\boldsymbol{\sigma_{yy}}|_{r=r_w}$) determine the orientation of fracture initiation in the event of fracturing fluid leakage around the wellbore. In (a) fluid leakage makes transverse fracture initiation harder because it reduces the p_b window and T_{crit}, while for (b) the p_b window and T_{crit} remain the same as without fluid leakage.

It has to be stated that the aforementioned results apply for the Barnett Shale case study performed, but can vary significantly for other shale plays as the results are highly sensitive to the local *in-situ* stress state and other geomechanical parameters (Table 5.1).

Utilizing allowable stress state diagrams to expand our analysis over the entire range of stress states stable in the subsurface, fracturing fluid leakage around the wellbore is shown to suppress total fracture initiation, either longitudinal or transverse. When leakage takes place, the red ($\sigma_{\theta L} = 0$) and blue solid lines ($\sigma_{\theta T} = 0$) indicating the limits of longitudinal and transverse fracture initiation on Figure 5.13a for $\theta = 90°$ and Figure 5.13c for $\theta = 0°$ are replaced respectively by the longitudinal fracture-inducing, $\sigma_{\theta\theta}|_{r_w} = 0$ and transverse fracture-inducing, $\sigma_{yy}|_{r_w} = 0$, the red and blue dash-dotted lines on Figures 5.13b and 5.13d.
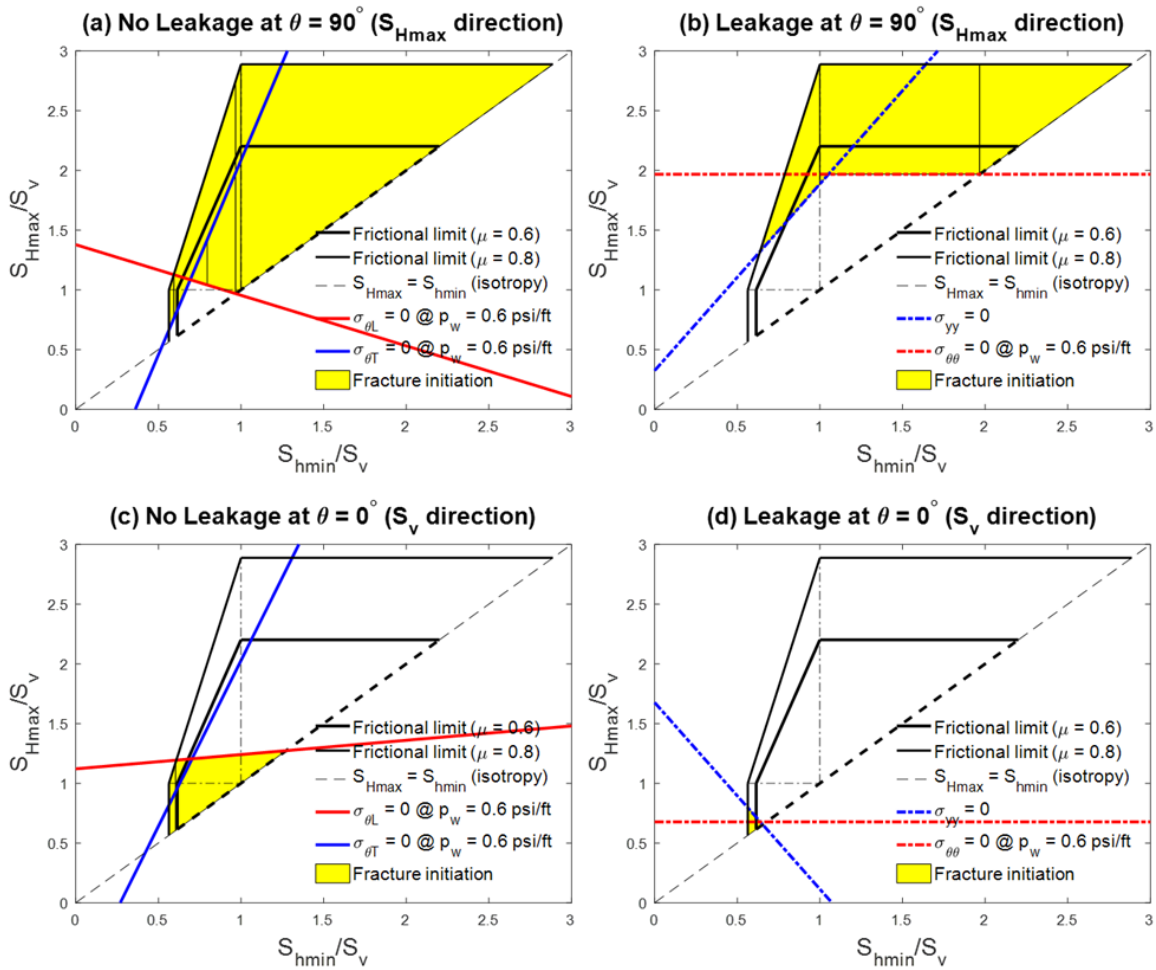
Figure 5.13. The effect of fracturing fluid leakage around the wellbore in for (a) perforations parallel to S_{Hmax}, without and (b) with leakage, (c) perforations parallel to S_v without and (d) with leakage. For both perforation directions, leakage reduces the range of stress states in which fracture initiation (either longitudinal, or transverse) takes place.

5.5.2 The Effect of Cemented Casing at the Point of Cement Curing

A well-cemented casing will potentially shield stress alterations induced by p_w variations (Fallazadeh et al., 2017; Michael et al., 2018; 2020). The radial strains the cemented wellbore experiences will be less than the radial strains of an openhole

configuration. Michael et al. (2018; 2020) mimicked this effect in a fully-analytical manner, by re-computing the analytical results for a perfectly cemented wellbore, where $\sigma_{\theta\theta}|_{r_w}$ is fixed at time cement is cured, assuming a balanced condition with $p_w = p_p$. These wellbore stresses remain the *de facto* "remote" loading at the perforation base and the pressure in the perforation tunnel, which is equal to p_w, continues as the fracturing pressure. Using Barnett Shale parameters (Table 5.1), it is apparent that the shielding effect induced by the cemented casing makes both $\sigma_{\theta L}$ and $\sigma_{\theta T}$ to become more tensile as p_w increases (Figure 5.14). This suggests that good cement jobs without annular leakage help transverse fracture initiation.

Furthermore, in this uniquely extreme case, p_i will decrease almost to the magnitude of p_p as shown on Figure 5.14, suggesting that transverse fracture initiation occurs as soon as injection of fracturing fluid commences from balanced conditions inside the wellbore. Hence, the magnitude of p_b is expected to decrease, responding to the extremely low p_i value becoming much lower than what Figure 5.14 shows for p_b (taken from Ketter et al., 2006). Subsequently, the yellow region will be considerably narrower than what is depicted on Figure 5.14. The case discussed here is however idealistic and its occurrence is expected to be extremely rare (Michael, 2019a; Michael et al., 2020).
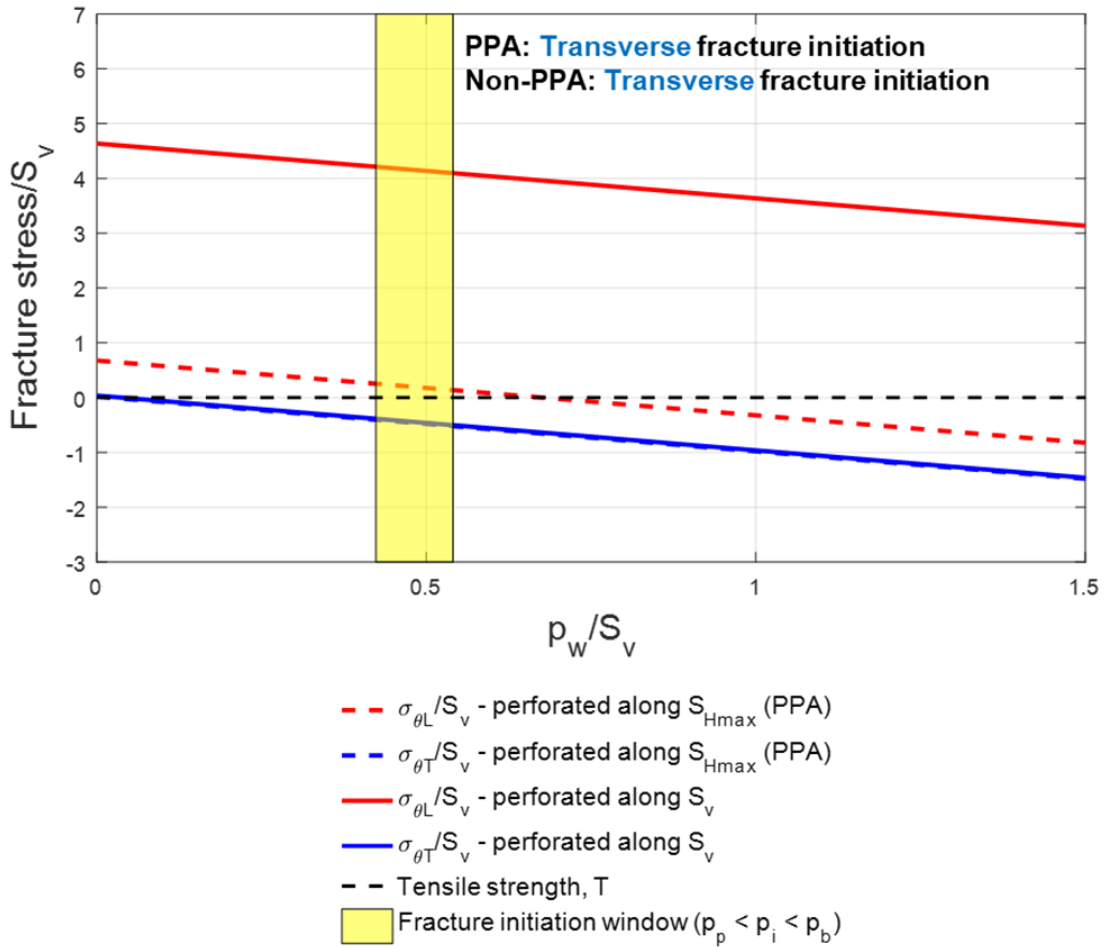
Figure 5.14. Extreme case of a perfectly-cemented borehole, with both $\sigma_{\theta L}$ and $\sigma_{\theta T}$ becoming more tensile (at the same slope) as p_w increases for Barnett Shale parameters (Table 5.1). In this case, transverse fracture initiation would always be promoted regardless of p_w, with p_i reduced to about p_p. The same fracture initiation window is shown with Figure 5.8, however in such case (which is highly idealistic and unlikely) p_b is expected to follow suit and decrease significantly.

5.6 CONCLUSIONS

The novelty of this work lies in the application of the variation in the stresses on the perforation base to develop a framework for a semi-analytical modeling approach to

predict p_i and the orientation of fracture initiation from perforated wells. The developed procedure was applied on a Barnett Shale case study and the following conclusions are obtained:

- Linear correction factors (C_m and C_c), can be calculated numerically and used to modify existing closed-form analytical (approximated) expressions for $\sigma_{\theta L}|_{p_w}$ and $\sigma_{\theta T}|_{p_w}$ to match exact solutions from the literature. Transverse fracture initiation occurs if p_b is below $p_{b,upper}$ and T is lower than T_{crit}.

- In wells drilled parallel to S_{hmin} in the Barnett Shale, which is under strong normal faulting stress regime, the p_b window and T_{crit} are maximized for perforations on the side of the borehole ($\theta = 90°$, S_{Hmax} direction). This perforation direction, which best promotes transverse fracture initiation is known as the preferred perforation alignment (PPA).

- Applying the semi-analytical modeling method developed in this work to the Barnett Shale, transverse fracture initiation occurs if p_b is kept lower than the $p_{b,upper}$ of 4,762 psi and T lower than the T_{crit} of 2,482 psi for perforations along PPA ($\theta = 90°$, S_{Hmax} direction). For perforations along the non-PPA ($\theta = 0°$, S_v direction), $p_{b,upper}$ and T_{crit} are both reduced by 71% and 32.5% respectively, to 1,393 psi and 1,676 psi. Transverse fracture initiation is predicted for the entire fracture initiation window at $0.42 \leq p_i/S_v \leq 0.54$ from perforations in the PPA direction, while for from perforations in the non-PPA direction, longitudinal fracture initiation is expected.

- For both perforation directions (PPA and non-PPA), the correction factors decrease the range of *in-situ* stress states promoting transverse fracture initiation. Application of the correction factor set developed for the Barnett Shale yields conservative predictions of transverse fracture initiation when applied over the

174

range of stress states stable in the Earth's subsurface. Aggregate correction factors can be developed considering a broad range of stress states, in future studies.

- Fracturing fluid leakages around the wellbore can compromise p_i predictions and suppress transverse fracture initiation. For the Barnett Shale conditions, leakage of fracturing fluid was found to reduce T_{crit} by 65% and the p_b window by 11% for perforations in the PPA direction, while for perforations along the non-PPA direction, transverse fracture initiation is made impossible. For the entire range of stress states possible to exist in the Earth's subsurface, fracturing fluid leakage is shown to suppress fracture initiation, either longitudinal or transverse.

The procedure used in this study may be extended to different reservoirs around the world. Numerical modeling can be employed to calculate correction factors for any given set of geomechanical conditions, which can be then used to estimate p_i and predict the orientation of fracture initiation for a given p_b. The results can be used to evaluate potential application of oriented perforating strategies in order to optimize a fracture treatment.

Chapter 6. Oriented Perforating: A Comparative Study on Seven Shale Plays

Oriented perforating strategies have been proposed as a method of suppressing fracture initiation pressures and optimizing the orientation of the initiated fractures, including a semi-analytical procedure for predicting the fracture initiation pressure for given *in-situ* stress conditions and the orientation of fracture initiation (longitudinal or transverse-to-the-wellbore). In this study, a comparative analysis is made on the fracture initiation in seven prolific shale gas plays, Barnett, Bakken, Fayetteville, Haynesville, Niobrara, Marcellus and Vaca Muerta, for cases of horizontal wells drilled parallel to the least horizontal principal stress. The semi-analytical model is employed to determine the optimal perforation direction for each play, targeting transverse fracture initiation and fracture initiation pressure minimization. This involves a numerical model used to derive correction factors for closed-form analytical approximations from the literature, which are used to evaluate the stresses acting on the perforation base. While the leak-off and breakdown pressures can easily be pointed out from pressure monitoring, the fracture initiation pressures are not easily distinguishable. Reliable fracture initiation pressure estimations is of importance to stimulation engineers planning a treatment, as it controls the number and capacity of the injection pumps needed as well as being a major input for computational modeling. For normal faulting stress states, transverse fracture initiation is best promoted by perforations on the side of the hole, while for strike-slip faulting stress states, by perforations on the top of the hole. When only longitudinal fracture initiation is possible, the fracture initiation pressure is minimized from perforations on top of the borehole in normal faulting stress states and from the side of the borehole for strike-slip faulting stress states. Fracturing fluid leakage around the wellbore makes transverse

176

fracture initiation harder and can also impose a major impact on the fracture initiation pressures, in either direction (increase or decrease).

6.1 INTRODUCTION

The industrial impact of hydraulic fracturing has been massive and is responsible for the advances in the development of tight unconventional resources such as shale gas, which would otherwise be non-producible (Economides and Martin, 2010). Oriented perforating strategies have been proposed for optimizing hydraulic fracturing treatments in horizontal wells (Kurdi, 2018; Michael, 2019a; Michael and Gupta, 2020b; Michael et al., 2020). Accurate prediction of the formation fracture initiation pressure, p_i, is important in designing of a hydraulic fracture stimulation treatment and a major factor to the treatment's eventual success (Michael and Gupta, 2020a). Hydraulic fracturing operations in wells perforated at a single phase angle, can achieve treatment pressure minimization and optimal fracture initiation geometry maximizing the stimulation treatment's net present value (Balen et al., 1988; Michael, 2019b). Current analytical models underestimate p_i, a parameter observed in laboratory and field-scale studies to be highly sensitive to the pressurization rates (Zoback et al., 1977; Weijers, 1995; Zhuang et al., 2018).

Numerical 3D models have been employed to assess the validity of the model for fracture initiation from perforated wellbores due to approximations involved in its derivation (Michael et al., 2020). Results of numerical simulations have been employed to develop correction factors for analytical expressions for evaluating the tangential stresses at the extreme positions on the perforation base, representing the longitudinal and transverse fracture initiation stresses (Michael and Gupta, 2019; 2020a). The well is modeled as an openhole completion (microannulus between the cement and the

surrounding rock, after Behrmann and Nolte, 1998) with a cylindrical perforation. *In-situ* stress state, wellbore pressure, p_w, and the formation's geomechanical properties are considered as independent variables, all controlling p_i, which is the p_w value at which the tensile failure criterion is exceeded. The general semi-analytical modeling approach for estimating fracture initiation pressures and the orientation of fracture initiation employed in this study was first presented in Michael and Gupta (2020a).

In this study, seven prolific shale plays from the United States namely the Barnett, Bakken, Fayetteville, Haynesville, Marcellus, and Niobrara, and Vaca Muerta (Argentina) are modeled using predictions from the true-3D numerical models (Michael et al., 2020). Values of p_i for each play are predicted for fracture treatments in horizontal wells.

Breakdown pressure, p_b values from the seven shale plays are taken from the literature (Kettler et al., 2006; Hammes et al., 2011; Barth et al., 2012; Kosset et al., 2014; Schlumberger, 2014; Koskella et al., 2015; Lynk et al., 2017) and are used to predict p_i values and the respective orientation of fracture initiation for the shale play. Besides wellbore trajectory, the results depend on perforation direction as well as the orientation of the resultant fracture initiation. For horizontal wells drilled parallel to S_{hmin} in strike-slip faulting regimes, the preferred perforation alignment (PPA) for promoting transverse fractures, thus along the preferred fracture plane (PFP) that maximizes the wells post-stimulation productivity.

Dimensionless plots are used to illustrate the results including comparative analyses. The numerically-corrected analytical approximations can be used to predict the p_i in oilfield fracturing operations for a given wellbore trajectory, perforation direction, and resultant fracture initiation orientations.

6.2 THEORETICAL BACKGROUND

6.2.1 Near-Wellbore Stress State and Fracture Orientation

The earliest derivation of stress concentrations for a circular hole under uniform compression were given by Kirsch (1898) and were later modified by Hubbert and Willis (1957) to incorporate biaxial stress loading and fluid pressure inside the hole. For a horizontal well drilled parallel to the y-axis, which is assumed to be parallel to the least horizontal principal stress, S_{hmin}, and perpendicular to the overburden and maximum horizontal principal stresses (S_v and S_{Hmax}, respectively) in a homogeneous, isotropic rock, the stresses on the wellbore radius, $r = r_w$ were analytically defined by Zoback (2007) and are summarized on Table 6.1. Figure 6.1a shows the configuration of the radial, tangential, and axial effective stresses (σ_{rr}, $\sigma_{\theta\theta}$, and σ_{yy}, respectively) on the radius of the horizontal well.

Table 6.1.   Summary of the near-wellbore cylindrical stresses (the "Kirsch solutions").

Stress name	Symbol	Stress concentration at $r = r_w$	Effective stress ($r \geq r_w$)	Equation number
Radial	S_{rr}	$S_{rr}\|_{r=r_w} = p_w$	$\sigma_{rr}\|_r = S_{rr}\|_r - p_p$	(6.1)
Tangential ("hoop" or circumferential)	$S_{\theta\theta}$	$S_{\theta\theta}\|_{r=r_w}$ $= S_v + S_{Hmax} - 2(S_{Hmax} - S_v)\cos 2\theta - p_w$	$\sigma_{\theta\theta}\|_r = S_{\theta\theta}\|_r - p_p$	(6.2)
Axial	S_{yy}	$S_{yy}\|_{r=r_w} = S_{hmin} - 2\nu(S_{Hmax} - S_v)\cos 2\theta$	$\sigma_{yy}\|_r = S_{yy}\|_r - p_p$	(6.3)
Shear	$S_{r\theta}$	$S_{r\theta}\|_{r=r_w} = 0$	$\sigma_{r\theta}\|_r \equiv S_{r\theta}\|_r$	(6.4)

θ is the angle around the wellbore cross section taken clockwise from S_v and ν is the Poisson's ratio for the rock formation. S_{rr}, $S_{\theta\theta}$, and S_{yy} represent total normal stress concentrations and can be converted to the corresponding effective stresses, σ_{rr}, $\sigma_{\theta\theta}$, and σ_{yy} (fourth column) respectively by subtracting pore pressure, p_p from the third column (Eq. 6.1-6.3). Shear stress, $\sigma_{r\theta}$ (sometimes denoted by $\tau_{r\theta}$), is zero at the wellbore radius (Eq. 6.4).
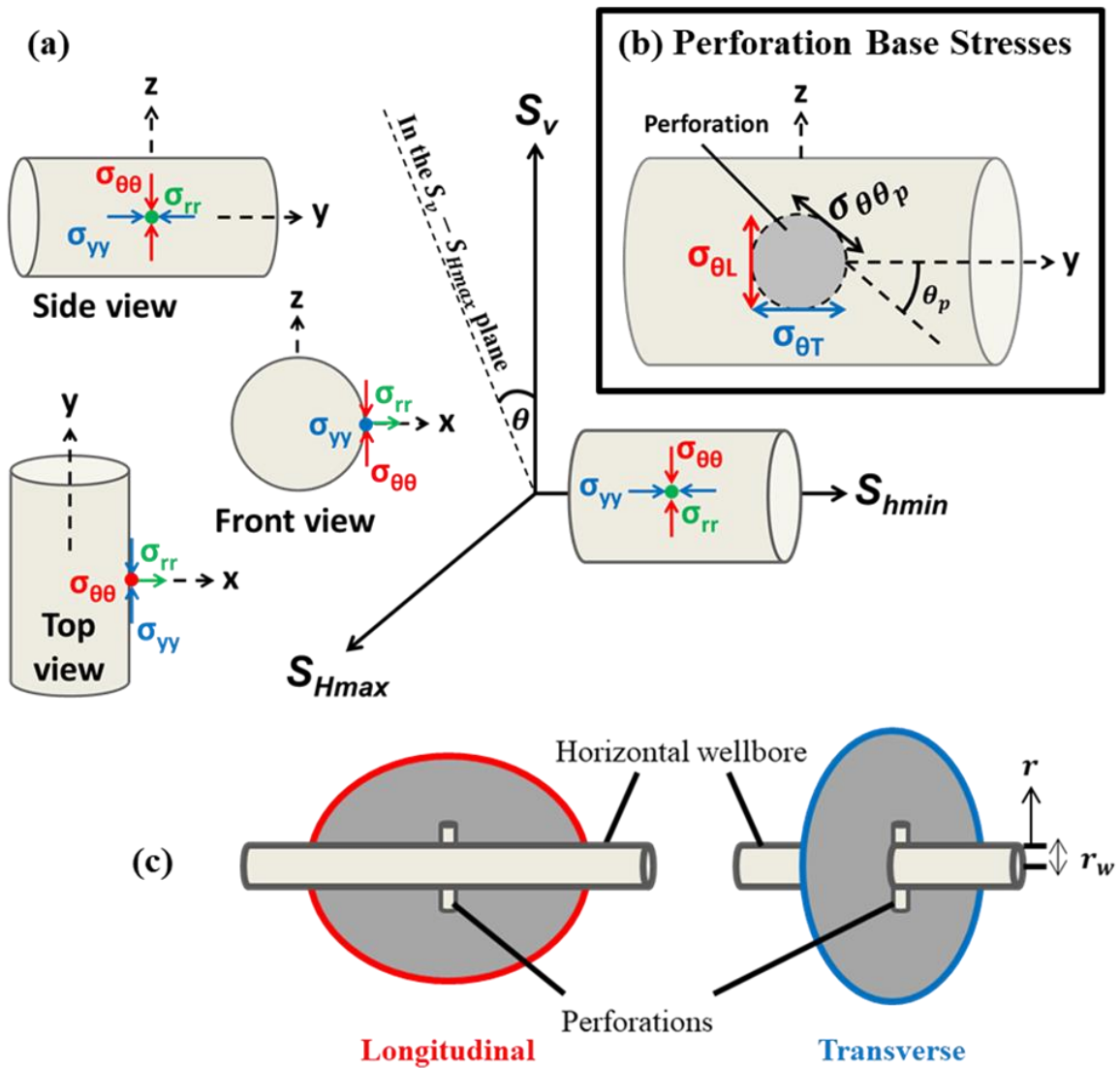
Figure 6.1. (a) Stresses configuration on the radius of a horizontal well drilled parallel to S_{hmin}. S_{Hmax}, S_{hmin} and S_v are then along the x, y and z-axis, respectively. Shear stress is not shown ($\sigma_{r\theta}|_{r=r_w,p_w} = 0$). (b) Longitudinal $\sigma_{\theta L}$ and transverse $\sigma_{\theta T}$ fracturing stresses on the perforation base ($\theta_p = 0°$ and $\theta_p = 90°$, respectively). The well is parallel to the y-axis with perforations parallel to the x-axis. (c) Fracture orientation configurations from a horizontal well, longitudinal (red) and transverse-to-the-wellbore (blue). The variable r represents a distance from the center of the wellbore. This figure is modified from Michael and Gupta (2019e).

180

For a horizontal well, initiated fractures can assume arbitrary orientations but with reference to the wellbore can be bounded by longitudinal and transverse configurations. Following Hossain et al.'s (2000) assumption that fractures initiate from the perforation base (i.e. the intersection point between the perforation tunnel and the wellbore), which is backed by the experimental results of Behrman and Elbel (1991), the orientation of fracture initiation is determined by the magnitude of the tangential stress on the perforation base, $\sigma_{\theta\theta_p}$ (Figure 6.1b), in two extreme locations; parallel and orthogonal to the axis through the center of the wellbore. θ_p (Figure 6.1b) is the positive angle on the perforation base, taken clockwise from the y-axis (the wellbore axis, parallel to S_{yy} and σ_{yy}). The tangential stress on the perforation base orthogonal to σ_{yy} ($\theta_p = 0°$ on Figure 6.1b) is the stress that should be overcome in tension to generate longitudinal fracture initiation, hence called the longitudinal fracturing stress, $\sigma_{\theta L}$. Similarly, the tangential stress on the perforation base parallel to σ_{yy} ($\theta_p = 90°$ on Figure 6.1b) is the stress that must be overcome in tension for transverse fracture initiation to take place and is called the transverse fracturing stress, $\sigma_{\theta T}$ (Hossain et al., 2020; Michael and Gupta, 2019; Michael et al., 2020). Fractures parallel to the wellbore axis are longitudinal/"axial", while fractures that propagate orthogonal are transverse/"lateral" (Figure 6.1c).

Hydraulic fracture orientation impacts well performance following a stimulation treatment with transverse fractures enhancing the productivity compared to longitudinal (relative to a horizontal wellbore), unless the latter are in higher permeability zones and frac-and-pack operations (Economides and Martin, 2010). In this study, p_b is used as an independent variable for predicting p_i and orientation for given *in-situ* stress conditions.

6.2.2 Fracture Initiation, Propagation, and Closure

Hydraulic fracture treatments need bottomhole pressure (BHP) and injection flowrate monitoring. At a steady injection flowrate, BHP increases linearly with time, but becomes non-linear when the injected fracturing fluid begins leaking into the formation (Figure 6.2). The pressure at which the leakage begins is called the leak-off pressure (LOP) and can be measured reliably using data from "leak-off tests" performed during drilling. Despite the leak-off, the BHP continues to build up until a sudden, distinct drop (Figure 6.2) occurs at p_b. Fracture initiation (initial crack) occurs at p_i, at $LOP < p_i < p_b$.
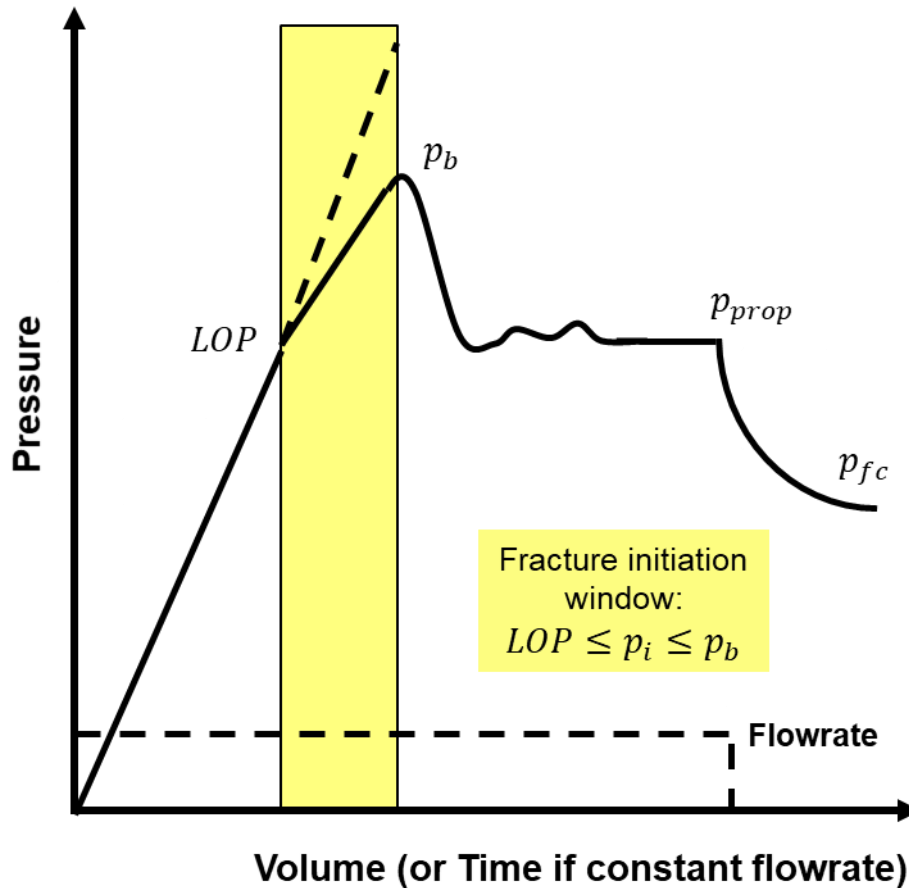
Figure 6.2.   BHP variation with time during a typical hydraulic fracture treatment (modified from Zoback et al., 2003).

After breakdown, further injection makes the initiated fracture(s) to extend from the induced crack(s). This happens at fracture propagation pressure, p_{prop}. Once injection stops the pressure drops, leveling off at fracture closure pressure, p_{fc}, which is considered a good proxy for the least compressive stress. For normal and strike-slip faulting stress states, the least compressive principal stress is S_{hmin}.

While LOP and p_b are distinct and easily observable by the practitioner on the surface during pressure monitoring, the p_i magnitude is often unclear, yet required for fracture modeling considerations. As mentioned previously, fracture initiation occurs at p_i, which can range from LOP to, and is often lower than, p_b (Detournay and Carbonell, 1997; Lecampion et al., 2017; Bunger and Lecampion, 2017). One of the primary factors the p_i value depends upon, is the orientation of the resultant fracture initiation with respect to the wellbore axis (Weijers, 1995; Hossain et al., 2000; Michael et al., 2018; Kurdi, 2018).

Multiple experimental studies using porous media (Zoback et al., 1977; Weijers, 1995; Zhuang et al., 2018) showed the p_i and hence p_b magnitudes to be highly dependent on the injection flowrate used. Thus, the higher the injection flowrate is, the higher the p_i and p_b are, for a given set of *in-situ* conditions.

Operators are highly motivated in keeping p_b as low as possible. Formation breakdown in hard rocks exhibiting high tensile strength values, under high *in-situ* stresses can be challenging, thus suppressing p_b will be highly convenient. Moreover, high p_b values can compromise the efficiency of perforation clusters in initiating fractures, leading to uneven flow distribution between the clusters (McClure et al., 2020). If breakdown occurs in some perforation clusters earlier than others and p_w decreases, it becomes more difficult to induce breakdown in the remaining perforation clusters. This is because p_{prop} is lower than p_b (Figure 6.2); the fracturing fluid following the path of least resistance would "prefer" to propagate an existing fracture than initiating a new fracture within the

stage. Higher p_b values accentuate this problem, leading to inactive perforation clusters yielding no fractures (Miller et al., 2011; Michael, 2016b). Limited entry techniques (Lagrone and Rasmussen, 1963) are often employed to mitigate such effects, nevertheless if p_b is too high, then the effectiveness of these limited entry techniques is challenged (Weddle et al., 2018; McClure et al., 2020).

6.2.3 The Seven Shale Plays in this Study

Seven unconventional shale formations (Figure 6.3) under current development (Barnett, Bakken, Fayetteville, Haynesville, Niobrara, Marcellus and Vaca Muerta) are used to evaluate fracture initiation and orientation. The values of $\sigma_{\theta L}|_{p_w}$ and $\sigma_{\theta T}|_{p_w}$ were calculated using published *in-situ* stress state data (Prioul et al., 2011; Moos, 2012; Yang and Zoback, 2014; Koskella et al., 2015; Kowan and Ong, 2016) shown on Table 2 and are displayed on a stress polygon (Zoback, 2007) on Figure 6.4.
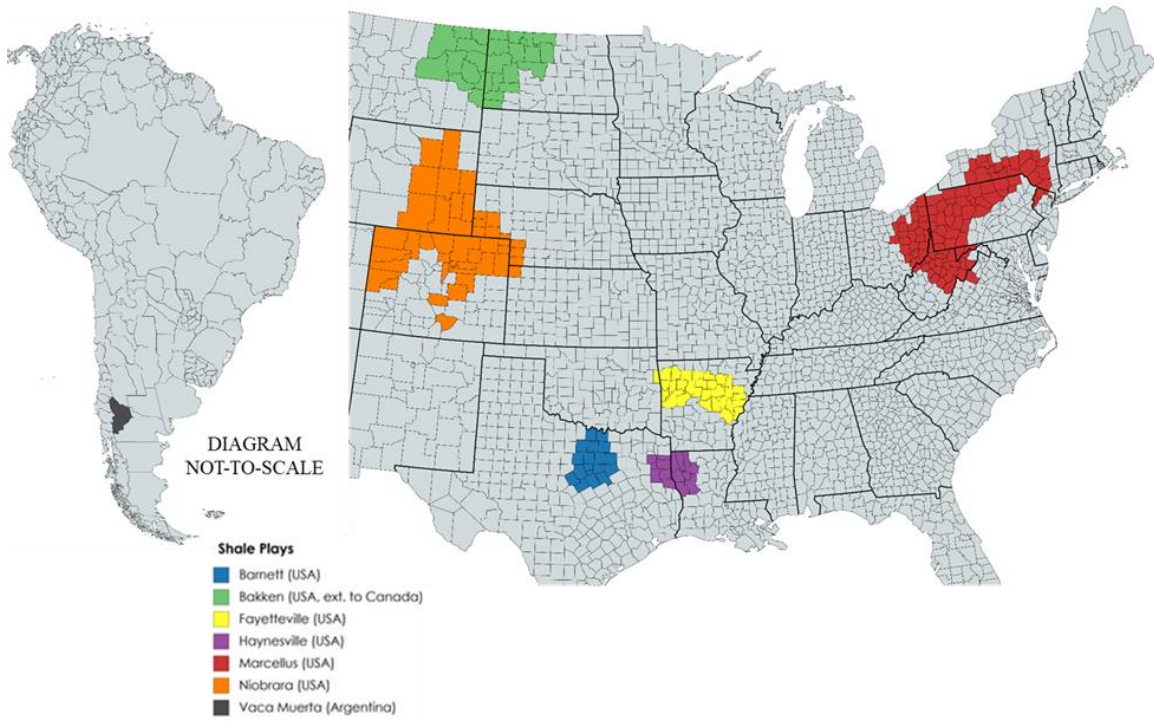
Figure 6.3.   Map of the counties/provinces active on the development of the seven shale plays studied (Source: www.mapchart.net, filled using information from the U.S. EIA).

The *in-situ* stress state of each shale gas play, is quantified by $A_\emptyset$ after Simpson (1997), which varies from zero for extreme normal faulting stress states to three for extreme reverse faulting stress states (Figure 6.4, modified from Lund Snee, 2020). For strike-slip faulting stress states, $1 < A_\emptyset < 2$ (Figure 6.4). The parameter $A_\emptyset$ relates to the absolute stress magnitudes by

$$A_\emptyset = \left(n + \frac{1}{2}\right) + (-1)^n \left(\left[\frac{S_2 - S_3}{S_1 - S_3}\right] - \frac{1}{2}\right) \tag{6.5}$$

185

where, S_1, S_2, and S_3 are respectively the most compressive, intermediate and least compressive *in-situ* principal stresses. Following Simpson (1997), for normal faulting stress states, $S_1 = S_v$, $S_2 = S_{Hmax}$, and $S_3 = S_{hmin}$, with parameter $n = 0$. Similarly, for strike-slip faulting stress states, $S_1 = S_{Hmax}$, $S_2 = S_v$, $S_3 = S_{hmin}$, and $n = 1$. Finally, for reverse faulting stress states, $S_1 = S_{Hmax}$, $S_2 = S_{hmin}$, $S_3 = S_v$, and $n = 2$ (Eq. 6.5).

Table 6.2.   Summary of the in-situ stress states and p_p of the seven shale gas plays studied (data taken from Kettler et al., 2006; Hammes et al., 2011; Barth et al., 2012; Kosset et al., 2014; Schlumberger, 2014; Koskella et al., 2015; Lynk et al., 2017).

Shale play	Location	S_v (psi)	S_{Hmax} (psi)	S_{hmin} (psi)	p_p (psi)	$\dfrac{S_2 - S_3}{S_1 - S_3}$	$A_\emptyset$
Barnett	TX	7,215	4,550	3,900	3,055	0.1961	0.1961
Bakken	MN, ND, and Canada	10,605	10,302	8,080	6,666	0.88	0.88
Fayetteville	AR and OK	5,085	4,388	4,050	1,913	0.3266	0.3266
Haynesville	AR, LA, and TX	13,320	12,600	12,000	10,200	0.4545	0.4545
Niobrara	CO, KS, NE, and WY	7,102	~5,360	5,025	3,283	0.1613	0.1613
Marcellus	NY, MD, NJ, OH, PA, VA, and WV	9,152	9,568	6,656	4,576	0.8571	1.1429
Vaca Muerta	Argentina	8,692	8,856	6,724	5,330	0.9231	1.0769

Frictional failure stability is determined by the Mohr-Coulomb failure limit which defines the bounds of the polygon on Figure 6.4. This is given by Jaeger et al. (2007) as

$$\frac{S_1 - p_p}{S_3 - p_p} < \left([1 + \mu^2]^{1/2} + \mu\right)^2 \approx 3.12 \tag{6.6}$$

where μ is the friction factor for the rock fault. Byerlee (1978) estimated $\mu \approx 0.6$, which sets the right-hand side (RHS) of Eq. 6.6 equal to 3.12. If the fraction on the left-hand side (LHS) of Eq. 6.6 exceeds 3.12 fault slippage will take place, as a result of shear failure, making the *in-situ* stress state considered (S_1 and S_3), unstable and virtually impossible to exist in the Earth's subsurface.
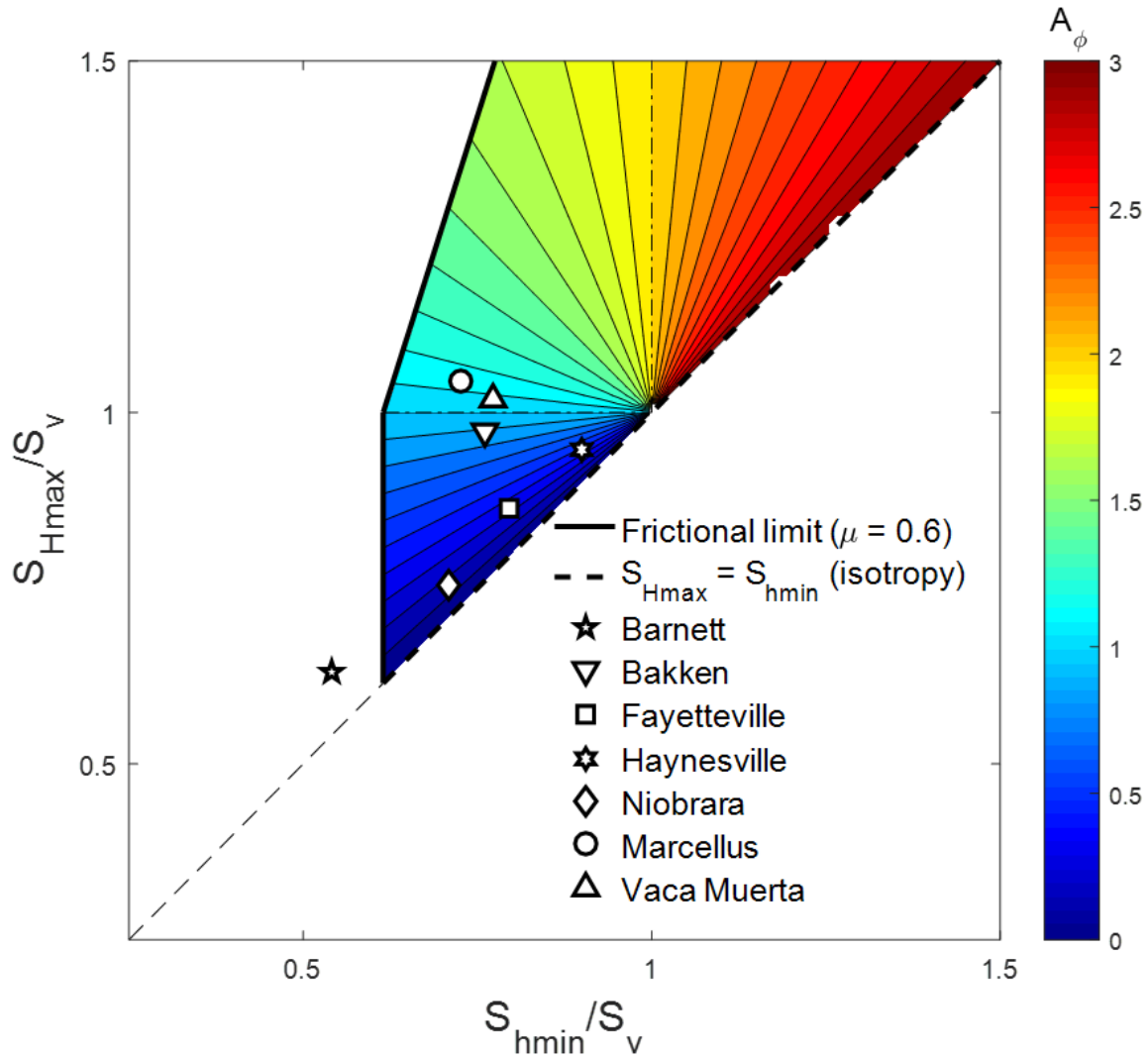
Figure 6.4. The *in-situ* stress state of each of the seven shale plays displayed on a stress polygon. The frictional limits on the polygon are drawn for a hydrostatic p_p gradient of 0.43 psi/ft.

Table 6.3 summarizes depth and p_b values for each of the seven plays using published data from published literature. These p_b values provide the upper-bound of the "fracture initiation window" that is the p_w range containing p_i. Due to unavailability of consistent LOP data for the seven shale gas plays, p_p replaces LOP as the lower-bound, such that $p_p < p_i < p_b$. This leads to a wider fracture initiation window compared to the yellow-shaded region on Figure 6.2. However, the authors advice caution when doing this, since low p_i predictions that are only marginally higher than p_p could be unrealistic, due to these p_i values been smaller than LOP (i.e. LOP $> p_i$), which cannot be true.

Table 6.3.   Summary of the average depth and p_b values for the seven shale plays.

Shale play	Average depth (ft)	Fracture gradient (psi/ft)	Estimated p_b (psi)	Source
Barnett	6,500	0.60	3,900	Ketter et al. (2006)
Bakken	10,070	0.90	9,063	Schlumberger (2014)
Fayetteville	5,000	1.10	5,500	Lynk et al. (2017)
Haynesville	13,000	1.00	13,000	Hammes et al. (2011)
Niobrara	7,500	0.85	6,375	Koskella et al. (2015)
Marcellus	6,250	1.10	6,875	Barth et al. (2012)
Vaca Muerta	9,500	1.18	11,210	Kosset (2014)

6.3   MODELING OF THE LONGITUDINAL AND TRANSVERSE FRACTURING STRESSES

The semi-analytical procedure used in this study for calculating the fracturing stresses from perforated wells was first presented in Michael and Gupta (2020a). Numerical modeling is employed to develop correction factors for closed-form analytical expressions describing the variation of the longitudinal and transverse fracture-inducing stresses with p_w.

188

6.3.1 Closed-Form Analytical Approximations

Hossain et al. (2000) proposed an approximation of the stresses on the perforation base by performing a second "Kirsch analysis" using σ_{yy} and $\sigma_{\theta\theta}$ as inputs (Eq. 6.7) to derive an expression for $\sigma_{\theta\theta_p}$. Assuming that the pressure in the perforation tunnel is equal to p_w for a specific perforation angle, θ

$$\sigma_{\theta\theta_p}\Big|_\theta = \sigma_{yy}\Big|_{\theta,r=r_w} + \sigma_{\theta\theta}\Big|_{\theta,r=r_w} - 2\left(\sigma_{yy}\Big|_{\theta,r=r_w} - \sigma_{\theta\theta}\Big|_{\theta,r=r_w}\right)\cos 2\theta_p + p_p - p_w \quad (6.7)$$

with the longitudinal and transverse fracturing stresses ($\sigma_{\theta L}$ and $\sigma_{\theta T}$, respectively) hence defined as

$$\sigma_{\theta L}\big|_{\theta,p_w} \equiv \sigma_{\theta\theta_p}\Big|_{\theta,p_w,\theta_p=0°} \quad (6.8a)$$

$$\sigma_{\theta T}\big|_{\theta,p_w} \equiv \sigma_{\theta\theta_p}\Big|_{\theta,p_w,\theta_p=90°} \quad (6.8b)$$

Kirsch's (1898) theory is purely 2D, assuming a state of plane strain. Hossain et al.'s (2000) idea of applying this theory twice in an attempt to simulate a 3D problem could not yield analytically-exact solutions for $\sigma_{\theta L}$ and $\sigma_{\theta T}$. Hence, the derived expressions (Eqs. 6.8a and 6.8b) are called the "approximated" solutions of the two fracturing stresses.

The fracture initiation equations are examined using numbers typical for the Marcellus Shale. The tensile strength of the rock formation, T, is assumed to be zero with E at 200,000 psi and ν at 0.32. The graphical solution of the two fracturing stresses against p_w, $\sigma_{\theta L}|_{p_w}$ and $\sigma_{\theta T}|_{p_w}$, is shown on Figure 6.5 for the Marcellus Shale, demonstrating the effect of p_w on the two fracturing stresses. According to the analytical solution, as p_w

189

increases the $\sigma_{\theta T}$ indicated with the blue line stays constant but $\sigma_{\theta L}$, indicated by the red line, becomes more tensile (negative).
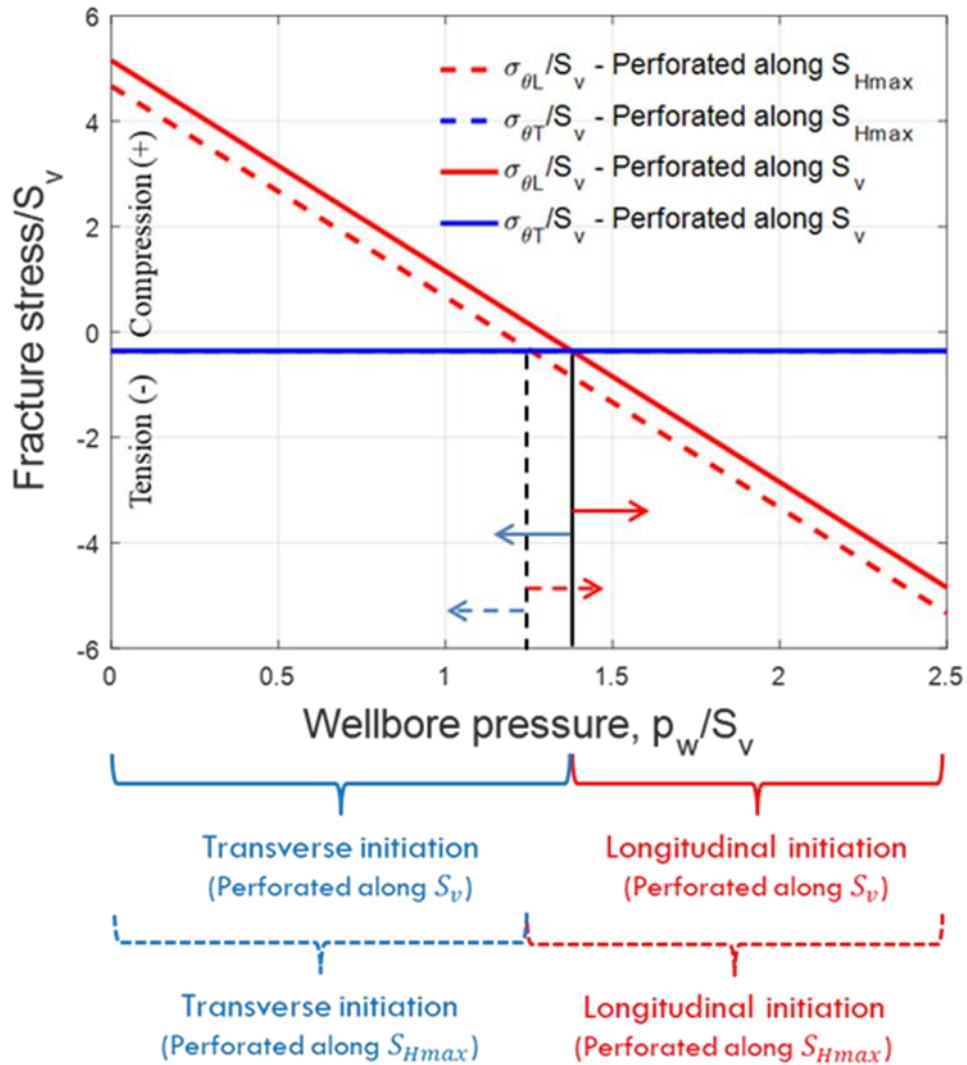
Figure 6.5. Variation of $\sigma_{\theta L}$ and $\sigma_{\theta T}$ with p_w for the Marcellus Shale stress state. For perforations parallel to S_v the p_b window is wider compared to perforations parallel to S_{Hmax}.

Following Michael et al.'s (2018) "p_b window" concept, if p_b (which is the highest pressure achieved during the hydraulic fracture treatment) falls within the region on the left of the $\sigma_{\theta L}$ and $\sigma_{\theta T}$ lines (red and blue, respectively) on Figure 6.5, transverse fracture initiation occurs because within this region, $\sigma_{\theta T} < -T = 0$ and $\sigma_{\theta T} = \sigma_{\theta L}$. For all purposes of this study, $T = 0$. If p_b is higher than the intersection of the $\sigma_{\theta L}$ and $\sigma_{\theta T}$ lines on Figure 6.5, longitudinal fracture initiation would occur because $\sigma_{\theta L}$ is more tensile than $\sigma_{\theta T}$ (i.e., $\sigma_{\theta T} > \sigma_{\theta L}$). If $\sigma_{\theta T} > -T = 0$ (i.e., compressive), no p_b window exists for transverse fracture initiation.

6.3.2   True-3D Numerical Solutions of $\sigma_{\theta L}|_{p_w}$ and $\sigma_{\theta T}|_{p_w}$

Numerical assessments performed using finite volume modeling (Michael et al., 2018; 2020; Michael, 2019a) indicated these approximated solutions to be error-bearing. A "true-3D" numerical model (Figure 6.6), built on *FLAC³D* (*Fast-Lagrangian Analysis of Continua in 3 Dimensions* by the Itasca Consulting Group), was presented in detail by Michael (2019a) and Michael et al. (2020). The true-3D numerical model was used to calculate the fully-exact solutions of $\sigma_{\theta L}|_{p_w}$ and $\sigma_{\theta T}|_{p_w}$, which features a 1/8th block model of height, H, length, L, width, W and includes a cylindrical wellbore of radius, r_w, intersected by a cylindrical perforation tunnel of radius, r_{perf}. The block model's relative geometry is stated in Figure 6.6.
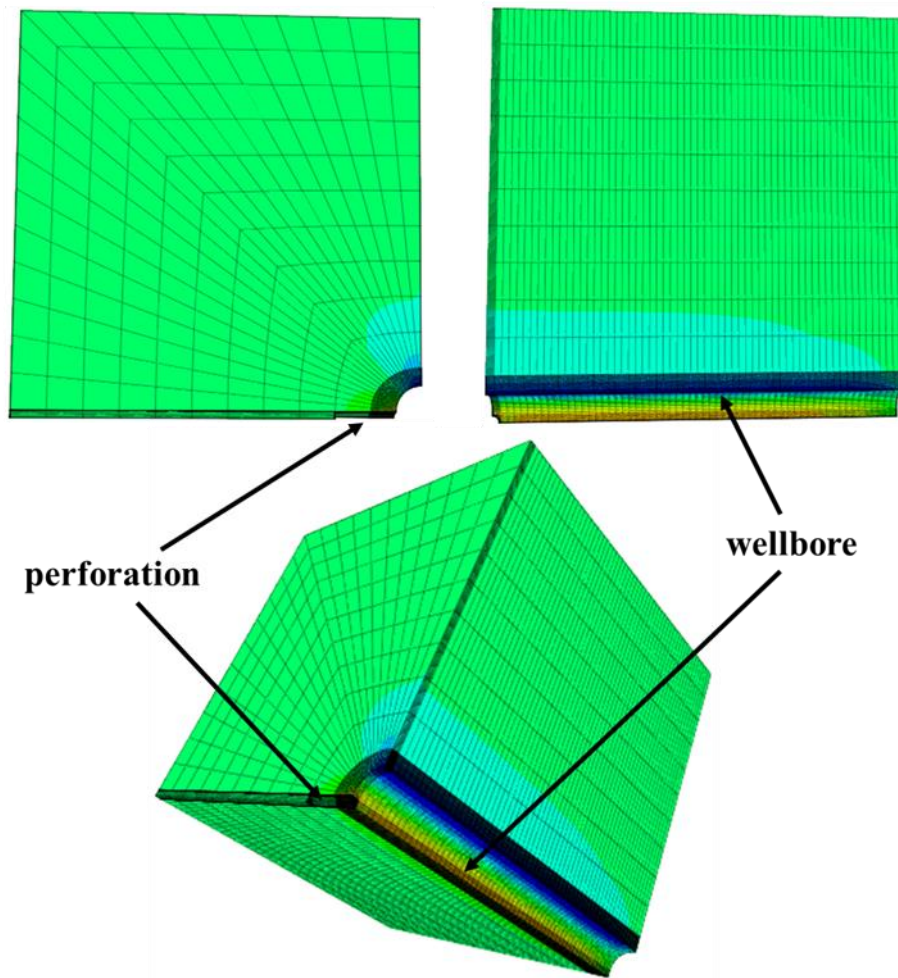
Figure 6.6. The true-3D numerical model written in $FLAC^{3D}$ and used to calculate $\sigma_{\theta L}|_{p_w}$ and $\sigma_{\theta T}|_{p_w}$ for the seven shale plays.

The simulations performed using the true-3D numerical model showed the stresses on the perforation base with variation in the p_w differing considerably with Hossain et al.'s (2000) analytical expressions (Michael et al., 2018; 2020; Michael, 2019a). In all simulations, $p_{perf} = p_w$. Increased compression with increasing p_w for $\sigma_{\theta T}$ was interpreted to be caused by the interaction between the σ_{rr} around the wellbore and the σ_{rr}

around the perforation. The way those σ_{rr} mutually interact alters the stress field around the wellbore, which in turn changes $\sigma_{\theta\theta_p}$ from which $\sigma_{\theta L}$ and $\sigma_{\theta T}$ are calculated.

The numerically-calculated exact solutions of $\sigma_{\theta L}|_{p_w}$ and $\sigma_{\theta T}|_{p_w}$ for the geomechanical parameters of the Marcellus Shale (Figure 6.7) shows $\sigma_{\theta T}$ becoming more compressive (positive) as p_w increases and $\sigma_{\theta L}$ becoming more tensile (negative), but at a shallower slope than what the analytical approximation (Hossain et al., 2000) dictates. This creates an additional constraint to transverse fracture initiation besides the p_b window. That is critical tensile strength, T_{crit}, which is equal to $\sigma_{\theta T}|_{p_w=0}$ and represents the maximum T at which transverse fracture initiation is possible (Figure 6.7). At $T > T_{crit}$, transverse fracture initiation is impossible, independent of the p_b.

Figure 6.7 suggests that pressurization of the wellbore yields to transverse fracture initiations from the top of the hole ($\theta = 0°$, S_v direction) at $p_w/S_v = 0.50$, which justifies the use of oriented perforating in this direction for the Marcellus Shale, despite the low anisotropy between S_v and S_{Hmax}. The effectiveness of oriented perforating strategies is expected to increase with ($S_v - S_{Hmax}$) anisotropy (Kurdi, 2018; Michael et al., 2020). The calculated p_i value is in close proximity with p_p and it is to be noted that if $p_p < 0.48S_v$ transverse fracture initiation would occur from perforations on the side of the borehole ($\theta = 90°$, S_{Hmax} direction).
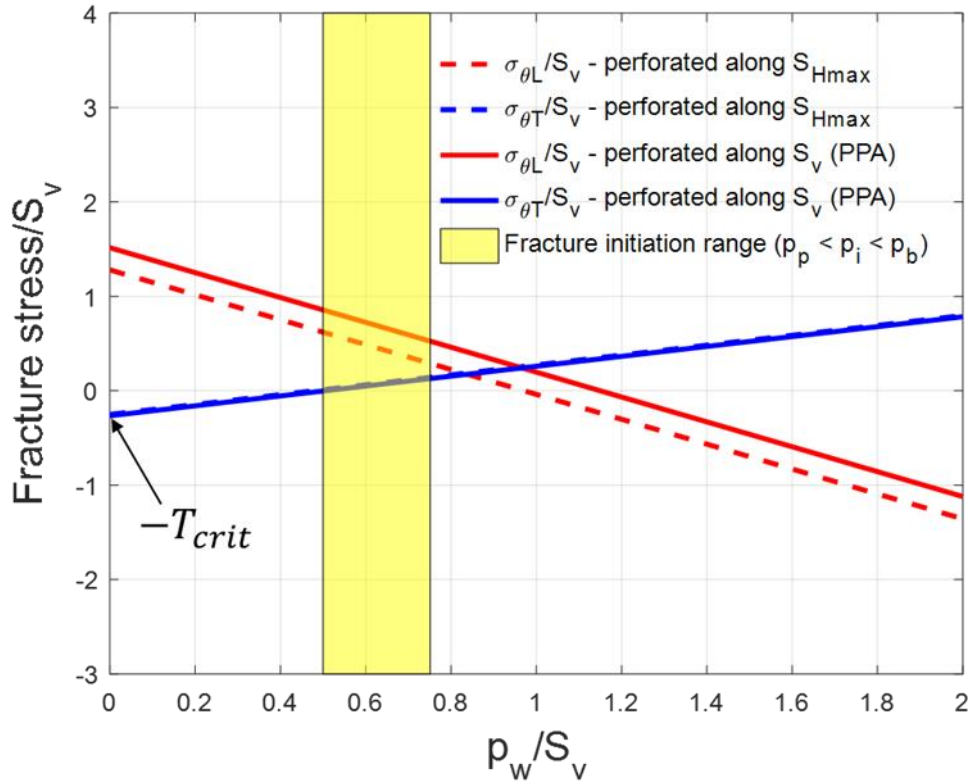
Figure 6.7.   Variation of $\sigma_{\theta L}$ and $\sigma_{\theta T}$ with p_w for the *in-situ* conditions of the Marcellus Shale calculated by the true-3D numerical model with the yellow region indicating the p_i range.

6.3.3 Numerically-Developed Correction Factors

Because the Hossain et al.'s analytical approximations yield straight lines for $\sigma_{\theta L}|_{p_w}$ and $\sigma_{\theta T}|_{p_w}$ just as the exact 3D solutions do, the approximated expressions can be made to match the numerical solutions by one hundred percent via the application of a set of correction factors.

For each play at a fixed well trajectory, these correction factors vary with perforation direction, θ. Therefore, two sets of two correction factors are necessary to evaluate $\sigma_{\theta L}|_{p_w}$ and $\sigma_{\theta T}|_{p_w}$ from the two perforation direction extremes; a total of four for

a specific θ. For a well drilled parallel to S_{hmin} and perforated along S_{Hmax} ($\theta = 90°$), $\sigma_{\theta L}|_{p_w}$ and $\sigma_{\theta T}|_{p_w}$ are given by

$$\sigma_{\theta L}|_{\theta=90°} = 9S_v - 3S_{Hmax} - S_{hmin} + 2v(S_{Hmax} - S_v) - p_p - 4p_w$$
$$+ [C_m]_{\sigma_{\theta L}|_{\theta=90°}} p_w + [C_c]_{\sigma_{\theta L}|_{\theta=90°}}$$

(6.9a)

$$\sigma_{\theta T}|_{\theta=90°} = 3S_{hmin} - S_{Hmax} - S_v - (2 - 6v)(S_v - S_{Hmax}) - p_p$$
$$+ [C_m]_{\sigma_{\theta L}|_{\theta=90°}} p_w + [C_c]_{\sigma_{\theta L}|_{\theta=90°}}$$

(6.9b)

where, C_m is ths correction factor on the slope of the $\sigma_{\theta L}$ or $\sigma_{\theta T}$ line with p_w and C_c is the correction factor on the vertical intercept at $p_w = 0$. Similar expressions with their respective correction factors C_m or C_c can be written for any well trajectory, as well as perforation direction.

6.3.4 Orienting Perforations to Promote Transverse Fracture Initiation or Minimize p_i

The preferred perforation alignment (PPA) is a concept introduced by Michael and Gupta (2019), where a perforation direction is identified as optimal considering the promotion of favourable fracture initiation *vis-à-vis* orientation (transverse to a horizontal well drilled parallel to S_{hmin}). The PPA direction (Figure 6.8) depends on the *in-situ* stress regime (Anderson, 1951). For normal faulting stress states such as the Barnett Shale, PPA is parallel to S_{Hmax} (side of the hole), whereas for strike-slip faulting stress states such as the Marcellus Shale, PPA is parallel to S_v (top of the hole).

Kurdi (2018) developed a computational model for predicting p_b in unconventional shale plays. The simulation results indicated minimum p_b to occur for perforations parallel

195

to S_{Hmax} for normal faulting stress states and parallel to S_v for strike-slip faulting stress states – same as PPA. Oriented perforating (Figure 6.9) is a practically easy-to-implement technique that can potentially exploit the performance variation between different perforation directions in order to promote favorable fracture initiation, optimizing for either transverse fracture initiation promotion or p_i and thus p_b minimization.
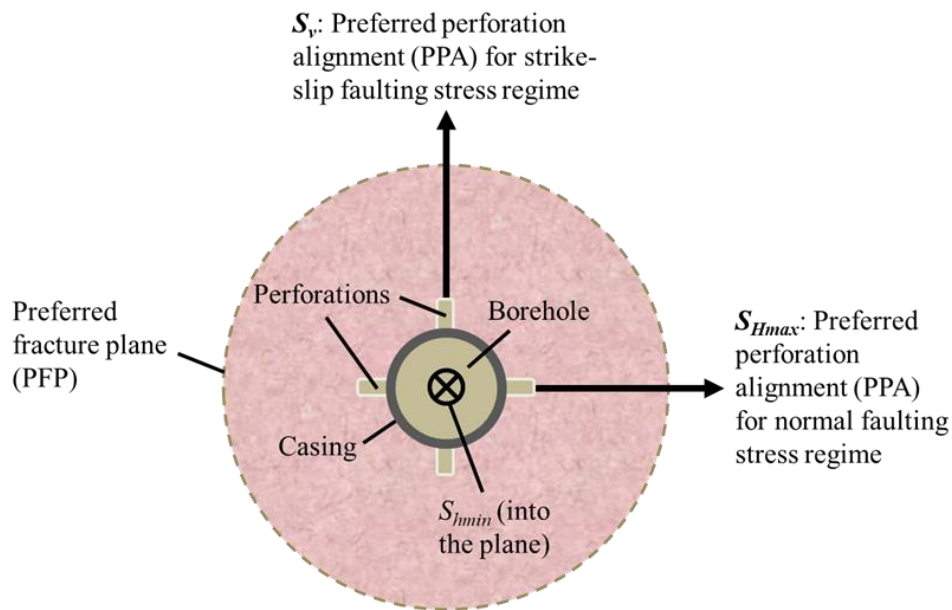
Figure 6.8. The preferred perforation alignment (PPA) configurations for horizontal wellbores drilled parallel to S_{hmin} under normal and strike-slip faulting stress regimes (modified from Michael and Gupta, 2019e).

(i) Oriented perforating on the top/bottom of the borehole (along $S_v, \theta = 0°$)

(ii) Oriented perforating on the sides of the borehole (along $S_{Hmax}, \theta = 90°$)
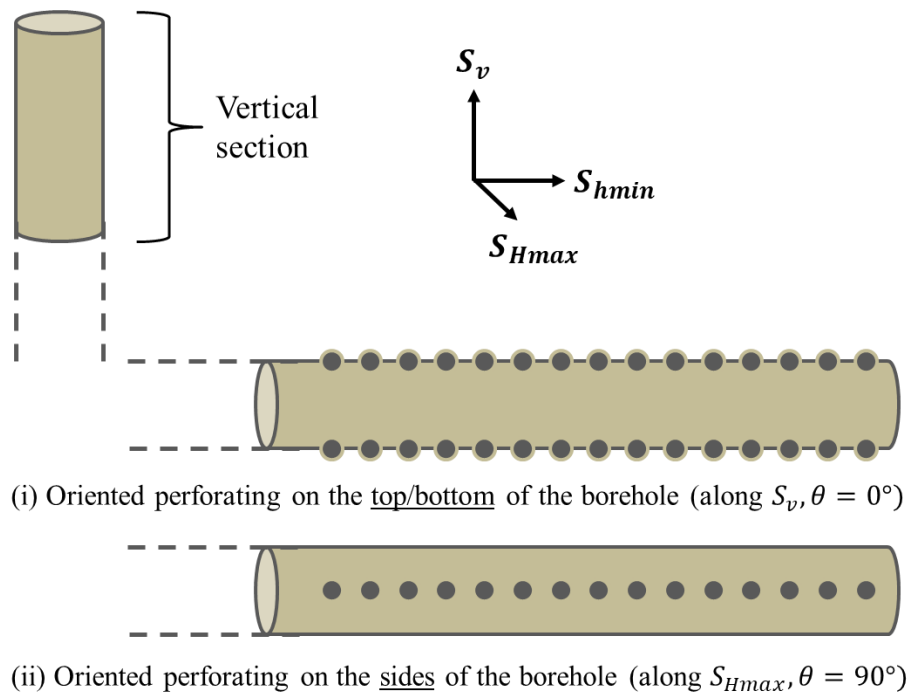
Figure 6.9.   Oriented perforating configurations for horizontal wells drilled parallel to S_{hmin} in locations under stress regimes that obey Anderson's (1951) theory.

Although the p_b window concept implies that transverse fracture initiation, when possible, occurs at lower the p_b values, perforations along PPA would not yield the lowest p_i and subsequently the lowest p_b, presuming a direct correlation between the two (Zoback et al., 1977; Weijers, 1995; Zhuang et al., 2018) in scenarios were transverse fracture initiation is impossible. When longitudinal fracture initiation is the only possible outcome due to the upper-bound of the p_b window being lower than LOP, then p_i will be minimized from perforations orthogonal to PPA, in what is called the non-PPA direction (Michael and Gupta, 2019e).

6.4   RESULTS

6.4.1   Normal Faulting Stress States

The Barnett, Bakken, Fayetteville, Haynesville and Niobrara (Table 6.2) are shale formations located in the United States (Figure 6.3) that are under normal faulting *in-situ* stress states where $S_v > S_{Hmax} > S_{hmin}$. The PPA for these formations is thus in the S_{Hmax} direction (Figure 6.8). Table 6.4 summarizes the C_m and C_c values for these five shale gas plays. Figure 6.10 shows the graphical solutions of $\sigma_{\theta L}|_{p_w}$ and $\sigma_{\theta T}|_{p_w}$ and the p_i range bounded from p_p (Table 6.2) due to absence of reliable and consistent LOP data to p_b (Table 6.3).

Table 6.4.   Numerically-developed correction factors for the shale plays, studied that are under normal faulting stress states.

(a) Barnett	C_m	C_c	Perforation direction
$\sigma_{\theta L}|_{\theta=0°}$	2.6752	-13,157.54	Non-PPA
$\sigma_{\theta T}|_{\theta=0°}$	0.5226	1,657.6	Non-PPA
$\sigma_{\theta L}|_{\theta=90°}$	2.6794	-28,013.4	PPA
$\sigma_{\theta T}|_{\theta=90°}$	0.5221	424.8	PPA

(b) Bakken	C_m	C_c	Perforation direction
$\sigma_{\theta L}|_{\theta=0°}$	2.5948	-36,951.7	Non-PPA
$\sigma_{\theta T}|_{\theta=0°}$	0.2513	2231.04	Non-PPA
$\sigma_{\theta L}|_{\theta=90°}$	2.6015	-38,615.1	PPA
$\sigma_{\theta T}|_{\theta=90°}$	0.2532	2121.06	PPA

(c) Fayetteville	C_m	C_c	Perforation direction
$\sigma_{\theta L}\|_{\theta=0°}$	2.5284	-13,359.4	Non-PPA
$\sigma_{\theta T}\|_{\theta=0°}$	-0.0211	1,152.86	Non-PPA
$\sigma_{\theta L}\|_{\theta=90°}$	2.5289	-17,090.3	PPA
$\sigma_{\theta T}\|_{\theta=90°}$	-0.0207	892.44	PPA

(d) Haynesville	C_m	C_c	Perforation direction
$\sigma_{\theta L}\|_{\theta=0°}$	2.6829	-46,534.3	Non-PPA
$\sigma_{\theta T}\|_{\theta=0°}$	0.5252	-30.96	Non-PPA
$\sigma_{\theta L}\|_{\theta=90°}$	2.6812	-50,522.1	PPA
$\sigma_{\theta T}\|_{\theta=90°}$	0.5231	-345.66	PPA

(e) Niobrara	C_m	C_c	Perforation direction
$\sigma_{\theta L}\|_{\theta=0°}$	2.6826	-16,631.7	Non-PPA
$\sigma_{\theta T}\|_{\theta=0°}$	0.5244	420.59	Non-PPA
$\sigma_{\theta L}\|_{\theta=90°}$	2.6693	-26,333.1	PPA
$\sigma_{\theta T}\|_{\theta=90°}$	0.5244	-365.28	PPA

[a] <u>PPA:</u> along S_{Hmax} and S_v for a well drilled parallel to S_{hmin} in a normal and strike-slip faulting stress regime, respectively. Location where transverse fracture initiation is promoted the most.

[b] <u>Non-PPA:</u> along S_v and S_{Hmax} for a well drilled parallel to S_{hmin} in a normal and strike-slip faulting stress regime, respectively. Location where transverse fracture initiation is least promoted.
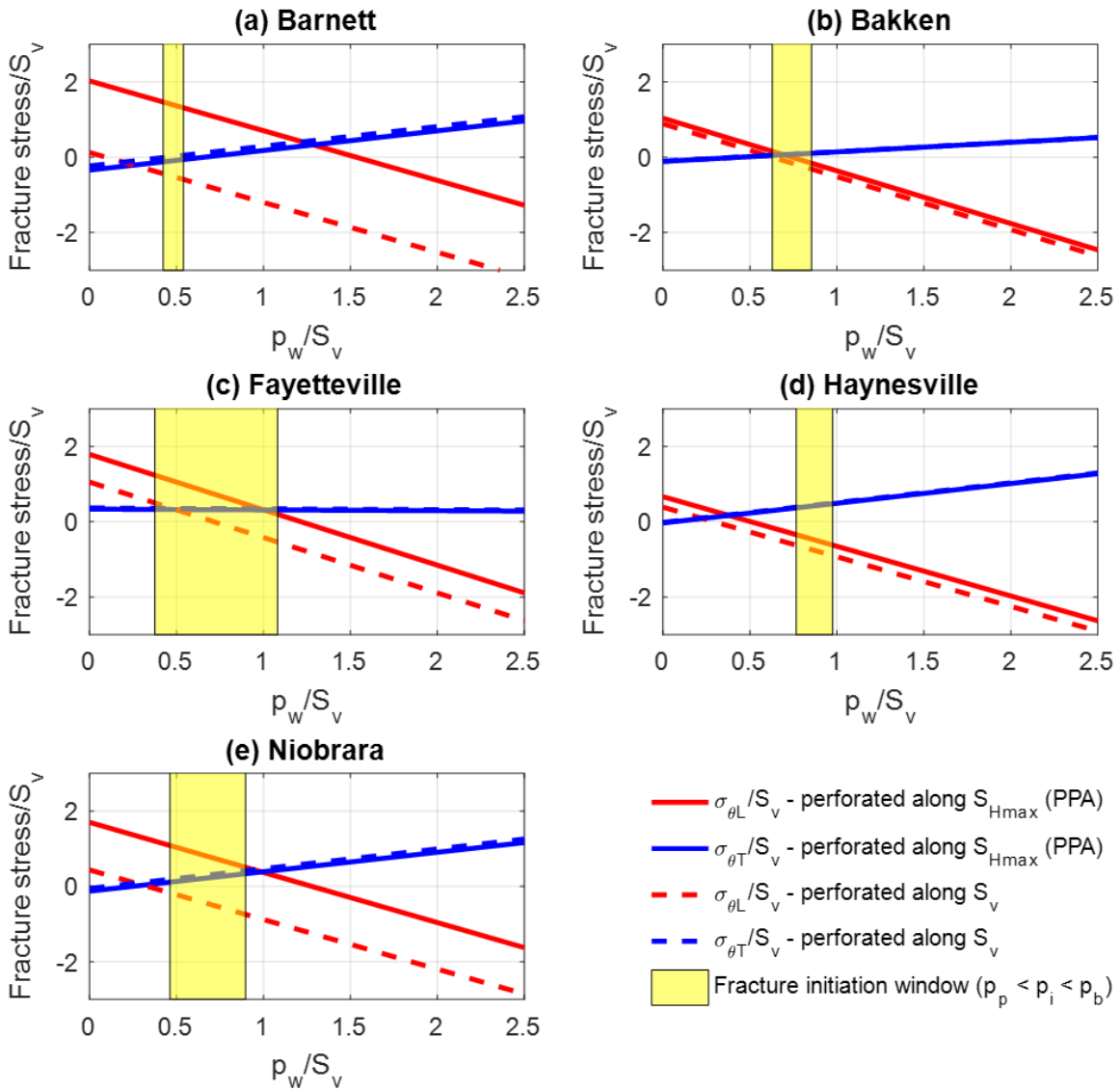
Figure 6.10. The exact 3D solutions of $\sigma_{\theta L}|_{p_w}$ and $\sigma_{\theta T}|_{p_w}$ for the five of the seven shale gas plays studied, which are under normal faulting stress states. The yellow-shaded region shows the p_i range ($p_p < p_i < p_b$).

6.4.2 Strike-Slip Faulting Stress States

The Marcellus in the United States and Vaca Muerta in Argentina (Table 6.2, Figure 6.3) are two shale formations where the *in-situ* stress state is strike-slip faulting with $S_{Hmax} > S_v > S_{hmin}$. The PPA for horizontal wells aligned with S_{hmin} in these plays is parallel to S_v (Figure 6.8). Table 5 summarizes the C_m and C_c values for these two shale gas plays. The graphical solutions of $\sigma_{\theta L}|_{p_w}$ and $\sigma_{\theta T}|_{p_w}$ is shown on Figure 6.11, with the p_i range shaded in yellow bounded by p_p and p_b (Tables 6.2 and 6.3, respectively).

Table 6.5.   Numerically-developed correction factors for the shale plays studied that are under strike-slip faulting stress states.

(a) Marcellus	C_m	C_c	Perforation direction
$\sigma_{\theta L}|_{\theta=0°}$	2.6824	-33,289.8	PPA
$\sigma_{\theta T}|_{\theta=0°}$	0.5243	875.22	PPA
$\sigma_{\theta L}|_{\theta=90°}$	2.6815	-30,979.2	Non-PPA
$\sigma_{\theta T}|_{\theta=90°}$	0.5243	1,068.98	Non-PPA

(b) Vaca Muerta	C_m	C_c	Perforation direction
$\sigma_{\theta L}|_{\theta=0°}$	2.6818	-31,138.2	PPA
$\sigma_{\theta T}|_{\theta=0°}$	0.5235	1085.58	PPA
$\sigma_{\theta L}|_{\theta=90°}$	2.6817	-30,863.8	Non-PPA
$\sigma_{\theta T}|_{\theta=90°}$	0.5235	868.72	Non-PPA

[a] PPA: along S_{Hmax} and S_v for a well drilled parallel to S_{hmin} in a normal and strike-slip faulting stress regime, respectively. Location where transverse fracture initiation is promoted the most.

[b] Non-PPA: along S_v and S_{Hmax} for a well drilled parallel to S_{hmin} in a normal and strike-slip faulting stress regime, respectively. Location where transverse fracture initiation is least promoted.
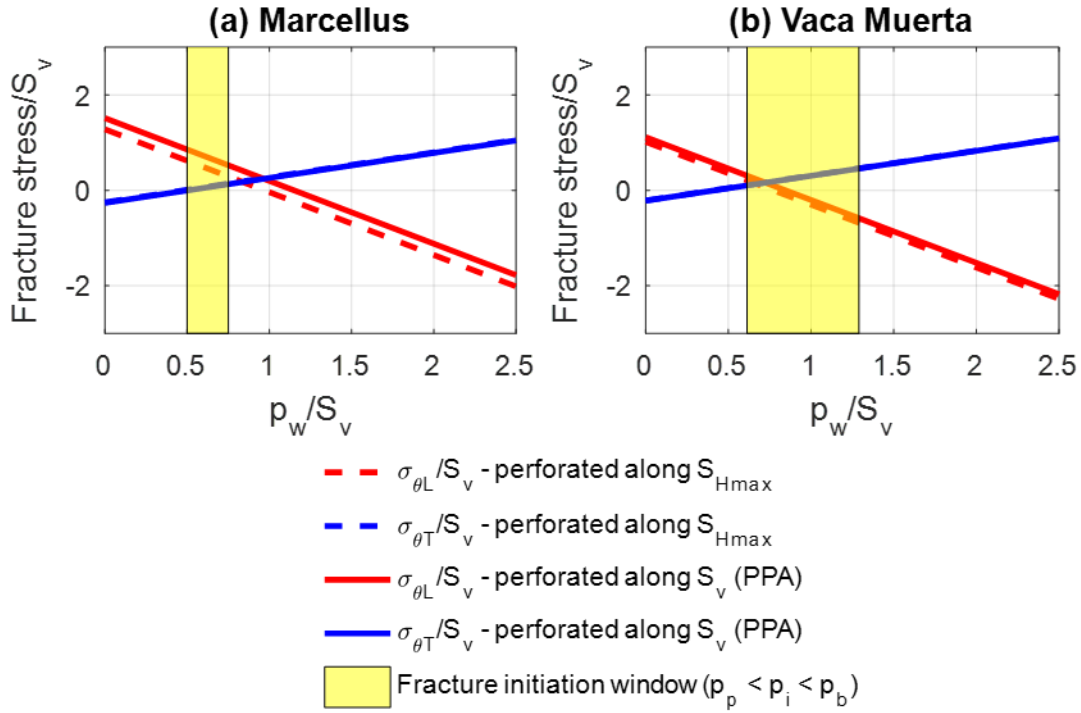
Figure 6.11. The exact 3D solutions of $\sigma_{\theta L}|_{p_w}$ and $\sigma_{\theta T}|_{p_w}$ for the two shale gas plays that are under strike-slip faulting stress states. Similar to Figure 6.10, the p_i range ($p_p < p_i < p_b$) is shown by the yellow-shaded region.

6.4.3 Orientation of Fracture Initiation, p_i, and Optimal Perforation Direction

Figures 6.10 and 6.11 can be used to provide an indication of the (i) p_i value, (ii) orientation of fracture initiation, and (iii) the perforation direction at which the fracture initiation takes place from each shale gas play. Table 6.5 summarizes these results for $T = 0$, $E = 200{,}000$ psi, and $\nu = 0.32$. Transverse fracture initiation is predicted only for two of the seven shale gas plays; the Barnett and the Marcellus (Figures 6.10 and 6.11), from perforations parallel to the respective PPA for each play (along S_{Hmax}, $\theta = 90°$ for the Barnett and along S_v, $\theta = 0°$, for the Marcellus Shale).

202

Longitudinal fracture initiation is predicted for the Bakken and Fayetteville Shales (Figure 6.10) as well as for the Vaca Muerta Shale (Figure 6.11). However, for the Bakken and Fayetteville Shales, fracture initiation is expected from perforations at the top of the borehole, which is the non-PPA direction for normal faulting stress states (along S_v, $\theta = 0°$), while for the Vaca Muerta Shale, fracture initiation is expected from perforations on the side of the borehole (parallel to S_{Hmax}, $\theta = 90°$); the non-PPA direction for strike-slip faulting stress states. The cases of the Haynesville and Niobrara Shales are more complex (Figure 6.10) with none of the four fracture initiation lines crossing the line for $T = 0$ within the p_i range. Thus, the most tensile of the four fracturing stresses dictates fracture initiation and orientation. Hence, longitudinal fracture initiation is expected from the top of the borehole (S_v direction, $\theta = 0°$) in both the Haynesville and Niobrara Shales (Figure 6.10), which is the non-PPA direction. The longitudinal fracture initiation predictions for the five of the seven shale gas plays (Bakken, Fayetteville, Haynesville, Niobrara, and Vaca Muerta), is expected to lead to either (i) premature termination of the fracture growth, or (ii) reorientation as the fracture propagates away from the wellbore (Economides and Martin, 2010; Michael, 2019a; Michael et al., 2020), when the *in-situ* (far-field) stresses begin to gradually dominate over the near-wellbore stresses (Kirsch, 1898). This subsequently generates near-wellbore tortuosity, which can be problem-bearing yielding short-term completion-related problems, such as early screenouts and long-term production-related problems such as poor post-stimulation well performance (Barree and Miskimins, 2015).

The modeling results provide motivation for the use of oriented perforating strategies (Figure 6.9) for either (i) promoting transverse fracture initiation, or (ii) when transverse fracture initiation is impossible, minimizing p_i and hence suppressing surface pumping horsepower and stimulation treatment costs. This is useful for completion

engineers; fracturing operations in wells perforated at a single, fixed phase angle, can achieve treatment pressure minimization or optimal fracture initiation orientation maximizing the stimulation treatment's net present value. The fourth column on Table 6.5 indicates the optimal oriented perforating direction with the reasoning the reasoning stated on the fifth column.

Table 6.6.   Predicted orientation of fracture initiation, p_i, and optimal oriented perforating direction forthe shale plays studied.

Shale play	Fracture initiation	p_i (psi)	Optimal perforation direction	Objective
Barnett	Transverse	<4,754	S_{Hmax} (PPA)	Transverse fracture initiation
Bakken	Longitudinal	6,689	S_v (non-PPA)	Minimize p_i
Fayetteville	Longitudinal	3,643	S_v (non-PPA)	Minimize p_i
Haynesville	Longitudinal	>10,200	S_v (non-PPA)	Minimize p_i
Niobrara	Longitudinal	>3,283	S_v (non-PPA)	Minimize p_i
Marcellus	Transverse	<4,615	S_v (PPA)	Transverse fracture initiation
Vaca Muerta	Longitudinal	6,711	S_{Hmax} (non-PPA)	Minimize p_i

Determining the optimal perforating strategy for promoting transverse fracture initiation may not lead to the minimum p_i and vice versa. Promotion of transverse fracture initiation suppresses near-wellbore tortuosity, which as mentioned earlier, can be highly problematic for fracture treatments (Economides and Martin, 2010; Barree and Miskimins, 2015; Michael, 2019a; Michael et al., 2020). Nevertheless, there are also numerous incentives for keeping p_i minimum regardless of the orientation of fracture initiation. In extreme stress state magnitudes and especially hard (high T) rock, fracture initiation *per se*, is difficult. High p_i leads to high p_b, which can negatively impact perforation efficiency in a multi-stage fracture treatment, where a main goal is to accomplish uniform fluid flow between clusters. Reservoir layering and heterogeneity of elastic properties generate variance in p_i and subsequently p_b across different areas of the reservoir even within the

horizontal lateral of a well. If p_b values are high, once fracture initiation is induced within a few perforation clusters, p_w falls off, making further fracture initiation from the remaining perforation clusters harder. Limited entry is often employed to help mitigate this, but as p_b increases, more and more limited entry is required, resulting in lower perforation efficiency and eventually lower production.

Figure 6.12 shows the variation of two types of fracture stresses against perforation direction (given by θ) for the Barnett and the Marcellus; p_i for longitudinal fracture initiation and $p_{b,upper}$ in regards to transverse fracture initiation. These are the two shale gas plays, where our analysis suggested that oriented perforating can be used to promote transverse fracture initiation. The two lines show p_i for longitudinal fracture initiation calculated without the correction factor set (the p_w value at which $\sigma_{\theta L} = -T$), yielding minimum values at the corresponding non-PPA point for each play; $\theta = 0°$ for the Barnett and $\theta = 90°$ for the Marcellus. The four red points added on Figure 6.12, indicate the numerically corrected values at the two extreme perforation directions, for which correction factors were calculated (Tables 6.4a and 6.5a). Although not overlapping the line, the relative trend is preserved with the non-PPA direction resulting in the lowest p_i for longitudinal fracture initiation.
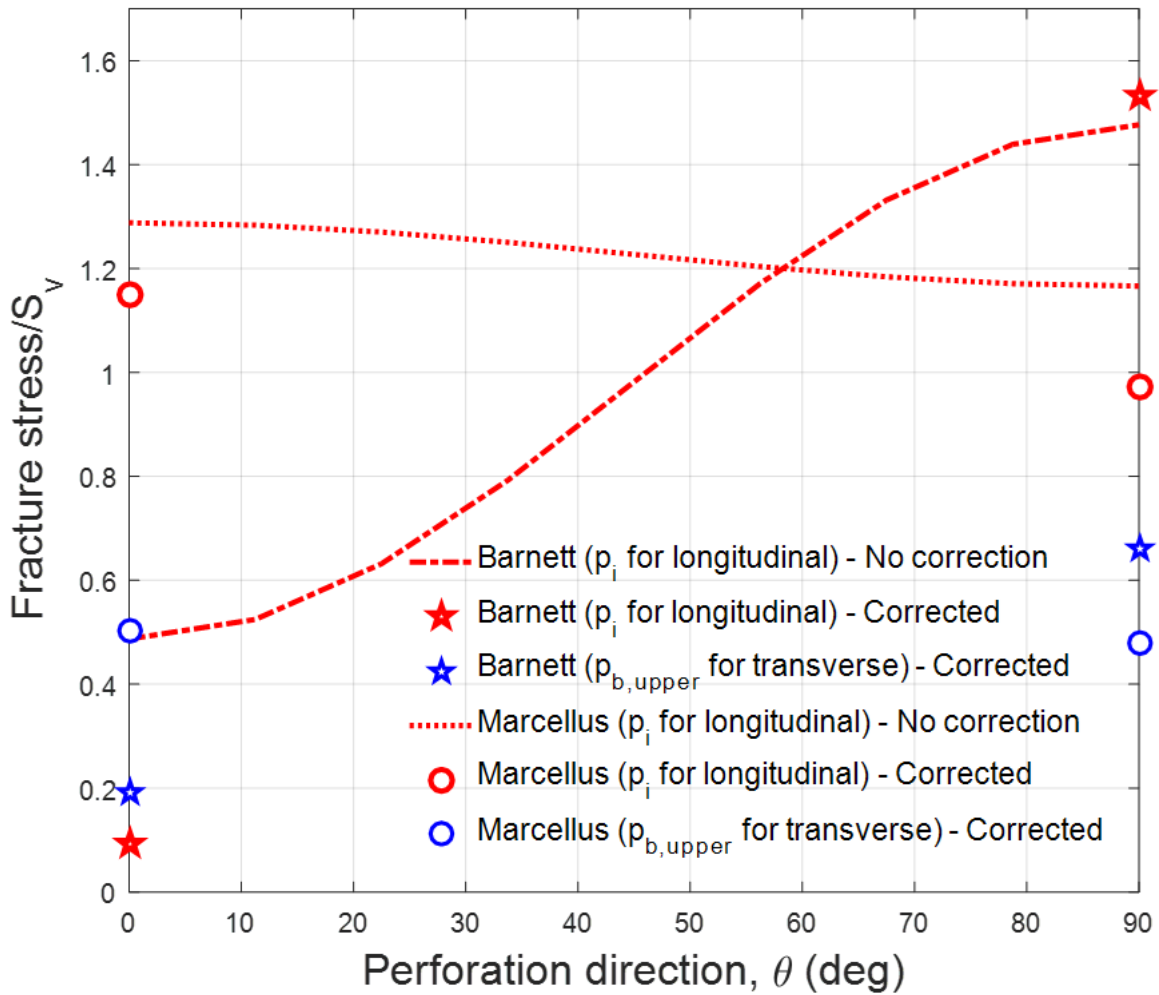
Figure 6.12. Diagram showing two types of fracture stress; the p_i for longitudinal fracture initiation and the $p_{b,upper}$ for transverse fracture initiation. In both cases presented (the Barnett and Marcellus Shale plays), the p_i for longitudinal fracture initiation is minimized for perforations in the non-PPA, while the $p_{b,upper}$ for transverse fracture initiation is maximized for perforations in the PPA direction.

Due to the non-corrected version of $\sigma_{\theta T}$ not containing p_w terms, p_i values for transverse fracture initiation cannot be calculated. The blue points added on Figure 6.12 indicate the $p_{b,upper}$ (the smallest p_w value at which either $\sigma_{\theta T} = -T$ or $\sigma_{\theta T} = \sigma_{\theta L}$) in

206

regards to transverse fracture initiation for the two extreme perforation directions for which correction factors were calculated (Tables 6.4a and 6.5a). For each shale play, $p_{b,upper}$ is maximized along the PPA direction, suggesting that perforations oriented in this direction ($\theta = 90°$ for the Barnett and $\theta = 0°$ for the Marcellus) enhance the likelihood of achieving transverse fracture initiation. For practicality, all p_i and $p_{b,upper}$ values reported are normalized by S_v.

6.5   DISCUSSION

6.5.1   Leakage of Fracturing Fluid around the Wellbore

For situations where fracturing fluid may leak around the cross-section of a wellbore (Alabbad, 2014; Barree and Miskimins, 2015; Michael, 2016b) generating possibilities of fracture initiation from all around the wellbore, the presence of the perforation must be "ignored" and the problem's geometry is simplified to the extent at which a fully-analytical solution can be defined. If the perforation is ignored, $\sigma_{yy}\big|_{p_w}$ and $\sigma_{\theta\theta}\big|_{p_w}$ will determine the orientation of fracture initiation substituting $\sigma_{\theta T}\big|_{p_w}$ and $\sigma_{\theta L}\big|_{p_w}$ respectively, as the transverse and longitudinal-inducing fracturing stresses (Figures 6.13a and 6.13b). This "reduces" the problem to that of drilling-induced tensile fractures (DITFs) for linearly elastic rock model (Nelson et al., 2005) and p_i can be given only for longitudinal fracture initiation, as

$$p_i|_\theta = min[S_v + S_{Hmax} - 2(S_{Hmax} - S_v)\cos 2\theta - p_p + T] \qquad (6.10)$$

Using the Marcellus Shale as an example, $\sigma_{yy}\big|_{p_w} > 0$, both the p_b window and

T_{crit} constraints for transverse fracture initiation vanish, suggesting that transverse fracture

initiation is impossible for oriented perforating either along S_v (Figure 6.13a) or along

S_{Hmax} (Figure 6.13b). Also, the intersection point of $\sigma_{\theta\theta}$ and σ_{yy} represents a compressive

(positive) stress. This leads to longitudinal fracture initiation taking place at $p_w/S_v = 1.45$

(Figure 6.13a) and $p_w/S_v = 1.64$ (Figure 6.13b) for wells perforated along S_v and S_{Hmax},

respectively This translates to a 190% (Figure 6.13a) and 228% (Figure 6.13b) increase

compared to p_i expected with no fracturing fluid leaks around the well (Figure 6.7).
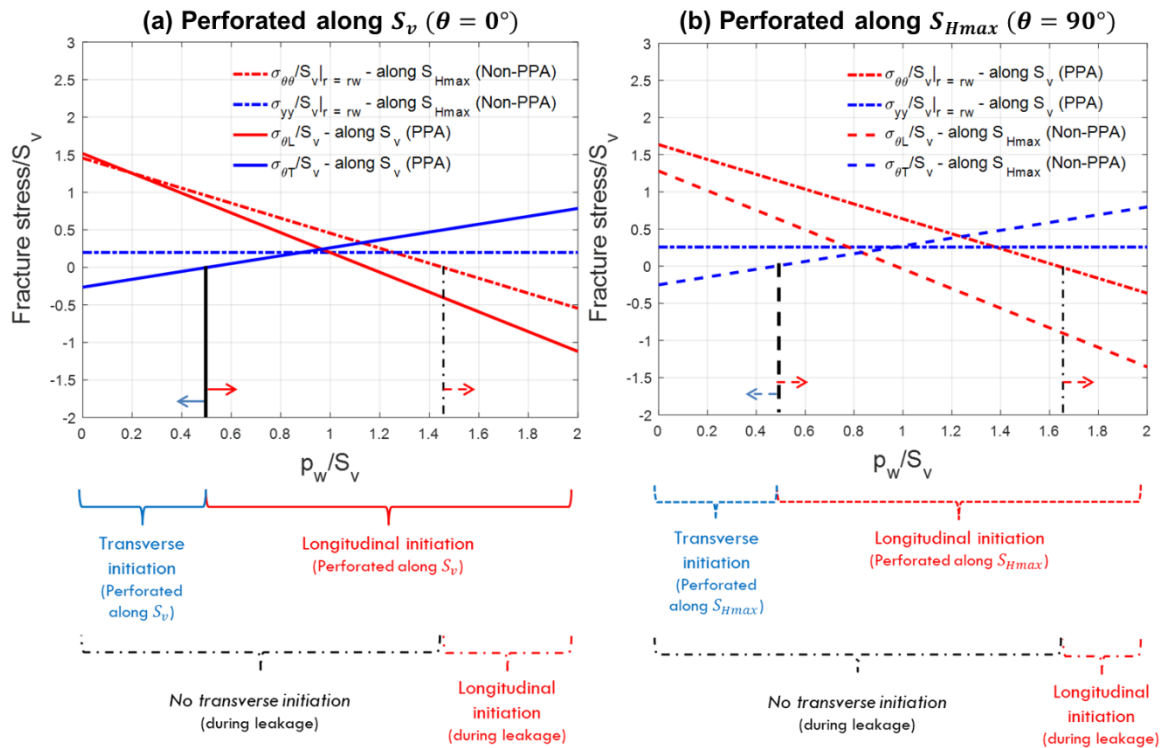
Figure 6.13. Comparison between the longitudinal fracture-inducing $\sigma_{\theta\theta}$ and the transverse fracture-inducing σ_{yy} (dash-dotted lines) and $\sigma_{\theta L}$ and $\sigma_{\theta T}$ for (a) perforations parallel to S_v (PPA) and (b) perforations parallel to S_{Hmax} (non-PPA), for the Marcellus Shale. During fracturing fluid leakage, both the p_b window and T_{crit} for vanish making transverse fracture initiation for the Marcellus Shale impossible.

For the Barnett Shale, the fracturing fluid leakage analysis is presented on Figure 6.14a and b. Similar to Figures 6.11a and 6.11b, fracturing fluid leakage around wellbores perforated along S_v (Figure 6.14a), makes the p_b window to vanish, making transverse fracture initiation impossible during leakage.
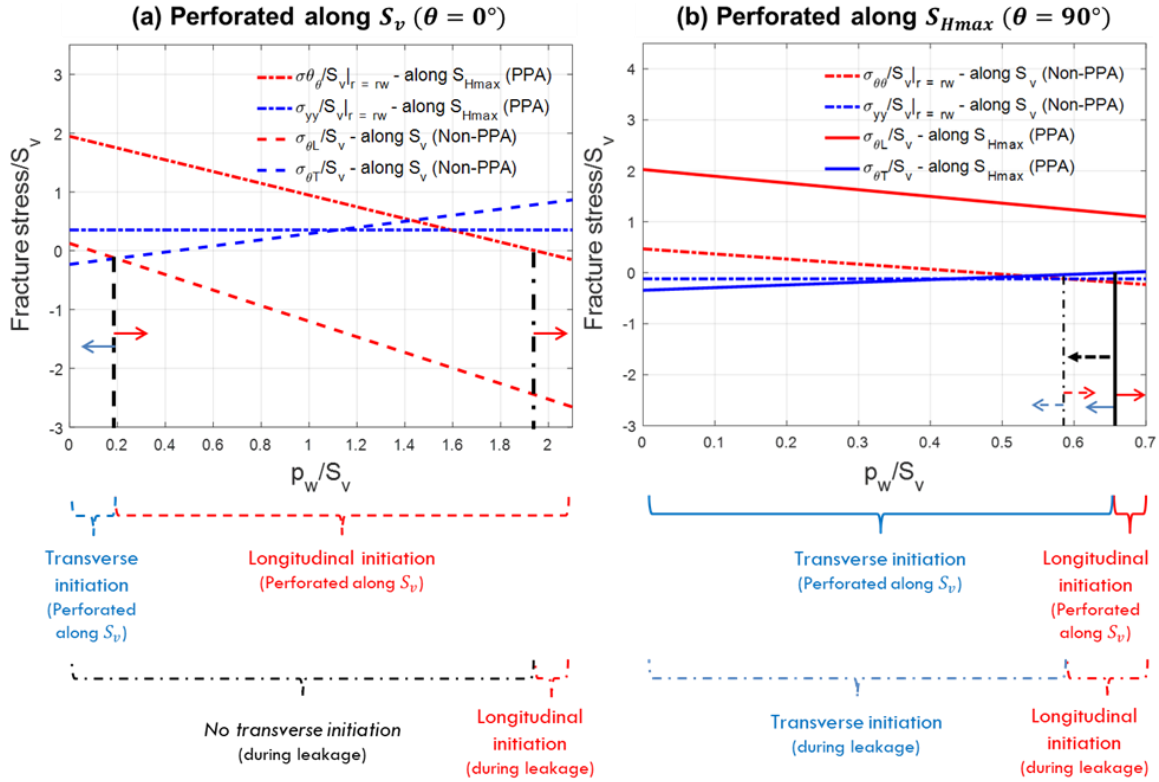
Figure 6.14. Comparison between the longitudinal fracture-inducing $\sigma_{\theta\theta}$ and the transverse fracture-inducing σ_{yy} (dash-dotted lines) and $\sigma_{\theta L}$ and $\sigma_{\theta T}$ for (a) perforations parallel to S_v (PPA) and (b) perforations parallel to S_{Hmax} (non-PPA), for the Barnett Shale. During fracturing fluid leakage, both the p_b window and T_{crit} for vanish for (a) making transverse fracture initiation impossible, while for (b) both the p_b window and T_{crit} decrease, making transverse fracture initiation harder to achieve.

Longitudinal fracture initiation takes place at $p_i = 1.97S_v$ (Figure 6.14a), a 294% increase from the p_i of the no fracturing fluid leakage scenario (Figure 6.7). Nevertheless, for perforations along S_{Hmax} (PPA for the Barnett Shale) the p_b window does not vanish, yet still shrinks by 12% (Figure 6.14b) compared to the p_b window when no fracturing fluid leakage occurs (Figure 6.7).

6.5.2   Rock Anisotropies and Natural Fractures

Stress and elastic properties anisotropy will strongly impact fracture propagation. Fracture initiation, which is the focus of this study, the stress and elastic property values to the analytical expressions (Eqs. 6.9a and 6.9b) must hold true for the fracture initiation location, assumed to be the perforation base. Rock formations such as shale tend to exhibit vertical transverse isotropy (VTI) with E parallel to the bedding layers often much higher than perpendicular to the bedding (Waters et al., 2011; Sone and Zoback, 2013). Studies (Karpfinger et al., 2011; Zhu et al., 2014; Sesetty, and Ghassemi, 2018) showed that VTI in E and v influences the magnitudes of $\sigma_{\theta\theta}$ and σ_{yy} on the wellbore radius impacting DITF initiation in VTI formations. Consequently, $\sigma_{\theta\theta_p}$ on the perforation base will be influenced (and hence the magnitudes of $\sigma_{\theta L}$ and $\sigma_{\theta T}$), impacting fracture initiation from perforated wells.

Interactions between induced hydraulic fractures with natural fractures were examined in experimental and numerical studies (Lee et al., 2015). The presence of a propagating hydraulic fracture may lead to either (i) crossing, (ii) divergence, or (iii) step-over, depending on various parameters such as the angle at which the fractures meet and the minerals present in the natural fracture, for instance calcite. Nonetheless, this falls into topics related to fracture propagation, beyond the scope of this study, which focuses on

initiation. Concerning fracture initiation *per se*, a natural fracture will have an impact only if it is located on the perforation base, the fracture initiation point. This is a rare, but possible situation and numerical models can be used to predict the outcome of such a unique occurrence.

6.6 CONCLUSIONS

The goal of this study is to develop a predictive model for p_i prediction and the orientation of fracture initiation from perforated wells. Numerically-developed correction factors are presented for closed-form analytical expressions for $\sigma_{\theta L}|_{p_w}$ and $\sigma_{\theta T}|_{p_w}$ for seven prolific shale gas plays. Based on the forgone analysis, the following conclusions can be warranted:

- An oriented perforating strategy can be effective for optimizing fracture treatments by either promoting transverse fracture initiation, or suppressing p_i and hence treatment pressures.

- Transverse fracture initiation is possible in the Marcellus and the Barnett Shales at p_i lower than 4,615 and 4,754 psi respectively, and is best promoted by perforations in the PPA direction (along S_v for the Marcellus and along S_{Hmax} for the Barnett Shale).

- Only longitudinal fracture initiation is possible for the Bakken, Fayetteville, Haynesville, and Niobrara Shales and p_i is minimized for perforations in the S_v direction (non-PPA for normal faulting stress states). Similarly, even though transverse fracture initiation is impossible from the Vaca Muerta Shale, however p_i is minimized when perforations are in the S_{Hmax} (non-PPA for strike-slip faulting stress states). The predicted p_i for the Bakken, Fayetteville, and the Vaca Muerta

211

Shales are respectively, 6,689, 3,643, and 6,711 psi. The p_i values for the Hayneville and Niobrara Shales are estimated to be higher than 10,200 and 3,283 psi, respectively.

- Leakage of fracturing fluid around the wellbore, hinders transverse fracture initiation and can significantly increase p_i. For the Marcellus Shale, fracturing fluid leakage is shown to shrink the p_b window for transverse fracture initiation by 12% and in other cases yield longitudinal fracture initiation at p_i 190-294% higher than without any leakages around the wellbore. These effects can compensate multi-stage fracture treatments leading to short-term completion and long-term production problems.

- Anisotropies in the rock formation and presence of natural fractures should be put into consideration, especially if fracture initiation of an unexpected orientation is observed.

Chapter 7. Loss of Well Control Fracturing Prevention via Selecting the Appropriate Capping Stack Shut-In Strategy

Following uncontrolled discharge during loss of well control events, fracture initiation occurring during the post-blowout capping stage can lead to reservoir fluids broaching to the seafloor. A classic example is Union Oil's 1969 oil spill in Santa Barbara Channel, where fracture initiation at various locations caused thousands of gallons per hour to broach onto the ocean floor over a month before it could be controlled (Mullineaux, 1970; Easton, 1972). Disasters such as these could be prevented if the effects of the post-blowout loss of well control stages (uncontrolled discharge and capping) are incorporated into the shut-in procedures and the wellbore architectures are modified accordingly.

In this study, analytical models are used to simulate the loads on the wellbore during the different stages of loss of control. Capping pressure build-up during the shut-in is modeled to indicate fracture initiation points during the capping stage. Using these models, the critical capping pressure for a well is determined and subsequent critical discharge flowrates are calculated. Fracture initiation would occur if the actual discharge flowrate is below the calculated critical discharge flowrate. A hypothetical case study using typical deepwater Gulf of Mexico (GoM) parameters is performed demonstrating the likelihood of fracture initiation during different discharge flowrates, discharge periods and capping stack shut-in methods (single-step/"abrupt" or multi-step/"incremental"). An abrupt shut-in for this case study leads to fracture initiation at about 8 hours after shut-in, while a 5-step incremental shut-in is shown to prevent any fracture initiation during the 48 hours after the beginning of the shut-in. Reservoir depletion through longer discharge periods or higher

---

discharge flowrates, despite the adverse environmental effect, can delay or even prevent fracture initiations during post-blowout capping.

The ability to model these fracture failures enhances the understanding of wellbore integrity problems induced during loss of control situations and helps create workflows for predicting possible broaching scenarios during the post-blowout capping stage. Dimensionless plots are used to present fracture initiation for different cases – this is useful for drilling and wellbore integrity engineers for making contingency plans for dealing with loss of well control situations.

7.1 INTRODUCTION

Broaching resulting from an underground blowout after loss of well control can lead to rig loss and an environmental catastrophe, placing a huge financial burden on the operator (Mullineaux, 1970; Easton, 1972). When targeting highly pressured formations as in the deepwater GoM, wellbore architecture must be made with considerations of the wellbore pressure variations during the two stages of loss of control (post-blowout discharge and capping).

Worst case discharge (WCD) is defined by BOEMRE as the maximum daily flowrate from an offshore well undergoing uncontrolled discharge (SPE Technical Report, 2015). During post-blowout discharge, the wellbore pressure drop may cause casing collapse at various locations along the casedhole section, exposing the formations to the fluid inside the wellbore (Michael and Gupta, 2018; 2019b; 2019c). As a result, the wellbore pressure build-up in the subsequent capping stage may exceed the pressure necessary to initiate a fracture either directly below the casing shoe or at any point along the casedhole section where casing failure had previously occurred during discharge (Zaki

et al., 2015). Wellbore pressure build-up during post-blowout capping can induce fracture initiation when the pressure inside the wellbore surpasses the fracture initiation pressures at a point where the rock surrounding rock formation is exposed to the fluid inside the wellbore, such as the openhole section underneath the casing shoe. If casing failure has previously taken place, then these casing failure location(s) replace the casing shoe as the location most vulnerable to fracture initiation in our analysis (in regards to its depth). The variation of pressure build-up with time during capping is translated to variation in the wellbore stresses with time. The tensile failure criterion is used to determine whether fracture initiation will take place or not considering the variation of the wellbore stresses on the borehole wall. Propagation of those fractures upwards towards the seafloor can provide a pathway for reservoir fluid broaching leading to an ecological disaster.

This study investigates tensile "Mode I" fracture initiation (Irwin, 1957) from possible locations on the wellbore radius following extreme loss of well control events, such as WCD. Mode I are tensile fractures "open" by doing work against the least compressive strength acting on the location of fracture initiation. A critical capping stack pressure and a corresponding critical discharge flowrate, below which fracture initiation would occur, during capping, can be calculated analytically for single-step/"abrupt" and multi-step/"incremental" capping stack shut-in procedures. These critical discharge flowrates can complement the law-mandated WCD calculations for offshore wells, aiding the development of protocols for effective well shut-in after a blowout. Intermediate casing type and casing shoe depth decisions should be made reflecting such extreme scenarios. Failures along the casing/cement, or cement sheath-rock formation interfaces are not examined. Thus for this study, the cased section of the well is assumed to be perfectly cemented without any microannuli present at the casing-cement sheath and cement sheath-rock formation interfaces.

7.2   THEORETICAL BACKGROUND

7.2.1   Stress State on the Wellbore Radius

Kirsch (1898) derived analytical solutions for the stress concentrations on a uniform plate, with a circular hole under uniform tension in a linearly elastic medium. Hubbert and Willis (1957) modified the Kirsch (1898) solutions to incorporate biaxial stress loading and fluid pressure inside the hole. Haimson and Fairhurst (1967) further modified Hubbert and Willis (1957) expressions for porous-permeable (poroelastic) media incorporating fluid infiltration (Eqs. 7.1 through 7.3). For a vertical well drilled parallel to the z-axis, parallel to the overburden principal stress S_v and perpendicular to the maximum and minimum horizontal principal stresses (S_{Hmax} and S_{hmin}, respectively) in a homogeneous, isotropic rock, the stresses on the wellbore radius ($r = r_w$), are analytically defined by

$$\sigma_{zz}|_{r=r_w} = S_v - 2v(S_{Hmax} - S_{hmin})\cos 2\theta + \alpha_B \frac{1-2v}{1-v}(p_w - p_p) - p_w \qquad (7.1)$$

$$\sigma_{\theta\theta}|_{r=r_w} = \frac{1}{2}(S_v + S_{Hmax}) - \frac{1}{2}(S_v + S_{Hmax})\cos 2\theta + \alpha_B \frac{1-2v}{1-v}(p_w - p_p)$$
$$- 2p_w \qquad (7.2)$$

$$\sigma_{rr}|_{r=r_w} = \alpha_B \frac{1-2v}{1-v}(p_w - p_p) \qquad (7.3)$$

where, θ is the positive clockwise angle taken from S_{Hmax}, p_w the wellbore pressure, p_p the formation pore pressure, v the rock Poisson's ratio, α_B the Biot's poroelastic coefficient, σ_{zz} is the axial stress, $\sigma_{\theta\theta}$ is the tangential stress, which is also known as the "hoop" or circumferential stress, and σ_{rr} is the radial stress. Compressive stresses are

indicated by positive values, consistent with the convention used in the petroleum geomechanics literature. Eqs. 7.1 through 7.3 are applicable to unrestricted flow from the rock formation into the well, which would be appropriate for blowouts, with the pressure on the wellbore radius ($r = r_w$) equal to p_w rather than the undisturbed p_p beyond the borehole influence ($r = \infty$). Figure 7.1 shows the configuration of σ_{zz}, $\sigma_{\theta\theta}$, and σ_{rr} on the wellbore radius of the openhole section of a vertical well.
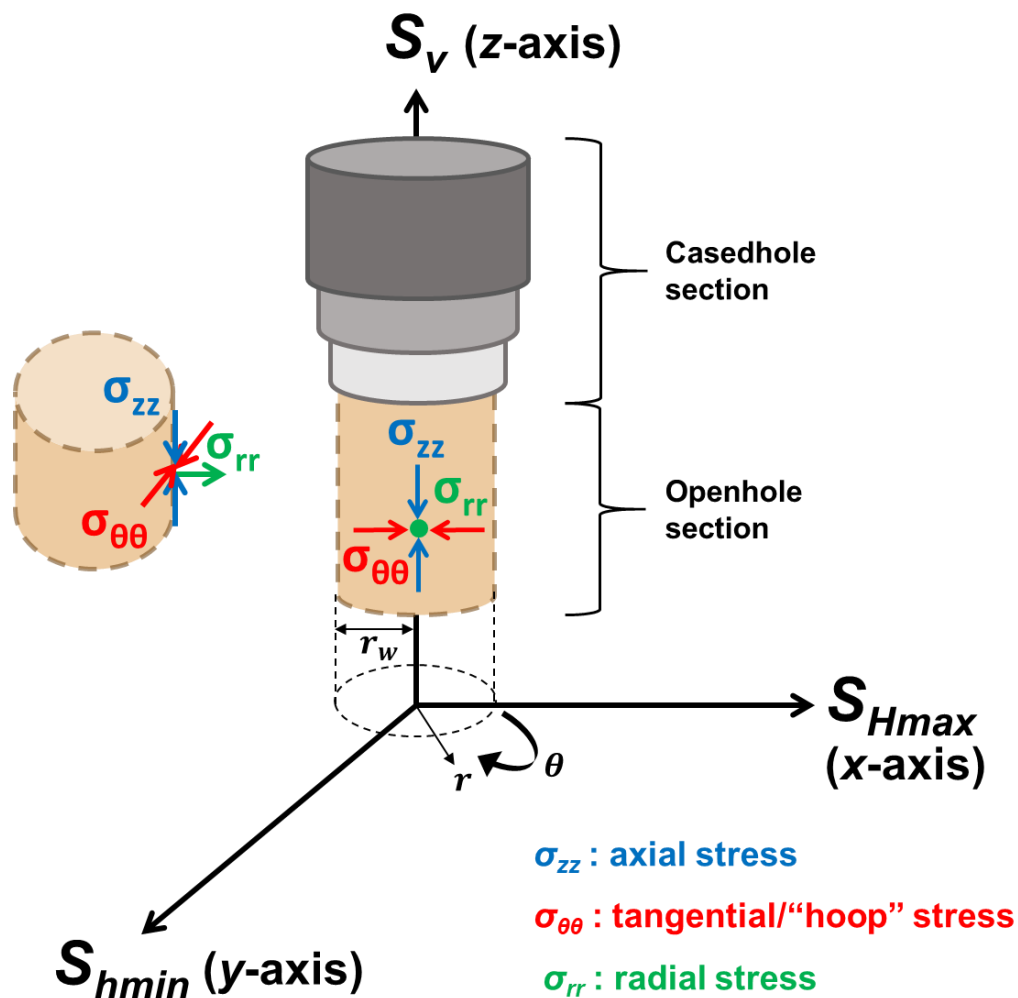
Figure 7.1.   Normal cylindrical (σ_{zz}, $\sigma_{\theta\theta}$, and σ_{rr}) stresses on the wellbore radius, $r = r_w$ in the openhole section. As r increases the far-field *in-situ* stresses (S_v, S_{Hmax}, and S_{hmin}) become more dominant.

217

7.2.2   Stresses Inside the Casing Wall

Although commonly known as the "Lamé solutions," the analytical expressions for elastic stresses inside a thick-walled circular cylinder under internal and external pressures (which can apply to strings of steel casing), was presented in a joint study by Lamé and Clapeyron (1831). Similar to Kirsch (1898), three normal stresses in cylindrical coordinates (Eqs. 7.4 through 7.6) are used to characterize the stress state inside the casing walls

$$\sigma_{zz,csg} = \frac{p_w R_i^2 - p_p R_o^2}{R_i^2 - R_o^2} \tag{7.4}$$

$$\sigma_{\theta\theta,csg} = \frac{p_w R_i^2 - p_p R_o^2}{R_i^2 - R_o^2} + \frac{R_o^2 R_i^2 (p_w - p_p)}{r^2 (R_i^2 - R_o^2)} \tag{7.5}$$

$$\sigma_{rr,csg} = \frac{p_w R_i^2 - p_p R_o^2}{R_i^2 - R_o^2} - \frac{R_o^2 R_i^2 (p_w - p_p)}{r^2 (R_i^2 - R_o^2)} \tag{7.6}$$

where, R_i and R_o are the inner and outer radii of the casing wall, respectively with $R_i \leq r \leq R_o$. The axial, tangential and radial stresses in the casing wall are indicated by $\sigma_{zz,csg}$, $\sigma_{\theta\theta,csg}$, and $\sigma_{rr,csg}$, respectively (Figure 7.2).
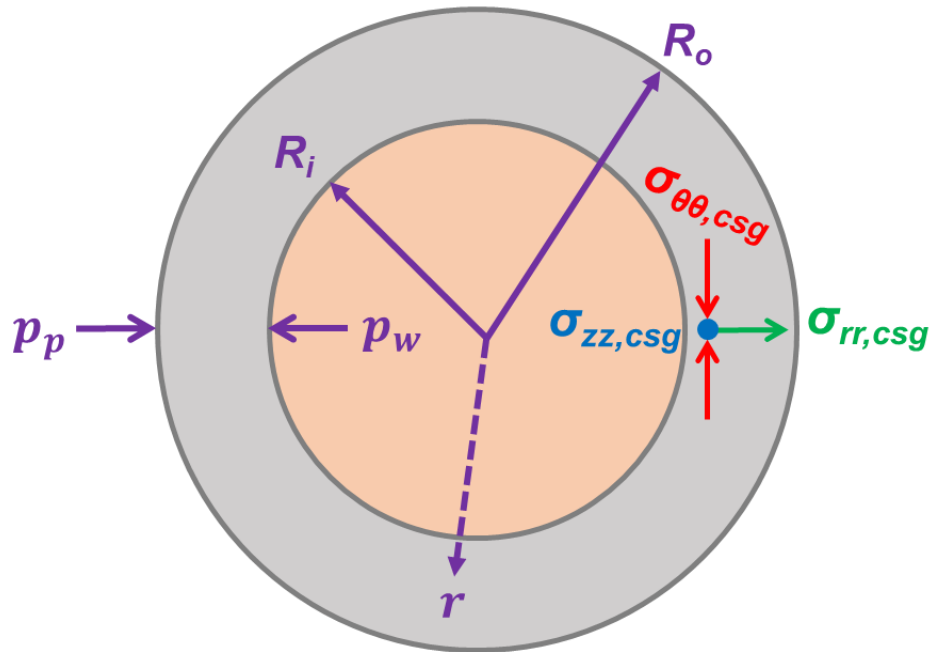
Figure 7.2. Normal stresses configuration inside a "thick-walled" cylindrical casing.

7.3   LOSS OF WELL CONTROL

Post-blowout loss of well control is a two-stage process, consisting of (i) the discharge stage where casing failure may take place, and (ii) the capping stage, where fracture initiation may take place.

7.3.1   The Post-Blowout Discharge Stage: Casing Failure Potential

In the immediate aftermath of a blowout, p_w drops dramatically, as reservoir fluids gush through the wellbore to the seafloor (or the surface in the case of onshore wells). This subjects the casing string already in place to tremendous stress loads, which may trigger failure. The two loads acting on the casing during discharge are collapse and compressive.

The von Mises (1913) criterion of maximum energy distortion, which is used to assess the integrity of "thick-walled cylinders" over a range of conditions, is applied to cylindrical steel casing at a variable p_w. In its simple form, under plane strain assumption, radial stresses are neglected and the criterion can be presented on a 2D plot (Figure 7.3). The tangential stress inside the casing wall, $\sigma_{\theta\theta,csg}$ is plotted on the vertical axis, with the axial stress inside the casing wall, $\sigma_{zz,csg}$, plotted on the horizontal axis. Both axes variables are normalized by the yield stress of the casing, σ_{yield}. According to the von Mises (1913) theory, the two stresses in the casing wall ($\sigma_{\theta\theta,csg}$ and $\sigma_{zz,csg}$) can be lumped into one term σ_e, or the "von Mises stress equivalent" as defined by

$$\sigma_e = \pm\sqrt{\left(\sigma_{\theta\theta,csg}\right)^2 - \sigma_{\theta\theta,csg}\sigma_{zz,csg} + \left(\sigma_{zz,csg}\right)^2} \qquad (7.7)$$

which results in an ellipse as shown on Figure 7.3.

Points outside the ellipsoid ($\sigma_e > \sigma_{yield}$) indicate casing failure; burst versus collapse from the vertical axis and tension versus compression on the horizontal axis. During the discharge stage following a blowout, tangential collapse and compressive axial stress loads suggest conditions relevant to the lower left quadrant of Figure 7.3 (green and yellow regions). The yellow region in Figure 7.3 indicates the stress states at which casing failure will take place.
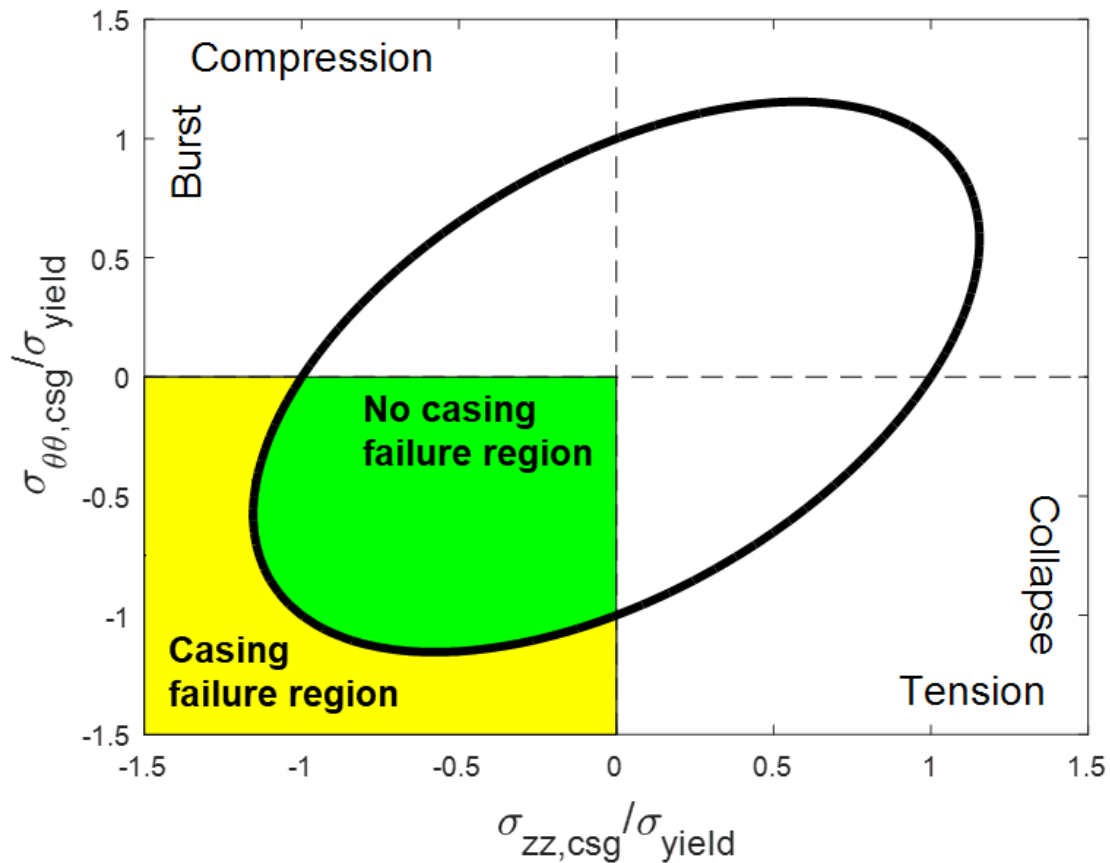
Figure 7.3. The von Mises failure criterion applied to casing failure. During the post-blowout discharge stage, collapse and compression loads are acting on the casing wall, suggesting locations in the lower left quadrant of the von Mises ellipse (green and yellow regions). As long as the conditions remain within the green region, no casing failure will take place. Points outside the ellipse (yellow region) indicate casing failure.

7.3.2 The Post-Blowout Capping Stage: Potential for Fracture Initiation

Once control of the discharging well is regained and flow stops, the shut-in wellbore pressure, p_{ws} builds up. At any point, p_{ws} may exceed the pressure needed for tensile (Mode I) fracture failure, either (i) directly below the casing shoe, or (ii) any point

on the casing string where casing collapse has occurred previously during the discharge stage.

There are two methods of sealing off a well via installing of a capping stack on top of the blowout preventer (BOP) of a well which is undergoing a WCD event. The fastest method is the "abrupt" shut-in, where the flow from the well is sharply stopped. The second method is the "incremental" shut-in, which is gentler compared to abrupt shut-in procedures, where the well discharge flow is gradually stopped over a predetermined time period/schedule involving a specific number of steps.

The orientation of the resulting fracture initiation is paramount to our modeling approach and can be either longitudinal or transverse concerning the wellbore (Figure 7.4). Longitudinal fractures initiate axially to the wellbore and are the most common, primarily due to stress reorientation (Kirsch, 1898) in the near-wellbore region (Daneshy, 1973; Michael and Gupta, 2019a; 2019d; 2019e; Michael, 2019a). Transverse fractures initiate orthogonal to the wellbore and are likely to initiate from shallow depths with low overburden stress.
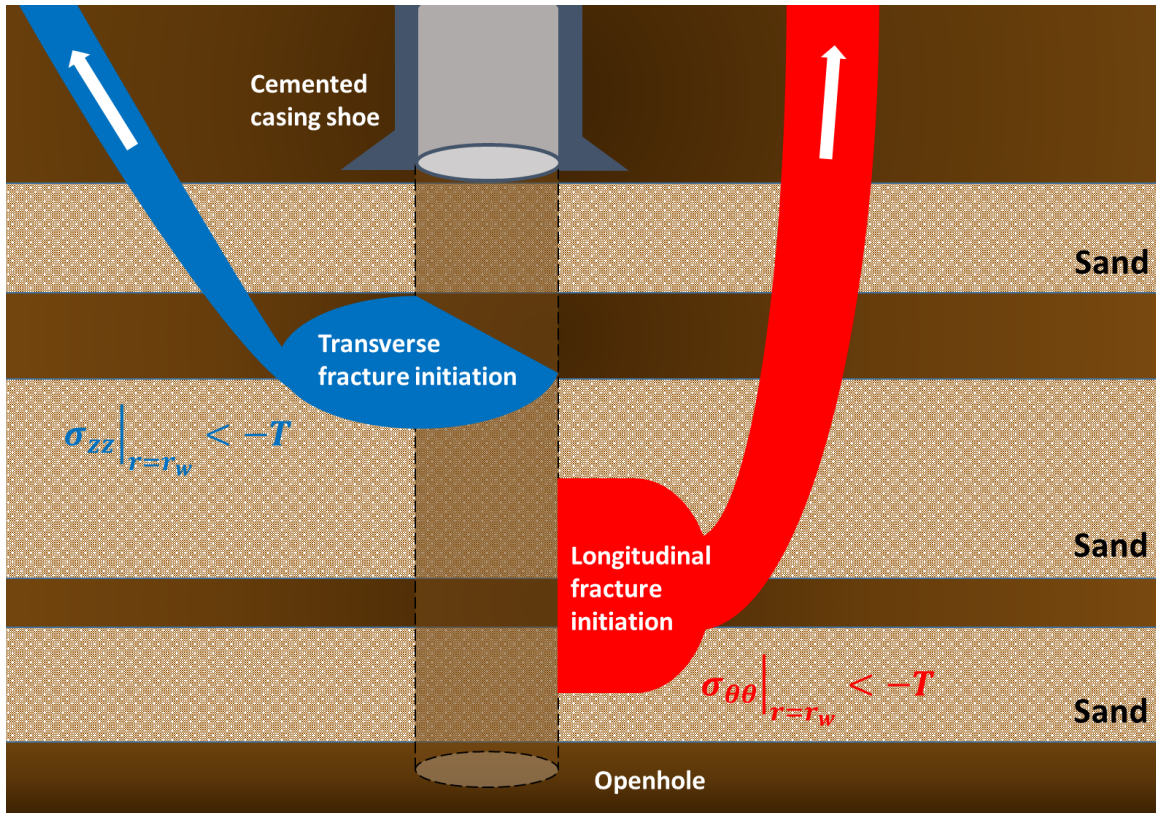
Figure 7.4.   Longitudinal versus transverse fracturing during the post-blowout capping stage. Longitudinal fracture initiation takes place when $\sigma_{\theta\theta}|_{r=r_w} < -T$, whereas transverse fracture initiation occurs when $\sigma_{zz}|_{r=r_w} < -T$.

7.4   ANALYTICAL APPROACH

A series of assumptions can be applied to simplify the problem to the point where closed-form analytical solutions can be derived, linking discharge flowrate to fracture initiation during post-blowout capping. Through this relationship, a critical discharge flowrate, q_{crit} can be computed as a function of the discharge period, below which either a longitudinal or transverse fracture will initiate.

7.4.1 Fracture Initiation Pressure

The orientation criteria for fractures initiated during post-blowout capping are the same as the orientation criteria for drilling-induced tensile fractures (Nelson et al., 2005; Michael and Gupta, 2019a; 2019b; 2019c). Longitudinal fracture initiation occurs if $\sigma_{\theta\theta}$ is less than the tensile strength of the rock, $-T$ while transverse fracture initiation takes place if σ_{zz} is less than $-T$. Following Haimson and Fairhurst (1967), an expression for the longitudinal fracture initiation pressure, $p_{frac,L}$ for vertical wells is derived (Weijers, 1995) by rearranging Eq. 7.2 for p_w at $\sigma_{\theta\theta}|_{r=r_w} < -T$ which yields

$$p_{frac,L}\big|_{\Delta t} = \frac{3S_{hmin} - S_{Hmax} - \left(\frac{1-2v}{1-v}\right)\alpha_B p_p\big|_{r=r_w,\Delta t} + T}{2 - \left(\frac{1-2v}{1-v}\right)\alpha_B} \tag{7.8}$$

Similarly, an expression for the transverse fracture initiation pressure, $p_{frac,T}$ can be derived by rearranging Eq. 7.1 for p_w such that $\sigma_{zz}|_{r=r_w} < -T$ and,

$$p_{frac,T}\big|_{\Delta t} = \frac{S_v - 2v(S_{Hmax} - S_{hmin}) - \left(\frac{1-2v}{1-v}\right)\alpha_B p_p\big|_{r=r_w,\Delta t} + T}{1 - \left(\frac{1-2v}{1-v}\right)\alpha_B} \tag{7.9}$$

7.4.2 Abrupt Capping Stack Shut-In Modeling

The Horner (1951) relationship (Eq. 7.10) used to analytically model the pressure build-up, p_{ws}, during an abrupt shut-in for a reservoir at average initial (pore) pressure p_{ini} is

$$p_{ws}|_{\Delta t} = p_{ini} - \frac{162.6 q \mu_o B_o}{kh} \log\left(\frac{t_p + \Delta t}{\Delta t}\right) \tag{7.10}$$

where, q and t_p are the respectively the discharge flowrate in stock tank barrels per day (positive value in STB/day) and the discharge period in days prior to the shut-in, Δt is the time elapsed, also in days since the shut-in, k is the reservoir permeability in mD, h is the net pay thickness of the exposed zone in ft, and μ_o and B_o are the oil viscosity in cp and formation volume factor in reservoir barrels per stock tank barrels (RB/STB), respectively. Fracture initiation takes place if p_{ws} exceeds the smallest of either $p_{frac,L}$ or $p_{frac,T}$ at a certain time $\Delta t > 0$ following the capping stack shut-in. Thus, setting $p_{ws}|_{\Delta t} > min\{p_{frac,L}|_{\Delta t}, p_{frac,T}|_{\Delta t}\}$ in Eq. 7.10 and solving for the discharge flowrate, $q = q_{crit}|_{\Delta t}$, such

$$q_{crit}|_{\Delta t} = \frac{kh(min\{p_{frac,L}|_{\Delta t}, p_{frac,T}|_{\Delta t}\} - p_{ini})}{162.6 \mu_o B_o \log\left(\frac{t_p + \Delta t}{\Delta t}\right)} \tag{7.11}$$

It has to be noted that q_{crit} depends on Δt. If $q < q_{crit}|_{\Delta t}$ fracture initiation is predicted to take place during capping if an abrupt shut-in is employed at a time before Δt and after t_p. Higher t_p or Δt values lead to lower q_{crit} values (Eq. 7.11) making fracture initiation during abrupt shut-in less likely.

7.4.3 Incremental Shut-In Modeling

If a flowing well is shut over a time period, the flowrate is reduced gradually to zero following a predetermined schedule. In the simplest case, the flowrate is reduced

linearly by a constant proportion in every step increment. Eq. 7.12 can be used to determine the flowrate in every step interval, q_i (STB/day) for a total of N steps

$$q_i = q\left(1 - \frac{i}{N}\right) \tag{7.12}$$

for $i = 1, 2, 3 \dots N$. As demonstrated in Matthews and Russell (1967), for multiple flowrate testing, the pressure variation in the wellbore with respect to time (build-up for drawdown tests) is expressed by

$$p_{ws}|_{\Delta t} = p_{ini} - \frac{162.6\mu_o B_o}{kh} \sum_{i=1}^{N}(q_i - q_{i-1})\log(\Delta t - \Delta t_{i-1}) \tag{7.13}$$

where, $q = q_i$ @ $\Delta t_{i-1} \leq \Delta t \leq \Delta t_i$ with $\Delta t = 0$, being the beginning of the incremental shut-in (i.e. the first step) and "q_0" $de\ facto$ being the post-blowout discharge flowrate q, which for this problem is assumed to be constant. All time parameters must be in hours contrary to Horner's (1951) expression (Eq. 7.10) for an abrupt shut-in, where consistent time units make the "Horner time" term, $\left(\frac{t_p+\Delta t}{\Delta t}\right)$, dimensionless. Similar to an abrupt shut-in, t_p when applied to an incremental shut-in, refers to the discharge period prior to the first shut-in step. Therefore, Eq. 7.13 can be modified to

$$p_{ws}|_{\Delta t} = p_{ini} - \frac{162.6\mu_o B_o}{kh}\left[q\log(\Delta t + t_p) + \sum_{i=2}^{N}(q_i - q_{i-1})\log(\Delta t - \Delta t_{i-1})\right] \tag{7.14}$$

Eq. 7.14 can be divided into N segments during which the flowrate is constant

$$p_{ws}|_{\Delta t} = p_{ini} - \frac{162.6\mu_o B_o}{kh} \big[q \log(\Delta t + t_p) + (q_2 - q_1)\log(\Delta t - \Delta t_1)$$
$$+ (q_3 - q_2)\log(\Delta t - \Delta t_2) \qquad (7.15)$$
$$+ \cdots (q_N - q_{N-1})\log(\Delta t - \Delta t_{N-1}) \big]$$

Substituting Eq. 7.12 into Eq. 7.15 for a constant flowrate decrease per shut-in step, makes $(q_i - q_{i-1}) = \frac{q}{N}$, which can be used to give an expression for $p_{ws}|_t$ in terms of q only

$$p_{ws}|_{\Delta t} = p_{ini} - \frac{162.6 q \mu_o B_o}{kh} \bigg[\log(\Delta t + t_p) + \frac{\log(\Delta t - \Delta t_1)}{N}$$
$$+ \frac{\log(\Delta t - \Delta t_2)}{N} + \cdots \frac{\log(\Delta t - \Delta t_{N-1})}{N} \bigg] \qquad (7.16)$$

where, N is dimensionless so it does not affect the relationship (Eq. 7.16) dimensionally in any way. Rearranging Eq. 7.16 to solve for $q = q_{crit}|_{\Delta t} @ p_{ws}|_{\Delta t} = min\{p_{frac,L}|_{\Delta t}, p_{frac,T}|_{\Delta t}\}$, which represents the limit of fracture initiation, yields

$$q_{crit}|_{\Delta t} = \frac{Nkh\left(p_{ini} - min\{p_{frac,L}|_{\Delta t}, p_{frac,T}|_{\Delta t}\}\right)}{162.6\mu_o B_o \big[N \log(\Delta t + t_p) + \sum_{i=1}^{N}\log(\Delta t - \Delta t_{i-1}) \big]} \qquad (7.17)$$

Eq. 7.17 shows that N can have either a positive or negative impact on q_{crit} depending on how the magnitude of the fracture initiation pressure compares to p_{ini}. Therefore, on a case-by-case basis an optimal well shut-in schedule requires that $q < q_{crit}$ ensuring no fracturing. As for an abrupt shut-in, longer discharge periods yield smaller q_{crit} values.

7.5 RESULTS

7.5.1 Hypothetical Case Study: Deepwater GoM

A representative scenario (modified from Willson, 2012) is considered for demonstrating the concept of q_{crit} and the influence of various parameters on its magnitude. Tables 7.1 and 7.2 summarize the reservoir, petrophysical and geomechanical properties. The mudline is at 5,100 ft under the rotary table, which is 100 ft above the average sea level. A $9^5/_8$ in casing is set at 17,200 ft TVD from the rotary table and a $5^1/_2$ in drillpipe is present in the borehole at the start of the blowout (i.e., the well is drilling ahead). The well is drilled with a 14.3 ppg drilling mud. Per Willson's (2012) analyses, in the event of a kick leading to a blowout, the well is expected to reach 155,040 STB/day flowrates at a bottomhole flowing pressure, p_{wf} of 7,072 psi.

Table 7.1.   Input reservoir properties.

Parameter	Symbol	Value
Average reservoir depth	d_{res}	18,135 ft
Casing shoe depth	d_{csg}	17,200 ft
Initial reservoir pressure	p_{ini}	12,247 psi
Permeability	k	400 mD
Net pay thickness	h	250 ft
Oil viscosity	μ_o	1.09 cp
Oil formation volume factor	B_o	1.1 RB/STB
Oil specific gravity	γ_o	0.75
Productivity index	J	30 STB/day/psi

228

Table 7.2.   Input geomechanical/petrophysical properties.

Parameter	Symbol	Value
Overburden stress (from seafloor)	S_v	0.82 psi/ft
Maximum horizontal stress	S_{Hmax}	$0.95 S_v$
Minimum horizontal stress	S_{hmin}	$0.87 S_v$
Poisson's ratio	v	0.25
Biot's poroelastic coefficient	α_B	0.8
Tensile strength	T	~0 psi

The zone of interest is under normal faulting stress regime ($S_v > S_{Hmax} > S_{hmin}$). Figure 7.5a shows the overburden, S_v, and shale/sand p_p profiles. This data, which was taken from Willson (2012) is used to calculate the corresponding longitudinal and transverse fracture initiation gradients versus depth (Figure 7.5b) using Eqs. 7.8 and 7.9. The magnitude of $p_p\big|_{r=r_w}$ is given by the purple line on Figure 7.5a (shale p_p). This procedure leads to underestimation of the fracture gradients ($p_{frac,L}$ and $p_{frac,T}$) in post-blowout capping considerations, because $p_p\big|_{r=r_w}$ increases with the pressure build-up inside the wellbore. Hence, evaluation of the wellbore stresses at the wellbore radius during the pressure build-up (shown later on Figures 7.7 and 7.9) is necessary for determining whether fracture initiation will take place or otherwise, rather than comparing $p_{ws}|_{\Delta t}$ against fixed $p_{frac,L}$ and $p_{frac,T}$ values. For estimating the variation of $p_{frac,L}\big|_{\Delta t}$ and $p_{frac,T}\big|_{\Delta t}$ using Eqs. 7.8 and 7.9 during capping procedures, $p_p\big|_{r=r_w,\Delta t} \approx p_{ws}|_{\Delta t}$ is a good approximation.
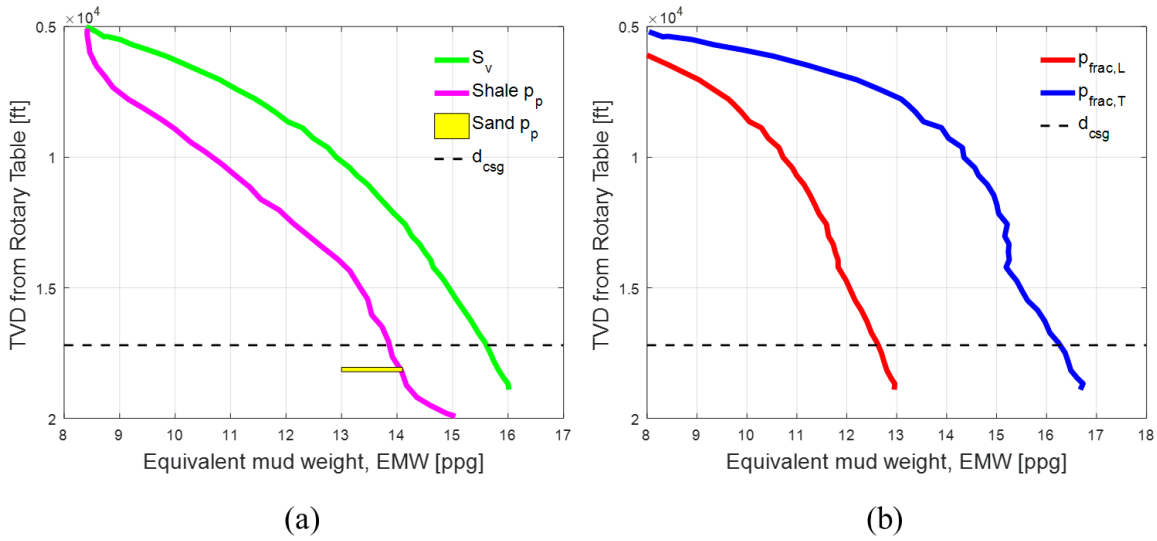
Figure 7.5. (a) Overburden, S_v and shale/sand p_p profiles. (b) Longitudinal ($p_{frac,L}$) and transverse ($p_{frac,T}$) fracture initiation pressure gradient profiles calculated using Eqs. 7.8 and 7.9. The quantities on the vertical axes are in 10,000 ft.

The inflow performance relationship (IPR) of the reservoir is shown on Figure 7.6a and is used to estimate the bottomhole flowing pressure, p_{wf} analogous to the flowrate coming from the wellbore. Figure 7.6b shows the expected wellbore discharge flowrate against time since the blowout took place and the corresponding p_{wf} variation during the same time period according to Willson (2012).
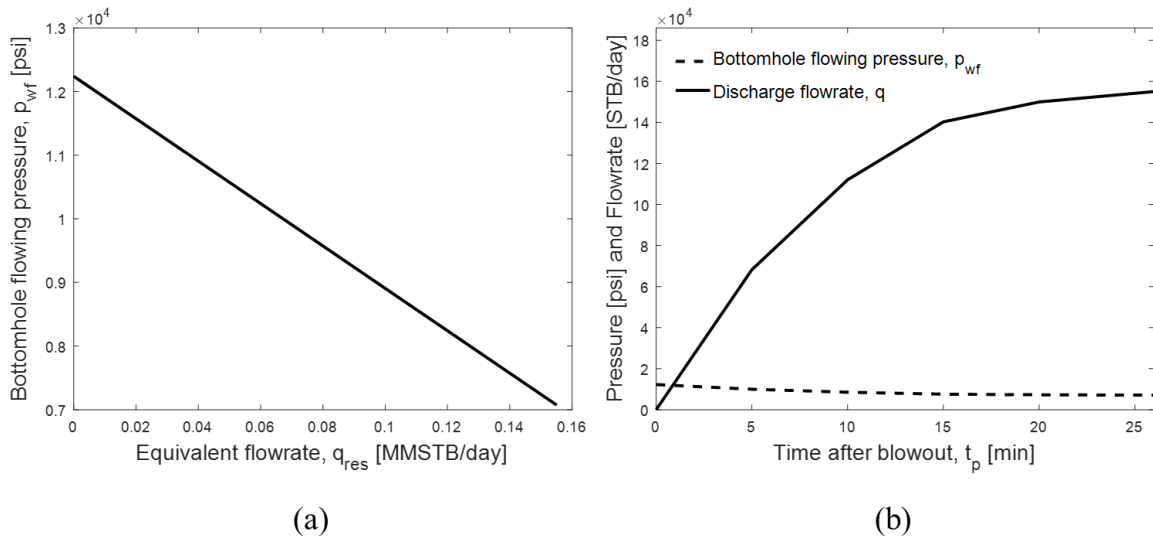
Figure 7.6.   (a) Inflow performance relationship (IPR) for the reservoir. (b) Predicted flowrates and subsequent bottomhole flowing pressures after a post-kick blowout (produced using the results of Willson, 2012).

Assuming perfect casing integrity during the preceding discharge period, the casing shoe depth is the primary line of defense against fracture initiation scenarios leading to broaching. An abrupt shut-in procedure is first considered. Figure 7.7a shows the pressure build-up in the wellbore using Eq. 7.10, for three different scenarios:

i.   Base Case: discharge flowrate, $q = 155,040$ STB/day and discharge period, $t_p = 1$ day.

ii.   A 5-fold increase in t_p compared to the Base Case, while q is kept the same as the Base Case.

iii. A 5-fold decrease in q compared to the Base Case, while t_p is kept the same as the Base Case.

231
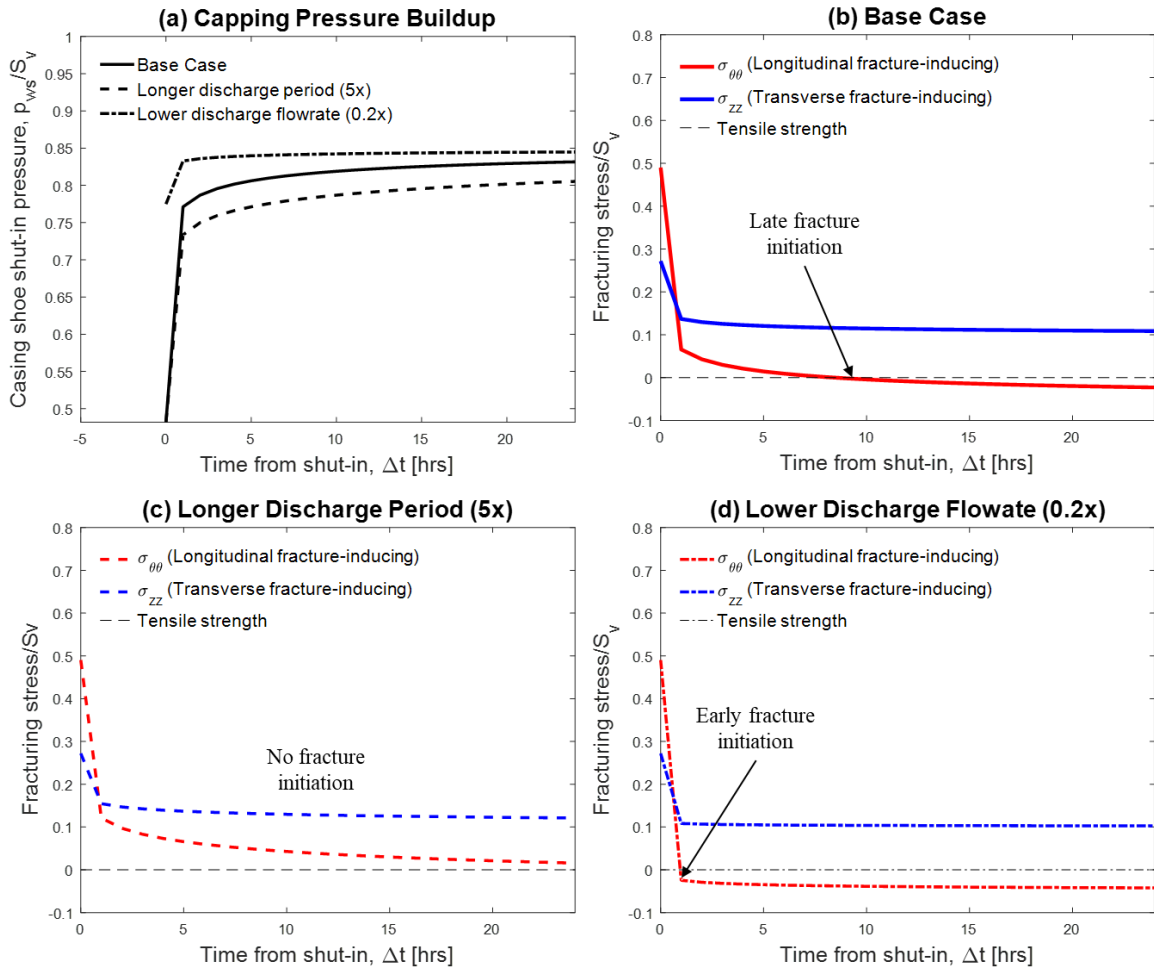
Figure 7.7. (a) Pressure build-up in the wellbore during the first 24 hours following an abrupt shut-in. (b) Variation of $\sigma_{\theta\theta}$ and σ_{zz} (Base Case) during the same time-period showing longitudinal fracture initiation about 8 hours after shut-in. (c) A 5-fold decrease in the discharge flowrate yields an increase from 1.5% to 7.9% in p_{ws} compared to the Base Case, preventing any fracture initiation. (d) A 5-fold increase in the discharge period leads to a lower p_{ws} value by from 3.4% to 4.7% compared to the Base Case, which leads to a longitudinal fracture initiation earlier, at about 2 hours after well shut-in.

The values of $\sigma_{\theta\theta}|_{\Delta t}$ and $\sigma_{zz}|_{\Delta t}$ induced during the capping stage (Figures 7.7b

through 7.7d) can be calculated using $p_{ws}|_{\Delta t}$ data from Figure 7.7a and Eqs. 7.1 and 7.2.

The variation in the magnitudes of $\sigma_{\theta\theta}|_{\Delta t}$ and $\sigma_{zz}|_{\Delta t}$ can be compared to $(-T)$ to indicate

232

longitudinal or transverse fracture initiation, respectively. Increasing t_p 5-fold to 5 days leads to a decreased p_{ws} value from 3.4% to 4.7% during 24 hours after the abrupt shut-in compared to the Base Case. Contrary, a 5-fold decrease in q to 31,008 STB/day, yields an increase in p_{ws} from 1.5% to 7.9% during 24 hours after the abrupt shut-in.

Using this procedure, the minimum capping pressures (at the stack, or anywhere along the wellbore), which lead to fracture initiation can be calculated, and from there the critical (maximum) discharge flowrate values corresponding to fracture initiation are hence evaluated. These critical discharge flowrates can be compared with WCD estimations to decide on appropriate shut-in strategies for capping the well undergoing uncontrolled flow.

An incremental shut-in procedure is considered next.

The discharge period before the start of the shut-in process is kept constant at 1 day. The total time the shut-in takes for the flow to completely stop is set at 1 day also. Thus, the interval period varies depending on the number of steps, N, but the flow from the well measured in million stock tank barrels per day (MMSTB/day) ceases completely 24 hours after the start of the beginning of the shut-in (Figure 7.8a). The first step, $i = 1$ at $\Delta t_1 = 0$ represents the flowrate, $q_1 = 124{,}032$ STB/day, after the first shut-in step is completed which is which is smaller than the post-blowout discharge flowrate, $q = 155{,}040$ STB/day. The flowrate after the second shut-in step ($i = 2$) is completed is $q_2 = 93{,}024$ STB/day and so on, such that $q > q_1 > q_2 \ldots > q_{N-1=4}$. The value of q_N (for this case, q_5) is always equal to zero. Figure 7.8b shows the $p_{ws}|_{\Delta t}$ at the casing shoe depth for a 5-step incremental shut-in.
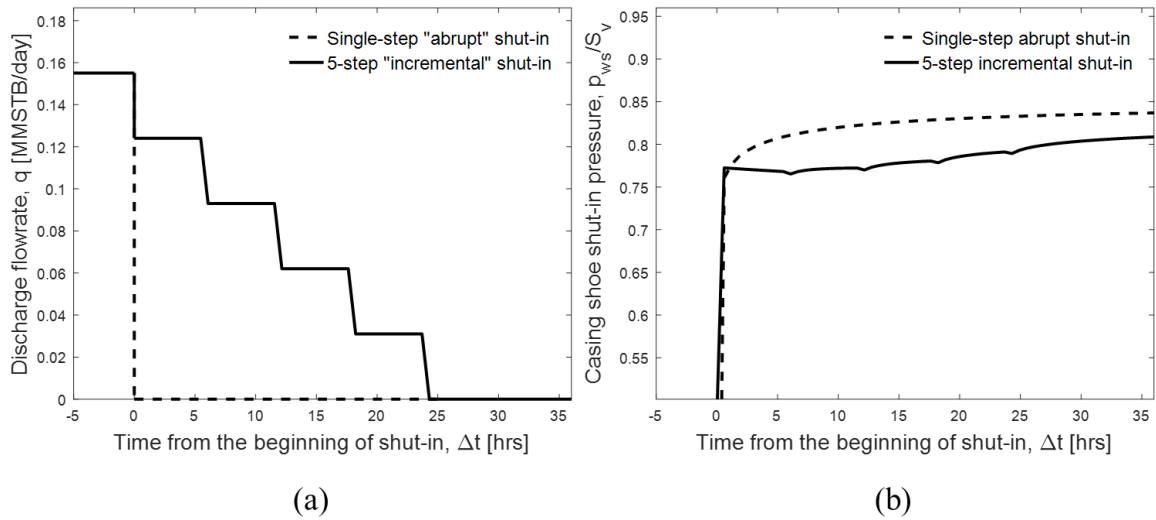
Figure 7.8. (a) Discharge flowrate versus time and (b) casing shoe pressure versus time for a 5-step incremental capping stack shut-in procedure.

Similar to the abrupt shut-in case, higher discharge flowrates and longer discharge periods suppress $p_{ws}|_{\Delta t}$ keeping $\sigma_{\theta\theta}|_{\Delta t}$ and $\sigma_{zz}|_{\Delta t}$ more compressive and decrease the possibility of longitudinal or transverse (tensile) fracture initiation at any point inside the wellbore. Figure 7.9 displays four incremental shut-in scenarios with a 5-step shut-in for Base Case parameters preventing fracture initiation for the first 48 hours after the beginning of the shut-in (24 hours after the well is fully shut-in) as shown on Figure 7.9a. A 5-fold increase in the post-blowout discharge period to 5 days makes $\sigma_{\theta\theta}$ and σ_{zz} more compressive by 123% and 14%, respectively compared to the Base Case (Figure 7.9b). This prevents fracture initiation at any point during the 48 hours after the beginning of the shut-in (72 hours from the blowout). A 5-fold decrease in the discharge period to 31,008 STB/day, makes $\sigma_{\theta\theta}$ and σ_{zz} more tensile relative to the values for the Base Case by 172% and 19%, respectively (Figure 7.9c). This leads to an early longitudinal fracture initiation. A 10-step incremental shut-in for Base Case parameters makes $\sigma_{\theta\theta}$ and σ_{zz} more tensile

234

than the corresponding values for Base Case parameters by 56% and 6.3%, respectively (Figure 7.9d). As for an abrupt shut-in, longer discharge periods and higher discharge flowrates suppress the possibility of fracturing during post-blowout capping (Figure 7.9b-c), although unattractive due to the higher associated adverse environmental impact. Although a 10-step incremental shut-in (Figure 7.9d) yields wellbore stresses more tensile than what a 5-step shut-in (Figure 7.9a) does, both capping stack shut-in strategies prevent fracturing during the 48 hours after the beginning of the shut-in.

Wellbore integrity engineers can use the estimates of WCD rates (SPE Technical Report, 2015, Vasquez Cordoba, 2018) and compare them with q_{crit} calculations deciding in advance on the optimal shut-in strategy for the possibility of a blowout considering all relevant parameters. This will prevent the need for costly well integrity tests (Hickman et al., 2012; McNutt et al., 2012; Michael and Gupta, 2019b) and quickly, safely, and effectively cap the discharging well, mitigating any undergoing or possible environmental disaster.
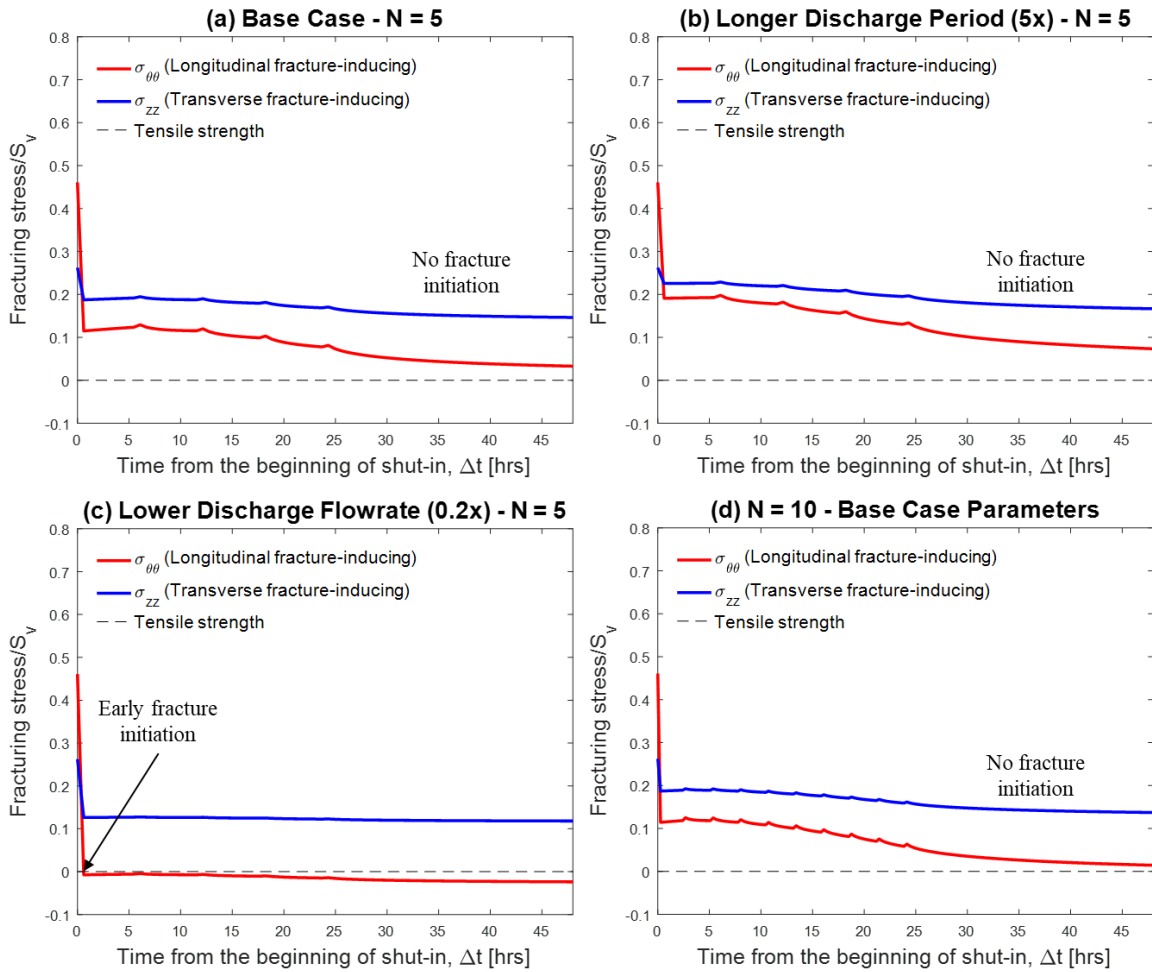
Figure 7.9. Longitudinal ($\sigma_{\theta\theta}$, red lines) and transverse (σ_{zz}, blue lines) fracturing stresses for four different combinations of shut-in parameters. (a) Base Case parameters with $N = 5$, (b) a 2-fold increase in the discharge flowrate compared to the Base Case, (c) a 10-fold increase in the discharge period compared to the Base Case, and (d) Base Case parameters with $N = 10$.

7.5.2   Allowable Stress State Diagrams

The range of *in-situ* stress states, which can occur in the Earth's subsurface can be visualized using a simple 2D plot called the allowable stress state diagram (Nelson et al., 2005; Zoback, 2007). This plot has S_{Hmax} normalized by S_v on the vertical axis and S_{hmin}

normalized by S_v on the horizontal axis (Figure 7.10). The dotted-diagonal is the line of horizontal isotropy, where $S_{Hmax} = S_{hmin}$ and the solid black lines represent the frictional limits according to Eq. 7.18 for rock friction factors, $\mu = 0.6$ (thicker line) and $\mu = 0.8$ (thinner line), consistent with Byerlee's (1978) findings (μ is equal to the tangent of the friction angle). The frictional limit lines are drawn using S_v and S_{Hmax} for S_1 and using S_v and S_{hmin} for S_3. Any stress state outside those bounds is virtually unstable; if a fault exists under those stress state conditions, it will automatically fail in shear as there will be fault slippage.

Following Nelson et al.'s (2005) use of the allowable stress state diagrams in drilling-induced tensile fracture diagnosis, Michael and Gupta (2018; 2019b; 2019c; 2020b) added two lines to Figure 7.10. The red line for the stress states for which $\sigma_{\theta\theta} = 0$ signifying longitudinal fracture initiation, and the blue line for the stress states for which $\sigma_{zz} = 0$ signifying transverse fracture initiation for a given p_w gradient. This p_w gradient is dictated by p_{ws} build-up during post-blowout capping and the most probable fracture initiation location (primarily the casing shoe) depth. Figure 7.11 shows an example of this graphical technique for the parameters of the hypothetical case study, $\nu = 0.25$, $\alpha_B = 0.8$, at balanced conditions, $p_w = p_p = 0.68$ psi/ft. The yellow region behind either of the two lines represents the range of *in-situ* stress states where either longitudinal or transverse fracture initiation is promoted at the given conditions.
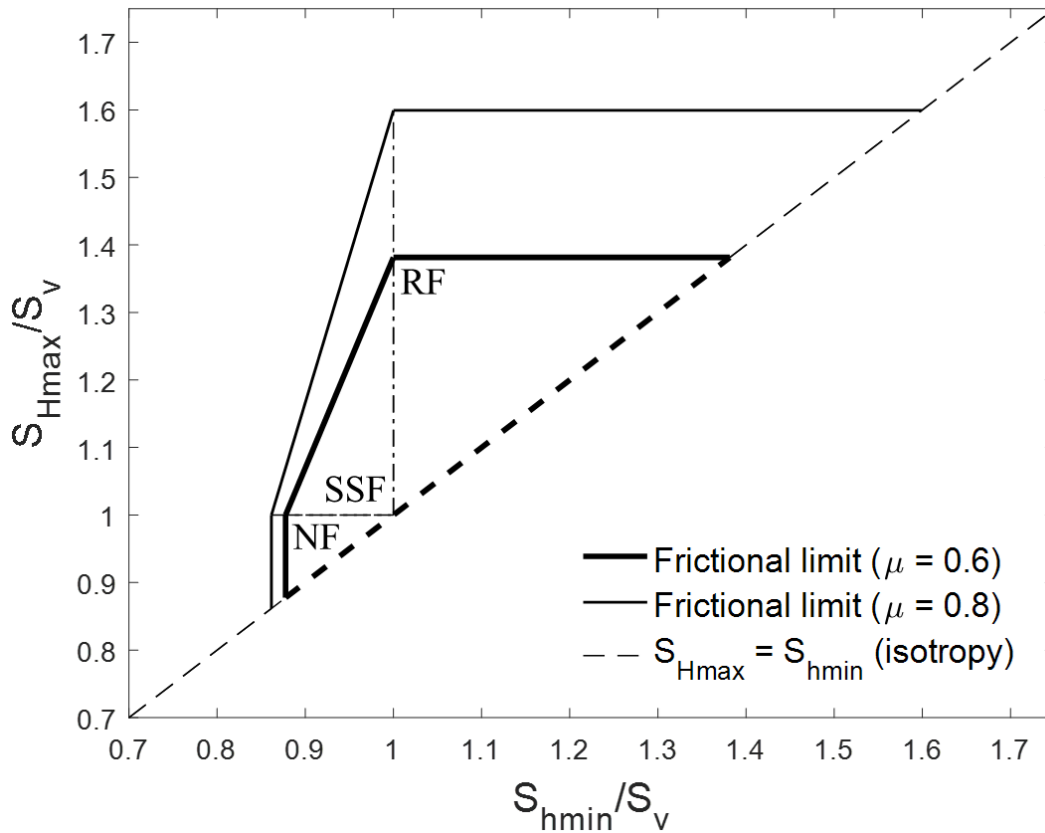
Figure 7.10. Allowable region for *in-situ* stress states in the Earth's subsurface for $p_p = p_{ini} = 0.68$ psi/ft ($p_p/S_v = 0.82$). The dotted diagonal line represents horizontal isotropy ($S_{Hmax} = S_{hmin}$), the thicker solid lines represent the frictional limits at $\mu = 0.6$ and the thinner lines represent the frictional limits at $\mu = 0.8$. The region bounded by the frictional limits and the horizontal isotropy diagonal, represents the range of possible subsurface stress states (NF: normal faulting; RF: reverse faulting; SSF: strike-slip faulting – Anderson, 1951).

Allowable stress state diagram analysis using published data was used by Michael and Gupta (2019b; 2019c; 2020) to demonstrate the fracture initiation during the 1969 Union Oil's A-21 well blowout in Santa Barbara, and the lack of fracture initiation during the 2010 BP's "Macondo" blowout in the GoM. The long discharge period combined with the high discharge flowrates led to high depletion of the reservoir after the Macondo

blowout, preventing any fracture initiation from taking place during capping (Hickman et al., 2012; McNutt et al., 2012; Michael and Gupta, 2019b; 2019c; 2020). On the contrary, the shallow casing shoe depth in Union Oil's A-21 allowed fractures to initiate, despite the lower capping pressures (Mullineaux, 1970; Easton, 1972, Michael and Gupta, 2019b). Assuming perfect integrity of the casing string, the casing shoe depth remains the primary line of defense against broaching scenarios.
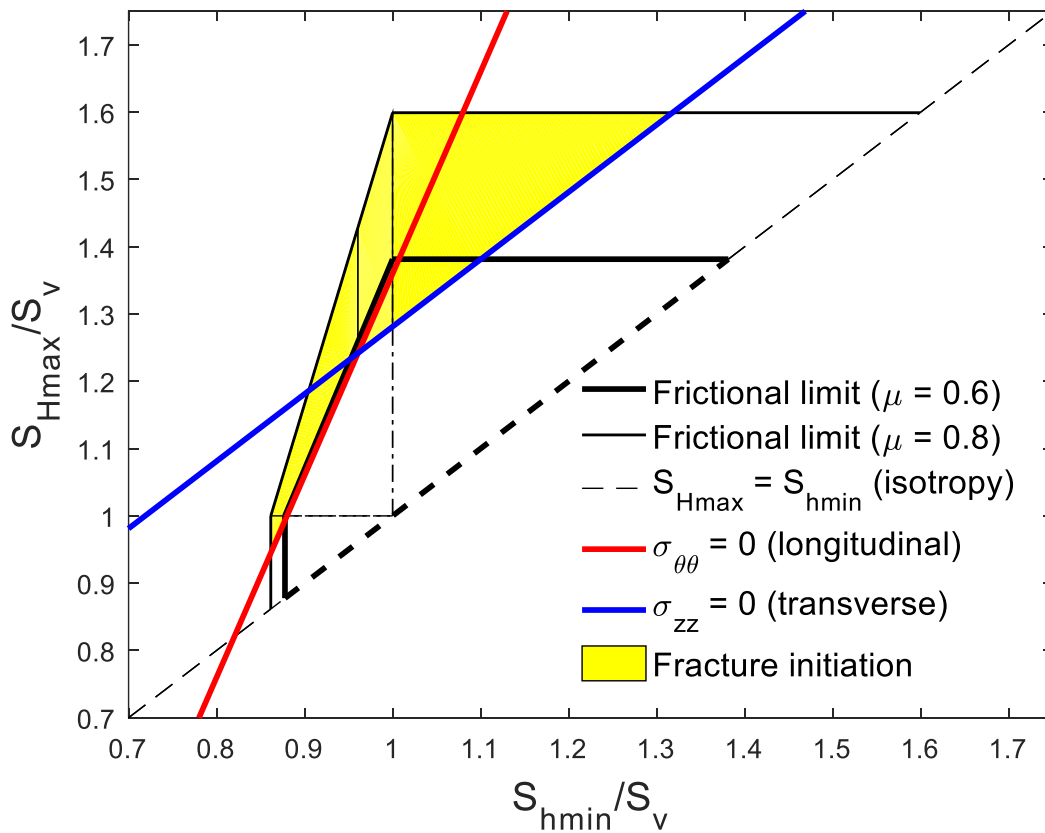
Figure 7.11. Allowable *in-situ* stress diagram example for $p_p = p_w = p_{ini} = 0.68$ psi/ft ($p_p/S_v = 0.82$), showing the longitudinal fracture-inducing $\sigma_{\theta\theta}$ (red line) and transverse fracture-inducing σ_{zz} (blue line). The red and blue lines indicate longitudinal and transverse fracture initiation, respectively for all stress states behind them. Hence, the yellow area represents the *in-situ* stress states in which fracture initiation (either longitudinal, or transverse) will occur under the given conditions.

Allowable stress state diagrams are used to illustrate the three different 5-step incremental shut-in scenarios examined in the hypothetical case study, where $p_p = p_{ini} = $ 12,247 psi at 18,135 ft from Table 7.1, and $S_v = 0.82$ psi/ft × 13,135 ft, resulting in p_p/S_v = 0.82. Figure 7.12a shows the diagram for the discharge stage immediately after the blowout when p_w is extremely low. The low p_w gradient pushes both fracture initiation lines to the left. The green dot (Figure 7.12a), indicating the *in-situ* conditions is well outside of the yellow region, signifying no fracture initiation. Figure 7.12b shows the diagram for the capping conditions for Base Case parameters. The maximum p_{ws} attained during the build-up moves both fracture initiation lines to the right, leaving the green dot narrowly outside of the yellow region, suggesting that a 5-step incremental shut-in would prevent any fracture initiation during the 48 hours after the beginning of the shut-in. The diagram for the scenario with the longer post-blowout discharge period (Figure 7.12c) displays the two fracture initiation lines shifted up and to the left, further away from the green dot, showing how reservoir depletion can effectively prevent (with everything else remaining constant) fracture initiation from taking place during the capping pressure build-up. On the contrary, a 5-fold decrease in the discharge flowrate (Figure 7.12d) enhances the possibility of fracture initiation, moving the two fracture initiation lines ($\sigma_{\theta\theta} = 0$ and $\sigma_{zz} = 0$) to the right, with the yellow region covering the green dot, indicating longitudinal fracture initiation.

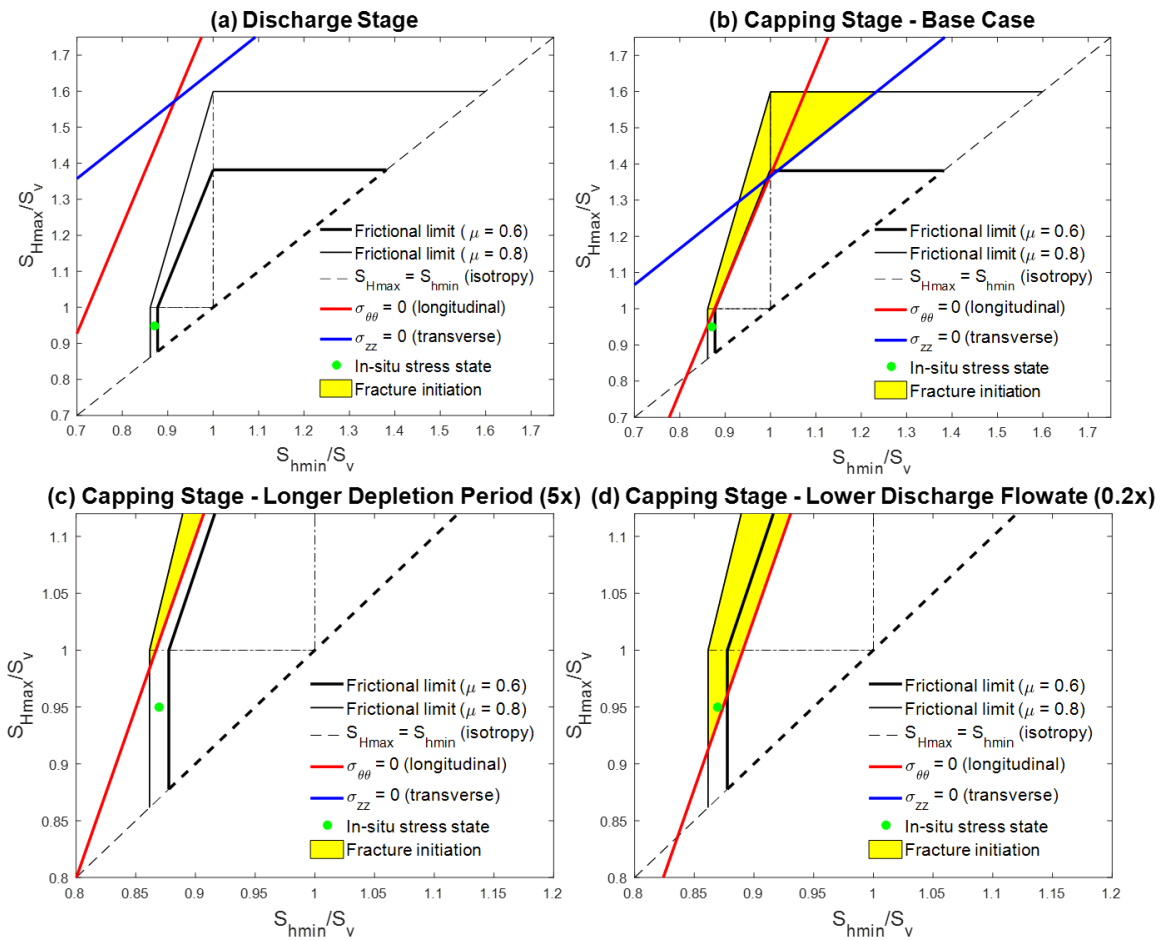Figure 7.12. Allowable stress state diagrams for the hypothetical case study using data calculated for a 5-step incremental capping stack shut-in procedure, showing (a) the post-blowout discharge stage, (b) the capping stage for Base Case parameters (Figure 7.9a), (c) the capping stage for a longer discharge period (Figure 7.9b), and (d) the capping stage for a lower discharge flowrate (Figure 7.9c).

241

7.6   DISCUSSION

7.6.1   Reservoir Depletion

Pressure depletion during the post-blowout discharge stage impacts both the *in-situ* stresses as well as the fracture initiation lines ($\sigma_{\theta\theta} = 0$ and $\sigma_{zz} = 0$) and the polygon size (Michael and Gupta, 2019b). For short discharge periods (Figure 7.12b and d), as well as small discharge flowrates, the change in the reservoir average p_p after discharge ends is assumed to be negligible, and thus the *in-situ* stresses and thus $p_{frac,L}$ and $p_{frac,T}$ remain constant.

This assumption is however questionable for a lengthy discharge period and high discharge flowrate scenarios such as that of the Macondo blowout, which lasted 83 days (Hickman et al., 2012). The longer the discharge period (or flowrate) is, the larger the total volume of hydrocarbons removed from the reservoir will be, leading to a larger decrease in p_p. Nevertheless, the effect of p_p depletion on the polygon size is secondary in importance to the effect on the two fracture initiation lines. A decrease in reservoir p_p (from 0.68 psi/ft, which is equivalent to $p_p/S_v = 0.82$ to 0.43 psi/ft, which is equivalent to $p_p/S_v = 0.52$ on Figure 7.13) enlarges the polygon increasing the range of *in-situ* stress states possible in the subsurface. However, lower p_p shifts both longitudinal and transverse fracture initiation lines to the left (Figure 7.13, for balanced conditions; $p_w = p_p$) shrinking the yellow region counteracting the effect on the polygon size. Furthermore, the magnitude of the two horizontal *in-situ* stresses will also decrease during depletion approximately by $\Delta S_{Hmax} \approx \Delta S_{hmin} \approx \alpha_B p_p$. This is reflected in the allowable stress state diagram by a movement of the *in-situ* stress state point on the diagram (green dot on Figures 7.12a through 7.12d) parallel to that of horizontal isotropy diagonal towards the bottom left corner, as shown by the green arrow on Figure 7.13.
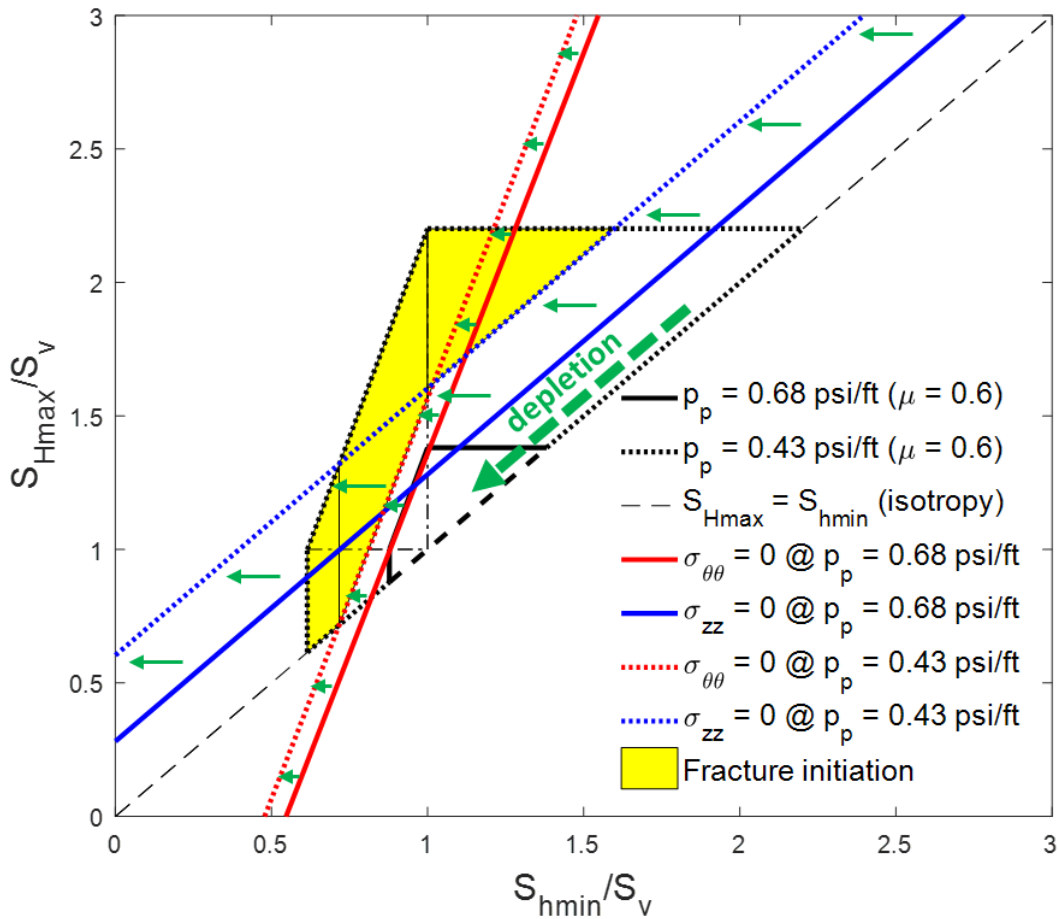
Figure 7.13. Allowable *in-situ* stress state diagram showing the effects of p_p reduction during depletion. The polygon expands as the p_p gradient decreases from 0.68 psi/ft ($p_p/S_v = 0.82$ after Figure 7.11) to 0.43 psi/ft, and the $\sigma_{\theta\theta} = 0$ and $\sigma_{zz} = 0$ lines shift to the left. The movement of the *in-situ* stress state during reservoir depletion is parallel to the direction shown by the green dotted arrow.

The actual reservoir p_p can be estimated analytically or numerically if the areal extent of the reservoir is known. In the absence of knowledge on the reservoir boundaries, common for wildcat wells, reliable estimations and projections of the average p_p are difficult. The geomechanical parameters need to be considered holistically to accurately

243

determine the net impact of p_p reduction during a prolonged discharge period before capping the well after a blowout.

7.6.2 Self-Killing Blowouts via Bridging

Scenarios of a well bridging-over and self-killing through the flow of cavings induced by the underbalanced conditions have been investigated (Willson, 2012; Willson et al., 2013). Analyses showed that self-killing via bridging is most likely if it takes place while the kick is under development within the wellbore; once the kick reaches the wellhead self-killing by bridging is no longer a possibility.

Bridging between the drillpipe and the formation wall in the openhole section (Figure 7.14) is more likely to occur than when drillpipe is not present (Willson, 2012), for instance during the development of a swabbing kick. Along with kick development, borehole collapse, cavings volume and transport, and cavings bridging analyses performed by Willson (2012) indicated the sanding rates shown in Figure 7.15 per specific wellbore discharge flowrate.
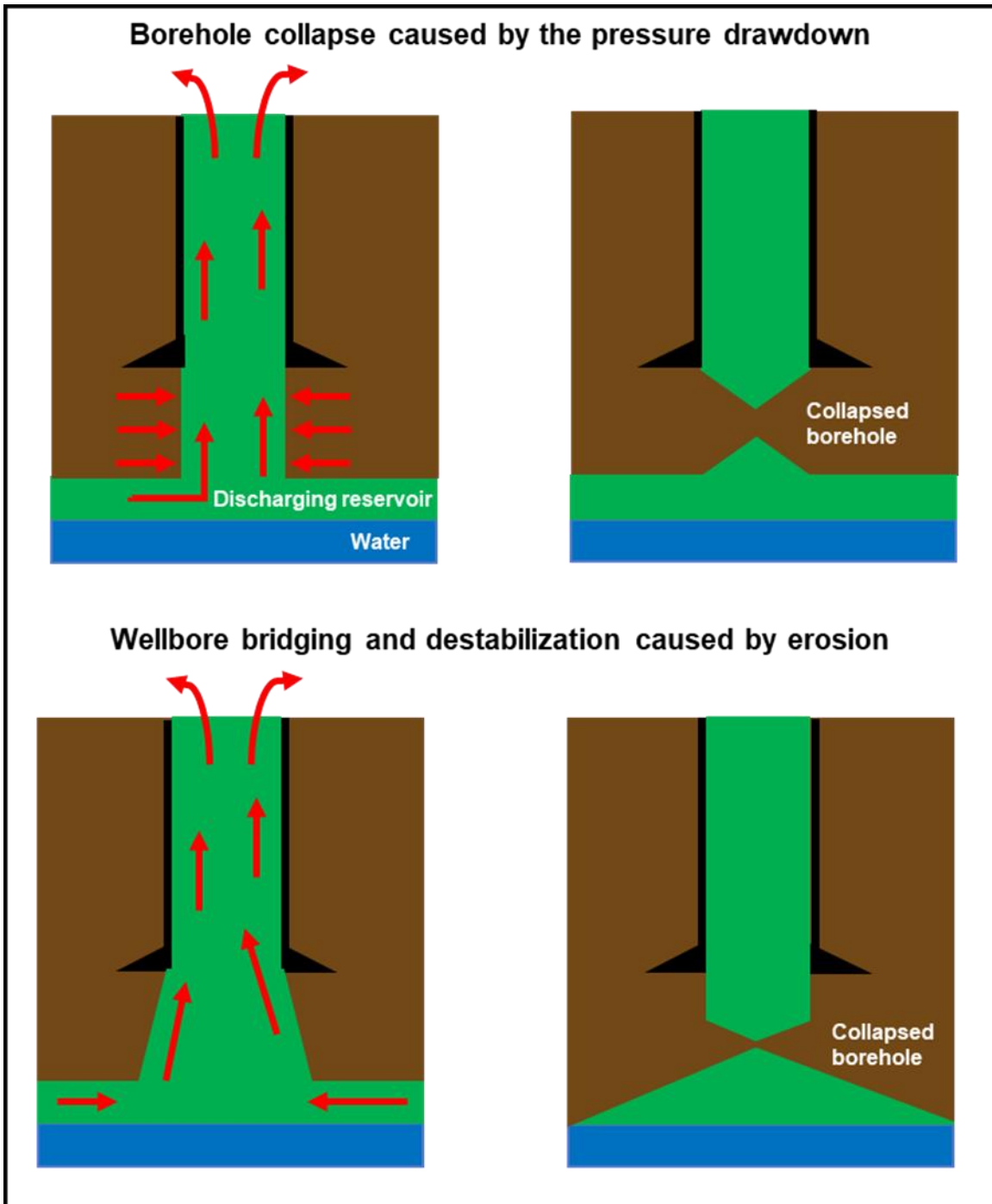
Figure 7.14. Wellbore bridging providing a passive cure to loss of well control (modified from Willson et al., 2013).
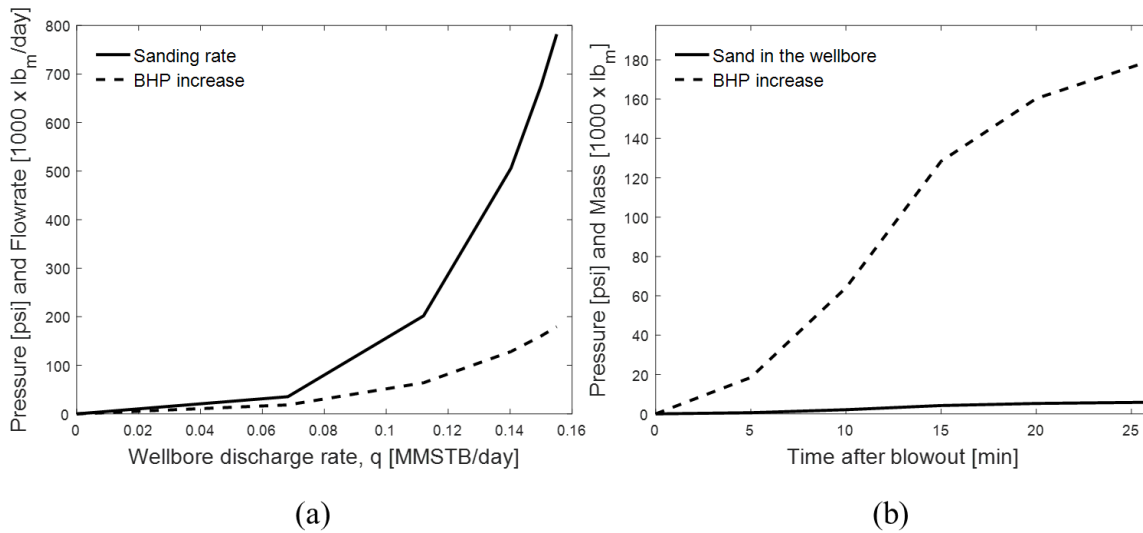
Figure 7.15. (a) Sanding rate and BHP increase induced by the wellbore discharge flowrate for the hypothetical case study parameters (produced using the results of Willson, 2012). (b) The sand mass accumulated in the wellbore and induced BHP increase with time (produced using the results of Willson, 2012).

7.6.3   Fracture Growth Containment in a Layered Rock Formation

Seafloor broaching of reservoir fluids resulting after loss of well control can lead to a severe environmental impact. The technical, economic and political implications of Union Oil's 1969 oils pill in the Santa Barbara Channel (Figure 7.16) are still strongly felt in the state of California, even to this day. Flowing at 5,000 barrels per day, this was a massive ecologic disaster (Figure 7.17) killing over 3,500 birds and other marine animals. In the wake of the Santa Barbara oil spill, a huge environmental movement was born, leading to the first "Earth Day" a year later in 1970. This incident changed California's oil industry forever.

246
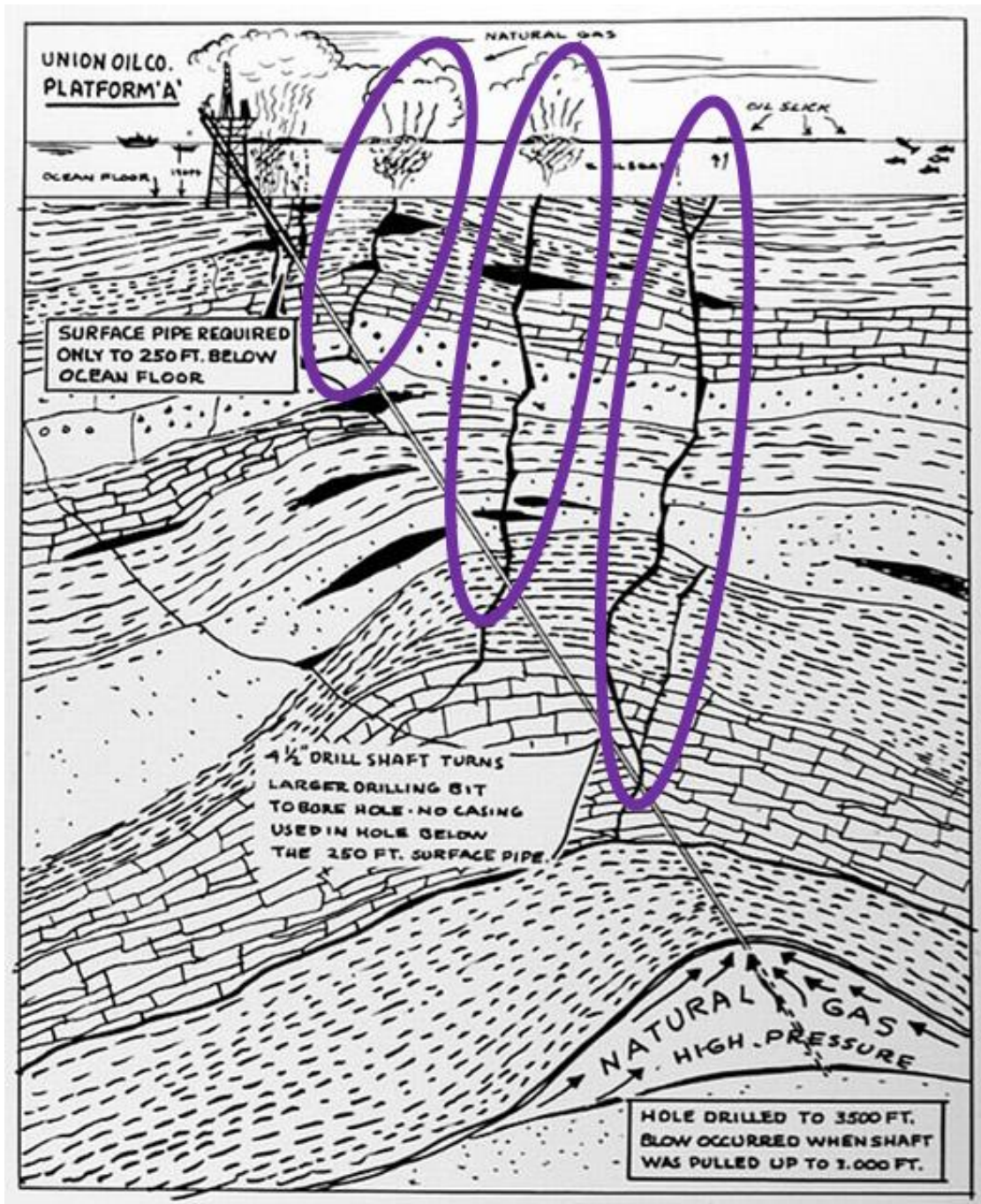
Figure 7.16. A schematic of Union Oil's A-21 well showing the fractures through which reservoir fluids broached to the seafloor (Dick Smith photo collection, UCSB, 1969-1971). Fractures initiating from the openhole section of the wellbore can be seen within the purple circles). These fractures enabled the reservoir fluids to broach to the seafloor.

247
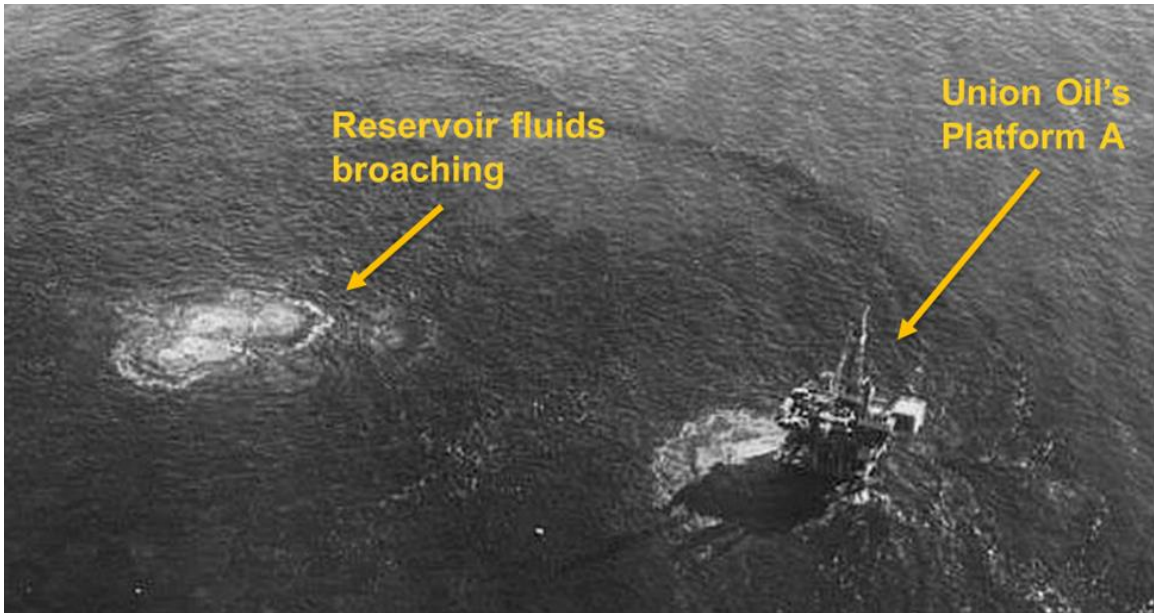
Figure 7.17. Aerial photo of the platform after the blowout with the broaching reservoir fluids "boil-ups" visible (modified from Trimborn, 1969).

Fracture propagation may often follow a plane different from the fracture initiation plane (Valko and Economides, 1995). This subsection discusses the propagation of fractures initiated in the rock formation during loss of well control. The mechanisms under which fracture initiation can occur during post-blowout capping was extensively discussed earlier in this chapter. The growth of a fracture initiated from the side of the wellbore is influenced by a variety of factors (Warpinski, 2016; Elnoamany et al., 2020), which are found in any reservoir.

7.6.3.1 In-Situ Stress State

Contrasts in the *in-situ* stresses impose the biggest influence on fracture growth (Simonson et al., 1978; Warpinski et al., 1982; Voegele et al., 1983; Palmer and Luiskutty,

1985; Warpinski, 2016). Fracture height growth is constrained if the layers above and below a growing fracture are under higher stress than the layer the fracture is propagating in. Static analysis of a symmetrically-growing fracture surrounded by higher stress layers was performed by Simonson et al. (1978). The stacked sequences common in the GoM (Vasquez Cordoba, 2018) can lead to layering. Each of these layers exhibits different *in-situ* stress loading and these contrasts may restrict fracture propagation to the seafloor after fracture initiation taking place during post-blowout capping.

7.6.3.2 Elastic Properties of Stacked Layers

A mechanical property interface can affect fracture growth, despite Simonson et al. (1978)'s indication that in ideal cases, material property interfaces can blunt fracture growth (Warpinski, 2016). Nevertheless, analysis by Cleary (1978) demonstrated that complexities in the property interfaces are difficult to analyze using standard tools. Additional energy is required to cross interfaces which restricts further fracture height growth. Modulus contrasts impact fracture width and can enhance or restrict the fluid flow through the fracture.

7.6.3.3 Fracture Toughness

A high value of fracture toughness can constrain fracture growth by inducing high pressure on the fracture tip and restricting the fracture height (Warpinski, 2016). Layered media, such as GoM's stacked sequences increase the complexity of the problem making the derivation of analytical expressions difficult, especially in the presence of heterogeneity in the layer's elastic properties.

7.6.3.4 Layer Interfaces

Presence of weak layer interfaces can blunt fracture growth (Perkins and Kern, 1961; Nierode, 1985; Warpinski, 2016) as noted in laboratory (Anderson, 1981; Teufel and Clark, 1984) and mineback studies (Warpinski et al., 1982; Warpinski and Teufel, 1987; Jeffrey et al., 1992; Zhang et al., 2007). This blunting effect is most important in shallow depths at low S_v values, which minimizes friction effects. However, overpressured zones can decrease friction in deeper locations. Specifically, weak interfaces can (i) stop vertical fracture growth completely, (ii) trigger fracture offsets, and (iii) initiate new fractures at the layer interfaces. Additionally, weak layer interfaces can lead to narrowing of the fractures across the interfaces (Barree and Winterfeld, 1998; Gu et al., 2008).

7.6.3.5 Discontinuities (e.g. Natural Fractures)

Discontinuities can influence fracture propagation. Natural fractures are the best example of such discontinuities. Studies (Teufel, 1979; Lee et al., 2015) have demonstrated the effect of angle of approach primarily and other factors (such as the interface material and its properties) in controlling the extent of blunting and offsetting the propagating fracture will experience. The highly complex fracture networks observed from mineback tests (Branagan et al., 1996) is thought to be due to such discontinuities. Single planar fracture growth is prevented, forcing the induced fracture to split into various intersecting components (Warpinski, 2016).

7.6.3.5 High Permeability Interval

The presence of a high permeability interval can terminate fracture growth through high leak-off. Those intervals, such as coal zones, provide a path of low resistance for the

fluid in the fracture stopping it from growing. Nevertheless, high permeability intervals can have the opposite effect providing a low resistance path for fluids to broach to the seafloor after a loss of well control situation.

7.7   CONCLUSIONS

The goal of this study was to investigate wellbore integrity *vis-à-vis* fracturing during extreme loss of well control situations that lead to blowouts. Based on analyses presented in this study, the following conclusions are made:

- Critical discharge flowrates can be calculated for a given capping stack shut-in strategy and preceding discharge period, below which fracture initiation must be expected during post-blowout capping. Upward propagation of these fractures can provide a path for reservoir fluids to broach to the seafloor/surface.

- These critical discharge flowrates can be compared with the mandatory-by-law WCD calculations, for determining an appropriate capping stack shut-in strategy, which would ensure safe and efficient capping of a well that has suffered a blowout.

- For a hypothetical case study performed using typical deepwater GoM parameters, a 5-fold increase in the discharge period leads to an decrease in p_{ws} from 3.4% to 4.7% and a 5-fold decrease in the discharge flowrate yields an increase in p_{ws} from 1.5% to 7.9% during 24 hours after an abrupt shut-in.

- A 5-step incremental capping stack shut-in prevents fracturing over a 48-hour timeframe after the beginning of the shut-in. Increasing the discharge period 5-fold makes $\sigma_{\theta\theta}$ and σ_{zz} more compressive by 123% and 14%, respectively. A 5-fold decrease in the preceding discharge flowrate, makes $\sigma_{\theta\theta}$ and σ_{zz} more tensile by 172% and 19%, respectively leading to an early longitudinal fracture initiation.

251

Increasing the number of shut-in steps to 10 and keeping all other parameters the same, makes $\sigma_{\theta\theta}$ and σ_{zz} more tensile by 56% and 6.3%, respectively, yet still prevent fracture initiation during the 48 hours after the beginning of the shut-in.

- Reservoir depletion is the biggest factor in preventing fracturing during post-blowout capping. Nevertheless, as depletion is proportional to larger hydrocarbon volumes discharged, well control engineers must look into other fracture/broaching prevention methods. Incremental shut-in capping stack strategies can be "tailored" to the well and reservoir's specific parameters, as well as the preceding discharge flowrate and period.

- Blowouts could be self-killed by sand bridging under specific conditions the most important of which is the bridging taking place while the kick is developing inside the borehole.

- Several factors, primarily *in-situ* stress contrasts, control the growth of the initiated fractures in a layered rock formation and can constrain fracture propagation to the seafloor.

Chapter 8. Stability Analysis During Loss of Well Control for a Casing-Cement Sheath-Rock Formation System

A robust evaluation of the casing-cement sheath-rock formation system is foundational to ensuring wellbore integrity at any point in the lifetime of a well. Published results from laboratory experiments show *a-priori* to cement curing, the cement stress decreases and followed by an increase, leading to an eventual stabilization at the pore pressure of the surrounding rock formation. This phenomenon is used to develop expressions for the aggregate stress distribution within the casing-cement sheath-rock formation system. Linear elasticity is used to model the mechanical behavior of steel casing and cured cement sheath. The rock formation is also modeled using linear elasticity, however with the incorporation of a static pore pressure. The tensile failures of debonding, radial cracking, and disking are considered along with shear compressive failures within the cement sheath. Once the cementation process is complete, the stress increments are withstood by the casing-cement sheath-rock formation system. The aggregate stress distribution model is applied on a hypothetical case study example, using numbers typical to deepwater Gulf of Mexico (GoM), for loss of well control situation, following a blowout. Loss of well control presents scenarios of high stress loading in the casing-cement sheath-rock formation system, with the wellbore pressure abruptly decreasing during post-blowout discharge, followed by an increase during the post-blowout capping procedures. The impact of reservoir depletion induced by prolonged discharge periods, or high discharge flowrates is discussed at the end.

8.1 INTRODUCTION

Reliable modeling of the casing-cement sheath-rock formation stress distribution is paramount for accurate wellbore integrity analysis in oil and gas wells both onshore and offshore. The stress state within the casing-cement sheath-rock formation system has been extensively studied analytically (Thiercelin et al., 1998; Yuan et al., 2013; Li et al., 2015; Liu et al., 2017; Luo et al., 2020) and numerically (Wong and Yeung, 2005; Nabipour et al., 2010). Conventional modeling considers the three-part system (casing, cement sheath, and rock formation) as a single-part structure with stress and displacement boundary conditions applied appropriately at given time-step (simultaneously) on the entire structure. This assumption overlooks the fact that the process of drilling, running casing, cement-liquid pouring, and cement curing are performed separately in a successive manner (Amziane and Andriamanantsilavo, 2004; Gray et al., 2009; Agofack et al., 2019; Zuo and Bennett, 2019; Luo et al., 2020), which makes the application of boundary condition unrealistic to apply simultaneously on the entire model.

Throughout the life of a well, the stress state continues to change with changing conditions (different stages in hydrocarbon recovery), with the stress state of a preceding stage impacting the subsequent stage (Hu et al., 2019). This implies that a thorough analysis of the evolution of the stress state along the stages of a well's life cycle is paramount to understanding and hence modeling the integrity of the casing-cement sheath-rock formation system.

Hu et al. (2019) evaluated the evolution of the stress state inside the casing-cement sheath-rock formation system during cement injection, cement curing, completions (stimulation via hydraulic fracturing), and production stages. The stress state of the aggregate casing-cement sheath-rock formation system upon wait-on-cement (WOC) is

called the "initial stress state" (Fourmaintraux et al., 2005; Saint-Marc et al., 2008; Bois et al., 2012; Shi et al., 2017; Luo et al., 2020). In order to solve for the initial stress state, the stress distribution of the cement sheath conception needs to be defined and verified, which is a challenging task. Luo et al. (2020) performed an experiment for examining the pore pressures and the lateral stresses during the cement curing period. The results showed the lateral stress becoming equal to the formation pore pressure once the formation became penetrative (Luo et al., 2020). Hence, the evolution of the stress state within the casing-cement sheath-rock formation system can be simplified by omitting the complex solidification process during cement curing in the evaluation of the system's initial stress state.

The resulting expressions for the stress state of the casing-cement sheath-rock formation system are applied to a hypothetical case study using numbers typical to deepwater GoM. The extreme conditions taking place during loss of well control represent the most critical stage of cement sheath integrity. The stability of the casing-cement sheath-rock formation is assessed analytically for the post-blowout discharge and capping periods.

8.2   THEORETICAL CONSIDERATIONS

The geometry of the wellbore and casing and cement layers (Figure 2.11) makes cylindriacal coordinates the most appropriate in modeling the casing-cement sheath-rock formation system. The deformation of the casing-cement and cement-rock subsystems can be modeled by the plane strain theory (Fjaer, 2008), because the axial dimension of the well (length) is much larger than the in-plane dimensions. The following assumptions are made:

i.   The steel casing and cement sheath are isotropic linearly elastic and cylindrical in shape. Because the casing is impermeable and the cement sheath exhibits only low permeability in the post-WOC period, the pore pressure variation in the casing-cement sheath portion of the system is very slow (Hu et al., 2019). Hence, poromechanical behavior is not considered in the casing and cement layers of the system.

ii. The casing is 100 percent centered, with the cement sheath completely filling the annular space.

iii. The rock formation is a porous-permeable medium and its mechanical response is governed by the pressure of the fluid inside the pores. Poroelastic effects induced by fluid infiltration in-and-out of the pores are neglected in this chapter, excluding the considerations of shear failure and reservoir depletion (Sections 8.3 and 8.5).

For a vertical well drilled parallel to the vertical *in-situ* principal (overburden) stress, S_v, the initial stress is limited by the most and least compressive horizontal in-situ principal stresses, S_{Hmax} and S_{hmin}, respectively. The casing-cement sheath-rock formation system can be split into its three components and evaluated discretely.

The presence of the wellbore, induces stress perturbations in the near-wellbore region, which alter the local stress state significantly in comparison to the far-field, *in-situ* stress state (S_v, S_{Hmax}, and S_{hmin} following Anderson, 1951). Kirsch (1898) derived analytical solutions for the stress concentrations on a uniform plate, with a circular hole under uniform tension in a linearly elastic medium. The stresses comprising the stress field are oriented in cylindrical coordinates and comprise of the axial stress, presumed to be parallel to the z-axis, σ_{zz}, tangential stress (commonly referred to as "hoop" or circumferential), $\sigma_{\theta\theta}$, and radial stress, σ_{rr}, oriented orthogonally to the circumference of

the wellbore. Figure 8.1 shows the configuration of σ_{zz}, $\sigma_{\theta\theta}$, and σ_{rr} on the wellbore radius, r_w, where θ is the angle on the wellbore cross-section taken clockwise from S_{Hmax} for vertical wells.
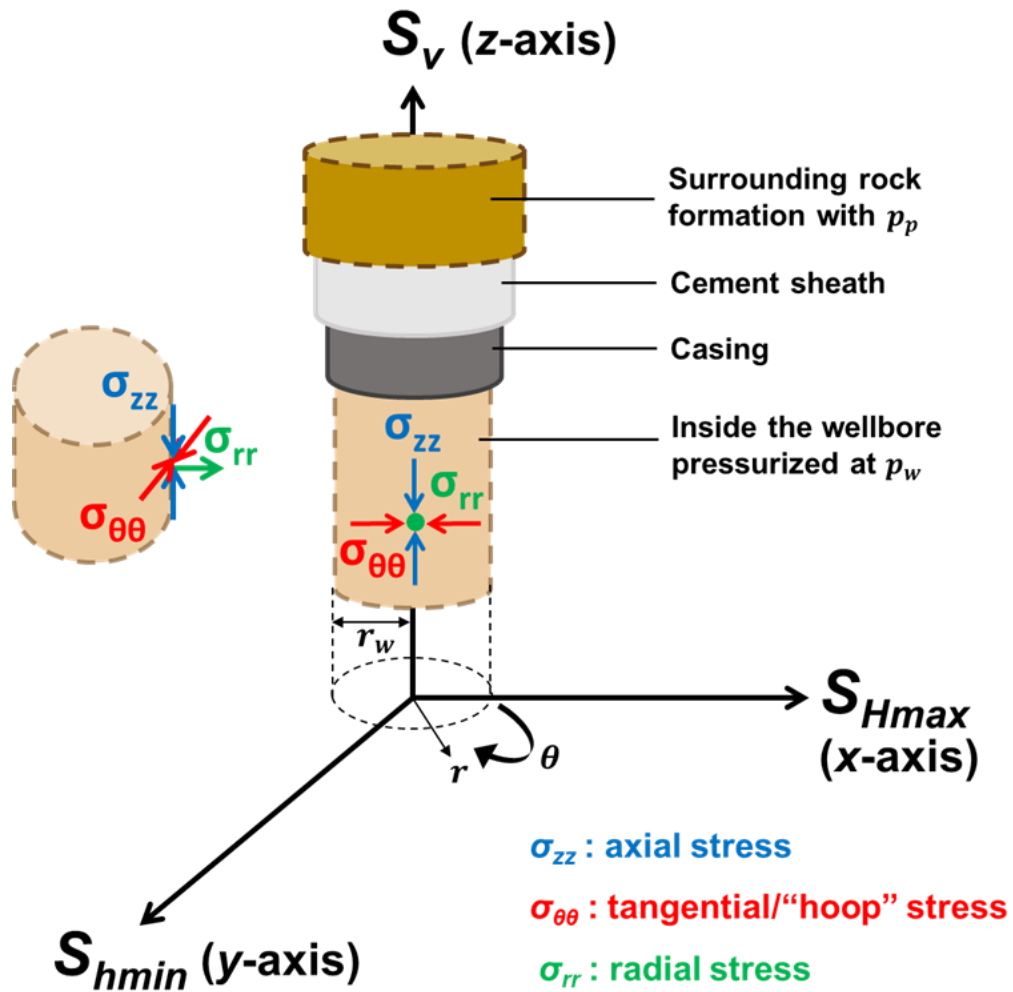

Figure 8.1.   Configuration of axial (σ_{zz}), tangential ($\sigma_{\theta\theta}$), and radial (σ_{rr}) stresses on the radius of the wellbore ($r = r_w$).

As the distance from the center of the wellbore, r increases, the near-wellbore stresses as σ_{zz}, $\sigma_{\theta\theta}$, and σ_{rr} are collectively known, gradually become identical to the far-

257

field, in-situ stresses (S_v, S_{Hmax}, and S_{hmin}). In order to model the stress distribution in the casing-cement sheath-rock formation system, the stress distribution in each of the three layers (casing, cement sheath, and rock formation) has to be analyzed separately. The distributions of each stress in all three layers are then superimposed to create the aggregate distributions of σ_{zz}, $\sigma_{\theta\theta}$, and σ_{rr}.

8.2.1   Stress State Inside the Casing Walls

The steel casing can be modeled as a thick-walled cylinder. The casing is subjected to the hydrostatic pressure of the fluid column in the wellbore ($p_w = \rho_w g D$) at the inner boundary, where ρ_w is the density of the fluid in the wellbore and D is the depth along the wellbore. On the outer boundary the casing is subjected by the cement slurry pressure, p_{cem}. The stress and displacement distribution within the thick-walled cylinder can be modeled by the "Lamé solutions." This refers to analytical expressions for the elastic stresses inside a thick-walled circular cylinder under internal and external pressure loading (which can apply to strings of steel casing), as was presented in a joint study by Lamé and Clapeyron (1831). Using a convention that defines compression to be positive and tension to be negative, the stress state inside the casing walls is given by

$$\sigma_{zz,csg} = \frac{p_w r_w^2 - p_{cem} r_{csg}^2}{r_w^2 - r_{csg}^2} \tag{8.1}$$

$$\sigma_{\theta\theta,csg} = \frac{p_w r_w^2 - p_{cem} r_{csg}^2}{r_w^2 - r_{csg}^2} + \frac{r_{csg}^2 r_w^2 (p_w - p_{cem})}{r^2 (r_w^2 - r_{csg}^2)} \tag{8.2}$$

$$\sigma_{rr,csg} = \frac{p_w r_w^2 - p_{cem} r_{csg}^2}{r_w^2 - r_{csg}^2} - \frac{r_{csg}^2 r_w^2 (p_w - p_{cem})}{r^2 (r_w^2 - r_{csg}^2)} \tag{8.3}$$

258

where $\sigma_{zz,csg}$, $\sigma_{\theta\theta,csg}$, $\sigma_{rr,csg}$ are respectively the axial, tangential (also circumferential or "hoop"), and radial stresses within the casing wall, at a point-of-interest dictated by radius, r, which extends from r_w to the outer radius of the casing, r_{csg} ($r_w \leq r \leq r_{csg}$). Notably, $\sigma_{zz,csg}$ (Eq. 8.1) is independent of r, while $\sigma_{\theta\theta,csg}$, $\sigma_{rr,csg}$ (Eqs. 8.2 and 8.3) depend r. The wellbore pressure is denoted by p_w and the formation pore pressure by p_p.

8.2.2 Stress State Within the Cement Sheath

8.2.2.1 The Cement Injection Stage

During cement injection, the cement slurry remains in liquid phase, not being able to withstand hydraulic pressure. According to Hu et al. (2019), the stress state in cement slurry is equal to the hydrostatic pressure in the cement slurry, $p_{cem} = \rho_{cem}gD$, where ρ_c is the cement slurry (liquid, pre-curing) density. On its outer boundary the cement slurry is subjected to the earth's local *in-situ* stresses.

The removal of the rock occupying the borehole volume during drilling made the pressure *a-priori* applied at the borehole by local *in-situ* stress state to be replaced by the hydraulic pressure of the drilling fluid (p_w). During cement injection, the cement only undertakes its own hydrostatic pressure, p_{cem} (Hu et al., 2019), making pressure variations at the borehole to be offset by rock deformations, with the *in-situ* stresses not transferred to the cement slurry and the steel casing (Hu et al., 2019). In a similar manner, p_w is not transferred from the casing to the cement slurry, or the surrounding rock formation.

8.2.2.2 The Cement Curing Stage

During cement curing (setting), hydration converts the cement slurry injected in the casing-rock formation annulus to a solid. During hydration, the cement's volume may shrink or expand according to the slurry formula and conditions in place (Hu et al., 2019), generating what is known as "free strain" – strain induced without stress (Ulm and Coussy, 1996). As the pressure inside the casing (p_w) remains constant, the system will undergo no change if the cement volume also remains constant during curing. However, if cement volume change occurs, the free strain in the cement will be constrained by the casing and rock formation, inducing incremental stress (Hu et al., 2019). When the cement shrinks, its ability to resist shear and tensile failure decreases, while when the cement sheath expands, its ability to resist tensile and to some extend shear failure increases. The increase in p_{cem} with increase in depth (D), improves the cement sheath's ability to resist any failure mode (radial, shear, tensile, and debonding).

Luo et al. (2020) performed a simple laboratory experiment with the objective of evaluating the stress and pore pressure within the cement sheath, while WOC. A simple laboratory setup (Figure 8.2) was used to simulate the casing-cement sheath-rock formation system. PVC pipes were used to simulate the casing and the formation with drilled holes used to mimic the porosity of the rock formation on the outer cylinder. Cement was pumped in the annular region between the two pipes and water was injected inside the inner PVC pipe and in the annular region between the outer PVC pipe and the outer cylinder. Filter paper was wrapped around the outer PVC pipe to prevent the cement slurry from escaping into the water. A computer system recorded lateral stress and pore pressure date, while the cement slurry was pumped inside the annulus.
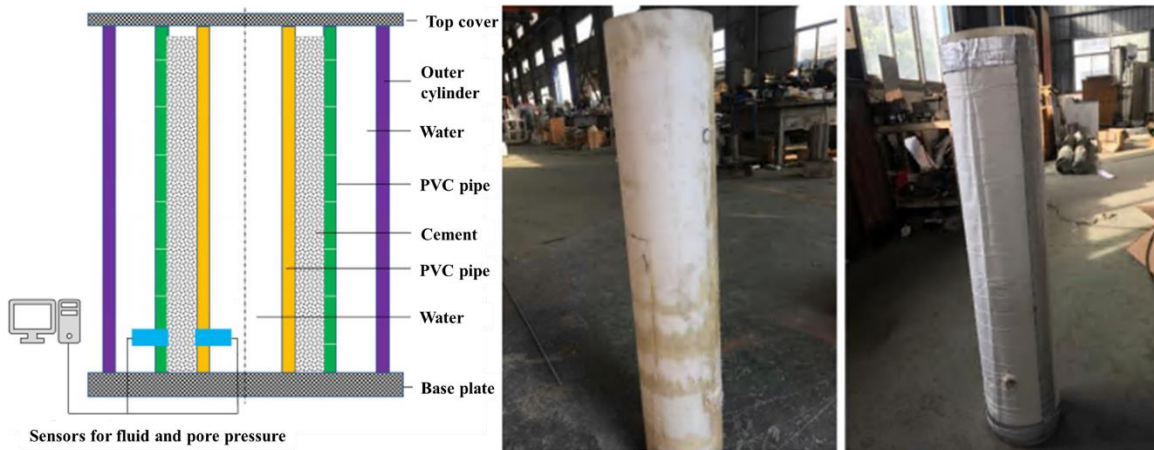
Figure 8.2.   A schematic of the laboratory setup used on the left and on the right a photograph of the drilled outer PVC pipe, before and after being wrapped with the filter paper (modified from Luo et al., 2020).

The results showed that the lateral stress variation of the cement sheath can be divided into three distinct intervals (Figure 8.3). The lateral stress is a good proxy for the three normal stresses acting on the edges of the cement sheath. Those are the axial, $\sigma_{zz,cem}$, tangential, $\sigma_{\theta\theta,cem}$, and radial, $\sigma_{rr,cem}$, stresses.
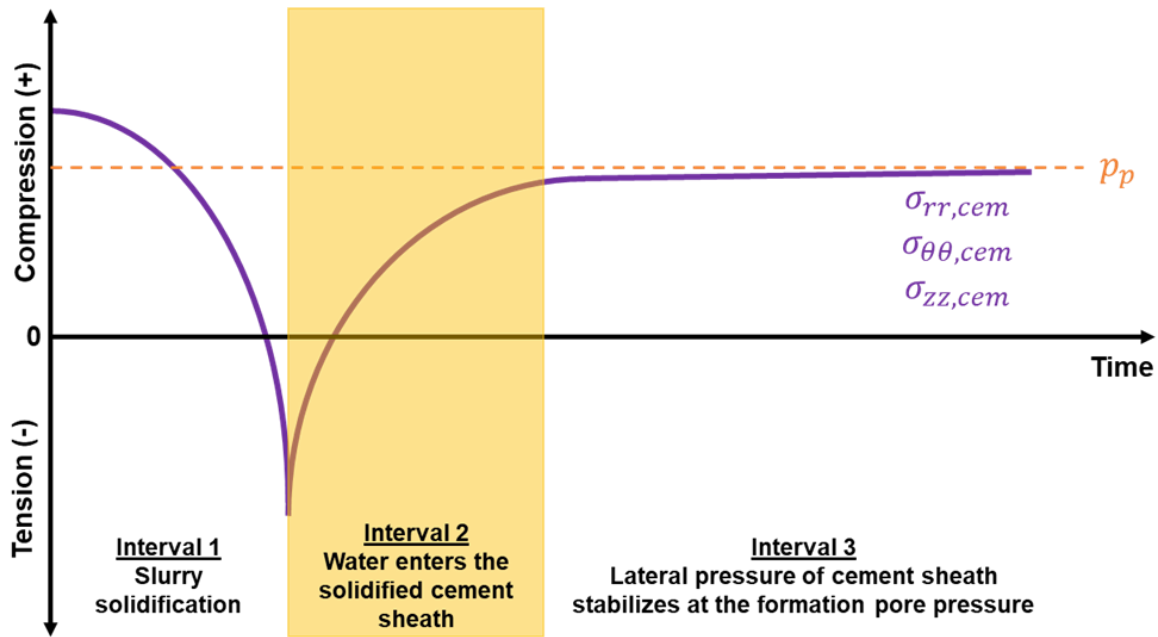
Figure 8.3. The lateral stress (proxy for $\sigma_{rr,cem}$, $\sigma_{\theta\theta,cem}$, and $\sigma_{zz,cem}$) during WOC (schematic generated from Luo et al., 2020).

During Interval 1, the solidification of the slurry takes place, when the cement gradually changes phase from liquid to solid, with the water within the cement sheath consumed which gradually decreases the lateral stress. Then during Interval 2, water starts entering the now fully-solidified cement sheath causing the lateral stress to increase rapidly. The lateral stress gradually stabilizes at a magnitude roughly equal to the p_p of the adjacent rock formation during Interval 3 (Figure 8.3).

In accordance with Luo et al.'s (2020) experimental results, the initial stress of the cement sheath following cement curing is equal to p_p. This is true all along the cement sheath radius which extends from r_{csg} to the outer radius of the cement sheath, r_{cem}. The radial strain within the casing wall, ε_{rr}, which is then represented by

$$\varepsilon_{rr} = \frac{r(1+v)(1-2v)\left(r_w^2 p_w - r_{csg}^2 p_p\right)}{E_{csg}\left(r_w^2 - r_{csg}^2\right)} + \frac{r_{csg}^2 r_w^2 (1+v)\left(p_w - p_p\right)}{r E_{csg}\left(r_w^2 - r_{csg}^2\right)} \tag{8.4}$$

where E_{csg} is the elastic "Young's" modulus of the casing walls. Using Luo et al.'s (2020) experimental findings, the initial stress state within the cement sheath is simply Sgiven by

$$\sigma_{zz,cem} = \sigma_{\theta\theta,cem} = \sigma_{rr,cem} = p_p \tag{8.5}$$

8.2.3 Stress State Within the Rock Formation

The rock formation surrounding the cemented wellbore is modeled as a non-axisymmetric problem assuming no internal and external pressure for the casing and the cement sheath (Luo et al., 2020). Hubbert and Willis (1957) modification of the Kirsch (1898) analytical solutions, to incorporate fluid pressure inside the hole in a linearly elastic medium under biaxial stress loading. For a vertical well in a homogeneous, isotropic rock, the initial stress state at $r \geq r_{cem}$ are defined (from Zoback, 2014) by

$$\sigma_{zz,for}\big|_{r \geq r_{cem}} = S_v - 2v(S_{Hmax} - S_{hmin})\frac{r_w^2}{r^2}\cos 2\theta - \frac{r_w^2}{r^2} p_p \tag{8.6}$$

$$\begin{aligned}
\sigma_{\theta\theta,for}\big|_{r \geq r_{cem}} = &\frac{1}{2}(S_{Hmax} + S_{hmin})\left(1 + \frac{r_w^2}{r^2}\right) \\
&- \frac{1}{2}(S_{Hmax} + S_{hmin})\left(1 + 3\frac{r_w^4}{r^4}\right)\cos 2\theta - \frac{r_w^2}{r^2}\left(p_w - p_p\right)
\end{aligned} \tag{8.7}$$

$$\sigma_{rr,for}\big|_{r \geq r_{cem}} = \frac{1}{2}(S_v + S_{Hmax})\left(1 - \frac{r_w^2}{r^2}\right) \tag{8.8}$$

$$+ \frac{1}{2}(S_v - S_{Hmax})\left(1 - 4\frac{r_w^2}{r^2} + 3\frac{r_w^4}{r^4}\right)\cos 2\theta + \frac{r_w^2}{r^2}\left(p_w - p_p\right)$$

where, $\sigma_{zz,for}$, $\sigma_{\theta\theta,for}$, $\sigma_{rr,for}$ are the rock formation axial, tangential, and radial stresses, respectively.

The initial stress state of a casing-cement sheath-rock formation system can be obtained by superimposing the casing wall, cement sheath and rock formation distributions for the axial ($\sigma_{zz} = \sigma_{zz,csg} + \sigma_{zz,cem} + \sigma_{zz,for}$), tangential ($\sigma_{\theta\theta} = \sigma_{\theta\theta,csg} + \sigma_{\theta\theta,cem} + \sigma_{\theta\theta,for}$), and radial stress ($\sigma_{rr} = \sigma_{rr,csg} + \sigma_{rr,cem} + \sigma_{rr,for}$). A different *in-situ* stress state (S_v, S_{Hmax}, and S_{hmin} combination) will only impact the stress state within the rock formation (Eqs. 8.6 through 8.8).

8.2.4 Casing Failure Criterion

The von Mises (1913) criterion of maximum energy distortion, which is used to assess the integrity of "thick-walled cylinders" over a range of conditions, is applied to cylindrical steel casing at a variable p_w. In its simple form, under the assumptions of the plane strain theory (Fjaer, 2008), the radial stresses are neglected and the criterion can be presented on a 2D plot (Figure 8.4). The tangential stress inside the casing wall, $\sigma_{\theta\theta,csg}$ is plotted on the vertical axis, with the axial stress inside the casing wall, $\sigma_{zz,csg}$, plotted on the horizontal axis. Both axes variables are normalized by the yield stress of the casing, σ_{yield}. According to the von Mises (1913) theory, the two stresses in the casing wall ($\sigma_{\theta\theta,csg}$ and $\sigma_{zz,csg}$) can be lumped into one term, σ_e, or the "von Mises stress equivalent" which is defined by

$$\sigma_e = \pm\sqrt{\left(\sigma_{\theta\theta,csg}\right)^2 - \sigma_{\theta\theta,csg}\sigma_{zz,csg} + \left(\sigma_{zz,csg}\right)^2} \qquad (8.9)$$

which results in an ellipse as shown on Figure 8.4.
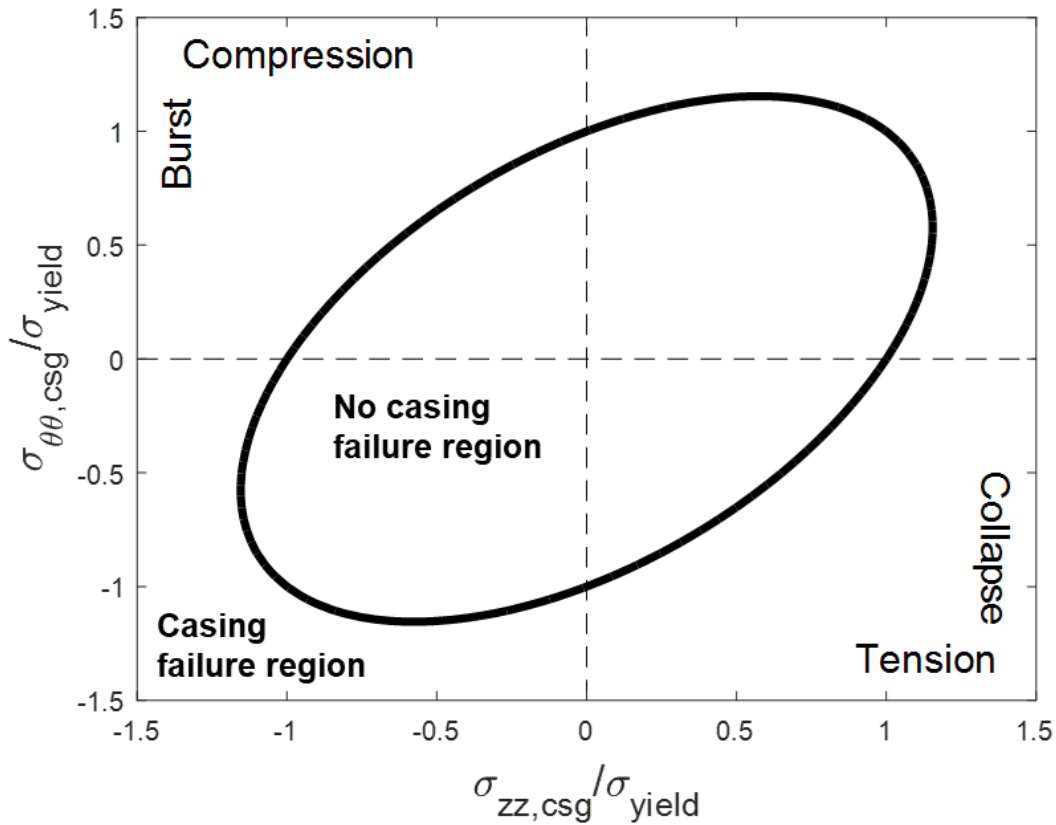

Figure 8.4.   The von Mises (1913) failure criterion applied to casing failure, considering four failure modes. These are (i) tension, (ii) compression, (iii) collapse, and (iv) burst. As long as the conditions remain within the region inside the ellipse, no casing failure will take place. Points outside the ellipse indicate casing failure.

Points outside the ellipsoid ($\sigma_e > \sigma_{yield}$) indicate casing failure; burst versus collapse from the vertical axis and tension versus compression on the horizontal axis.

265

8.2.5 Cement Sheath Failure Criteria

There are four main failure mechanisms observable in the cement sheath, which can compromise the integrity of the casing-cement sheath-rock formation system. These were described by Bois et al. (2011), as (i) inner and outer debonding, (ii) radial cracking, (iii) shear cracking, and (iv) disking (Figure 8.5).
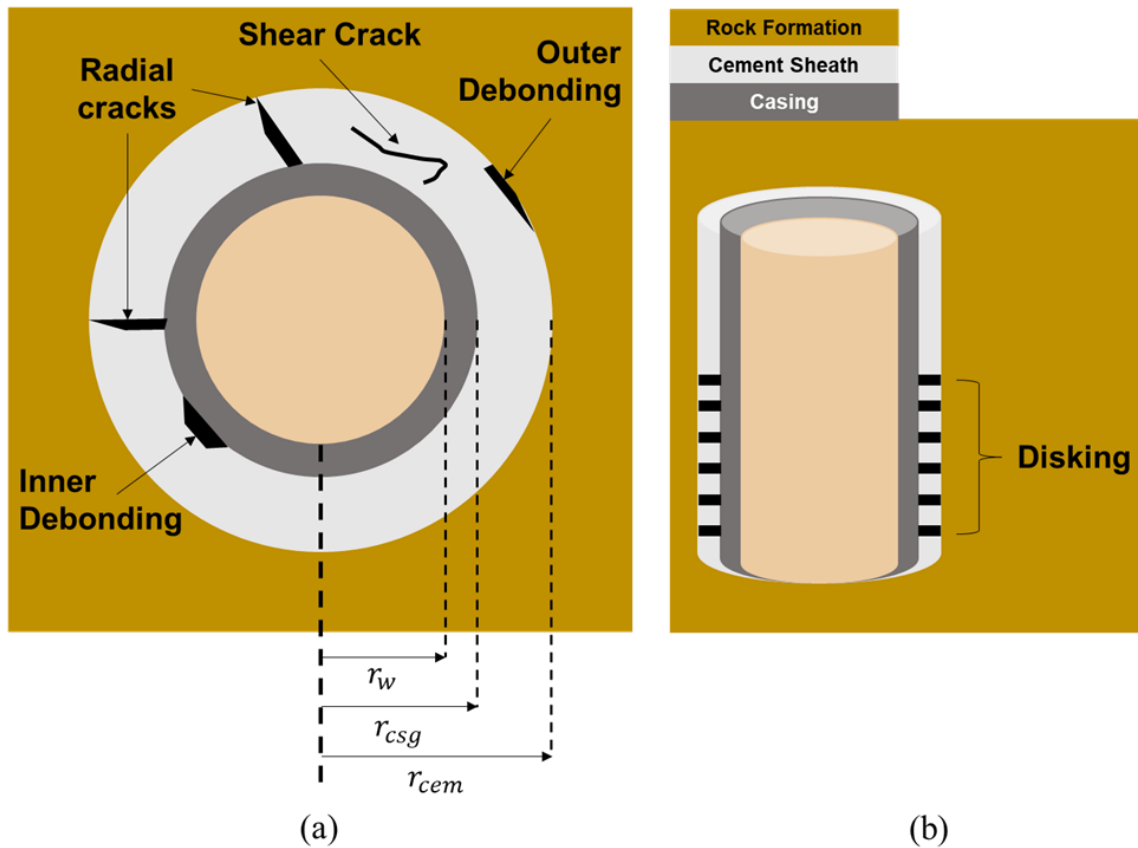

Figure 8.5.   Mechanisms of failure within the cement sheath, (a) shows inner and outer debonding, radial cracking, and shear cracking, with (b) showing disking.

For each failure mechanism an analytical criterion specifies the conditions under which the particular failure mode takes place. Debonding is a form of tensile failure, which

occurs when σ_{rr} at either of the two interfaces in the casing-cement sheath-rock formation system (at $r = r_{csg}$ or $r = r_{cem}$) becomes tensile, satisfying the condition on Eq. 8.10. Inner debonding takes place on the casing-cement sheath interface (first interface), while outer debonding occurs on the cement sheath-rock formation interface (second interface), as

$$\sigma_{rr}|_{r=r_{csg}or\ r=r_{cem}} < -T_{cem} \tag{8.10}$$

where T_{cem} is the tensile strength of the cement. Radial cracking is also a form of tensile failure, taking place when $\sigma_{\theta\theta}$ becomes more tensile than T_{cem} as presented by Eq. 8.11, as

$$\sigma_{\theta\theta}|_{r_{csg}\leq r\leq r_{cem}} < -T_{cem} \tag{8.11}$$

These are tensile fractures initiating longitudinally to the axis parallel to the wellbore. Disking takes place when σ_{zz} becomes more tensile than T_{cem} (Eq. 8.12), generating tensile fractures transversely to the wellbore.

$$\sigma_{zz}|_{r_{csg}\leq r\leq r_{cem}} < -T_{cem} \tag{8.12}$$

The initiation of shear cracks is determined by the Mohr-Coulomb failure criterion, presented on Eq. 8.13. When the shear stress, $\sigma_{r\theta}$, (often denoted by "$\tau_{r\theta}$") is greater than the maximum shear stress possible within the cement, as

$$\sigma_{r\theta}|_{r_{csg}\leq r\leq r_{cem}} > C_o + \mu_{cem}\sigma_n \tag{8.13}$$

where C_o is the cohesion of cement, μ_{cem} is the internal friction factor of the cement sheath, equal to the tangent of the internal friction angle, and σ_n is the normal stress on the plane of failure given by

$$\sigma_n = \frac{\sigma_1 + \sigma_3}{2} + \left(\frac{\sigma_1 - \sigma_3}{2}\right)\cos 2\beta \tag{8.14}$$

where β is the failure angle, with σ_1 and σ_3 being respectively, the greatest and least compressive effective principal stresses, such

$$\sigma_i = S_i - \alpha_B p_p \tag{8.15}$$

where S_i may be S_v, S_{Hmax}, or S_{hmin} and i in σ_i can be 1, 2, 3 depending on the relative magnitude signifying the greatest, intermediate, and least compressive principal stresses, respectively. The Biot's (1941) poroelastic coefficient, α_B, is used to incorporate the mechanical effects of fluid infiltration in-and-out of the pores (see Chapter 3 and Appendix B). According to the Mohr-Coulomb theory, shear failure is independent of σ_2 and p_w.

Debonding, tensile, and shear failures become less likely with increasing depth. Cement volume shrinkage decreases the cement sheath's resistance in all failure modes, while moderate expansion enhances the cement sheath's overall integrity (Hu et al., 2019). Well pressurization followed by depressurization can yield plastic deformation (Hu et al., 2019) in the cement sheath, which presents the risk of debonding. Although in this study, plastic behavior is neglected, Chu et al. (2015) assess the impact of plastic behavior on the cement sheath.

When calculating the system's stress state, the in-situ stresses and internal casing pressure are applied to the overall system. Nevertheless, due to the cement being in liquid phase during injection, formation and casing take over leaving only post-cement curing pressure variations to be applied on the casing-cement sheath-rock formation system. This can yield an overestimation in the risk of cement sheath failure (Hu et al., 2019).

8.3   THE INITIAL STRESS STATE: A DEEPWATER GOM CASE STUDY

A hypothetical case study of a vertical well is performed as an application example for evaluating the initial stress state of a casing-cement sheath-rock formation system, using typical deepwater GoM numbers. The input geomechanical and petrophysical parameters are taken from Michael and Gupta (2020c) and are shown in Table 8.1.

Table 8.1.   Input parameters for the deepwater GoM case study.

Parameter	Symbol	Value
Average reservoir depth	d_{res}	18,135 ft
Casing shoe depth	d_{csg}	17,200 ft
Formation pore pressure	p_p	12,247 psi
Overburden stress (from seafloor)	S_v	0.82 psi/ft
Maximum horizontal stress	S_{Hmax}	$0.95S_v$
Minimum horizontal stress	S_{hmin}	$0.87S_v$
Poisson's ratio	v	0.25
Biot's poroelastic coefficient[1]	α_B	0.8
Cement tensile strength	T_{cem}	~0 psi

[1] **Please note that in this Chapter, all poroelastic effects were neglected in the calculation of the stresses in the rock formation as per Eqs. 8.6 through 8.8.**

The mudline is at 5,100 ft under the rotary table, which is 100 ft above the average sea level. A $9^5/_8$ in casing is set at 17,200 ft true vertical depth (TVD) from the rotary table and a $5^1/_2$ in drillpipe is present in the borehole at balanced drilling conditions.

Figures 8.6 through 8.8 show the initial stress state of the casing-cement sheath-rock formation system for $\theta = 0°$, which is in the direction along S_{Hmax} and $\theta = 90°$, which is in the direction along S_{hmin}, for a vertical well. Due to the cement sheath stress being nearly equal to p_p based on Luo et al.'s (2020) experimental results, the stress state within the cement sheath would hence uniform, despite variations in the stress state of the casing walls and the rock formation.
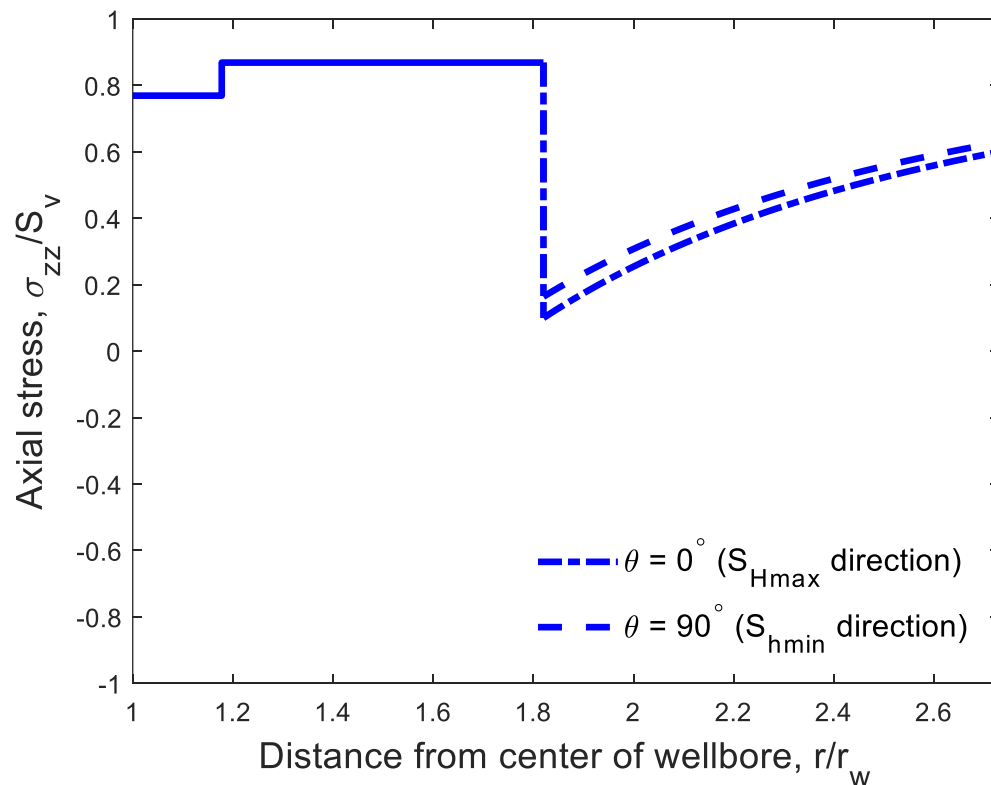
Figure 8.6. The axial stress, σ_{zz}, distribution of the casing-cement sheath-rock formation system at slightly overbalanced conditions, with $p_w = 12,790$ psi.
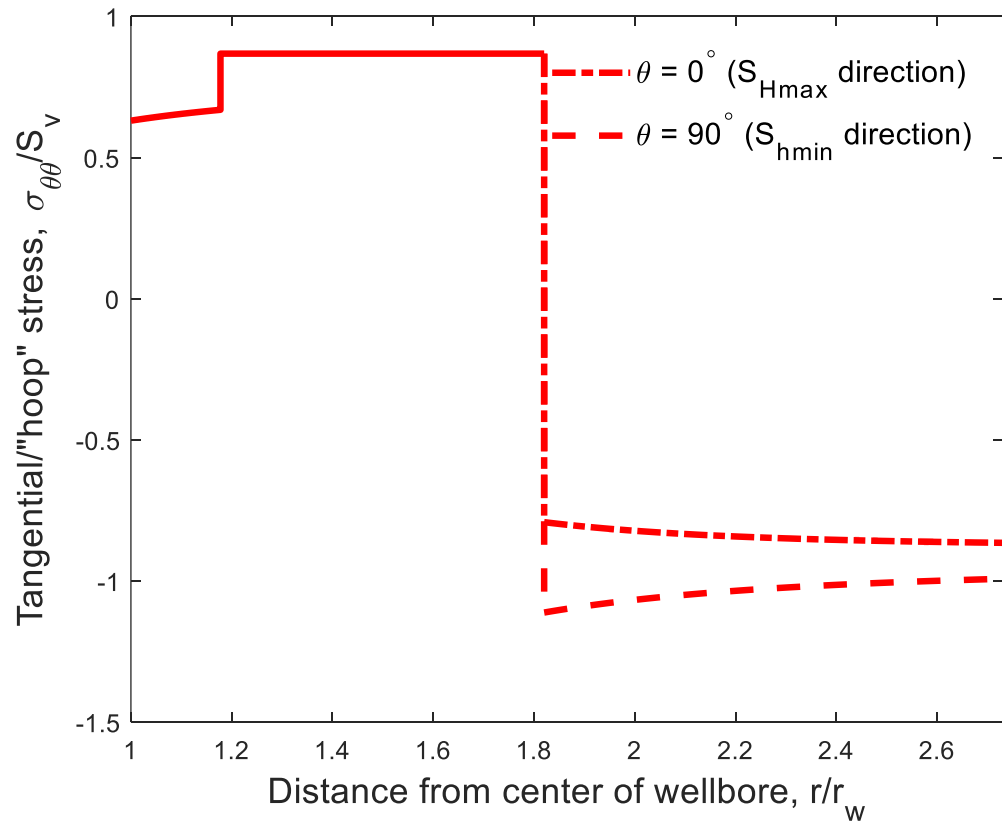
Figure 8.7. The tangential stress, $\sigma_{\theta\theta}$, distribution of the casing-cement sheath-rock formation system at slightly overbalanced conditions, with $p_w = 12,790$ psi.
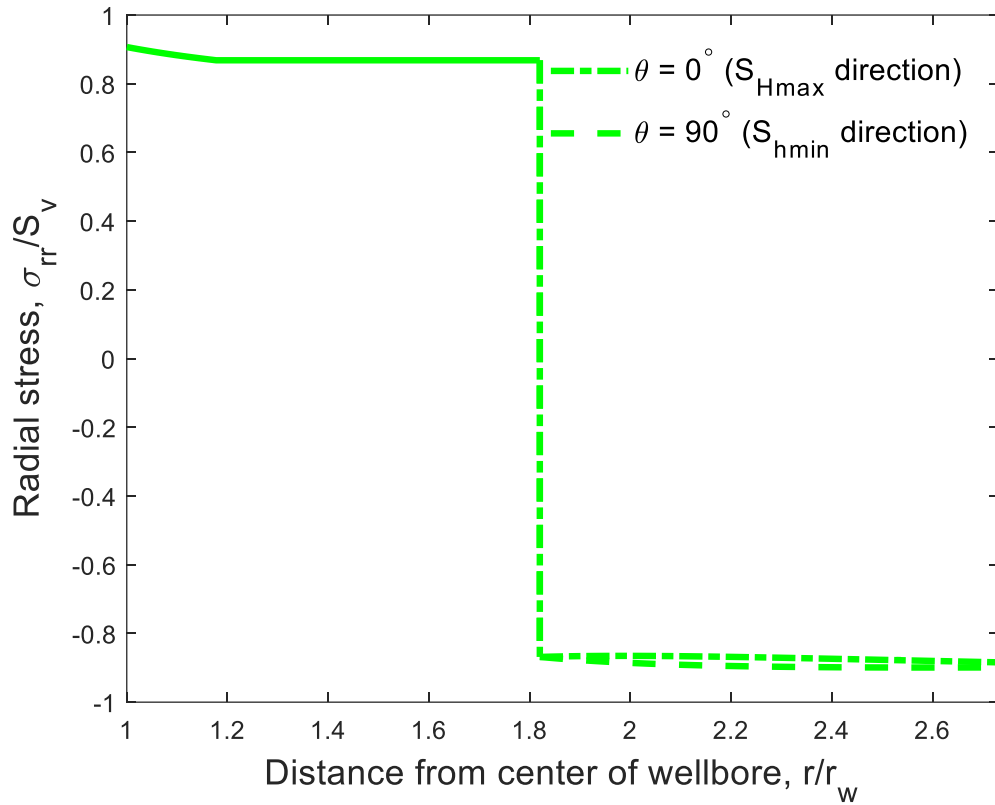
Figure 8.8. The radial stress, σ_{rr}, distribution of the casing-cement sheath-rock formation system at slightly overbalanced conditions, with $p_w = 12,790$ psi.

The Mohr Circle diagram for the cement sheath on Figure 8.9 is showing good stability to shear compressive failure with the circumference of the Mohr Circle far from the yellow Mohr-Coulomb failure envelope.
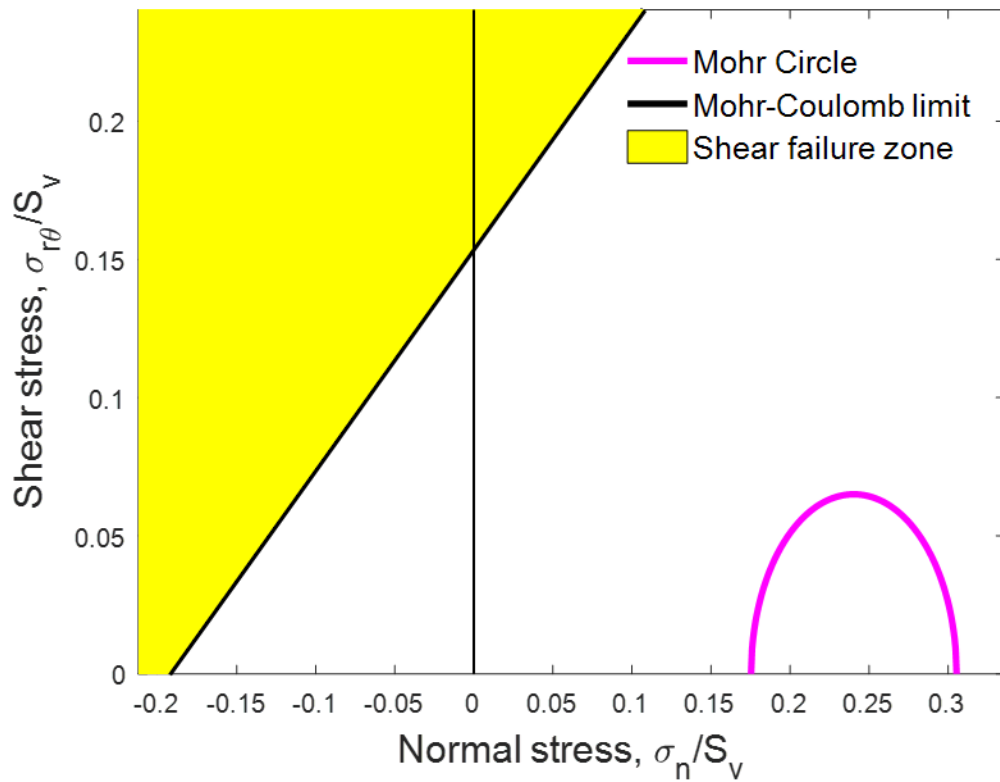
Figure 8.9.   Mohr Circle diagram used to evaluate the stability of the cement sheath to shear cracking via the Mohr-Coulomb failure criterion.

8.4   WELLBORE INTEGRITY DURING LOSS OF WELL CONTROL

A mismanaged loss of control situation during drilling can easily lead to a blowout. Following the blowout, there is a period of extremely low p_w, when reservoir fluids are gushing out of the wellbore usually at extremely high flowrates (the discharge period), which is followed by (sometimes more than one) capping attempts, where p_w builds up. Loss of well control are the events which induce the most extreme fluctuations in the stress loads acting on the casing-cement sheath-rock formation system, during the life of a well.

8.4.1 Post-Blowout Discharge Period

For the parameters on Table 8.1 as well as the wellbore specifications measured in the Section 8.3, Willson (2012) estimated the post-blowout discharge flowrate, q, to reach 155,040 STB/day at 26 minutes after the blowout, with the bottomhole flowing pressure, p_{wf}, equal to 7,072 psi. As mentioned by Luo et al. (2020), the updated stress state of the casing-cement sheath-rock formation system is a superposed value on the initial stress state of the entire system. The procedure for determining the stress state of the casing-cement sheath-rock formation system can be divided into to two steps, (i) calculate the system's initial stress state, and (ii) add or subtract the p_w difference to the system.

If p_w is decreased from 12,047 psi (balanced conditions) to 7,072 psi during discharge, it means that the 4,975 psi pressure difference are applied on the inner wall of the casing. This puts the casing walls under collapse and compressive stress loads. Figure 8.10a indicates that the stress loads experienced by the casing during discharge are expected to induce casing failure, as the point on the von Mises diagram is outside the ellipse. This is dangerous, because locations of casing failure, because they are located shallower than the casing shoe, can provide a location of possible fracture initiation during the subsequent capping procedures.

Nevertheless, on the account that the cement sheath has already solidified, the stress distributions within the cement sheath and rock formation (Figures 8.10b through 8.10d) remain the same as Figures 8.6 through 8.8. Only the stress distribution inside the casing wall changes, responding to the underbalanced conditions ($p_p \ll p_w$). The Mohr Circle diagram on Figure 8.9 remains unaltered following the drop in p_w from slightly overbalanced conditions at $p_w = 12,790$ psi to significantly underbalanced conditions at $p_w = 7,072$ psi.
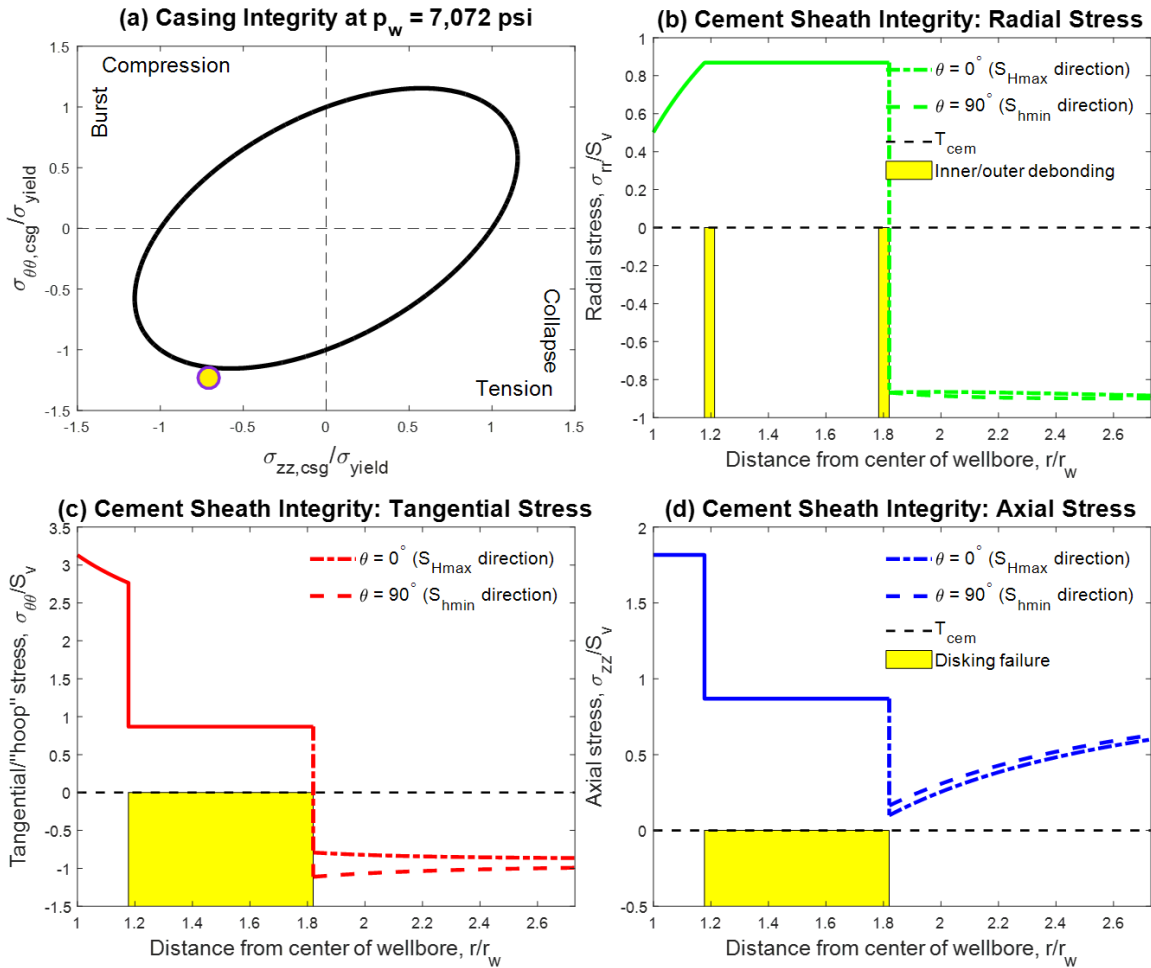
Figure 8.10. Evaluation of the casing-cement sheath-rock formation system during post-blowout discharge at $p_w = 7{,}072$ psi, which is the flowing bottomhole pressure corresponding to a discharge flowrate of 155,040 STB/day (from Willson, 2012).

During rapid discharge, the casing is heated up by the fluid flow and heat from the reservoir formation, leading to casing expansion, which induces thermal stress. The temperature increase during post-blowout discharge increases the likelihood of tensile and shear cement sheath failure (Hu et al., 2019). The incremental stress induced by

temperature variation in the cement sheath is smaller than the stress caused by p_w differences with this disparity intensified during p_w build-up during post-blowout capping.

8.4.2   Post-Blowout Capping Procedures

Michael and Gupta (2020c; 2020d) investigated potential fracture initiation during the capping procedures following an offshore blowout. During capping, a capping stack is installed on top of the severed – damaged or fully destroyed – blowout preventer (BOP) and then is shut-in following a pre-determined schedule (Michael and Gupta, 2020c; 2020d). There are two method of capping stack shut-in. The fastest method is the "abrupt" shut-in (Figure 8.11a), where the discharge flow from the well is suddenly stopped. The second method is the "incremental" shut-in (Figure 8.11a), which is gentler compared to abrupt shut-in procedures, where the well discharge flow is gradually stopped over a predetermined time period/schedule involving a specific number of steps.

The capping stack shut-in induces p_w build-up (Figure 8.11b), during which p_w can exceed the breakdown pressure, p_b, either (i) directly below the casing shoe, or (ii) at any point within the casing string where casing failure has previously taken place. This will lead to tensile fracture initiation(s) from those locations. Vertical or lateral propagation of those fractures can lead to them cutting across overlying layers and even reach the surface or seafloor, providing a low resistance path for hydrocarbons from the reservoir to flow to the ground or seawater causing an ecologic disaster.
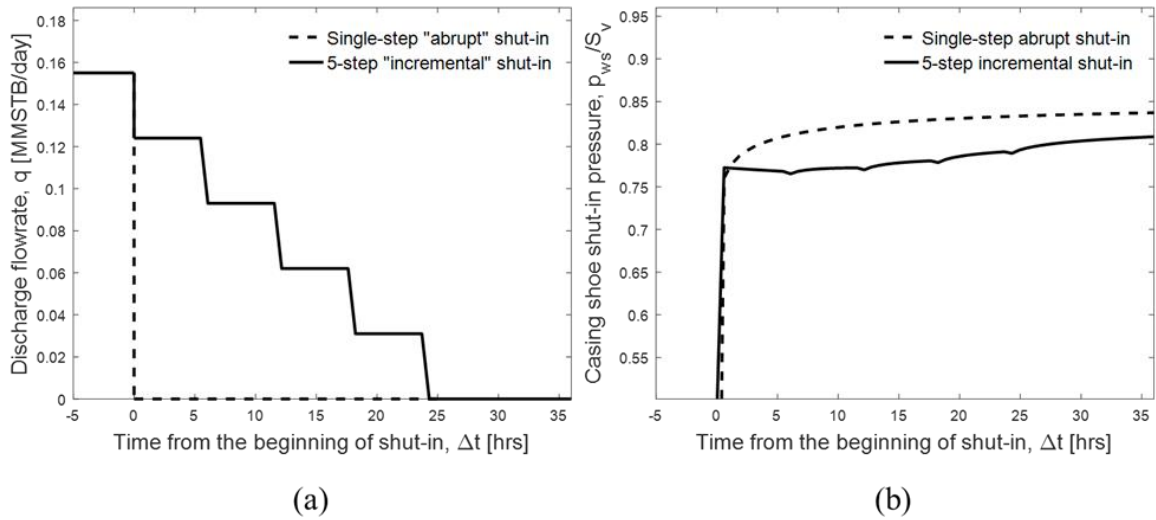
Figure 8.11. Comparison of the two methods of capping stack shut-in; single-step/"abrupt" and multi-step/"incremental," *vis-à-vis* (a) discharge flowrate and (b) casing shoe pressure versus time (from Michael and Gupta, 2020c).

Hu et al. (2019) evaluated cement sheath integrity during hydraulic fracture stimulation, identifying this as the most critical stage in lifetime of a well *vis-à-vis* the integrity to cement sheath failure. The pressure inside the wellbore changes by $\Delta p_w = (\rho_{frac} - \rho_w)gD + p_{wh}$, where ρ_{frac} is the fracturing fluid density and p_{wh} is the fracturing pressure applied on the wellhead during the stimulation treatment. Due to the Δp_w, additional radial compression along with additional tangential and axial tension are generated in the casing and the rock formation. Pressure build-up during post-blowout capping imposes *de facto* the same effects on the casing-cement sheath-rock formation system as a hydraulic fracture stimulation treatment.

The pressure build-up was estimated for an abrupt shut-in by Michael and Gupta (2020c) to reach maximum shut-in wellbore pressure, p_{ws}, reaches 11,823 psi, 24 hours after an abrupt shut-in was implemented (Figure 8.11b). The calculated p_{ws} value was used

to evaluate casing (Figure 8.12a) and cement sheath integrity (Figures 8.12b through 8.12d) during post-blowout capping procedures at $p_{ws} = 11,823$ psi.
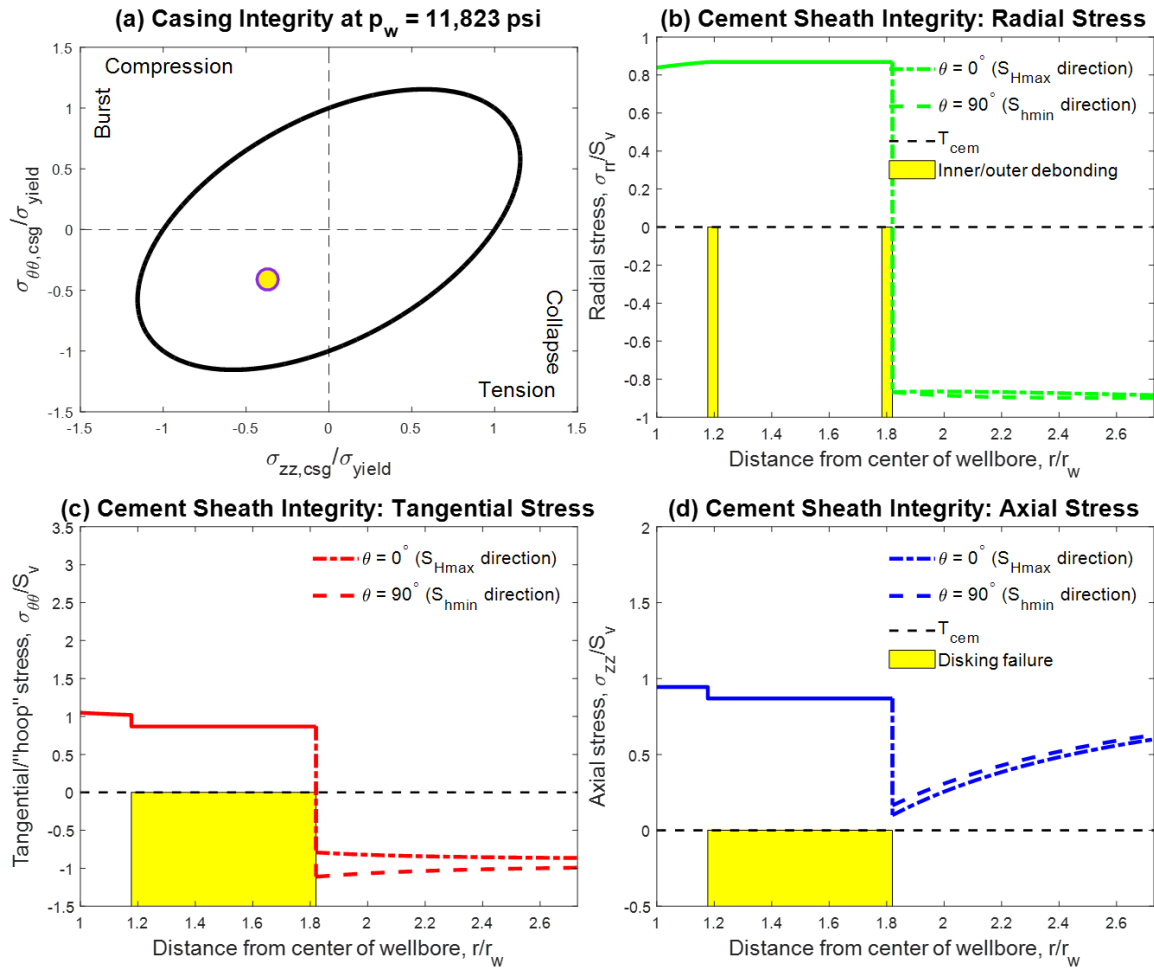
Figure 8.12. Evaluation of the casing-cement sheath-rock formation system during post-blowout capping at $p_w = 11,823$ psi, which is the pressure at the casing shoe depth at 24 hours (from Michael and Gupta, 2020c) following a single-step/"abrupt" capping stack shut-in.

8.5 DISCUSSION

8.5.1 The Impact of Reservoir Depletion

Depletion of reservoir pressure during the post-blowout discharge stage impacts both the *in-situ* stresses and hence the stability of the casing-cement sheath-rock formation system. For short discharge periods and small discharge flowrates, the change in the reservoir average p_p after the ending of the post-blowout discharge period is assumed to be negligible, and thus the *in-situ* stress state remains virtually constant. This assumption however, is questionable for lengthy discharge period and high discharge flowrate scenarios, such as that of the Macondo blowout that lasted 83 days (Hickman et al., 2012).

The longer the discharge period (at a given flowrate) is, the larger the total volume of hydrocarbons removed from the reservoir will be, leading to a larger decrease in p_p. A decrease in p_p from 0.68 psi/ft, which is equivalent to $p_p/S_v = 0.82$ to 0.43 psi/ft, which is equivalent to $p_p/S_v = 0.52$ decreases the two horizontal *in-situ* stresses will also decrease during depletion approximately by $\Delta S_{Hmax} \approx \Delta S_{hmin} \approx \alpha_B p_p$. Since the deepwater GoM location considered is under normal faulting stress regime (Table 8.1) and S_v remains constant, the decrease in S_{hmin} enlarges the Mohr Circle (Figure 8.13) making its circumference to get closer to the Mohr-Coulomb failure limit. Further decrease in p_p to 0.18 psi/ft, which corresponds to $p_p/S_v = 0.22$, further enlarges the Mohr Circle. Reservoir depletion appears to hinder the cement sheath's stability to shear compressive failure.
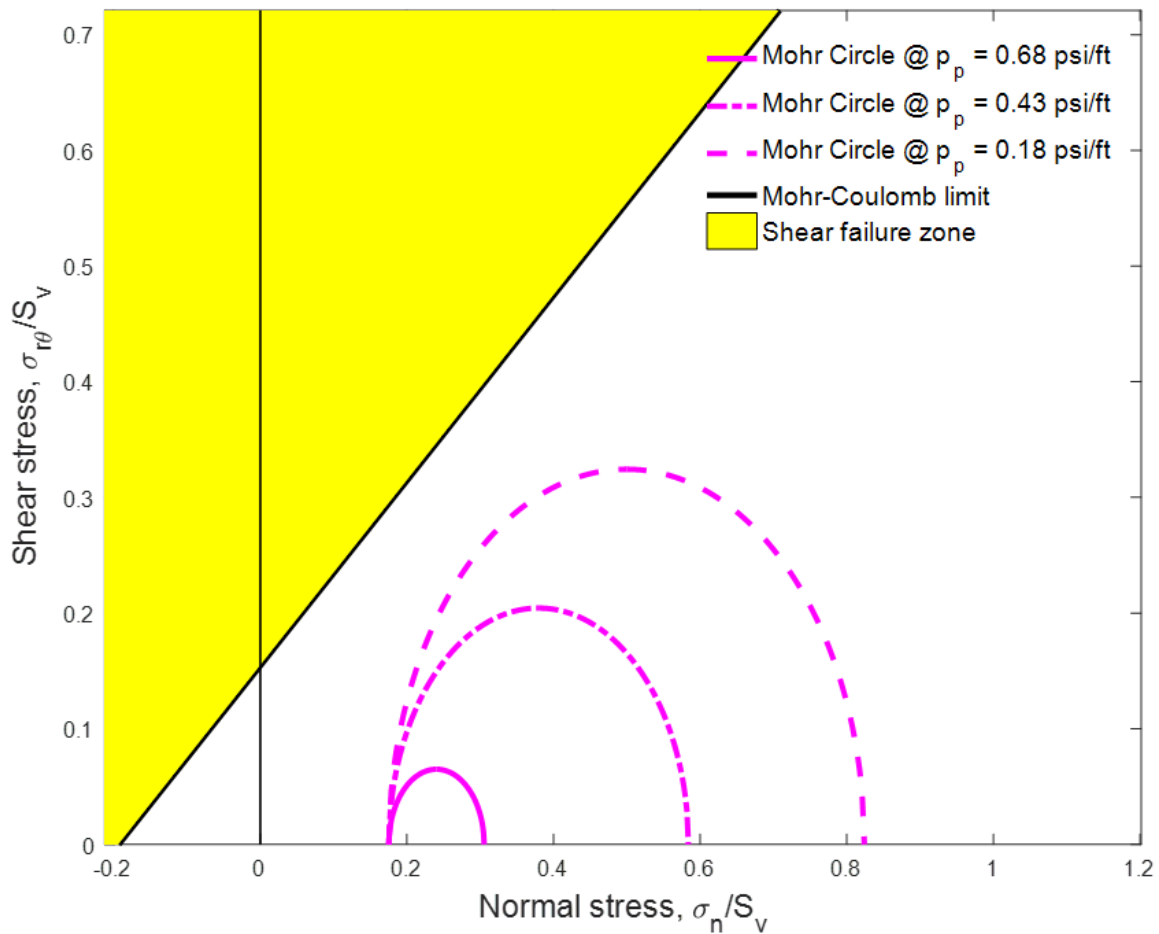
Figure 8.13. The impact of reservoir depletion on the cement sheath's stability to shear failure. As p_p decreases, the radius of the Mohr-Circle increases bringing its circumference closer to the limit of the yellow shear failure zone according to the Mohr-Coulomb failure criterion.

Reservoir p_p can be reliably estimated if the areal extent of the reservoir is known. In lieu of knowledge on the reservoir's outer boundaries, something common in wildcat wells, robust estimations and projections of the average p_p are difficult. All geomechanical and reservoir *in-situ* parameters need to be considered collectively in order to accurately determine the net impact of p_p reduction during a prolonged discharge period before capping the well, following a blowout.

8.5.2 Presence of a Microannulus on the Cement Sheath Interfaces

Bois et al. (2011) investigated the creation of a micoroannulus on the casing-cement sheath and cement sheath-rock formation interfaces. These microannuli are induced by chemical shrinkage and expansion (cement volume variations) during the cement hydration process or casing contraction or casing contraction due to mud weight reduction or temperature decrease. A microannulus, which can be seen as an extreme form of inner and outer debonding (Figure 8.5) can compromise the aggregate stress distribution of the casing-cement sheath-rock formation system, by establishing discontinuities in the stress variation at the casing-cement sheath and cement sheath-rock formation interfaces.

To prevent the formation of a microannulus, cementing techniques that strengthen the contact force of cement sheath with casing and rock formation can be taken such as the use of the expansive cement slurry system, which applies annular pressure and reduces fluid density during cement setting (Hu et al., 2019). Well integrity is strongly controlled by this contact stress. Following post-blowout discharge and capping, if the contact stress decreases, a microannulus might appear. Nevertheless, with increasing depth, the compressive stress increases along with the ability of cement sheath to resist the microannulus and tensile failure.

8.6 CONCLUSIONS

The thrust of this study was to develop expressions for the stress distribution in a casing-cement sheath-rock formation system and investigate the effects of extreme loss of well control situations on the system. The influence of the cement solidification process was incorporated using conclusions of published laboratory work from the literature. Based on the preceding analysis, the following conclusions are apparent:

- In porous-permeable formations, with good permeability, the initial stress in the cement sheath can be assumed to be equal to p_p.

- Cement volume shrinkage adversely impacts the casing-cement sheath-rock formation system's resistance to debonding, tensile, and shear failures. Contrary, small cement volume expansions enhance cement sheath's integrity. Hence, cement slurries with no shrinkage or minor expansion are recommended.

- During a loss of well control hypothetical GoM application scenario, tensile failures, such as inner/outer debonding, radial cracking, and disking are more likely to take place than shear cracking.

- Reservoir depletion during post-blowout discharge, although effective in preventing tensile fracture initiation, following the capping stack shut-in, enhances the likelihood of shear failure.

- Presence of a microannulus either at the casing-cement sheath, or the cement sheath-rock formation interfaces can compromise the aggregate stress distribution of the casing-cement sheath-rock formation system destroying the continuity in the stress variations.

Chapter 9. Conclusion

This dissertation explored fluid-driven fracture initiation from oil and gas wells, considering lifetime stresses. Topics addressed were related to fracture initiation during drilling, completions (stimulation), and loss of well control following a blowout. The prime dependent variables were the orientation of fracture initiation and fracture initiation pressures. Independent variables were many with the *in-situ* stress loading, as well as mechanical and fluid properties of the reservoir and the well.

Chapters 3 through 8 contain detailed conclusions with the chapter introductions summarizing the findings of each chapter. The findings and conclusions help develop better understanding on avariety of related topics and deliver practically useful recommendations.

9.1   DRILLING-INDUCED FRACTURES FOR DIAGNOSTIC PURPOSES

Fully-analytical modeling of drilling-induced tensile fracture (DITF) initiation was performed incorporating the impact of fluid infiltration from the pressurized wellbore into the surrounding porous-permeable rock formation. Although the impact of the effects of fluid infiltration from the wellbore are minimal during balanced drilling conditions, as shown on Chapter 2, neglecting these effects in overbalanced or underbalanced drilling conditions, can impact DITF initiation and orientation.

In Chapter 3, DITF orientation is shown to be a useful diagnostic tool for constraining the local *in-situ* stress tensor, in particular the magnitude of the maximum horizontal principal stress, S_{Hmax}, which is commonly the most difficult aspect of the *in-situ* stress tensor to constrain. Longitudinal DITFs can be used to constrain the lower-bound of S_{Hmax} magnitude if S_{hmin} magnitude is known (presumably from leak-off testing). Transverse DITFs are a rarity compared to longitudinal DITFs, thus are much more

effective in constraining S_{Hmax}. A graphical method was presented in Chapter 3, where the range of *in-situ* stress states where transverse DITFs are promoted is clearly indicated as the region between three lines. These lines are, (i) that of the stress states where the axial stress on the wellbore radius equal to the tensile strength of the rock, $\sigma_{yy}\big|_{r=r_w} < -T$, (ii) that of the stress states where the axial and tangential stress on the wellbore radius are equal, $\sigma_{yy}\big|_{r=r_w} < \sigma_{\theta\theta}\big|_{r=r_w}$, and (iii) the line of the magnitude of S_{hmin}. Higher values of the Biot's poroelastic coefficient, α_B, and Poisson's ratio, ν, increase the range of stress states promoting transverse DITF initiation. Higher wellbore pressures, p_w, in overbalanced drilling environments decreases the range of stress states in which transverse DITFs are promoted.

9.2 COMPLETION-INDUCED HYDRAULIC FRACTURES FOR STIMULATION PURPOSES

In Chapter 3, an orientation criterion is developed for completion-induced hydraulic fractures (CIHFs) from perforated wells, using closed-form analytical expressions from the literature for longitudinal and transverse fracturing stresses. This was achieved through the evaluation of the tangential stress in two extreme locations on the perforation base. Transverse CIHF initiation, similar to transverse DITF initiation is a rarity over longitudinal CIHF initiation and occurs when the breakdown pressure, p_b, is within a specific range, "window". Nevertheless, transverse CIHF initiation is relatively more frequent than transverse DITF initiation for the *in-situ* stress states that are stable in the Earth's subsurface, which implies that effective perforating aids transverse fracture initiation.

In Chapter 4, the orientation criterion presented on Chapter 3 is numerically-assessed using a true-3D model and found to overestimate transverse CIHF initiation. Case

studies were performed on seven shale plays; the Barnett, Bakken, Fayetteville, Haynesville, Niobrara, Marcellus, and the Vaca Muerta Shales of the United Sates and Argentina. A second constraint to transverse CIHF initiation is identified, besides the p_b window and that is the "critical tensile strength," T_{crit}; if $T > T_{crit}$, transverse CIHF is impossible irrespective of the magnitude of p_b. The perforation direction for a stress state at which the p_b window and critical tensile strength are maximized is called the "preferred perforation alignment" (PPA). The frequent occurrence of longitudinal CIHF initiation in horizontal wells drilled parallel to S_{hmin}, leads to (i) premature fracture growth termination, or (ii) reorientation as the fracture propagates away from near-wellbore vicinity. This generates near-wellbore fluid tortuosity which leads to short-term completion-related and long-term production-related problems, such as early screenouts and poor post-stimulation well performance.

In Chapter 5, correction factor sets are derived using the true-3D numerical model. The resultant semi-analytical approach can be used at a known p_b to evaluate the orientation of CIHF initiation and the fracture initiation pressure, p_i. While the analytical portion of the model derivation is basin-agnostic, the correction factors vary for every stress state. In Chapter 6, this semi-analytical modeling approach is used to derive correction factor sets for each of the seven shale plays (Barnett, Bakken, Fayetteville, Haynesville, Niobrara, Marcellus, and Vaca Muerta). The results were used to comparatively assess oriented perforating in those seven shale plays. As demonstrated, oriented perforating strategies can be employed to promote transverse CIHF initiation, or when only longitudinal CIHF initiation is possible, minimize p_i. Fluid leakages around the wellbore can compromise oriented perforating strategies.

9.3 LOSS OF WELL CONTROL-INDUCED FRACTURES FOR BROACHING PREVENTION

During loss of well control situations after a mismanaged kick, a blowout can take place. The post-blowout period is divided into two parts. The first part is the post-blowout discharge period, p_w decreases dramatically putting the casing string in place to extremely high stress loads making it vulnerable to collapse or compressive failure. The second part is the post-blowout capping period, which follows the installation of a capping stack on top of the damaged blowout preventer (BOP). During the capping stack shut-in, p_w builds up and this can lead to tensile fracture(s) initiating either from (i) directly below the casing shoe, or (ii) locations within the casing string where casing failure has taken place. Propagation of these initiated fractures to the seafloor provide a migration pathway for reservoir fluids to broach into the seawater.

In Chapter 7, capping stack shut-in strategy was coupled to fracture initiation in a fully-analytical manner. For every capping stack shut-in configuration, a critical discharge flowrate, q_{crit}, is calculated which is used to indicate fracture initiation or not during the shut-in, when compared with the actual post-blowout discharge flowrate for a specifc post-blowout-discharge period (from the blowout until the beginning of the capping stack shut-in). This calculation can complement the worst case discharge (WCD) estimations, which are mandated by the U.S. Bureau of Ocean Energy Management, Regulation, and Enforcement (BOEMRE) *a-priori* to drilling an offshore well, following BP's Macondo blowout in 2010. For the case of a multi-step/"incremental" capping stack shut-in (as opposed to a single-step/"abrupt"), this calculation can be used to determine the optimal number of shut-in steps and the duration per step at which any fracture initiation is effectively prevented. The calculation procedure is presented for a hypothetical case study with numbers typical to deepwater GoM.

The calculation of q_{crit} assumes perfect integrity of the interfaces between (i) the steel casing and the cement sheath, and (ii) the cement sheath and the surrounding rock formation. In Chapter 8, the implications from the results of a laboratory test from the literature are used to derive a fully-analytical expression for the initial stress state of the casing-cement sheath-rock formation system.

9.4   FUTURE WORK

There are many opportunities to extend the work presented in this dissertation. These opportunities are divided into, (1) other sources of fluid-driven fracture initiation, (2) time-dependent multiple fracture initiation, and (3) propagation and interaction of already-initiated fractures.

9.4.1   Other Sources of Fluid-Driven Fracture Initiation

Besides drilling, completion (stimulation) and loss of well control, there can be other scenarios during the lifetime of a well at which fluid-driven fractures may initiate. Arguably, the most important other scenario is during plug-and-abandonment (P&A) of a wellbore. This is when a previously active well is shut-in via the placement of a permanent barrier, such as a cement column ("plug") in the borehole, which prevents fluid flow from the reservoir to the surface and vice versa.

Long-term P&A in deepwater wells is subject to changes in the reservoir over time. Governmental regulation has been imposed on operators in an effort to prevent abandoned wells from leaking into the seawater contaminating it. Investigation of modeling aspects of fluid-driven interface debonding along the cross section of a system following P&A is a

field under current investigation. Reliable modeling of the P&A barrier material's behavior over reservoir depletion and repressurization cycles is paramount when trying to assess long-term post-abandonment wellbore integrity. After a well is plugged, integrity loss via fluid-driven interfacial debonding has been identified as the primary root of wellbore leakages.

Hydrocarbon production is modeled as a fatigue mechanism, while fluid leakage is driven by long-term reservoir repressurization at the casing shoe, following abandonment. Complex numerical simulations can be employed to quantify debonded fracture geometries in the near-wellbore region and in the interface between the plug and the steel casing. Laboratory experiments can be designed to assess proposed theoretical modeling approaches and applicable for wellbore leakage detection, and long-term performance assessment of industry acceptable plugging materials.

9.4.2   Time-Dependent Multiple Fracture Initiation

Multiple fracture (multi-frac) initiation is in many ways more complicated than single fracture initiation. A fracture treatment within a stage involves pumping fluid simultaneously to multiple perforation clusters from the same fluid source. Simultaneous multi-frac initiation is something that virtually every theoretical modeler assumes for a single-stage fracture treatment. Nevertheless, simultaneous multi-frac initiation within a stage is an extreme rarity if at all a possibility. This renders the results of simultaneous multi-frac initiation theoretical modeling to be highly unrealistic as fracture initiation at different time-steps renders that each fracture tip encounters a different stress state. Additionally, inactive perforation clusters, as well as dominant fracture creation (also known as "runaway" fractures, when one fracture receives the vast majority of the fluid

and thus its geometry dominates that of all other fractures) are aspects that need to be addressed before reliable multi-frac modeling becomes possible. Both inactive perforation clusters and dominant fractures were shown to exist, not following a certain pattern, through scaled-laboratory testing and field-scale microseismic monitoring.

9.4.3   Fluid-Driven Fracture Propagation and Interaction

A typical fracture treatment of a horizontal well is comprised a number of stages. Every stage consists of a number of perforation clusters; usually from three to six each with multiple of perforations per cluster. Out of all perforations in each cluster "active" perforations are the ones generating fractures.

The creation of a fracture generates a perturbation in the surrounding stress regime, affecting the propagation of other fractures. This interference phenomenon is known as the "stress shadow" effect. Quantitatively, in a transversely fractured horizontal well, stress shadowing is manifested as an increase in the in-situ stress parallel to the wellbore (in the majority of cases, S_{hmin}). During simultaneous multiple fracture initiation, the combined stress shadow effects of the propagating fractures makes them grow dissimilarly as seen on for three, five and six perforation clusters.

Mitigation of stress shadowing can significantly enhance the impact of hydraulic fracturing treatments, increasing stimulated reservoir volume (SRV) leading to higher production of hydrocarbons and subsequently raise the net present value (NPV) generated from the development of unconventional resources.

Appendix A. Unit Conversions

Table A.1.   SI/metric – oilfield/English unit conversion factors.

Variable	Dimension	SI unit	Oilfield unit	Conversion factor
Length	$[L]$	m	ft	3.281 ft/m
Area	$[L^2]$	m^2	acres	$2.475{\times}10^{-4}$ acre/m^2
Pressure	$[ML^{-1}T^{-2}]$	Pa	psi	$1.450{\times}10^{-4}$ psi/Pa
Compressibility	$[LT^2M^{-1}]$	Pa^{-1}	psi^{-1} "sip"	6895 Pa/psi
Permeability	$[L^2]$	m^2	mD	$1.013{\times}10^{-15}$ mD/m^2
Viscosity	$[ML^{-1}T^{-1}]$	Pa·s	cp	1,000 cp/Pa·s
Flowrate (liquid)	$[L^3T^{-1}]$	m^3/s	STB/day	$5.434{\times}10^5$ STB·s/m^3·day
Flowrate (gas)	$[L^3T^{-1}]$	m^3/s	Mscf/day	3,049 Mscf·s/m^3·d

Appendix B. Fluid Infiltration from a Pressurized Wellbore

The near-wellbore stress field can be significantly altered by fluid penetration in a porous, permeable medium. The total component of the stress at particular position in the medium will therefore include a poroelastic component (Weijers, 1995). This modifies the stress-strain expressions to include an extra term for the pore pressure, such

$$\varepsilon_{rr} = \frac{1}{E}\left(\sigma_{rr} - v\sigma_{\theta\theta} + \alpha_B p_p [1+v][1-2v]\right) \tag{B.1}$$

$$\varepsilon_{\theta\theta} = \frac{1}{E}\left(\sigma_{\theta\theta} - v\sigma_{rr} + \alpha_B p_p [1+v][1-2v]\right) \tag{B.2}$$

$$\varepsilon_{r\theta} = \frac{2(1+v)}{E}\sigma_{r\theta} \tag{B.3}$$

where α_B is defined by Eq. 3.5, effectively as the fluid volume change induced by bulk volume changes in the drained condition and can range from 0 to 1.0. Using these stress-strain expressions (Eqs. B.1 through B.3) a biharmonic equation can be derived in cylindrical coordinates applied to the near-wellbore stress field,

$$\left(\frac{\partial^2}{\partial r^2} + \frac{1}{r^2}\frac{\partial^2}{\partial \theta^2} + \frac{1}{r}\frac{\partial}{\partial r}\right)(\sigma_{\theta\theta} + \sigma_{rr})$$
$$= \left(\frac{\partial^2}{\partial r^2} + \frac{1}{r^2}\frac{\partial^2}{\partial \theta^2} + \frac{1}{r}\frac{\partial}{\partial r}\right)\left(\frac{\partial^2\Phi}{\partial r^2} + \frac{1}{r^2}\frac{\partial^2\Phi}{\partial \theta^2} + \frac{1}{r}\frac{\partial\Phi}{\partial r}\right) \equiv \nabla^4\Phi \tag{B.4}$$

$$\nabla^4\Phi = A\nabla^2 p_p \tag{B.5}$$

where A is the poroelastic constant, $A = \left(\frac{1-2v}{1-v}\right)\alpha_B$. Hence, the poroelastic component for the tangential ("hoop" or circumferential) stress at radius r and r_e the drainage radius of the wellbore, becomes

$$\sigma_{\theta\theta}^{(5)}(r) = A\left(-p_p + r^{-2}\int_{r_w}^{r}\rho p_p d\rho + r_e^{-2}[1+r^{-2}]\int_{r_w}^{r_e}\rho p_p d\rho\right) \tag{B.6}$$

If the drainage radius approaches infinity ($r_e \to \infty$), the last integral can be approximated, such that Eq. A.6 can be reduced to

$$\sigma_{\theta\theta}^{(5)}(r) = A\left(-p_p + r^{-2}\int_{r_w}^{r}\rho p_p d\rho + [1+r^{-2}]\frac{p_p}{2}\right) \tag{B.7}$$

considering that for an infinite drainage radius the average value of pore pressure is equal to that in the virgin formation (Weijers, 1995). Finally, the poroelastic component of the tangential stress at r_w becomes

$$\sigma_{\theta\theta}^{(5)} = A(p_p - p_w) - p_w \tag{B.8}$$

Appendix C. A 2D Application of the Fracture Orientation Criteria

Analytical modeling starting from the plane-strain solutions from the stress field in the near-wellbore region is used to present closed form analytical expressions for the stresses controlling fracture initiation (Chapters 3 and 4). For non-perforated wells, fractures are assumed to initiate from the radius of the wellbore. AlTammar et al. (2018) performed experiments on thin square plate samples (2D proxy) observing longitudinal fracture initiation (Figures C.1 and C.2). During AlTammar et al.'s (2018) lab-scale experiments, the sample was viewed through a polycarbonate and an adhesive layer on top of the specimen (not shown on Figure C.1). No stress is applied on a direction other than the plane of the plat (*xy*-plane).
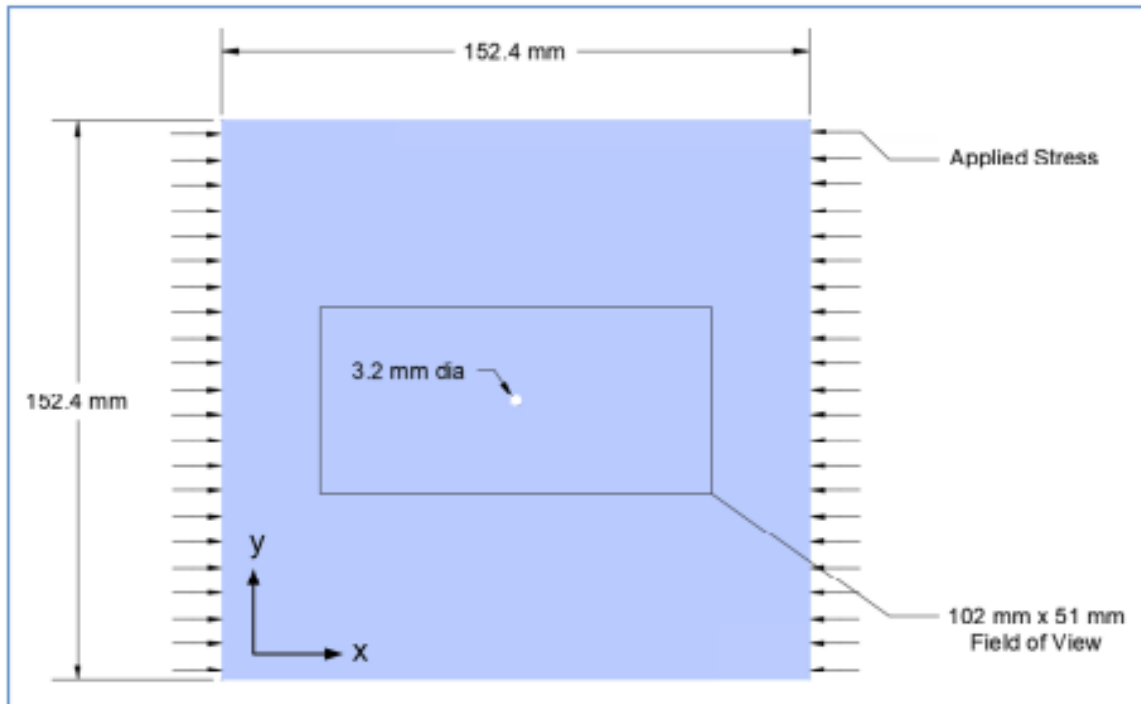
Figure C.1. The specimen configuration used in AlTammar et al.'s (2018) lab-scale experiments (reproduced with the author's permission).

293
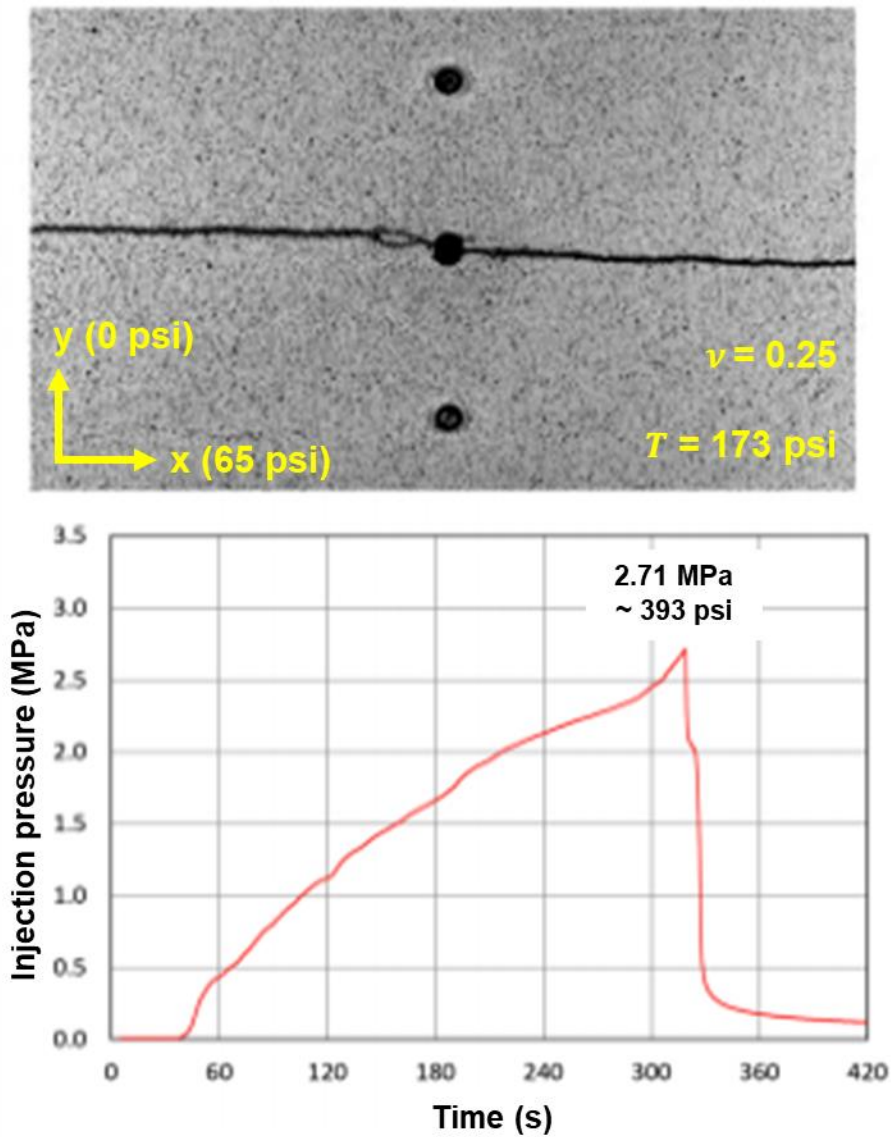
Figure C.2. Fracture trajectory and fluid injection history of one of AlTammar et al.'s (2018) experimental tests (reproduced with the author's permission). A longitudinal fracture is observed opening against the least compressive stress, which is in the *y*-direction and propagating along the *x*-direction.

Due to the absence of pore pressure ($p_p = 0$), any poroelastic effects are ignored and thus Eqs. 4.5 and 4.6 are used, which for AlTammar et al.'s (2018) configuration (which follows in cartesian coordinates) become

$$\sigma_{zz} = 2v\left(\pm S_{xx} \mp S_{yy}\right) \tag{C.1}$$

$$\sigma_{\theta\theta} = \left\{3S_{xx} - S_{yy} - p_w, 3S_{yy} - S_{xx} - p_w\right\} \tag{C.2}$$

Eqs. C.1 and C.2 allow the two criteria for fracture initiation (Eqs. 4.2 and 4.3) to be simplified to

$$2v\left(\pm S_{yy} \mp S_{xx}\right) + T < 0 \tag{C.3}$$

$$\left\{(1 - 2v)S_{yy} + (2v - 3)S_{xx} + p_w, (1 - 2v)S_{xx} + (2v - 3)S_{yy} + p_w\right\} < 0 \tag{C.4}$$

Applying AlTammar et al.'s (2018) conditions, $T = 173$ psi and $v = 0.25$. A 65 psi compressive stress is applied along the x-direction (i.e. $S_{xx} = 65$ psi), while no stress is applied along the y-direction (i.e. $S_{yy} = 0$ psi).

Table C.1 shows the quantitative results of the criterion's application. With the conditions used in AlTammar et al. (2018) none of the two conditions necessary for transverse initiation are satisfied (Eqs. C.3 and C.4). With $\sigma_{\theta\theta}|_{r=r_w} < -T$ in the x-direction (-458 psi) it is implied that longitudinal fracture initiation is promoted in that direction, which is what was observed in AlTammar et al.'s (2018) experiment (Figure C.2). The observed fracture initiation pressure of 393 psi is very close to the longitudinal

fracture initiation pressure prediction of 386 psi one can obtain analytically using Hubbert and Willis' (1957) expression for $\sigma_{\theta\theta}$, setting $\sigma_{\theta\theta}$ equal to $-T$ and solving for p_w.

Table C.1. Application of the fracture initiation criterion on AlTammar et al.'s (2018) experimental conditions.

S_{xx} (psi)	S_{yy} (psi)	p_w (psi)	$\sigma_{zz}\|_{r=r_w}$ (psi) in x and y-directions	Corresponding $\sigma_{\theta\theta}\|_{r=r_w}$ (psi)	Eq. C.3 condition	Eq. C.4 condition	Fracture initiation
65	0	393	32.5 and -32.5	-458 and -198	Not satisfied	Not satisfied	Longitudinal
325	0	1,148[I]	162.5 and -162.5	-1,473 and -173	Not satisfied	Not satisfied	Longitudinal
350	0	<1,225[II]	175 and -175	<-1,575 and <-175	Satisfied	Satisfied	Transverse
550	200	<1,975[III]	175 and -175	<-2,025 and <-175	Satisfied	Satisfied	Transverse

[I] Calculated using the expression of $p_w = \sigma_{\theta\theta}\|_{r=r_w}$ (after Hubbert and Willis, 1957) for longitudinal fracture initiation.
[II] The longitudinal fracture initiation pressure, calculated using Hubbert and Willis' (1957) expression is 1,223 psi.
[III] The longitudinal fracture initiation pressure, calculated using Hubbert and Willis' (1957) expression is 1,623 psi.

A 5-fold increase in S_{xx} to 325 psi (and stress anisotropy, since S_{yy} remains zero), still is not satisfying neither Eq. C.3 nor C.4. Yet, longitudinal fracture initiation is still promoted along the x-direction, as $\sigma_{\theta\theta}\|_{r=r_w} = -1,473$ psi $< -T$. It has to be noted that the p_w value given on the third column represents an estimate, calculated using Hubbert and Willis' (1957) expression for $\sigma_{\theta\theta}\|_{r=r_w} = -T$, which is applicable exclusively to longitudinal fracture initiation.

Further increasing S_{xx} and stress anisotropy to 350 psi, makes transverse fracture initiation to be promoted marginally along the y-direction if p_w (*de facto* fracture initiation pressure) is kept below 1,225 psi. The values of $\sigma_{\theta\theta}\|_{r=r_w}$ are calculated using a p_w that considers longitudinal fracture initiation, after Hubbert and Willis (1957). This makes it an unrealistic prediction when it comes to transverse fracture initiation, for which the Hubbert

and Willis (1957) expressions cannot calculate the p_w, as these expressions consider σ_{zz} to be completely independent of p_w (i.e. $\sigma_{zz} \neq f(p_w)$). Using a non-zero, compressive value for S_{yy}, can still promote transverse fracture initiation, but at S_{xx} values that are higher than the examples where S_{yy} was kept at zero. For instance, a combination with $S_{xx} = 550$ psi and $S_{yy} = 200$ psi will also promote transverse fracture initiation, marginally along the y-direction.

Appendix D. Approximation of the Tangential Stress on the Perforation Base

Following Hossain et al., (2000) the expressions for $\sigma_{\theta\theta}|_{r=r_w}$ and $\sigma_{yy}|_{r=r_w}$ from Eq. 4.2 and 4.3 can be inserted back into the original expression for $\sigma_{\theta\theta}|_{r=r_w}$ (Eq. 4.2) substituting the principal stresses S_v and S_{Hmax} respectively, for a horizontal wellbore aligned with σ_{yy}, which in this study is assumed to be parallel to S_{hmin}. This makes $\sigma_{\theta\theta_p}$, the tangential stress around an arbitrarily-oriented perforation at angle θ take the form

$$
\sigma_{\theta\theta_p} = \sigma_{yy}|_{r=r_w} + \sigma_{\theta\theta}|_{r=r_w} - 2\left(\sigma_{yy}|_{r=r_w} - \sigma_{\theta\theta}|_{r=r_w}\right)\cos 2\theta_p - p_{perf} \\
+ p_p
\tag{D.1}
$$

where θ_p is the angle measured from the azimuth of σ_{yy}. Substituting Eq. 4.2 and 4.3 at $r = r_w$ into Eq. D.1 yields

$$
\begin{aligned}
\sigma_{\theta\theta_p} = {} & (S_{Hmax} + S_{hmin} - 2v[S_v - S_{Hmax}]\cos 2\theta + S_v) \\
& + 2(S_{Hmax} + S_v - S_{hmin} + 2v[S_v - S_{Hmax}]\cos 2\theta)\cos 2\theta_p \\
& - 2(S_v - S_{Hmax})\left(\cos 2\theta + 2\cos 2\theta\cos 2\theta_p\right) \\
& - p_{perf}\left(2\cos 2\theta_p + 2\right) - p_p
\end{aligned}
\tag{D.2}
$$

For a perforation parallel to S_{Hmax}, $\theta = 90°$ and $p_{perf} = p_w$, Eq. D.2 simplifies to

$$
\begin{aligned}
\sigma_{\theta\theta_p}\Big|_{\theta=90°} = {} & (1 - 2\cos 2\theta_p)S_{hmin} + \left([4v - 2]\cos 2\theta_p - 2v - 1\right)S_{Hmax} \\
& + \left(2v + 3 + [6 - 4v]\cos 2\theta_p\right)S_v - p_w\left(2\cos 2\theta_p + 2\right) - p_p
\end{aligned}
\tag{D.3}
$$

Appendix E. Permissions for Published Work

There are four chapters (3, 4, 5 and 7) in this dissertation that have been already published. Their citation and acknowledgement have been included on the first page of the corresponding chapters. The publisher permissions are provided in this appendix.

Contents from Chapter 3 were published in a peer-reviewed article titled "Analytical Orientation Criteria for Drilling and Completion-Induced Fracture Initiation Considering Fluid Infiltration from the Wellbore" in the *Journal of Petroleum Science and Engineering* from Elsevier. Elsevier allows its authors to include the article in a dissertation if the publication is not commercial as in this case (https://www.elsevier.com/about/policies/copyright/permissions).

Contents from Chapter 4 were published in a peer-reviewed article titled "Orientation Prediction of Fracture Initiation from Perforated Horizontal Wells: Application in Shale Reservoirs" in the same *Journal of Petroleum Science and Engineering* from Elsevier, and copyright permissions apply as before as long as the publication is not commercial which is true for this case here (https://www.elsevier.com/about/policies/copyright/permissions).

Contents from Chapter 5 were published in a conference paper titled "A Semi-Analytical Modeling Approach for Hydraulic Fracture Initiation and Orientation from Perforated Wells," which was presented in the 2020 Unconventional Resources Technology Conference (URTeC). URTeC permits authors to reproduce the work.

Contents from Chapter 7 were published in a peer-reviewed article titled "Fracture Prevention Following Offshore Well Blowouts: Selecting the Appropriate Capping Stack Shut-In Strategy" in the *Society of Petroleum Engineers' (SPE) Drilling & Completions* journal.

The requesting person / organization to appear on the license	Andreas Michael

REUSE CONTENT DETAILS

Title, description or numeric reference of the portion(s)	Fracture Prevention Following Offshore Well Blowouts: Selecting the Appropriate Capping Stack Shut-In Strategy	Title of the article/chapter the portion is from	Fracture Prevention Following Offshore Well Blowouts: Selecting the Appropriate Capping Stack Shut-In Strategy
Editor of portion(s)	N/A	Author of portion(s)	SOCIETY OF PETROLEUM ENGINEERS (U.S.)
Volume of serial or monograph	N/A	Issue, if republishing an article from a serial	September 2020
Page or page range of portion	1-13	Publication date of portion	2020-09-30

PUBLISHER SPECIAL TERMS AND CONDITIONS

The person requesting republication permission is an author of SPE-199673-PA.

CCC Republication Terms and Conditions

1. Description of Service; Defined Terms. This Republication License enables the User to obtain licenses for republication of one or more copyrighted works as described in detail on the relevant Order Confirmation (the "Work(s)"). Copyright Clearance Center, Inc. ("CCC") grants licenses through the Service on behalf of the rightsholder identified on the Order Confirmation (the "Rightsholder"). "Republication", as used herein, generally means the inclusion of a Work, in whole or in part, in a new work or works, also as described on the Order Confirmation. "User", as used herein, means the person or entity making such republication.

2. The terms set forth in the relevant Order Confirmation, and any terms set by the Rightsholder with respect to a particular Work, govern the terms of use of Works in connection with the Service. By using the Service, the person transacting for a republication license on behalf of the User represents and warrants that he/she/it (a) has been duly authorized by the User to accept, and hereby does accept, all such terms and conditions on behalf of User, and (b) shall inform User of all such terms and conditions. In the event such person is a "freelancer" or other third party independent of User and CCC, such party shall be deemed jointly a "User" for purposes of these terms and conditions. In any event, User shall be deemed to have accepted and agreed to all such terms and conditions if User republishes the Work in any fashion.

3. Scope of License; Limitations and Obligations.

   3.1. All Works and all rights therein, including copyright rights, remain the sole and exclusive property of the Rightsholder. The license created by the exchange of an Order Confirmation (and/or any invoice) and payment by User of the full amount set forth on that document includes only those rights expressly set forth in the Order Confirmation and in these terms and conditions, and conveys no other rights in the Work(s) to User. All rights not expressly granted are hereby reserved.

   3.2.
   General Payment Terms: You may pay by credit card or through an account with us payable at the end of the month. If you and we agree that you may establish a standing account with CCC, then the following terms apply: Remit Payment to: Copyright Clearance Center, 29118 Network Place, Chicago, IL 60673-1291. Payments Due: Invoices are payable upon their delivery to you (or upon our notice to you that they are available to you for downloading). After 30 days, outstanding amounts will be subject to a service charge of 1-1/2% per month or, if less, the maximum rate allowed by applicable law. Unless otherwise specifically set forth in the Order Confirmation or in a separate written agreement signed by CCC, invoices are due

and payable on "net 30" terms. While User may exercise the rights licensed immediately upon issuance of the Order Confirmation, the license is automatically revoked and is null and void, as if it had never been issued, if complete payment for the license is not received on a timely basis either from User directly or through a payment agent, such as a credit card company.

3.3. Unless otherwise provided in the Order Confirmation, any grant of rights to User (i) is "one-time" (including the editions and product family specified in the license), (ii) is non-exclusive and non-transferable and (iii) is subject to any and all limitations and restrictions (such as, but not limited to, limitations on duration of use or circulation) included in the Order Confirmation or invoice and/or in these terms and conditions. Upon completion of the licensed use, User shall either secure a new permission for further use of the Work(s) or immediately cease any new use of the Work(s) and shall render inaccessible (such as by deleting or by removing or severing links or other locators) any further copies of the Work (except for copies printed on paper in accordance with this license and still in User's stock at the end of such period).

3.4. In the event that the material for which a republication license is sought includes third party materials (such as photographs, illustrations, graphs, inserts and similar materials) which are identified in such material as having been used by permission, User is responsible for identifying, and seeking separate licenses (under this Service or otherwise) for, any of such third party materials; without a separate license, such third party materials may not be used.

3.5. Use of proper copyright notice for a Work is required as a condition of any license granted under the Service. Unless otherwise provided in the Order Confirmation, a proper copyright notice will read substantially as follows: "Republished with permission of [Rightsholder's name], from [Work's title, author, volume, edition number and year of copyright]; permission conveyed through Copyright Clearance Center, Inc. " Such notice must be provided in a reasonably legible font size and must be placed either immediately adjacent to the Work as used (for example, as part of a by-line or footnote but not as a separate electronic link) or in the place where substantially all other credits or notices for the new work containing the republished Work are located. Failure to include the required notice results in loss to the Rightsholder and CCC, and the User shall be liable to pay liquidated damages for each such failure equal to twice the use fee specified in the Order Confirmation, in addition to the use fee itself and any other fees and charges specified.

3.6. User may only make alterations to the Work if and as expressly set forth in the Order Confirmation. No Work may be used in any way that is defamatory, violates the rights of third parties (including such third parties' rights of copyright, privacy, publicity, or other tangible or intangible property), or is otherwise illegal, sexually explicit or obscene. In addition, User may not conjoin a Work with any other material that may result in damage to the reputation of the Rightsholder. User agrees to inform CCC if it becomes aware of any infringement of any rights in a Work and to cooperate with any reasonable request of CCC or the Rightsholder in connection therewith.

4. Indemnity. User hereby indemnifies and agrees to defend the Rightsholder and CCC, and their respective employees and directors, against all claims, liability, damages, costs and expenses, including legal fees and expenses, arising out of any use of a Work beyond the scope of the rights granted herein, or any use of a Work which has been altered in any unauthorized way by User, including claims of defamation or infringement of rights of copyright, publicity, privacy or other tangible or intangible property.

5. Limitation of Liability. UNDER NO CIRCUMSTANCES WILL CCC OR THE RIGHTSHOLDER BE LIABLE FOR ANY DIRECT, INDIRECT, CONSEQUENTIAL OR INCIDENTAL DAMAGES (INCLUDING WITHOUT LIMITATION DAMAGES FOR LOSS OF BUSINESS PROFITS OR INFORMATION, OR FOR BUSINESS INTERRUPTION) ARISING OUT OF THE USE OR INABILITY TO USE A WORK, EVEN IF ONE OF THEM HAS BEEN ADVISED OF THE POSSIBILITY OF SUCH DAMAGES. In any event, the total liability of the Rightsholder and CCC (including their respective employees and directors) shall not exceed the total amount actually paid by User for this license. User assumes full liability for the actions and omissions of its principals, employees, agents, affiliates, successors and assigns.

6. Limited Warranties. THE WORK(S) AND RIGHT(S) ARE PROVIDED "AS IS". CCC HAS THE RIGHT TO GRANT TO USER

THE RIGHTS GRANTED IN THE ORDER CONFIRMATION DOCUMENT. CCC AND THE RIGHTSHOLDER DISCLAIM ALL OTHER WARRANTIES RELATING TO THE WORK(S) AND RIGHT(S), EITHER EXPRESS OR IMPLIED, INCLUDING WITHOUT LIMITATION IMPLIED WARRANTIES OF MERCHANTABILITY OR FITNESS FOR A PARTICULAR PURPOSE. ADDITIONAL RIGHTS MAY BE REQUIRED TO USE ILLUSTRATIONS, GRAPHS, PHOTOGRAPHS, ABSTRACTS, INSERTS OR OTHER PORTIONS OF THE WORK (AS OPPOSED TO THE ENTIRE WORK) IN A MANNER CONTEMPLATED BY USER; USER UNDERSTANDS AND AGREES THAT NEITHER CCC NOR THE RIGHTSHOLDER MAY HAVE SUCH ADDITIONAL RIGHTS TO GRANT.

7. Effect of Breach. Any failure by User to pay any amount when due, or any use by User of a Work beyond the scope of the license set forth in the Order Confirmation and/or these terms and conditions, shall be a material breach of the license created by the Order Confirmation and these terms and conditions. Any breach not cured within 30 days of written notice thereof shall result in immediate termination of such license without further notice. Any unauthorized (but licensable) use of a Work that is terminated immediately upon notice thereof may be liquidated by payment of the Rightsholder's ordinary license price therefor; any unauthorized (and unlicensable) use that is not terminated immediately for any reason (including, for example, because materials containing the Work cannot reasonably be recalled) will be subject to all remedies available at law or in equity, but in no event to a payment of less than three times the Rightsholder's ordinary license price for the most closely analogous licensable use plus Rightsholder's and/or CCC's costs and expenses incurred in collecting such payment.

8. Miscellaneous.

   8.1. User acknowledges that CCC may, from time to time, make changes or additions to the Service or to these terms and conditions, and CCC reserves the right to send notice to the User by electronic mail or otherwise for the purposes of notifying User of such changes or additions; provided that any such changes or additions shall not apply to permissions already secured and paid for.

   8.2. Use of User-related information collected through the Service is governed by CCC's privacy policy, available online here:https://marketplace.copyright.com/rs-ui-web/mp/privacy-policy

   8.3. The licensing transaction described in the Order Confirmation is personal to User. Therefore, User may not assign or transfer to any other person (whether a natural person or an organization of any kind) the license created by the Order Confirmation and these terms and conditions or any rights granted hereunder; provided, however, that User may assign such license in its entirety on written notice to CCC in the event of a transfer of all or substantially all of User's rights in the new material which includes the Work(s) licensed under this Service.

   8.4. No amendment or waiver of any terms is binding unless set forth in writing and signed by the parties. The Rightsholder and CCC hereby object to any terms contained in any writing prepared by the User or its principals, employees, agents or affiliates and purporting to govern or otherwise relate to the licensing transaction described in the Order Confirmation, which terms are in any way inconsistent with any terms set forth in the Order Confirmation and/or in these terms and conditions or CCC's standard operating procedures, whether such writing is prepared prior to, simultaneously with or subsequent to the Order Confirmation, and whether such writing appears on a copy of the Order Confirmation or in a separate instrument.

   8.5. The licensing transaction described in the Order Confirmation document shall be governed by and construed under the law of the State of New York, USA, without regard to the principles thereof of conflicts of law. Any case, controversy, suit, action, or proceeding arising out of, in connection with, or related to such licensing transaction shall be brought, at CCC's sole discretion, in any federal or state court located in the County of New York, State of New York, USA, or in any federal or state court whose geographical jurisdiction covers the location of the Rightsholder set forth in the Order Confirmation. The parties expressly submit to the personal jurisdiction and venue of each such federal or state court.If you have any comments or questions about the Service or Copyright Clearance Center, please contact us at 978-750-8400 or send an e-mail to support@copyright.com.

v 1.1

References

Aadnoy, B. S. (1990). Inversion Technique to Determine the *In-Situ* Stress Field from Fracturing Data. *Journal of Petroleum Science and Engineering*, vol. 4, no. 2, pp. 127–141., doi:10.1016/0920-4105(90)90021-t.

Agofack, N., Ghabezloo, S., Sulem, J., Garnier, A., and Urbanczyk, C. (2019). Experimental Investigation of the Early-Age Mechanical Behaviour of Oil-Well Cement Paste. *Cement and Concrete Research*, *117*, 91-102.

Alabbad, E. A. (2014). *Experimental Investigation of Geomechanical Aspects of Hydraulic Fracturing Unconventional Formations*, Master's Thesis at the University of Texas at Austin.

Altammar, M. J., Sharma, M. M., and Manchanda, R. (2018). The Effect of Pore Pressure on Hydraulic Fracture Growth: An Experimental Study. *Rock Mechanics and Rock Engineering*, vol. 51, no. 9, pp. 2709–2732., doi:10.1007/s00603-018-1500-7.

Amziane, S., and Andriamanantsilavo, N. (2004). Prediction of Cement Paste Pore Water Pressure Variations During Setting Period. *Advances in cement research*, *16*(1), 23-28.

Anderson, E. M. (1951). *The Dynamics of Faulting*. 2nd ed., Edinburgh: Oliver & Boyd.

Anderson, G. D. (1981). Effects of Friction on Hydraulic Fracture Growth Near Unbonded Interfaces in Rocks. February 1. Society of Petroleum Engineers. doi:10.2118/8347-PA

Balen, R. M., Mens, H.-Z., and Economides, M. J. (1988). Applications of the Net Present Value (NPV) in the Optimization of Hydraulic Fractures. Society of Petroleum Engineers. doi:10.2118/18541-MS

Barree, R. D., and Miskimins, J. L. (2015). Calculation and Implications of Breakdown Pressures in Directional Wellbore Stimulation. Society of Petroleum Engineers. February 3, doi:10.2118/173356-MS

Barree, R. D., and Winterfeld, P. H. (1998). Effects of Shear Planes and Interfacial Slippage on Fracture Growth and Treating Pressures. Society of Petroleum Engineers. doi:10.2118/48926-MS

Barth, J. O., et al. (2012). Frac Diagnostics Key in Marcellus Wells. *The American Oil & Gas Reporter*, May, www.aogr.com/magazine/frac-facts/frac-diagnostics-key-in-marcellus-wells.

Barton, C. A., and Zoback, M. D. (1994). Stress Perturbations Associated with Active Faults Penetrated by Boreholes: Possible Evidence for near-Complete Stress Drop and a New Technique for Stress Magnitude Measurement. *Journal of Geophysical Research: Solid Earth*, vol. 99, no. B5, pp. 9373–9390., doi:10.1029/93jb03359.

Barton, C. A., et al. (1988). In-Situ Stress Orientation and Magnitude at the Fenton Geothermal Site, New Mexico, Determined from Wellbore Breakouts. *Geophysical Research Letters*, vol. 15, no. 5, pp. 467–470., doi:10.1029/gl015i005p00467.

Behrmann, L. A., and Elbel, J. L. (1991). Effect of Perforations on Fracture Initiation. Society of Petroleum Engineers. May 1, doi:10.2118/20661-PA

Behrmann, L. A., and Nolte, K. G. (1998). Perforating Requirements for Fracture Stimulations. Society of Petroleum Engineers. doi:10.2118/39453-MS

Belyadi, Hoss, et al. (2016). *Hydraulic Fracturing in Unconventional Reservoirs: Theories, Operations, and Economic Analysis*. Elsevier Science & Technology.

Biot, M. A. (1941). General Theory of Three-Dimensional Consolidation. *Journal of Applied Physics*, vol. 12, no. 2, pp. 155–164., doi:10.1063/1.1712886.

Bois, A.-P., Garnier, A., Galdiolo, G., and Laudet, J.-B. (2012). Use of a Mechanistic Model to Forecast Cement-Sheath Integrity. Society of Petroleum Engineers. Jun 1, doi:10.2118/139668-PA

Bois, A.-P., Garnier, A., Rodot, F., Sain-Marc, J., and Aimard, N. (2011). How To Prevent Loss of Zonal Isolation Through a Comprehensive Analysis of Microannulus Formation. Society of Petroleum Engineers. Mar 1, doi:10.2118/124719-PA

Branagan, P, Peterson, R, Warpinski, N, and Wright, T. (1996). Results of Multi-Site Project Experimentation in the B-Sand Interval: Fracture Diagnostics and Hydraulic Fracture Intersection. Gas Research Institute Report GRI-96/0225, Chicago, Illinois.

Brudy, M, and Zoback M. D. (1999). Drilling-Induced Tensile Wall-Fractures: Implications for Determination of *In-Situ* Stress Orientation and Magnitude. *International Journal of Rock Mechanics and Mining Sciences*, vol. 36, no. 2, pp. 191–215., doi:10.1016/s0148-9062(98)00182-x.

Brunet, J., Pierrat, B., and Badel, P. (2020). Review of Current Advances in the Mechanical Description and Quantification of Aortic Dissection Mechanisms. *IEEE Reviews in Biomedical Engineering*.

Bunger, A. P., and Lecampion, B. (2017). Four Critical Issues for Successful Hydraulic Fracturing Applications. *Rock Mechanics and Engineering*, pp. 551–593., doi:10.1201/9781315364223-16.

Byerlee, J. D. (1978). Friction of Rocks. *Pure and Applied Geophysics PAGEOPH*, vol. 116, no. 4-5, pp. 615–626., doi:10.1007/bf00876528.

Chu, W., Shen, J, Yang, Y., Li, Y., and Gao, D. (2015). Calculation of micro-annulus size in casing-cement sheath-formation system under continuous internal casing pressure change. *Petroleum Exploration and Development*, *42*(3), 414-421.

Clark, J. B. (1949). A Hydraulic Process for Increasing the Productivity of Wells. Society of Petroleum Engineers. doi:10.2118/949001-G

Cleary, M. P. (1978). Primary Factors Governing Hydraulic Fractures in Heterogeneous Stratified Porous Formations. Paper 78-Pet-47 presented at the 1978 ASME ETC Conference. Houston, Texas, Nov 5-9.

Daneshy, A. A. (1973). A Study of Inclined Hydraulic Fractures. Society of Petroleum Engineers. April 1, doi:10.2118/4062-PA

Deimbacher, F. X., Economides, M. J., and Jensen, O. K. (1993). Generalized Performance of Hydraulic Fractures with Complex Geometry Intersecting Horizontal Wells. Society of Petroleum Engineers. doi:10.2118/25505-MS

Detournay, E., and Carbonell, R. (1997). Fracture-Mechanics Analysis of the Breakdown Process in Minifracture or Leak-off Test. Society of Petroleum Engineers. Aug. 1, doi:10.2118/28076-PA

Dontsov, E. V. (2016). An approximate solution for a penny-shaped hydraulic fracture that accounts for fracture toughness, fluid viscosity and leak-off. *Royal Society open science*, *3*(12), 160737.

Easton, R. O. (1972). *Black Tide: The Santa Barbara Oil Spill and its Consequences*. New York, New York: Delacorte Press.

Economides, M. J., and K. G. Nolte (2000). *Reservoir Stimulation*. Wiley.

Economides, M. J., Porcu, M. M., Yang, M., and Martin, A. N. (2010). Fracturing Horizontal Transverse, Horizontal Longitudinal and Vertical Wells: Criteria for Decision. Society of Petroleum Engineers. doi:10.2118/137328-MS

Economides, M., and Martin, A. N. (2010). How to Decide Between Horizontal Transverse, Horizontal Longitudinal, and Vertical Fractured Completions. Society of Petroleum Engineers. doi:10.2118/134424-MS

El Rabaa, W. (1989). Experimental Study of Hydraulic Fracture Geometry Initiated From Horizontal Wells. Society of Petroleum Engineers. doi:10.2118/19720-MS

Elnoamany, Y. A., Michael, A., and Gupta, I. (2020). Numerical Modeling of Fracture Propagation During Post-Blowout Capping in Offshore Wells. American Rock Mechanics Association. Sept 18

Fallahzadeh, S., et al. (2017). Near Wellbore Hydraulic Fracture Propagation from Perforations in Tight Rocks: The Roles of Fracturing Fluid Viscosity and Injection Rate. *Energies*, vol. 10, no. 12, pp. 359–381., doi:10.3390/en10030359.

Fjaer, E. (2008). *Petroleum Related Rock Mechanics*. Elsevier

Fourmaintraux, D. M., Bois, A.-P., Franco, C., Fraboulet, B., and Brossolllet, P. (2005). Efficient Wellbore Cement Sheath Design Using the SRC (System Response Curve) Method. Society of Petroleum Engineers. doi:10.2118/94176-MS

Ghasemi, M. F., et al. (2018). Coupled Thermo-Poro-Elastic Modeling of Near Wellbore Zone with Stress Dependent Porous Material Properties. *Journal of Natural Gas Science and Engineering*, vol. 52, 2018, pp. 559–574., doi:10.1016/j.jngse.2018.01.039.

Grandi, S., Rao, R. V., and Toksoz, M. N. (2002). *Geomechanical modeling of in-situ stresses around a borehole*. Massachusetts Institute of Technology. Earth Resources Laboratory.

Gray, K. E., Podnos, E., and Becker, E. (2009). Finite-Element Studies of Near-Wellbore Region During Cementing Operations: Part I. Society of Petroleum Engineers. March 1, doi:10.2118/106998-PA

Gu, H., Siebrits, E., and Sabourov, A. (2008). Hydraulic Fracture Modeling with Bedding Plane Interfacial Slip. Society of Petroleum Engineers. doi:10.2118/117445-MS

Haimson, B., and Fairhurst, C. (1967). Initiation and Extension of Hydraulic Fractures in Rocks. Society of Petroleum Engineers. September 1, doi:10.2118/1710-PA

Haimson, H. C., and Herrick, C. G. (1986). Borehole Breakouts - A New Tool for Estimating In Situ Stress? International Society for Rock Mechanics and Rock Engineering. Aug 31

Hallam, S. D., and Last, N. C. (1991). Geometry of Hydraulic Fractures from Modestly Deviated Wellbores. Society of Petroleum Engineers. June 1, doi:10.2118/20656-PA

Hammes, U., et al. (2011). Geologic Analysis of the Upper Jurassic Haynesville Shale in East Texas and West Louisiana. *AAPG Bulletin*, vol. 95, no. 10, pp. 1643–1666., doi:10.1306/02141110128.

Hickman, S. H., et al. (2012). Scientific Basis for Safely Shutting in the Macondo Well after the April 20, 2010 Deepwater Horizon Blowout. *Proceedings of the National Academy of Sciences*, vol. 109, no. 50, pp. 20268–20273., doi:10.1073/pnas.1115847109.

Himmelberg, N. C. (2014). *Numerical Simulations for Wellbore Stability and Integrity for Drilling and Completions*, Master's Thesis at the Missouri Science & Technology University.

Horner, D. R. (1951). Pressure Build-up in Wells. World Petroleum Congress.

Hossain, M. M., et al. (2000). Hydraulic Fracture Initiation and Propagation: Roles of Wellbore Trajectory, Perforation and Stress Regimes. *Journal of Petroleum Science and Engineering*, vol. 27, no. 3-4, pp. 129–149., doi:10.1016/s0920-4105(00)00056-5.

Hsieh, P. A. (2011). Application of MODFLOW for Oil Reservoir Simulation During the Deepwater Horizon Crisis. *Ground Water*, vol. 49, no. 3, pp. 319–323., doi:10.1111/j.1745-6584.2011.00813.x.

Hu, J. et al. (2019). Full-Life-Cycle Analysis of Cement Sheath Integrity. *Mathematical Problems in Engineering*, vol. 2019, pp. 1–11., doi:10.1155/2019/8279435.

Huang, L., Liu, J., Zhang, F., Fu, H., Zhu, H., and Damjanac, B. (2020). 3D Lattice Modeling of Hydraulic Fracture Initiation and Near-Wellbore Propagation for Different Perforation Models. *Journal of Petroleum Science and Engineering*, 107169.

Hubbert, M. K., and Willis, D. G. (1957). Mechanics of Hydraulic Fracturing. Society of Petroleum Engineers.

Itasca Consulting Group (2009). *FLAC3D: Fast Lagrangian Analysis of Continua in 3 Dimensions - Version 4.0*.

Irwin, G. R. (1957). Analysis of Stresses and Strains Near the End of a Crack Transversing a Plate. *ASME, Ser. E, J. Appl. Mech.*, *24*, 361-364.

Jaeger, J. C., et al. (2007). *Fundamentals of Rock Mechanics*. Blackwell Publishing.

Jeffrey, R. G., Brynes, R. P., Lynch, P. J., and Ling, D. J. (1992). An Analysis of Hydraulic Fracture and Mineback Data for a Treatment in the German Creek Coal Seam. Society of Petroleum Engineers. doi:10.2118/24362-MS

Jia, Q., and Schmitt, D. R. (2014). Effects of Formation Anisotropy on Borehole Stress Concentrations: Implications to Drilling Induced Tensile Fractures. American Rock Mechanics Association. August 18

Karpfinger, F., Prioul, R., Gaede, O., and Jocker, J. (2011). Revisiting Borehole Stresses In Anisotropic Elastic Media: Comparison of Analytical Versus Numerical Solutions. American Rock Mechanics Association.

Ketter, A. A., Daniels, J. L., Heinze, J. R., and Waters, G. (2006). A Field Study Optimizing Completion Strategies for Fracture Initiation in Barnett Shale Horizontal Wells. Society of Petroleum Engineers. doi:10.2118/103232-MS

King, G. E. (1989). Perforating the Horizontal Well. Society of Petroleum Engineers. July 1, doi:10.2118/19888-PA

Kirsch, G. (1898). Die theorie der elasticitaet und die beduerfnisse der festigkeitskehre. VDI-Z 42, 707.

Koskella, D., et al. (2015). Northside: Observation from an Underground Laboratory: An Integrated Approach to Unlocking Performance in the Niobrara. *SPE-GCS*, Noble Energy, Inc., Jan. 21, www.spegcs.org/events/2713/.

Kosset, T. (2014). Wellbore Integrity Analysis for Wellpath Optimization and Drilling Risks Reduction: The Vaca Muerta Formation in the Formation in Neuquén Basin, Master's Thesis Colorado School of Mines.

Kowan, J., and Ong, S. H. (2016). Geoscience Technology Workshop (GTW). AAPG, *Search and Discovery Article #80533*, May 16, www.searchanddiscovery.com/pdfz/documents/2016/80533kowan/ndx_kowan.pdf.html.

Kurdi, M. (2018). A New Computational Model to Predict Breakdown Pressures in Cased and Perforated Wells in Unconventional Reservoirs. Society of Petroleum Engineers. September 24, doi:10.2118/194038-STU

Lagrone, K. W., and Rasmussen, J. W. (1963). A New Development in Completion Methods – The Limited Entry Technique. Society of Petroleum Engineers. Jul 1, doi:10.2118/530-PA

Lamé G., and Clapeyron B. P. E. (1831). Mémoire sur l'équilibreintérieur des corps solides homogènes. *Journal für diereine und angewandte Mathematik* (Crelle's Journal)

    Vol. 1831, Issue 7: 381–413. [Online] Goettingen Stateand University Library, Available from: http://gdz.sub.uni-goettingen.de

Lecampion, B., et al. (2017). Experiments Versus Theory for the Initiation and Propagation of Radial Hydraulic Fractures in Low-Permeability Materials. *Journal of Geophysical Research: Solid Earth*, vol. 122, no. 2, pp. 1239–1263, doi:10.1002/2016jb013183.

Lee, H. P., J. E. Olson, J. Holder, J. F. W. Gale, and R. D. Myers (2015). The Interaction of Propagating Opening Mode Fractures with Preexisting Discontinuities in Shale, *J. Geophys. Res. Solid Earth*, 120, 169–181, doi:10.1002/2014JB011358.

Lee, M., Eckert, A., and Nygaard, R. (2011). Mesh Optimization for Finite Element Models of Wellbore Stress Analysis. American Rock Mechanics Association.

Li, B., Guo, B., Li, H., and Shi, Y. (2015). An analytical solution to simulate the effect of cement/formation stiffness on well integrity evaluation in carbon sequestration projects. *Journal of Natural Gas Science and Engineering*, *27*, 1092-1099.

Li, Y. et al. (2017). Evaluation Method of Rock Brittleness Based on Statistical Constitutive Relations for Rock Damage. *Journal of Petroleum Science and Engineering*, vol. 153, pp. 123–132., doi:10.1016/j.petrol.2017.03.041.

Li, Y. et al. (2018). Experimental of Hydraulic Fracture Propagation Using Fixed-Point Multistage Fracturing in a Vertical Well in Tight Sandstone Reservoir. *Journal of Petroleum Science and Engineering*, vol. 171, pp. 704–713., doi:10.1016/j.petrol.2018.07.080.

Li, Y. et al. (2020). A Hydraulic Fracture Height Mathematical Model Considering the Influence of Plastic Region at Fracture Tip. *Petroleum Exploration and Development*, vol. 47, no. 1, pp. 184–195., doi:10.1016/s1876-3804(20)60017-9.

Liu, W., Yu, B., and Deng, J. (2017). Analytical method for evaluating stress field in casing-cement-formation system of oil/gas wells. *Applied Mathematics and Mechanics*, *38*(9), 1273-1294.

Lund Snee, J. E., and Zoback, M. D. (2020). Multiscale Variations of the Crustal Stress Field Throughout North America. *Nature Communications*, *11*(1), 1-9.

Lund Snee, J. E. (2020). *State of Stress in North America: Seismicity, Tectonics, and Unconventional Energy Development* (Doctoral Dissertation, Stanford University).

Luo, Y., Shan, Y., Liu, H., Liu, W., Cao, W., and Wang, Y. (2020). Influence of the Initial Stress State of the Cement Sheath on the Casing-Cement Sheath-Formation System

Stress Distribution. American Rock Mechanics Association. ARMA 20-1868. September 18

Lynk, J. M., et al. (2017). Hydraulic Fracture Completion Optimization in Fayetteville Shale: Case Study. *International Journal of Geomechanics*, vol. 17, no. 2, Feb., p. 04016053., doi:10.1061/(asce)gm.1943-5622.0000713.

Matthews, C. S., and Russell, D. G. (1967). *Pressure Build-up and Flow Tests in Wells*. SPE Monograph Series Vol. 1. Henry L. Doherty Memorial Fund of AIME.

McClure, M., Picone, M., Fowler, G., Ratcliff, D., Kang, C., Medam, S., and Frantz, J. (2020). Nuances and Frequently Asked Questions in Field-Scale Hydraulic Fracture Modeling. Society of Petroleum Engineers. Jan 28, doi:10.2118/199726-MS

McNutt, M. K., et al. (2012). Applications of Science and Engineering to Quantify and Control the Deepwater Horizon Oil Spill. *Proceedings of the National Academy of Sciences*, vol. 109, no. 50, pp. 20222–20228., doi:10.1073/pnas.1214389109.

Michael, A. (2014). Economic Implications of the Current Geopolitical Forces Vis-à-vis Hydrocarbons on Global Energy Markets. Society of Petroleum Engineers. May 19, doi:10.2118/169832-MS

Michael, A. (2016a). Financial Impact of Price Volatility on the Oilfield Services Sector of the Petroleum Industry. Society of Petroleum Engineers. May 10, doi:10.2118/179962-MS

Michael, A. (2016b). *Hydraulic Fracturing Optimization: Experimental Investigation of Multiple Fracture Growth Homogeneity via Perforation Cluster Distribution*, Master's Report at the University of Texas at Austin.

Michael, A. (2019a). Orientation of Hydraulic Fracture Initiation from Perforated Horizontal Wellbores. Society of Petroleum Engineers. September 23, doi:10.2118/199766-STU

Michael, A. (2019b). The Net Present Value of a Hydraulic Fracture Treatment. Society of Petroleum Engineers. *The Way Ahead*, www.spe.org/en/twa/twa-article-detail/?art=5557

Michael, A., and Gupta, I. (2018). Fluid-Driven Fracture Initiation During Loss of Control Situations. Abstract (MR51B-0062) presented at 2018 AGU Fall Meeting, Washington, D.C., 10-14 December

Michael, A., and Gupta, I. (2019a). Analysis of Drilling-Induced Tensile Fracture Initiation in Porous, Permeable Media Considering Fluid Infiltration. American Rock Mechanics Association. ARMA 19-2053.

Michael, A., and Gupta, I. (2019b). Analysis of Fracture Initiation and Broaching Resulting from Worst Case Discharge Events. American Rock Mechanics Association. August 28

Michael, A., and Gupta, I. (2019c). Geomechanics of Post-Blowout Fracture Initiation and Broaching During Loss of Control in Offshore Wells. European Association of Geoscientists & Engineers. 81st EAGE Annual Conference and Exhibition. doi:10.3997/2214-4609.201900943

Michael, A., and Gupta, I. (2019d). Orientation of Hydraulic Fracture Initiation in Poroelastic Media: An Analytical Criterion for Perforated Wellbores. European Association of Geoscientists & Engineers. 81st EAGE Annual Conference and Exhibition. doi:10.3997/2214-4609.201901438

Michael, A., and Gupta, I. (2019e). Orientation Criteria of Fracture Initiation in Poroelastic Media: Application in Unconventional Reservoirs. Society of Petroleum Engineers. Jun 3, doi:10.2118/195494-MS

Michael, A., and Gupta, I. (2020a). A Semi-Analytical Modeling Approach for Hydraulic Fracture Initiation and Orientation in Shale Reservoirs. Unconventional Resources Technology Conference. Jul 20, doi:10.15530/urtec-2020-3137

Michael, A., and Gupta, I. (2020b). Analytical Orientation Criteria for Drilling and Completion-Induced Fracture Initiation Considering Fluid Infiltration from the Wellbore. *Journal of Petroleum Science and Engineering*, 107033, doi.org/10.1016/j.petrol.2020.107033

Michael, A., and Gupta, I. (2020c). Fracture Prevention Following Offshore Well Blowouts: Selecting the Appropriate Capping Stack Shut-In Strategy. Society of Petroleum Engineers. *SPE Drilling & Completions*, doi:10.2118/199673-PA

Michael, A., and Gupta, I. (2020d). Wellbore Integrity During Blowouts: Broaching Prevention and Control. Society of Petroleum Engineers. doi:10.2118/199673-MS

Michael, A., and Gupta, I. (In Press). A Semi-Analytical Modeling Approach for Hydraulic Fracture Initiation and Orientation from Perforated Wells. Society of Petroleum Engineers. *SPE Production & Operations*, doi:10.2118/204480-PA

Michael, A., and Habibi, A. (2018). Three Stress Shadowing Mitigation Techniques for Hydraulic Fracturing Operations: An Overview. Society of Petroleum Engineers. *The Way Ahead*, www.spe.org/en/twa/twa-article-detail/?art=4671

Michael, A., Olson, J. E., and Balhoff, M. T. (2018). Analysis of Hydraulic Fracture Initiation from Perforated Horizontal Wellbores. American Rock Mechanics Association. ARMA 18-029. August 21

Michael, A., Olson, J. E., and Balhoff, M. T. (2020). Orientation Prediction of Fracture Initiation from Perforated Horizontal Wells: Application in Shale Reservoirs. *Journal of Petroleum Science and Engineering*, 107355, doi.org/10.1016/j.petrol.2020.107355

Miller, C. K., Waters, G. A., and Rylander, E. I. (2011). Evaluation of Production Log Data from Horizontal Wells Drilled in Organic Shales. Society of Petroleum Engineers. doi:10.2118/144326-MS

Moos, D. (2012). Geosciences Technology Workshop (Hydraulic Fracturing). AAPG, *Search and Discovery Article #80533*, Sept. 14, www.searchanddiscovery.com/pdfz/documents/2012/80255moos/ndx_moos.pdf.html.

Mullineaux, D. R. (1970). *Geology of the Renton, Auburn, and Black Diamond Quadrangles, King County, Washington*. U.S. Government Printing Office.

Nabipour, A., Joodi, B., and Sarmadivaleh, M. (2010). Finite Element Simulation of Downhole Stresses in Deep Gas Wells Cements. Society of Petroleum Engineers. doi:10.2118/132156-MS

Nelson, E. J., et al. (2005). Transverse Drilling-Induced Tensile Fractures in the West Tuna Area, Gippsland Basin, Australia: Implications for the *In Situ* Stress Regime. *International Journal of Rock Mechanics and Mining Sciences*, vol. 42, no. 3, Apr., pp. 361–371., doi:10.1016/j.ijrmms.2004.12.001.

Nierode, D. E. (1985). Comparison of Hydraulic Fracture Design Methods to Observed Field Results. Society of Petroleum Engineers. Oct. 1, doi:10.2118/12059-PA

Olson, J. E. (1995). Fracturing from Highly Deviated and Horizontal Wells: Numerical Analysis of Non-planar Fracture Propagation. Society of Petroleum Engineers. doi:10.2118/29573-MS

Owens, K. A., Andersen, S. A., and Economides, M. J. (1992). Fracturing Pressures for Horizontal Wells. Society of Petroleum Engineers. doi:10.2118/24822-MS

315

Palmer, I. D., and Luiskutty, C. T. (1985). A Model of the Hydraulic Fracturing Process for Elongated Vertical Fractures and Comparisons of Results With Other Models. Society of Petroleum Engineers. doi:10.2118/13864-MS

Pearson, C. M., Bond, A. J., Eck, M. E., and Schmidt, J. H. (1992). Results of Stress-Oriented and Aligned Perforating in Fracturing Deviated Wells. Society of Petroleum Engineers. doi:10.2118/22836-PA

Perkins, T. K., and Kern, L. R. (1961). Widths of Hydraulic Fractures. September 1. Society of Petroleum Engineers. doi:10.2118/89-PA

Peška, P., and Zoback, M. D. (1995). Compressive and Tensile Failure of Inclined Well Bores and Determination of in Situ Stress and Rock Strength. *Journal of Geophysical Research: Solid Earth*, vol. 100, no. B7, pp. 12791–12811., doi:10.1029/95jb00319.

Peška, P., and Zoback, M. D. (1995). Observations of borehole breakouts and tensile wall-fractures in deviated boreholes: A technique to constrain in situ stress and rock strength. American Rock Mechanics Association.

Postler, D. P. (1997). Pressure Integrity Test Interpretation. Society of Petroleum Engineers. doi:10.2118/37589-MS

Prioul, R., Karpfinger, F., Deenadayalu, C., and Suarez-Rivera, R. (2011). Improving Fracture Initiation Predictions on Arbitrarily Oriented Wells in Anisotropic Shales. Society of Petroleum Engineers. doi:10.2118/147462-MS

Rybacki, E., et al. (2015). What Controls the Mechanical Properties of Shale Rocks? Part I: Strength and Young's Modulus. *Journal of Petroleum Science and Engineering*, vol. 135, pp. 702–722., doi:10.1016/j.petrol.2015.10.028.

Saint-Marc, J., Garnier, A., and Bois, A.-P. (2008). Initial State of Stress: The Key to Achieving Long-Term Cement-Sheath Integrity. Society of Petroleum Engineers. doi:10.2118/116651-MS

Schlumberger (2014). *Case Study: BroadBand Sequence Service Enables Successful Fracturing of Openhole Section*. Schlumberger, www.slb.com/~/media/Files/stimulation/case_studies/broadband_sequence_bakken_cs.pdf.

Sesetty, V., and Ghassemi A. (2018). Effect of Rock Anisotropy on Wellbore Stresses and Hydraulic Fracture Propagation. *International Journal of Rock Mechanics and Mining Sciences*, vol. 112, pp. 369–384., doi:10.1016/j.ijrmms.2018.09.005.

Shi, Y., Guo, B., Guan, Z., Xu, Y., and Zhang, B. (2017). Influence of the initial loaded state on the stress distribution of a wellbore system. *Journal of Petroleum Science and Engineering*, *157*, 547-557.

Simonson, E. R., Abou-Sayed, A. S., and Clifton, R. J. (1978). Containment of Massive Hydraulic Fractures. February 1. Society of Petroleum Engineers. doi:10.2118/6089-PA

Simpson, R. W. (1997). Quantifying Anderson's Fault Types. *Journal of Geophysical Research: Solid Earth*, vol. 102, no. B8, 10 Aug, pp. 17909–17919., doi:10.1029/97jb01274.

Sone, H., and Zoback, M. D. (2013). Mechanical Properties of Shale-Gas Reservoir Rocks — Part 1: Static and Dynamic Elastic Properties and Anisotropy. *Geophysics*, vol. 78, no. 5, doi:10.1190/geo2013-0050.1.

SPE Technical Report (2015). Calculation of Worst-Case Discharge (WCD). Society of Petroleum Engineers.

Tang, J. et al. (2018). Numerical Investigation of the Interactions between Hydraulic Fracture and Bedding Planes with Non-Orthogonal Approach Angle. *Engineering Fracture Mechanics*, vol. 200, pp. 1–16., doi:10.1016/j.engfracmech.2018.07.010.

Tang, J., Wu, K., Zuo, L., Xiao, L., Sun, S., and Ehlig-Economides, C. (2019). Investigation of Rupture and Slip Mechanisms of Hydraulic Fractures in Multiple-Layered Formations. Society of Petroleum Engineers. October 1, doi:10.2118/197054-PA

Tang, L., and Luo, P. (1998). The Effect of the Thermal Stress on Wellbore Stability. Society of Petroleum Engineers. doi:10.2118/39505-MS

Taylor, T., Waters, G. A., Sturm, S., Singh, M., Hamilton, D., Le Calvez, J. H., and Miller, C. K. (2013). Evaluating the Impact of Mineralogy, Natural Fractures and In Situ Stresses on Hydraulically Induced Fracture System Geometry in Horizontal Shale Wells. Society of Petroleum Engineers. doi:10.2118/163878-MS

Teufel, L. W., and Clark, J. A. (1984). Hydraulic Fracture Propagation in Layered Rock: Experimental Studies of Fracture Containment. February 1. Society of Petroleum Engineers. doi:10.2118/9878-PA

Teufel, L.W. (1979). An Experimental Study of Hydraulic Fracture Propagation in Layered Rock. PhD Dissertation. Texas A&M University. College Station, Texas.

Thiercelin, M. J., Dargaud, B., Baret, J. F., and Rodriquez, W. J. (1998). Cement Design Based on Cement Mechanical Response. Society of Petroleum Engineers. December 1, doi:10.2118/52890-PA

Trimborn, H. (1969) "Battle Shaping Up Over Offshore Oil," *Los Angeles Times*, February 2, p. 1.

Ulm, F.-J., and Coussy. O. (1996). Strength Growth as Chemo-Plastic Hardening in Early Age Concrete. *Journal of Engineering Mechanics*, vol. 122, no. 12, pp. 1123–1132., doi:10.1061/(asce)0733-9399(1996)122:12(1123).

Vakó, P., and Economides, M. J. (1995). *Hydraulic Fracture Mechanics*. Chichester: Wiley, Print.

Van de Ketterij, R. G., and de Pater, C. J. (1997). Experimental Study on the Impact of Perforations on Hydraulic Fracture Tortuosity. Society of Petroleum Engineers. doi:10.2118/38149-MS

Vasquez Cordoba, F. A. (2018). *Integrated Reservoir-Wellbore Nodal Analysis Workflow For Worst-Case Discharge Modeling*. *LSU Master's Theses*. 4762. https://digitalcommons.lsu.edu/gradschool_theses/4762

Voegele, M. D., Abou-Sayed, A. S., and Jones, A. H. (1983). Optimization of Stimulation Design Through the Use of In-Situ Stress Determination. June 1. Society of Petroleum Engineers. doi:10.2118/10308-PA

Von Mises, R. (1913). *Mechanik der festen Körper im plastisch deformablen Zustand*. Göttin. Nachr. Math. Phys., vol. 1, pp. 582–592.

Warpinski , N. (2016). "Fracture Growth in Layered and Discontinuous Media." *EPA*, Environmental Protection Agency, 7 Dec, www.epa.gov/hfstudy/fracture-growth-layered-and-discontinuous-media.

Warpinski, N. R., and Teufel, L. W. (1987). Influence of Geologic Discontinuities on Hydraulic Fracture Propagation (includes associated papers 17011 and 17074). February 1. Society of Petroleum Engineers. doi:10.2118/13224-PA

Warpinski, N. R., Schmidt, R. A., and Northrop, D. A. (1982). In-Situ Stresses: The Predominant Influence on Hydraulic Fracture Containment. March 1. Society of Petroleum Engineers. doi:10.2118/8932-PA

Waters, G. A., and Weng, X. (2016). The Impact of Geomechanics and Perforations on Hydraulic Fracture Initiation and Complexity in Horizontal Well Completions. Society of Petroleum Engineers. Sept 26, doi:10.2118/181684-MS

Waters, G. A., Lewis, R. E., and Bentley, D. (2011). The Effect of Mechanical Properties Anisotropy in the Generation of Hydraulic Fractures in Organic Shales. Society of Petroleum Engineers. doi:10.2118/146776-MS

Weddle, P., Griffin, L., and Pearson, C. M. (2018). Mining the Bakken II – Pushing the Envelope with Extreme Limited Entry Perforating. Society of Petroleum Engineers. doi:10.2118/189880-MS

Weijers, L., and de Pater, C. J. (1992). Fracture Reorientation in Model Tests. Society of Petroleum Engineers. doi:10.2118/23790-MS

Weijers, L., de Pater, C. J., Owens, K. A., and Kogsbøll, H. H. (1994). Geometry of Hydraulic Fractures Induced from Horizontal Wellbores. Society of Petroleum Engineers. May 1, doi:10.2118/25049-PA

Weijers, L. (1995). *The Near-wellbore Geometry of Hydraulic Fractures Initiated from Horizontal and Deviated Wells*, Ph.D. Thesis, Delft University of Technology, Delft, The Netherlands.

Willson, S. M. (2012). A Wellbore Stability Approach for Self-Killing Blowout Assessment. Society of Petroleum Engineers. doi:10.2118/156330-MS

Willson, S. M., Nagoo, A. S., and Sharma, M. M. (2013). Analysis of Potential Bridging Scenarios During Blowout Events. March 5. Society of Petroleum Engineers. doi:10.2118/163438-MS

Wiprut, D., et al. (1997). Constraining the Full Stress Tensor from Observations of Drilling-Induced Tensile Fractures and Leak-off Tests: Application to Borehole Stability and Sand Production on the Norwegian Margin. *International Journal of Rock Mechanics and Mining Sciences*, vol. 34, no. 3-4, doi:10.1016/s1365-1609(97)00157-3.

Wong, R. C. K., and Yeung, K. C. (2005). Structural Integrity of Casing and Cement Annulus in a Thermal Well Under Steam Stimulation. In *Canadian International Petroleum Conference*. Petroleum Society of Canada.

Yang, F. (2014). *Performance Comparison of Transverse and Longitudinal Fractured Horizontal Wells Over Varied Reservoir Permeability*, Master's Thesis at the Missouri Science & Technology University.

Yang, Y., and M. D. Zoback (2014). The Role of Preexisting Fractures and Faults during Multistage Hydraulic Fracturing in the Bakken Formation. *Interpretation*, vol. 2, no. 3, doi:10.1190/int-2013-0158.1.

Yuan, Z., Gardoni, P., Schubert, J., and Teodoriu, C. (2013). Cement failure probability analysis in water injection well. *Journal of Petroleum Science and Engineering*, *107*, 45-49.

Zaki, K. S., Dirkzwager, J. B., Hilarides, W. K., Connolly, P. T., Niemann, J., and Hawkins, J. G. (2015). Assessment of Fracture Containment and Broaching Resulting From Worst-Case-Discharge Events. March 1. Society of Petroleum Engineers. doi:10.2118/174079-PA

Zeng, F., Peng, F., Zeng, B., Guo, J., Pati, S., Zhang, S., and Chen, Z. (2019). Perforation orientation optimization to reduce the fracture initiation pressure of a deviated cased hole. *Journal of Petroleum Science and Engineering*, *177*, 829-840.

Zhang, F. et al. (2019). Investigating Hydraulic Fracturing Complexity in Naturally Fractured Rock Masses Using Fully Coupled Multiscale Numerical Modeling. *Rock Mechanics and Rock Engineering*, vol. 52, no. 12, pp. 5137–5160., doi:10.1007/s00603-019-01851-3.

Zhang, R., et al. (2018). Hydraulic Fracturing Initiation and Near-Wellbore Nonplanar Propagation from Horizontal Perforated Boreholes in Tight Formation. *Journal of Natural Gas Science and Engineering*, vol. 55, 2018, pp. 337–349., doi:10.1016/j.jngse.2018.05.021.

Zhang, X., Thiercelin, M. J., and Jeffrey, R. G. (2007). Effects of Frictional Geological Discontinuities on Hydraulic Fracture Propagation. Society of Petroleum Engineers. doi:10.2118/106111-MS

Zhu, H., et al. (2014). Hydraulic Fracture Initiation Pressure of Anisotropic Shale Gas Reservoirs. *Geomechanics and Engineering*, vol. 7, no. 4, pp. 403–430., doi:10.12989/gae.2014.7.4.403.

Zhuang, L., Kim, K.Y., Jung, S.G. et al. (2018). Effect of Water Infiltration, Injection Rate and Anisotropy on Hydraulic Fracturing Behavior of Granite. *Rock Mech Rock Eng* **52,** 575–589 (2019). https://doi.org/10.1007/s00603-018-1431-3

Zoback, M. D. (2014). *Reservoir Geomechanics*. Cambridge: Cambridge UP. Print.

Zoback, M. D., et al. (2003). Determination of Stress Orientation and Magnitude in Deep Wells. *International Journal of Rock Mechanics and Mining Sciences*, vol. 40, no. 7-8, pp. 1049–1076., doi:10.1016/j.ijrmms.2003.07.001.

Zoback, M. D., Rummel, F., Jung, R., and Raleigh, C. B. (1977). Laboratory hydraulic fracturing experiments in intact and pre-fractured rock. In *International Journal of*

Rock Mechanics and Mining Sciences & Geomechanics Abstracts (Vol. 14, No. 2, pp. 49-58). Pergamon. March

Zuo, Z., and Bennett, T. (2019). Simulation of the Degradation of Oilwell Cement for the Prediction of Long-Term Performance. *Construction and Building Materials*, *202*, 669-680.

Vita

Andreas Michael was born in Larnaca, Cyprus in 1989. After completing his secondary school studies at the American Academy of Larnaca he joined the Cyprus National Guard for two years of military service. In August 2010, he enrolled at The University of Texas at Austin, receiving his Bachelor's degree in December 2013 and Master's degree in May 2016. At Louisiana State University (LSU), he has conducted research on fluid-driven fracture initiation and orientation during drilling, completions, and loss of well control events. In 2019, he captained LSU's PetroBowl World Championship winning team and placed second in the Ph.D. Division of the International Student Paper Contest at the Society of Petroleum Engineer's (SPE) Annual Technical Conference and Exhibition (ATCE) in Calgary, Canada. He is the 2020 recipient of the Louis Cagniard Award from the European Association of Geoscientists and Engineers (EAGE) and is the Managing Editor (*de facto* Editor-in-Chief) of SPE's *The Way Ahead* magazine for Young Professionals for 2020-2021.